Imperial College London

Lead Isotope Tracing of Terrigenous, Hydrothermal and Anthropogenic Lead Sources in the Ocean

Yee Lap Leung

Imperial College London

Department of Earth Science and Engineering

Thesis submitted for the degree of Doctor of Philosophy (Ph.D.)

June 2023

Statement of Originality

I hereby declare that the content of this thesis is my own work under the supervision of Prof. Mark Rehkämper and Prof. Tina van de Flierdt. Any work of others presented in this thesis, published or otherwise, has been appropriately acknowledged and/or referenced.

Yee Lap Leung

Copyright Declaration

The copyright of this thesis rests with the author. Unless otherwise indicated, its contents are licensed under a Creative Commons Attribution-Non Commercial 4.0 International Licence (CC BY-NC).

Under this licence, you may copy and redistribute the material in any medium or format. You may also create and distribute modified versions of the work. This is on the condition that: you credit the author and do not use it, or any derivative works, for a commercial purpose.

When reusing or sharing this work, ensure you make the licence terms clear to others by naming the licence and linking to the licence text. Where a work has been adapted, you should indicate that the work has been changed and describe those changes.

Please seek permission from the copyright holder for uses of this work that are not included in this licence or permitted under UK Copyright Law.

Acknowledgements

First and foremost, I would like to express my deepest gratitude to my supervisors, Mark Rehkämper and Tina van de Flierdt, for inviting me – someone new to marine geochemistry, on board their science team and entrusting me with their precious samples to work on. They provided me with unceasing guidance, support, insights and patience throughout my PhD journey, and offered me the space in which I can develop the skills to become a junior research scientist. Both of them, being exceptionally busy academics, have dedicated significant amounts of their time to meet with me, to carefully review my manuscripts and to answer my (sometimes rather silly) questions. This thesis is a testimony of our partnership over the past five years.

My sincere gratitude goes to Richard Lee for his generous financial support of my PhD study through the gifting of the Lee Family Scholarship.

Furthermore, this thesis would not have been possible without contributions from the following collaborators: Alex Griffiths, Susan Little, Rhian O'Callaghan, Maeve Lohan, Alastair Lough, Joseph Resing, Bill Jenkins, Andrew Bowie and Melanie East.

I would also like to thank the examiners, Dominik Weiss and William Homoky, for their constructive comments that helped improve the final version of this thesis.

I would like to thank all members of the MAss Spectrometry and Isotope Geochemistry at Imperial College London (MAGIC) research group during my five years in the group, whom there are too many to be listed individually. Among them, enormous thanks go to the Katharina Kreissig and Barry Coles, for their technical expertise and their meticulous efforts in keeping the clean laboratories and the mass spectrometers running at exceptional standards. All the analytical work of this PhD would not have been possible without their support. A special thanks goes to Alex Griffiths for showing me the analytical side of things during my first year. He had been very patient in teaching me amid his extremely stretched final year. A big thanks to Hollie Packman for sharing her expertise in overcoming the analytical challenges during my research work. Both Alex and Hollie also deserve special thanks for their moral support throughout the past five years. I am very grateful for the companionships of the MAGIC members, especially since they were the only group of people that I could regularly meet face-to-face outside my household during a large part of my PhD research work, which took place at the height of the COVID-19 pandemic.

I would also like to extend my gratitude to other members of staff in the Department of Earth Science and Engineering whom I have crossed paths with over the past years. In particular, big thanks go to Philippa Mason, Steve Banham and Alan Spencer, who invited me to assist with their many lecture courses and field trips (both being physically present at or virtually 'flying' to the field sites!) These experiences were amazing, and they had enabled me to persevere through various difficult phases in my main PhD research.

Outside the academic realm, I would like to first give thanks to my mum and dad, whom I am hugely indebted to for their unconditional love and support. To my sister – thank you for bearing with me all these years, and it must be far from easy to live alongside a nerd who spent years in an ivory tower, oblivious to the lives of others. Big thanks also go to all my supportive friends and cell group members. Ben, Solomon, Jun Yi, Josh, Zi Kai and a few others – our fellowships have constantly kept me grounded in the fact that life is more than lead isotopes and analytical blanks. Stuart and Ollie are thanked for their encouragement and/or pastoral support over the course of my PhD. Tobias and Victor are thanked for their unwavering friendships. To Anson and Marco – after more than a decade, we have not grown weary of our exotic passions, which have been a key lifeline upon the inevitable monotonies within this PhD journey.

Finally, to the Lord – thank you!

Abstract

The anthropogenic perturbation of the oceanic lead (Pb) budget during the last 200 years has generated a unique Pb tracer that offers numerous applications for research in marine geochemistry. This thesis improves understanding of the marine sources and the internal cycling of Pb in the modern ocean. To this end, Pb concentrations and isotope compositions are presented for seawater and hemipelagic sediments, which are employed to study the terrigenous and hydrothermal fluxes of Pb to the oceans and the mechanisms responsible for the observed distribution of anthropogenic Pb in the ocean interior.

Lead and additional neodymium (Nd) isotope results are presented for two hemipelagic sediment core-tops from the Eastern Equatorial Pacific Ocean. The results suggest that proximal Mexican and Northern Andean sources dominate the detrital sedimentary component, with local weathering inputs impacting the dissolved deep water budgets of both elements. The data also indicate that Pb of hydrothermal origin is dispersed much more efficiently compared to Nd.

Dissolved Pb concentration and isotope data were obtained for five seawater depth profiles collected at and near the TAG Hydrothermal Field in the North Atlantic Ocean. Dissolved Pb deficits in the buoyant TAG plume demonstrate that hydrothermal activity can act as a net sink for dissolved seawater Pb, due to intense scavenging by hydrothermal particles. The results also reveal unexpected anthropogenic Pb isotope signatures in some seawater samples from the hydrothermal plume, which most likely reflect enhanced Pb exchange between sinking aerosol particles and ambient seawater.

Finally, dissolved Pb concentration and isotope data were obtained for two seawater depth profiles from the Southern Ocean. Together with previous data, the results provide a full meridional transect between Tasmania and Antarctica, which enables investigations of the sources of dissolved Pb, water mass origins and vertical flux dynamics in this poorly explored ocean region.

Table of Contents

Statement of Originality 2
Copyright Declaration 3
Acknowledgements 4
Abstract 6
Table of Contents 7
List of Tables 13
List of Figures 14

Chapter 1. Introduction 18
1.1 Lead Isotopes as a Tracer of the Ocean 19
1.1.1 The GEOTRACES Programme and Long-lived Radiogenic Isotope Tracers 19
1.1.2 Anthropogenic Pb as a Tracer of the Ocean 19
1.1.3 Aim of this Thesis 20
1.2 Geochemistry of Pb and its Isotopes 20
1.2.1 Chemical Properties and Distribution in the Terrestrial Reservoir 20
1.2.2 Lead Isotope Systematics 21
1.3 Mobilisation of Pb in the Earth's Surface Environment 22
1.3.1 Natural Sources 22
1.3.2 Anthropogenic Sources 23
1.4 Marine Pb Cycle 24
1.4.1 Inputs 24
1.4.1.1 Atmospheric Pathway 26
1.4.1.2 Fluvial Pathway 26
1.4.1.3 Hydrothermal Pathway 27
1.4.1.4 Benthic Fluxes at Continental Margins 28
1.4.2 Lead Speciation in Seawater 28
1.4.3 Particle Dynamics of Pb in the Ocean 29
1.4.4 Distribution 29

1.4.5 Internal Cycling 30
1.4.6 Output 31
1.5 Anthropogenic Pb Pollution as a Transient Tracer 32
1.5.1 Lead Isotope Variability of Anthropogenic Sources 32
1.5.2 Spatiotemporal Variability in Anthropogenic Pb Emissions over the Past Century 33
1.5.2.1 Northern Hemisphere 34
1.5.2.2 Southern Hemisphere 35
1.5.3 Fate of Anthropogenic Pb in the North Atlantic Ocean: the Bermuda Time Series 37
1.6 Tracing Natural Fluxes using Pb-Nd Isotopes 39
1.7 Neodymium Geochemistry 40
1.7.1 Chemical Properties and Isotope Systematics of Nd 40
1.7.2 The Marine Nd Cycle 41
1.8 Seawater Pb Concentration and Isotope Data, Analytical Challenges and Current Data Coverage 41
1.9 Research Objectives and Thesis Outline 43

Chapter 2. Lead Isotope Compositions of Seafloor Sediments in the Guatemala Basin, Eastern Equatorial Pacific Ocean: Implications for Terrigenous and Hydrothermal Inputs 46

2.1 Introduction 47
2.2 Setting and Samples 49
2.2.1 Atmospheric Circulation 49
2.2.2 Hydrographic Setting 49
2.2.3 Submarine Volcanism and Hydrothermal Activities 52
2.2.4 Studied Sites 52
2.2.5 Sampling 54
2.3 Analytical Methods 54
2.3.1 Sediment Digestion and Determination of Nd and Pb Concentrations 54
2.3.2 Sequential Acid-Reductive Leaching 55
2.3.3 Purification and Isotope Analyses of Nd 56
2.3.4 Purification and Isotope Analyses of Pb 56

2.4 Results 61
2.5 Discussion 62
2.5.1 Assessing Possible Analytical Artefacts in the Measured Pb-Nd Isotope Compositions 62
2.5.1.1 Efficacy in Isolating the Authigenic and Detrital Signatures 62
2.5.1.2 Bioturbation and Diagenesis 63
2.5.1.3 Anthropogenic Pb Contamination 64
2.5.2 Detrital Sediments: Characterisation of Potential Source Areas 67
2.5.2.1 Proximal terrestrial sources 69
2.5.2.2 Distal dust sources 69
2.5.3 Sources of Detrital Sediments 70
2.5.3.1 Regional detrital isotope signatures in the EEP 70
2.5.3.2 Detrital sources of MANOP Site H 70
2.5.3.3 Detrital sources of MANOP Site M 76
2.5.4 Water Mass Signatures and Hydrothermal Sedimentation 77
2.6 Conclusions 81
2.7 Researcher Contributions 81

Chapter 3. Lead and Hydrothermal Plumes in the Ocean: A Study at the TAG Hydrothermal Field, Mid-Atlantic Ridge 83

3.1 Introduction 84
3.1.1 Submarine Hydrothermal Activities and Metal Flux to the Ocean 84
3.1.2 Hydrothermal Activities and Marine Pb Cycling 84
3.1.3 This Study 86
3.2 Setting 87
3.2.1 Hydrographic Setting 87
3.2.1.1 Hydrography of the North Atlantic Ocean 87
3.2.1.2 Water masses in the vicinity of the TAG Hydrothermal Field 90
3.2.2 Geological Setting 91
3.3 Methods 92

3.3.1 Samples 92
3.3.2 Dissolved Pb Concentrations and Isotopes 93
3.3.3.1 Lead concentrations 93
3.3.3.2 Lead isotope compositions 94
3.3.3 Other parameters 97
3.4 Results 97
3.4.1 Distributions of Dissolved Pb Concentrations and Isotopes 97
3.4.2 Anomalous Samples 101
3.4.3 Distributions of Dissolved δ^3He, Mn and Fe 102
3.5 Discussion 105
3.5.1 Variabilities of Pb Concentrations and Isotope Compositions in the Upper Water Column 105
3.5.2 Intermediate and Deep Waters 107
3.5.3 Identification of the TAG Hydrothermal Plume 109
3.5.3.1 Tracers of hydrothermal plumes 109
3.5.3.2 Locations of the TAG hydrothermal plume 109
3.5.4 Hydrothermal Scavenging of Pb in the TAG Plume 110
3.5.4.1 Buoyant TAG plume 110
3.5.4.2 Neutrally buoyant TAG plume 112
3.5.5 Lead Isotope Variability Below 2500 m Depth – TAG Plume and Beyond 113
3.5.5.1 Lead isotope signatures 113
3.5.5.2 Covariations of Pb concentration and isotope composition: stable isotope fractionation versus mixing relationships 114
3.5.5.3 Dissolved-particulate exchange processes in the deep ocean 116
3.6 Conclusions 119
3.7 Researcher Contributions 120

Chapter 4. Lead Concentrations and Isotope Compositions along Southern Ocean GEOTRACES Section GS01 121

4.1 Introduction 122

4.2 The GS01 Expedition and Setting 125
4.2.1 The GEOTRACES GS01 Expedition and the SR3 Line 125
4.2.2 Geographical and Hydrographic Setting 125
4.2.2.1 Geographical setting 125
4.2.2.2 Frontal structure and oceanographic zones 126
4.2.2.3 Regional circulation 126
4.3 Methods 127
4.3.1 Sample Locations and Collection 127
4.3.2 Determination of Dissolved Pb Concentrations and Isotopes 128
4.3.3 Determination of the Dissolved Concentrations of Pb and Other Trace Metals at the University of Tasmania (UTAS) 129
4.4 Results 132
4.4.1 Water Mass Distributions 132
4.4.2 Dissolved Pb Concentrations and Isotopes 133
4.4.2.1 Subantarctic Zone (SAZ) 133
4.4.2.2 Latitudinal variations in Pb concentrations and isotopes across the GS01 transect 137
4.5 Discussion 137
4.5.1 Inter-laboratory Comparison of Dissolved Pb Concentration Data 137
4.5.2 Natural and Anthropogenic Sources of Pb to the Southern Ocean Sector South of Tasmania 141
4.5.3 Sources and Cycling of Pb in the Upper and Intermediate Waters of the SAZ (SASW, SAMW and AAIW) 144
4.5.3.1 Surface mixed layer (SASW) 144
4.5.3.2 Subsurface and intermediate depth layers (SAMW and AAIW) 144
4.5.4 Temporal Evolution of Dissolved Pb Concentrations in the SAZ 147
4.5.4.1 Upper and intermediate waters (2002-18) 147
4.5.4.2 Deep waters (2008-18) 148
4.5.5 Sources and Cycling of Pb in the Deep Water of the SAZ (UCDW and LCDW) 148
4.5.5.1 Advective inputs to UCDW (and LCDW) along the GS01 transect 149
4.5.5.2 Role of particulate exchange processes along the GS01 transect 150

4.6 Conclusions 153

4.7 Researcher Contributions 154

Chapter 5. Summary 155

5.1 Key Findings 156

5.1.1 Chapter 2: Terrigenous and Hydrothermal Inputs of Pb and Nd in the Eastern Equatorial Pacific Ocean 156

5.1.2 Chapter 3: Fluxes and Cycling of Pb Above and in the Vicinity of the TAG Hydrothermal Field 157

5.1.3 Chapter 4: Variations in the Sources of Input and the Redistribution Mechanisms of Pb across the Southern Ocean between Antarctica and Tasmania 157

5.2 Implications and Future Work 158

5.2.1 Terrigenous Provenance Tracing in the Eastern Equatorial Pacific Ocean 158

5.2.2 Hydrothermal Activities and the Marine Pb Cycle: Net Flux and Sources of Pb in the Hydrothermal Plume 158

5.2.3 Lateral Versus Vertical Fluxes of Pb in the Ocean Traced by Isotope Signatures 161

Bibliography 163

Appendices 199

Appendix 1. Literature Compilation of Source Signatures for the Eastern Equatorial Pacific Ocean (Chapter 2) 200

(1) Terrestrial Sources 200

(2) MORB 202

Appendix 2. Resin Coagulation during Nobias PA-1 Solid Phase Extraction (Chapter 3) 203

Appendix 3. Air Mass Back Trajectory Analyses for the TAG Hydrothermal Area (Chapter 3) 205

Appendix 4. Dissolved Pb Concentration Results and Isotope from the GEOTRACES Section GS01 by Griffiths (2019) (Chapter 4) 206

Appendix 5. Inter-Laboratory Comparison of Dissolved Pb Concentration Results from the GEOTRACES Section GS01 (Chapter 4) 208

Appendix 6. Behaviour of Pb in Hydrothermal Plumes along the GEOTRACES Section GS01 (Chapter 4) 211

Bibliography for the Appendices 214

List of Tables

Table 1.1. Estimates of the global natural and anthropogenic emissions of Pb during the late 20th century. 23

Table 2.1. Column chemistry procedure for the separation of Nd from sediment samples. 58

Table 2.2. Column chemistry procedure for the separation of Pb from sediment samples..... 58

Table 2.3. Isotope compositions and concentrations of Pb and Nd for the sediment samples from MANOP Sites H and M. 59

Table 3.1. Summary of the major endmember water masses and their potential density (σ_θ) ranges in the subtropical North Atlantic Ocean..... 89

Table 3.2. Information about the five GEOTRACES GA13 stations that were sampled for the determination of Pb concentrations and isotope compositions. 93

Table 3.3. Lead concentration and isotope data obtained for two in-house seawater reference materials and the GEOTRACES intercalibration sample GSP. 96

Table 3.4. Lead concentration and isotope data for filtered seawater samples from five depth profiles collected during the GEOTRACES GA13 section cruise. 100

Table 4.1. Summary of the major oceanographic fronts and zones along the SR3 line during the GEOTRACES GS01 section cruise in January/February 2018. 126

Table 4.2. Information about the eight stations with seawater depth profiles collected for Pb isotope analysis during the GEOTRACES GS01 section cruise. 128

Table 4.3. Summary of the water masses and characteristics along the SR3 line. 131

Table 4.4. Lead concentration and isotope data for seawater samples from the GEOTRACES section GS01 presented in this study..... 134

List of Figures

Figure 1.1. Conceptual illustration of the cycle of dissolved Pb (sources, internal cycling processes and sinks) in the modern global ocean..... 25

Figure 1.2. Plot of $^{206}Pb/^{207}Pb$ versus $^{208}Pb/^{207}Pb$ for aerosols sampled in different countries / regions and key Pb ore deposits..... 33

Figure 1.3. Historical trends of annual Pb emissions from road vehicles and all primary anthropogenic sources in various continental regions, 1930-2012. 36

Figure 1.4. (a) Map of the North Atlantic Ocean showing the location of the Bermuda Atlantic Time Series (BATS) station, and vertical profiles of dissolved (b) Pb concentrations ([Pb]) and (c) $^{206}Pb/^{207}Pb$ isotope ratios at the BATS station between 1984 and 2011..... 38

Figure 1.5. Global map showing the sampling locations with published GEOTRACES seawater Pb concentration and isotope data for depth profiles, as well as the sediment and seawater samples that were analysed for this PhD thesis. 42

Figure 2.1. Overview map of the Eastern Pacific Ocean, showing the annual mean wind field and the locations of MANOP Sites H and M of this study. 50

Figure 2.2. Map of the Eastern Equatorial Pacific Ocean showing the locations of the two MANOP sites of this study, other sampled sites referred to in the text and the ocean circulation regime..... 51

Figure 2.3. Vertical profiles of Pb and Nd isotope compositions and concentrations of sediments from MANOP Sites H and M. 61

Figure 2.4. Vertical profiles of the solid phase concentrations, elemental ratios and/or isotope ratios of various trace elements (Pb, Nd, Fe, Mn) and radionuclides (^{210}Pb, ^{137}Cs, $^{239, 240}Pu$) for ≤ 20 cm sediment depth at MANOP Sites H and M. 65

Figure 2.5. Plot of $^{208}Pb/^{204}Pb$ versus $^{206}Pb/^{204}Pb$ ratios for the bulk and leachate samples from MANOP Sites H and M and potential sources of anthropogenic contamination. 67

Figure 2.6. Map showing the major arid regions and mountain belts used to characterise the Pb-Nd isotope signatures of the terrigenous sediment sources across the western side of the American continent. 68

Figure 2.7. Plots of (a) $^{207}Pb/^{204}Pb$, (b) $^{208}Pb/^{204}Pb$, and (c) ε_{Nd} versus $^{206}Pb/^{204}Pb$ for the detrital sediment fractions from the two MANOP sites in comparison to the isotope compositions of potential source areas and previously published marine sediment data for the Eastern Equatorial Pacific Ocean. 71

Figure 2.8. Plots of (a) $^{207}Pb/^{204}Pb$, (b) $^{208}Pb/^{204}Pb$, and (c) ε_{Nd} versus $^{206}Pb/^{204}Pb$ for the detrital sediment fractions from the two MANOP sites in comparison to the bulk rock isotope compositions from the western and eastern sectors of the North American Basin and Range Province (BRP). 73

Figure 2.9. Maps of (a) $^{206}Pb/^{204}Pb$, (b) $^{208}Pb/^{204}Pb$, and (c) ε_{Nd} data for the detrital sediment fractions of MANOP Sites H and M and published values for other sediment samples in the Eastern Equatorial Pacific Ocean. 74

Figure 2.10. Plots of (a) $^{207}Pb/^{204}Pb$, (b) $^{208}Pb/^{204}Pb$, and (c) ε_{Nd} versus $^{206}Pb/^{204}Pb$ for the leachate fractions from the two MANOP sites in comparison to literature values of Fe-Mn sediments in the Pacific Ocean and potential lithological sources. 79

Figure 2.11. Plot of ε_{Nd} values for the leachate fractions from the MANOP sites in comparison to literature values of Fe-Mn sediments, potential lithological sources and present-day deep water measurements of dissolved Nd isotopes. 80

Figure 3.1. (a) Map of the North Atlantic Ocean, showing the locations of the GEOTRACES GA13 sampling stations near the TAG vent site that are relevant for this study and of other stations with previously published seawater Pb isotope data. (b) Enlargement of map (a) for the TAG Hydrothermal Field region and the GA13 seawater stations relevant for this study. 88

Figure 3.2. Hydrographic data for stations from the TAG hydrothermal area, sampled during the GEOTRACES GA13 expedition. 89

Figure 3.3. Vertical profiles of Pb concentrations ([Pb]), $^{206}Pb/^{207}Pb$, and $^{208}Pb/^{207}Pb$ for the four GA13 stations sampled for Pb concentrations and isotope compositions. 98

Figure 3.4. (a) Map showing the four GA13 sampling stations relevant to this study and (b-d) quasi-zonal section plots of (b) Pb concentrations, (c) $^{206}Pb/^{207}Pb$ ratios and (d) $^{208}Pb/^{207}Pb$ ratios..... 99

Figure 3.5. Vertical profiles of dissolved Pb, Mn and Fe concentrations, Pb and He isotope compositions as well as sensor data for samples collected from depths > 1500 m at the four GA13 stations in the TAG hydrothermal area. 103

Figure 3.6. Plots of $^{206}Pb/^{207}Pb$ versus $^{208}Pb/^{207}Pb$ ratios for GA13 seawater samples (a) from depths ≤ 400 m and (b) from depths ≥ 600 m, in comparison to relevant literature results for seawater, potential

sources of atmospheric aerosols for the study area, and archive data of historic surface seawater compositions. 104

Figure 3.7. Plots of $^{206}Pb/^{207}Pb$ and $^{208}Pb/^{207}Pb$ versus the inverse of [Pb] for seawater samples collected at depths ≤ 400 m from the GA13 stations in the TAG hydrothermal area and the GA03 stations across the subtropical North Atlantic Ocean..... 106

Figure 3.8. Vertical profiles of dissolved and particulate Pb, Mn and Fe concentrations and $^{208}Pb/^{207}Pb$ ratios in the buoyant TAG plume for samples from the GA13 and GA03 section cruises. 111

Figure 3.9. Cross plots of dissolved [Pb], [Mn] and Pb isotope ratios for the GA13 samples collected at depths > 2000 m from this study and GA03 stations USGT11-12 and USGT11-20. 112

Figure 3.10. Plot of $^{206}Pb/^{207}Pb$ versus $^{208}Pb/^{207}Pb$ ratios for the GA13 seawater samples collected at depths ≥ 2500 m for this study, in comparison to literature data of the potential sources of dissolved Pb for the deep water samples. 116

Figure 3.11. Conceptual illustration that summarises physicochemical mechanisms that drive reversible dissolved-particulate exchange of Pb in ambient seawater and in hydrothermal plumes. 118

Figure 4.1. Schematic illustration of the hydrography of the Southern Ocean between Australia and Antarctica. 123

Figure 4.2. (a) Map of the Atlantic Ocean, Indian Ocean and the Southern Ocean (Atlantic, Indian and Australian sectors), showing the locations of seawater sampling along the GEOTRACES GS01 transect and reference stations along the GEOTRACES section GI04 in the Indian Ocean and section GA10 in the South Atlantic Ocean. (b) Enlargement of map (a) showing the study area of Chpater 4, the GS01 cruise track along the WOCE SR3 line and the stations sampled for dissolved Pb concentrations and isotopes during the expedition. 124

Figure 4.3. Hydrography of the study area of Chapter 4, sampled during the GEOTRACES GS01 expedition..... 131

Figure 4.4. Meridional section plots of measured (a) Pb concentrations and (b) $^{206}Pb/^{207}Pb$ ratios along the GS01 transect. 135

Figure 4.5. Vertical depth profiles of Pb concentrations ([Pb]), $^{206}Pb/^{207}Pb$ and $^{208}Pb/^{207}Pb$ ratios for the eight stations sampled for Pb concentrations and isotopes from the GS01 transect. 136

Figure 4.6. Inter-laboratory (ICL and UTAS) comparison of measured Pb concentrations along the GS01 transect. 140

Figure 4.7. (a) $^{206}Pb/^{207}Pb$ versus $^{208}Pb/^{207}Pb$ ratios for all seawater samples from the GS01 transect in comparison to literature data. (b) $^{206}Pb/^{207}Pb$ ratios versus Pb concentrations for all seawater samples from the GS01 transect. 143

Figure 4.8. Profiles of $^{206}Pb/^{207}Pb$ versus neutral density ($\gamma^n > 27.0$) for four stations from the GS01 transect (stations 9, 23, 30 and 40) in comparison to published data from reference stations in the Atlantic and Indian Oceans. 146

Figure 4.9. Time series profiles of Pb concentrations obtained near three GS01 stations (SAZ stations 9 and 15; PFZ station 30) during the period 2002-2018. 146

Figure 4.10. Conceptual illustration of the explanatory models for the observed deep water Pb isotope variations across the oceanographic zones (AZ, PFZ and SAZ) along the GS01 section. 152

Figure 5.1. Summary illustration of the major findings in this thesis relevant to the Pb cycle in the modern global ocean. 160

Chapter 1

Introduction

1.1 Lead Isotopes as a Tracer of the Ocean

1.1.1 The GEOTRACES Programme and Long-lived Radiogenic Isotope Tracers

Trace elements and isotopes (TEIs) are ingredients and regulators of ocean processes, and they serve as chemical tracers of these processes. Constraints on the biogeochemical cycling of TEIs are key to understanding the physical, chemical and biological processes in the global ocean and to broader research areas such as climate change, carbon cycle and environmental pollution (GEOTRACES Planning Group, 2006). In light of advancements in clean sampling techniques and analytical techniques for a wide array of TEIs in the ocean, GEOTRACES was established as a coordinated global research programme almost two decades ago. The aim of the programme is to improve understanding of the modern distributions of key trace elements and their isotopes in the global ocean, and to evaluate the processes and quantify the fluxes that regulate these distributions (SCOR Working Group, 2007).

Within the range of key TEIs in the GEOTRACES programme, the radiogenic isotopes of lead (Pb) and neodymium (Nd) are designated as tracers of natural and/or anthropogenic sources of trace metals to the ocean. These radiogenic isotopes are generated by the slow decay of radioactive nuclides, which have half-lives that are comparable to or longer than the age of the solar system (4.56 Ga). This results in variations in the abundances of these radiogenic isotopes among the different crustal and environmental reservoirs of the Earth as a function of age (Goldstein and Hemming, 2003). In turn, these sources deliver the elements to the ocean with their distinct isotope signatures or 'fingerprints'. For Nd, any overprint of the radiogenic isotope variations by mass-dependent isotope fractionations is automatically corrected for during the analyses by internal normalisation to the constant ratio defined by two non-radiogenic isotopes of Nd (see review by White et al., 2000). For Pb, internal normalisation cannot be carried out as Pb has only one non-radiogenic isotope (^{204}Pb). However, as the relative mass differences between the isotopes of Pb are small (< 0.5%), mass-dependent Pb isotope fractionations are expected to be negligible in nature relative to radiogenic Pb isotope variations. Furthermore, both elements are characterised by average ocean residence times that are shorter than (Pb, ~10^1-10^2 years) or comparable to (Nd, ~10^3 years) the timescale of global ocean mixing (~1500 years), and spatial heterogeneities in the source signatures are preserved within the global ocean (Broecker and Peng, 1982; Frank, 2002). These properties, therefore, enable the applications of the two radiogenic isotope systems as tracers of the sources of the individual elements in the ocean.

1.1.2 Anthropogenic Pb as a Tracer of the Ocean

Lead is a non-essential, toxic trace element that naturally occurs at extremely low concentrations of < 15 pmol/kg in the open ocean (Schaule and Patterson, 1981; Henderson and Maier-Reimer, 2002; Kelly et al., 2009). Over the last two centuries, the budget of Pb in the global ocean has been heavily perturbed by anthropogenic sources, notably due to emissions associated with the worldwide

consumption of leaded petrol in vehicles throughout the 20th century (e.g. Boyle et al., 2014). Fortunately, these inputs did not produce bioavailable Pb concentrations in the open ocean that triggered harmful impacts on the marine ecosystem (Boyle et al., 2014).

The time-dependent, location-specific 'spiking' of anthropogenic Pb to the ocean, on the other hand, provides a unique opportunity to study the marine input pathways and cycling of Pb as well as to investigate various other oceanographic processes. As such, Pb and its isotopes resemble other transient anthropogenic pollutants, such as chlorofluorocarbons (CFCs) and tritium (^{3}H), which have been employed in marine research. The premise is that anthropogenic Pb inputs have a distinct isotope fingerprint compared to influxes of natural Pb within the same ocean region. When seawater Pb isotope data are available, the distinct Pb isotope fingerprints of natural and anthropogenic sources can be employed to reveal the type and location of key input sources and even the time when the Pb entered the ocean. This enables tracking of the migration of Pb in the ocean interior and of the processes that control its distribution, such as the movement of water masses and particulate dynamics. The advantage of Pb over the other transient tracers such as CFCs is twofold. First, the anthropogenic Pb emissions from different continental regions often exhibit distinct isotope fingerprints according to the sources of raw material in Pb-emitting activities, which enables better constraints on the source areas of water masses and in investigating the pathways of metal transport in the ocean. Second, whilst CFCs have largely been phased out over the last decade, Pb emissions and their fingerprints persist and continue to evolve with time and space, making the latter more useful in tracing water masses that were ventilated relatively recently.

1.1.3 Aim of this Thesis

This thesis is part of and contributes to the GEOTRACES research programme in improving understanding of the inputs and internal cycling of Pb in the modern ocean, through studies of the Pb (and Nd) concentrations and isotope compositions of carefully selected seawater and marine sediment samples from various regions of the global ocean. In detail, this thesis focuses on two ocean settings or regions that remain poorly explored for the cycling of Pb, encompassing (1) the vicinity of high-temperature hydrothermal activities and (2) the Southern Ocean.

1.2 Geochemistry of Pb and its Isotopes

1.2.1 Chemical Properties and Distribution in the Terrestrial Reservoir

Lead, with an atomic number of 82 and an atomic weight of 207.2, belongs to Group IVA of the periodic table. Metallic Pb is bluish white in colour and lustrous. It has high density (11.34 g/cm^3 at 20°C) but is soft, malleable and ductile and is resistant to corrosion. It is also a relatively volatile metal, with a low melting point of 327°C and a boiling point of 1749°C. Because of these properties and the relative ease of extraction, the human production and release of Pb has occurred for at least five

millennia (Settle and Patterson, 1980). Lead is highly toxic to most organisms and is known for its ability to accumulate in biological tissues.

Lead has three oxidation states: Pb(0) (metallic Pb), Pb(II) and Pb(IV). Metallic Pb is readily oxidised in the surface environment to form the soluble Pb(II), whilst Pb(IV), a powerful oxidising agent, is rare at the Earth's surface conditions. Therefore, Pb(II) is the predominant form of Pb in the environment. Divalent Pb forms a large range of inorganic salts with major anions, of which only the nitrate and acetate salts are soluble, whilst most other major salts are sparingly soluble, including salts of carbonate, oxide, chloride, sulphate, sulphide and hydroxide. Lead is chalcophilic (sulphur-loving) and is classified with other chalcophile elements, such as copper (Cu), zinc (Zn), cadmium (Cd) and silver (Ag), under the Goldschmidt classification, but also shows lithophilic properties with affinities to the oxygen atom and silicate phases.

Lead is a trace constituent in the Earth's crust with a bulk concentration of 15 ppm (Wedepohl, 1995) and an estimated crustal budget of about 2×10^{20} g (Rauch and Pacyna, 2009). Galena (PbS) is the primary ore mineral of Pb and is typically found in massive sulphide deposits. In the surface environments, galena readily oxidises to form secondary minerals such as plattnerite (PbO_2), cerussite ($PbCO_3$) and anglesite ($PbSO_4$). However, most of the crustal budget of Pb occurs as lattice substitutes in rock-forming phases, especially potassium feldspar, mica and apatite, which are largely hosted in felsic meta-igneous rocks and clastic sedimentary rocks. In the oceanic crust, the bulk concentration of Pb (0.6 ppm, White and Klein, 2014) is more than a factor of ~10 lower than in the continental crust. This reflects that Pb is depleted in the Earth's upper mantle, the source of mid-ocean ridge basalts. This depletion is a consequence of the complementary enrichment of Pb in the continental crust, due to the incompatible nature of Pb during melting of the mafic phases present in the mantle.

1.2.2 Lead Isotope Systematics

Lead has four naturally occurring stable isotopes: ^{208}Pb (52%), ^{206}Pb (24%), ^{207}Pb (23%) and ^{204}Pb (1%). Whilst ^{204}Pb is a primordial nuclide, ^{206}Pb, ^{207}Pb and ^{208}Pb are the final products of the radioactive decay of ^{238}U, ^{235}U and ^{232}Th. The latter radioactive parent isotopes have contrasting half-lives of 4.47 Ga, 0.704 Ga and 14.01 Ga, respectively (Jaffey et al., 1971). In Earth and environmental sciences, Pb isotope compositions are commonly expressed either as ratios of two radiogenic isotopes, such as ^{206}Pb/^{207}Pb and ^{208}Pb/^{207}Pb, or as ratios of a radiogenic isotope to the primordial ^{204}Pb, i.e. ^{206}Pb/^{204}Pb, ^{207}Pb/^{204}Pb and ^{208}Pb/^{204}Pb. For the characterisation of dissolved Pb sources in open ocean seawater, the determination of primordial ^{204}Pb poses significant analytical challenges due to its low abundance. As it was also shown that ^{20x}Pb/^{204}Pb ratios provide no significant advantages for tracing marine sources of Pb (Bridgestock et al., 2018), ratios of two radiogenic isotopes are more commonly used in marine geochemistry.

Lithological variations in Pb isotope compositions arise from variations in the relative abundances of U, Th and Pb, age and reservoir mixing processes. For example, a Th-enriched reservoir will have accumulated relatively high levels of thorogenic ^{208}Pb relative to uranogenic ^{206}Pb and ^{207}Pb over time. Due to the 0.704 Ga half-life of ^{235}U, most of the Earth's primordial inventory of ^{235}U has already decayed to ^{207}Pb, and variations in the relative abundance of ^{207}Pb in most geological reservoirs younger than 1 Ga are therefore small (Erel et al., 2001). However, Archean and Proterozoic Pb ores have unusually low $^{206}Pb/^{207}Pb$ and $^{208}Pb/^{207}Pb$ ratios, due to the more rapid radiogenic ingrowth of ^{207}Pb relative to ^{206}Pb and ^{208}Pb during earlier stages of the Earth's history. Furthermore, crustal processes, such as magmatism, metamorphism and hydrothermal activity, often involve mixing of reservoirs with distinct Pb isotope signatures, and this can generate a range of intermediate Pb isotope compositions (Patterson and Settle, 1987; Bollhöfer and Rosman, 2000). The large Pb isotope variations observed in the natural environment (e.g. > 30% for $^{206}Pb/^{207}Pb$ and $^{208}Pb/^{207}Pb$) can hence be used to accurately resolve different source signatures, and this ability is further enhanced through the use of two or more Pb isotope ratios.

1.3 Mobilisation of Pb in the Earth's Surface Environment

1.3.1 Natural Sources

Natural mobilisation of the lithospheric Pb budget into the Earth's surface environment is driven by volcanic activities and weathering processes (Nriagu, 1989; Rauch and Pacyna, 2009). This Pb budget is stored in soils, biomass, air and aquatic bodies.

Lead in soils was naturally released from bedrock materials through physical and chemical weathering. Lead exhibits low mobility in typical soils, in which only between less than 0.01% and 1% of Pb resides in dissolved form (Sauvé et al., 1998, 2000). The predominant fraction of soil Pb is strongly adsorbed to clay minerals, Fe oxides and particulate organic matter or forms insoluble secondary phases (e.g. Sauvé et al., 2000). The adsorption affinity of Pb thereby increases at more alkaline pH values (Sauvé et al., 2000). At circumneutral and alkaline pH (> 6), the predominant proportion of dissolved Pb in soil is complexed by dissolved organic matter (> 90%), and the activity of free Pb^{2+} ions is very low ($\leq 10^{-10}$ M) (Sauvé et al., 1997, 1998). At more acidic pH (3-6), mobilisation of Pb from particle surfaces is favoured and the activity of free Pb^{2+} ions increases ($\sim 10^{-5}$ M at pH = 3) (Sauvé et al., 1998). High levels of dissolved organic matter in soil solutions also favour mobility of Pb in soil solutions through the formation of stable organo-Pb complexes (Sauvé et al., 1998). Soil Pb is transferred into freshwater systems as suspended particles and dissolved solutes, and eventually transported into the oceans. Dissolved Pb in freshwater is largely complexed with inorganic (e.g., CO_3^{2-}, OH^-, SO_4^{2-}) and organic ligands (Town and Filella, 2002; Powell et al., 2009).

Prior to the massive release of Pb by human activities in recent centuries, the global natural emissions of Pb to the atmosphere were estimated to be $1.2 \pm 1.1 \times 10^{10}$ g per year (g/yr) (Table 1.1)

(Nriagu, 1989). Wind-blown soil dust and volcanic emissions account for about 60% of the natural inventory of Pb in aerosols, followed by release from biomass (30%) through biological emissions of organic matter and forest fires, and by sea salt sprays (10%) (Nriagu, 1989). The mean residence time of Pb in the lower atmosphere is short (~10 days), due to efficient deposition on land and ocean surfaces (Turekian, 1977; Balkanski et al., 1993). Understandably, the atmosphere is a small reservoir of Pb (2.0×10^{10} g) (Reuer and Weiss, 2002).

Table 1.1. Estimates of the global natural and anthropogenic emissions of Pb during the late 20th century.

Natural (1983 estimate)[a]		Anthropogenic				
Source	Pb Emission ($\times 10^9$ g)	Source	Pb Emission ($\times 10^9$ g)			
			1975[b]	1983[c]	1995[d]	2012[e]
Wind-blown soil dust	3.9	Coal combustion	14	8	12[f]	14
Volcanoes	3.3	Liquid fuel combustion	273[g]			
Forest fires	1.9	- Stationary sources		2		15
Biogenic	1.9	- Motor vehicles		248	89	2
Sea salt spray	1.4	Non-ferrous metal production	85	50	15	12
		Steel and iron production	50	8	3	2
		Waste incineration	9	24	0.8	0.01
		Miscellaneous	18	14	0.3	3
Total natural emission	12.4	Total anthropogenic emission	449	354	120	48

(a) Nriagu (1989).
(b) Nriagu (1979).
(c) Nriagu and Pacyna (1988). Mean values of the ranges of estimates given.
(d) Pacyna and Pacyna (2001).
(e) Zhu et al. (2020).
(f) Combined estimate for the combustion of coal and liquid hydrocarbon at stationary sources.
(g) Combined estimate for liquid fuel combustion in vehicles (petrol) and at stationary sources.

1.3.2 Anthropogenic Sources

Over the last century, human activities have dramatically increased the mobilisation of Pb to the environment, and anthropogenic sources have dominated the budgets and cycle of Pb across the atmosphere, soils and aquatic bodies (Patterson and Settle, 1987; Nriagu and Pacyna, 1988; Pacyna and Pacyna, 2001; Rauch and Pacyna, 2009). Major anthropogenic sources of Pb include the combustion of fossil fuels (coal and liquid fuel) at mobile and stationary sources, mining and smelting of non-ferrous metals, iron and steel manufacturing and waste incineration (Table 1.1).

Significant atmospheric Pb contamination can be traced back to the early 19th century in the Northern Hemisphere and the late 19th century in the Southern Hemisphere, following the post-industrial boom in metal production and fossil fuel consumption (Murozumi et al., 1969; Boutron and Patterson, 1987; Candelone et al., 1995; Vallelonga et al., 2002; Van de Velde et al., 2005; McConnell et al., 2014). However, the most significant episode of environmental Pb contamination in history

occurred throughout a large span of the 20th century (between the 1930s and 1990s), driven by the worldwide consumption of leaded petrol in motor vehicles. During this period, petrol consumption contributed to 60-70% of the global anthropogenic Pb emissions and dictated the trend of the latter, whilst non-ferrous metal production accounted for another 15% (Nriagu, 1979; Nriagu and Pacyna, 1988; Pacyna and Pacyna, 2001).

Tetraethyllead additive was first introduced to petrol in 1923, as an anti-knocking agent for vehicle combustion engines (Nriagu, 1990). Thereafter, the global consumption of Pb in vehicular petrol rose dramatically until a peak in the 1970s (Nriagu and Pacyna, 1988; Nriagu, 1990). In the year 1975, anthropogenic Pb emissions reached 4.5×10^{11} g/yr. This exceeded the natural Pb fluxes (of ~1.2×10^{10} g/yr) by an order of magnitude and thereby accounted for an overwhelming 97% of the total atmospheric inventory (Nriagu, 1979). Compelled by the recognition of the environmental health impacts of vehicular lead exhausts and the mandate for equipping combustion engine vehicles with catalytic converters that are susceptible to Pb poisoning, the phasing-out of leaded petrol by governments began in the early 1970s, starting with a few more developed countries (Japan, the USA and West Germany) and followed by the rest of the world over the subsequent five decades (Nriagu, 1990; Dörr et al., 1990; Ritchie, 2022). In 2021, Algeria became the last country to ban leaded petrol in road vehicles (UN Environment Programme, 2021). Furthermore, emissions from other industrial sectors also decreased following the implementation of advanced emission control technologies (von Storch et al., 2003; Zhu et al., 2020). As a result, the global emissions of Pb from anthropogenic sources have fallen successively, to $4.8 \pm 2.2 \times 10^{10}$ g/yr in 2012 (Zhu et al., 2020). However, even the latter emissions still overwhelmed the natural Pb fluxes and accounted for about 80% of the atmospheric Pb inventory.

1.4 Marine Pb Cycle

1.4.1 Inputs

A conceptual illustration of the marine Pb cycle is given in Figure 1.1. The key sources of dissolved Pb to the global ocean are the atmosphere and rivers, with possible contributions from hydrothermal emanations and continental margin sediments (Henderson and Maier-Reimer, 2002; Chen et al., 2023b).

Prior to major anthropogenic perturbations in recent centuries, the influx of dissolved Pb to the global ocean based on the transfer of marine Pb to authigenic sediments was estimated to be 1.3×10^{10} g/yr (Chow and Patterson, 1962). The contribution by aeolian particles in the forms of soil dust and volcanic aerosols is 3.0×10^{9} g/yr or 23% of the natural influx (Patterson and Settle, 1987), whilst the dissolved Pb flux from hydrothermal activities is limited to ~10^{8} g/yr or ~1% of the natural Pb input (Chen et al., 1986; German and Angel, 1995). The extent of contributions from fluvial materials remains a matter of debate, but this source likely acts as a dominant pathway for the natural Pb input to the ocean, in order to provide the missing ~70% of the natural input (Henderson and Maier-Reimer, 2002; Chen et al., 2023b).

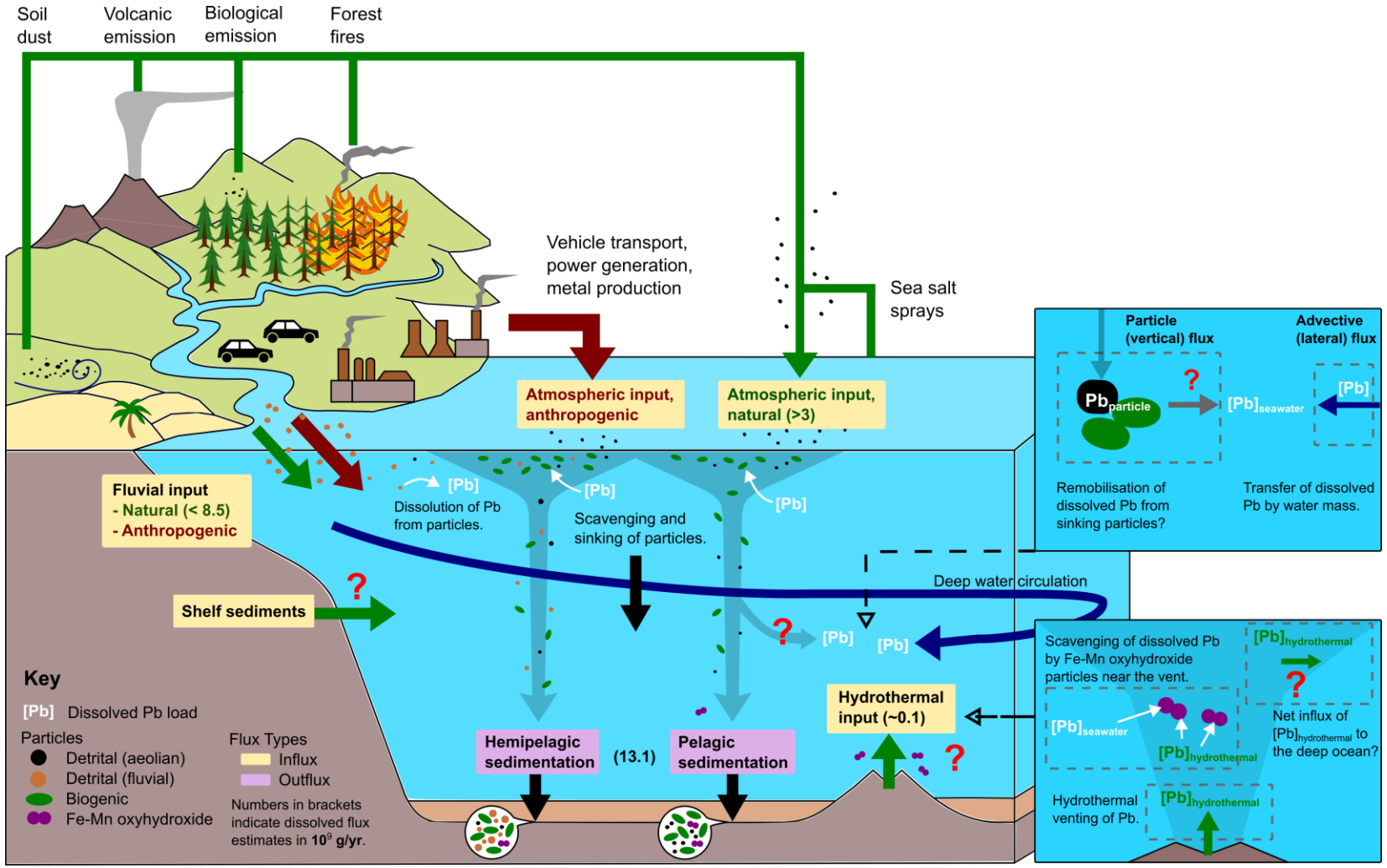


Figure 1.1. Conceptual illustration of the cycle of dissolved Pb (sources, internal cycling processes and sinks) in the modern global ocean. The inset figures on the right illustrate the (known and uncertain) sources and behaviour of dissolved Pb in the deep ocean and in the vicinity of hydrothermal activities, respectively.

The massive, rapidly evolving fluxes of Pb from human activities in recent centuries have significantly altered the Pb cycle in the modern ocean. Throughout the last century, atmospheric emissions of Pb increased beyond ~10 times the pre-anthropogenic level, whilst the riverine Pb loads also increased significantly (Patterson and Settle, 1987; Nriagu and Pacyna, 1988; Henderson and Maier-Reimer, 2002). Aeolian fluxes have become the dominant pathway of Pb input to the ocean (Schaule and Patterson, 1981; Patterson and Settle, 1987), favoured by the efficient transport and high Pb solubility of aerosols of anthropogenic origin (see Section 1.4.1.1). Furthermore, due to the rapid evolution of anthropogenic Pb influxes in comparison to a Pb residence time of ~10 to ~100 years in the ocean interior, the latter is, at present, in a transient rather than a steady state with respect to Pb and its isotopes (Schaule and Patterson, 1981; Boyle et al., 2014). In other words, the influxes are not in balance with the natural outflux as calculated from authigenic sedimentation rates. In the 1980s, close to the maximum global Pb emissions (in the early 1970s), anthropogenic Pb accounted for 95% of the dissolved Pb budget in North Atlantic surface waters (Weiss et al., 2003 and references therein). By the 2010s, global Pb emissions were reduced to ~10% of the mid-20th century maximum (Nriagu, 1979; Zhu et al., 2020), and the fractional contribution of anthropogenic Pb to the Pb inventory of Atlantic surface waters was found to have decreased to about 50-70% in 2011 (Bridgestock et al., 2016; Olivelli et al., 2023).

1.4.1.1 Atmospheric Pathway

Aerosol particles are key carriers of Pb inputs to the ocean. Atmospheric Pb of anthropogenic origin exhibits more efficient land-to-ocean transfer behaviour compared to that of natural origin (mainly mineral dust), due to the distinct physicochemical properties of the respective aerosol carriers. Anthropogenic Pb is released predominantly by high-temperature processes. The emitted gaseous Pb species adsorb to or react with fine particles in the atmosphere (Murphy et al., 2007; Cziczo et al., 2009), which enable their dispersal and deposition over long distances away from the emission sources (Reuer and Weiss, 2002). The anthropogenic Pb component in marine aerosols also shows enhanced solubility relative to the natural (mineral dust) component, which reflects the former generally residing in more labile halide, oxide and carbonate species and in finer particles, whilst the latter is typically bound in more refractory silicate species and in larger particles (Chester et al., 1989; Maring and Duce, 1990; Koçak et al., 2007; Fishwick et al., 2018).

1.4.1.2 Fluvial Pathway

Rivers transport the products of physical and chemical weathering from land to the ocean, in both dissolved and particulate forms (suspended and bed loads) (Viers et al., 2009). Even in the pre-anthropogenic world, the combined dissolved and particulate fluvial Pb input to the ocean was large (1.6×10^{12} g/yr) and exceeded the atmospheric emissions (1 to 9×10^{10} g/yr) by two orders of magnitude (Nriagu, 1989; Duce et al., 1991). However, direct contributions from dissolved fluvial Pb to the open

ocean are small and likely limited to ~10% of the natural Pb flux to the ocean (Chen et al., 2023b). This is attributed to the fact that only a small fraction (< 1%) of the fluvial Pb budget resides in the dissolved form (Viers et al., 2009), and the efficient scavenging of dissolved Pb in estuaries and near continental margins (Turekian, 1977; Benninger and Krishnaswami, 1981; Elbaz-Poulichet et al., 1984; Duce et al., 1991).

Nonetheless, mass balance calculation suggests a remaining flux imbalance of ~60% in the natural dissolved Pb budget, and a number of workers have argued that this is most likely supplied by fluvial particles through dissolved-particulate exchange reactions with seawater (von Blanckenburg et al., 1996; Vlastélic et al., 2001; Henderson and Maier-Reimer, 2002; Oelkers et al., 2012; Chen et al., 2023b). In particular, Chen (2023b) suggested that exchange with fluvial particles added about 6.1×10^9 g/yr (range: 4.8 to 7.4×10^9 g/yr) of dissolved Pb to the ocean. Such contributions from fluvial particles represent 36-56% of the pre-anthropogenic Pb flux, whereby the maximum estimate is able to balance the marine Pb budget.

1.4.1.3 Hydrothermal Pathway

Hydrothermal activity at mid-ocean ridges remains one of the key uncertainties in the understanding of marine Pb fluxes. High-temperature hydrothermal fluids are enriched in total Pb by 3 to 4 orders of magnitude relative to deep seawater (Von Damm et al., 1985; Chen et al., 1986; Chen, 1987; Hinkley and Tatsumoto, 1987; Douville et al., 2002), and would yield a gross dissolved Pb output on the order of $\sim 10^{10}$ g/yr to the global ocean (Chen et al., 1986; German and Angel, 1995). However, most early studies of Pb cycling associated with hydrothermal plumes suggested negligible contributions of hydrothermally derived Pb to the dissolved oceanic Pb budget, due to the rapid scavenging of dissolved hydrothermal Pb by hydrothermal particles near the vent sources (Trocine and Trefry, 1988; Mottl and McConachy, 1990; German et al., 1991a; Rudnicki and Elderfield, 1993). In particular, German and Angel (1995) estimated that no more than 1% of the dissolved Pb output from hydrothermal activities escaped into the overlying water column, which limits the net marine dissolved Pb flux from this source to $\sim 10^8$ g/yr.

Hydrothermally derived Pb can be identified by its distinct, mantle-like isotope signature. Lead isotope studies of seawater and sediments collected near hydrothermal systems concluded that dissolved Pb was scavenged from seawater, suggesting that hydrothermal systems are possibly a sink for dissolved Pb in the overlying water column (Godfrey et al., 1994; Noble et al., 2015; Boyle et al., 2020). However, significant contributions of hydrothermal Pb (of 20-30%) were found in authigenic sediments collected up to 1000 km away from the mid-ocean ridge sources, and this indicates that distal transport of hydrothermal Pb may be possible within the oceans (Barrett et al., 1987; van de Flierdt et al., 2004). These differing observations show that the fate of hydrothermal Pb in the oceans remains elusive.

1.4.1.4 Benthic Fluxes at Continental Margins

Dissolved-particulate exchange reactions between sediments and seawater at continental margins, also known as 'boundary exchange', have received increasing attention as a potential source or sink for the dissolved Pb budget in the ocean. In detail, near-bottom enrichments in dissolved Pb are observed in the Eastern Atlantic margin (Noble et al., 2015; Rusiecka et al., 2018) and the Northwest Pacific margin (Chien et al., 2017), which are attributed to the remobilisation of Pb from recently deposited and/or resuspended seafloor sediments. Furthermore, other observations in the margins of the Northeast Indian Ocean (Lee et al., 2015), Northwest Pacific Ocean (Chen et al., 2023a) and Equatorial Southeast Asia (Chen et al., 2023b) revealed contributions from local sediments to the Pb isotope compositions of deep water masses without concurrent enrichment in Pb concentrations. This suggests that two-way exchange of Pb between sediments and water masses are likely responsible for modifying the dissolved Pb isotope compositions of deep water masses, as the latter travel over continental margins.

1.4.2 Lead Speciation in Seawater

The stability and fate of dissolved Pb in seawater depend on its chemical speciation. In natural aquatic systems at circumneutral pH (6-8), dissolved Pb is largely complexed by inorganic carbonate and chloride ligands and by organic complexes (Powell et al., 2009; Woosley and Millero, 2013). In a model surface seawater environment (salinity = 35, ionic strength = 0.7) at pH = 8.2 and in equilibrium with a 25°C atmosphere, the inorganic speciation of dissolved Pb is dominated by complexes with carbonate ions ($PbCO_3$, $Pb(CO_3)Cl^-$, $Pb(CO_3)_2^{2-}$; 66%) and chloride ions ($PbCl^+$, $PbCl_2$, $PbCl_3^-$; 24%), whilst only about 2% of the dissolved Pb pool exists as free Pb^{2+} ions (Powell et al., 2009). At these model seawater conditions, the stability constant for $PbCO_3$ (aq), the most dominant inorganic Pb complex in slightly alkaline natural waters, is approximately $\sim 10^{5.4}$ (Powell et al., 2009; Woosley and Millero, 2013). In more acidic seawater environments, e.g., at pH ≤ 6.5, chloride complexes are the dominant group of inorganic Pb species (≈ 90%), whilst the proportions of free Pb^{2+} ions (8%) and Pb-sulphate complexes (2%) increase slightly (Powell et al., 2009).

In the presence of excess levels of dissolved organic matter, dissolved Pb forms organic complexes and the proportion of inorganic Pb species (including free Pb^{2+} ions) decrease. Sample analyses in the North Pacific Ocean showed that 35-52% of dissolved Pb in the seawater samples are organically complexed (Capodaglio et al., 1990; Ren et al., 2023). In estuarine and coastal environments, characterised by high concentrations of dissolved organic matter and low salinity, the degree of Pb-organic ligand complexation increases, for example to 67-94% in the Narragansett Bay estuary in Rhode Island, USA (Kozelka and Bruland, 1998; Wells et al., 1998) and to 61% in the Terra Nova Bay off Antarctica (Capodaglio et al., 1998). In such coastal settings, organic complexation hence dominates the speciation of dissolved Pb.

Whilst little is known about the composition of organic Pb-binding ligands in seawater, laboratory experiments showed that dissolved Pb preferentially binds to aromatic and humic over aliphatic substances in natural waters (Pinheiro et al., 1999; Chen et al., 2018). Furthermore, organic Pb-binding ligands in estuarine and open ocean surface waters generally appear to form labile complexes (Bi et al., 2013), with conditional stability constants on the order of ~10^8 to ~10^{12} (Capodaglio et al., 1990; Kozelka et al., 1997; Wells et al., 1998; Ren et al., 2023).

1.4.3 Particle Dynamics of Pb in the Ocean

Lead exhibits high particle reactivity in aquatic environments. Particle adsorption experiments found distribution coefficients (K_d = equilibrium particulate concentration / equilibrium dissolved concentration) for Pb in pelagic sediments on the order of ≥ ~10^5, which is significantly higher than K_d values for other key chalcophile elements (e.g., ~10^3 for Cu and Zn) (Li, 1991; Koschinsky et al., 2003).

Ferromanganese oxyhydroxides are the most important scavengers of Pb in the ocean. This is attributed to their high adsorption densities for Pb and the formation of strong multidentate, inner-sphere Pb complexes on the particle surfaces (Benjamin and Leckie, 1981; Brown and Parks, 2001). Lead is preferentially associated with the Fe phases, due to the dominant speciation of Pb in seawater as neutral or anionic carbonate complexes (e.g. $PbCO_3$, $Pb(CO_3)_2^{2-}$), which can adsorb to the slightly positively charged surface of amorphous Fe oxyhydroxides (Koschinsky et al., 2003; Koschinsky and Hein, 2003). Nevertheless, adsorption by Mn oxides is potentially important in some settings, since a fraction of dissolved Pb exists as cationic chloride complexes (e.g. $PbCl^+$), which adsorb preferentially to the slightly negatively charged surface of Mn oxides (Dong et al., 2000; Koschinsky et al., 2003). Furthermore, Pb exhibits strong adsorption to particulate organic matter, phosphate minerals (e.g., apatite), and to some extent, aluminosilicate clay minerals (Lion et al., 1982; Dong et al., 2000; Koschinsky et al., 2001, 2003).

Whilst Pb has no known biological function, it can become adsorbed ('passively scavenged') onto the surfaces of biogenic particles (Bruland et al., 2014; Cullen and McAlister, 2017). Experimental studies based on radioactive ^{210}Pb demonstrated its presence in both calcium carbonate tests and the organic matter embedded in the tests and cell walls of diatoms (Fisher et al., 1983; Chuang et al., 2014; Lin et al., 2017). However, the significance of these biogenic particles in marine Pb scavenging is likely overwhelmed by the more important adsorption to Fe-Mn oxyhydroxide phases (Koschinsky et al., 2001, 2003).

1.4.4 Distribution

Lead is present in the global ocean at low dissolved concentrations in the range of picomoles (10^{-12} mol) per kilogram. Lead and other highly reactive trace metals, such as Al, Th, Mn and Co, are classified as 'scavenged-type' elements in the ocean, as they are readily removed from the water column by adsorption onto and/or reaction with particles in the water column followed by eventual deposition of

the particles as sediments, a process that is known as 'scavenging' (Goldberg, 1954; Turekian, 1977). The high particle reactivity of Pb results in its relatively short marine residence time. The residence time of Pb in the surface mixed layer is about 2 years or shorter (Bacon et al., 1976; Nozaki et al., 1976), whilst estimates of its residence time in the ocean interior range from several decades up to about 400 years (e.g. Henderson and Maier-Reimer, 2002).

Scavenged-type metals typically exhibit maximum concentrations in the upper ocean and decreasing concentrations at depth and along the flow paths of deep water masses (Bruland et al., 2014). This is due to continued scavenging of the dissolved trave metals in the deeper water masses. The scavenged-type behaviour of Pb is hence also reflected in the inferred pre-anthropogenic marine distribution, which was characterised by an extremely low mean ocean concentration of about 2 pmol/kg (Henderson and Maier-Reimer, 2002), with higher concentrations, for example of 15 pmol/kg in North Atlantic surface waters, in the upper ocean (Kelly et al., 2009).

Anthropogenic inputs during the last century have led to significant perturbations to both the budget and distribution of dissolved Pb concentrations across the global ocean. In the North Atlantic Ocean, which is surrounded by highly industrialised nations, Pb concentrations, [Pb], of up to ~200 pmol/kg were observed in open surface waters near Bermuda in the 1970s, during the time of peak anthropogenic Pb emissions in the region (Boyle et al., 2014). Due to the rapid evolution of anthropogenic Pb influxes in comparison to the Pb residence time of ~10 to ~100 years in the ocean interior, the intermediate and deep water masses are in a transient rather than a steady state with respect to Pb and its isotopes (Schaule and Patterson, 1981; Boyle et al., 2014). In other words, the observed Pb distributions in the modern ocean reflect the spatiotemporal evolution of predominantly anthropogenic inputs, rather than the typical distribution for a scavenged-type element with steady input fluxes.

1.4.5 Internal Cycling

The dissolved Pb inputs to the surface waters are exported into the ocean interior through the lateral advection of water masses along isopycnals (surfaces of constant density) (Boyle et al., 1986; Shen and Boyle, 1988; Sherrell et al., 1992; Alleman et al., 1999; Noble et al., 2015). Further export is mediated by the scavenging of dissolved Pb in the upper ocean by particles. As these particles sink through the water column, they may partially release or exchange their Pb content in the deep ocean, thus providing a vertical shuttle of Pb from the upper into the deep ocean (Wu et al., 2010; Zurbrick et al., 2017; Lanning et al., 2023).

The relative roles of advection and exchange processes in the down-column export of Pb appear to vary significantly between different ocean basins. In the North Atlantic Ocean, which is characterised by rapid ventilation and strong deep water circulation, lateral advection appears to be primarily responsible for the down-column transfer of the anthropogenic Pb spike (Boyle et al., 1986; Shen and Boyle, 1988; Sherrell et al., 1992; Alleman et al., 1999; Noble et al., 2015; Bridgestock et al., 2018). In

other ocean regions, a vertical Pb flux, facilitated by particle sinking and Pb exchange, appears to play a more significant role in shuttling the recent input of anthropogenic Pb into deeper waters. In the deeper, poorly ventilated water (> 1500 m) of the North Pacific Ocean (North Pacific Deep Water), which has a ^{14}C circulation age of about 900 years (Matsumoto, 2007), the recent detection of a predominantly anthropogenic Pb signature suggests a major role of particulate processes in the down-column transfer of Pb (Wu et al., 2010; Zurbrick et al., 2017; Lanning et al., 2023). Lee et al. (2015) also found isotope evidence of particle-mediated transfer of anthropogenic Pb into the weakly ventilated deep waters of the North Indian Ocean.

The down-column transfer of Pb in the Southern Ocean is poorly understood, owing to the extremely limited availability of deep seawater data for this ocean region (Lee et al., 2015; Ndungu et al., 2016). The Southern Ocean is a key conduit for the transfer of reactive trace metals across the global ocean. It is where deep water masses from all meridional ocean basins upwell to the surface and sink to form the Antarctic Bottom Water (AABW), which flows northward to fill the deepest portions of all ocean basins (Marshall and Speer, 2012; Talley, 2013). It is also the site of ventilation for the key intermediate depth water masses, of Subantarctic Mode Water (SAMW) and Antarctic Intermediate Water (AAIW), in the meridional ocean basins (McCartney, 1977, 1982; Hanawa and Talley, 2001). The Southern Ocean is characterised by strong physical circulation, notably the Antarctic Circumpolar Current (ACC), a powerful current system that moves eastward across the entire zonal extent of the Earth. Therefore, lateral advection is suspected to be important for the Pb budget of the Southern Ocean interior, akin to the cycling of Pb in the Atlantic Ocean. However, further observational data are required to assess the transfer mechanisms of Pb in this ocean region.

1.4.6 Output

Marine sediments, which form as suspended particles deposit slowly from the overlying water column, act as the ultimate marine sink of many trace metals, including Pb. The pelagic sediments that are deposited in the ocean interiors are mainly comprised of terrigenous detritus (aluminosilicates and silicates) of predominantly aeolian origin, biogenic oozes (calcium carbonate, silica and particulate organic matter), and authigenic minerals (mainly Fe-Mn oxyhydroxides) that precipitate slowly from the deeper part of the water column (Li and Schoonmaker, 2014). Ferromanganese oxyhydroxide phases typically account for only a tiny fraction (~1% by weight) of pelagic sediments but are significantly more abundant near hydrothermally active mid-ocean ridges (Boström et al., 1969; Lam et al., 2015). Along the continental margins of the ocean basins, terrigenous detritus originating from rivers and marine shelves are transported by turbidity and bottom currents and they dominate the terrigenous sediment supply there. These proximal sediments are commonly termed ‘hemipelagic sediments’, to be distinguished from the pelagic sediments of open ocean environments.

1.5 Anthropogenic Pb Pollution as a Transient Tracer

The utility of anthropogenic Pb as a marine tracer has been increasingly explored over the last four decades, based on a growing volume of dissolved Pb concentration and isotope data for the global ocean. Such data can be compared against the isotope fingerprints of emission sources and the historical emission trends to establish the provenance of dissolved Pb throughout the water column. In particular, the Pb signatures of surface waters have been employed to track the spatiotemporal evolution of anthropogenic Pb inputs at decadal and even shorter timescales (Véron et al., 1993; Wu and Boyle, 1997; Weiss et al., 2003; Kelly et al., 2009; Bridgestock et al., 2016; Olivelli et al., 2023). In contrast, the Pb signatures of the ocean interior have been employed to understand the internal cycling of Pb, including the role of particle scavenging in the vertical transfer of Pb in the water column (Boyle et al., 1986; Wu et al., 2010; Chen et al., 2016a), and the pathways and timescales of ocean ventilation (Boyle et al., 1986; Shen and Boyle, 1988; Lee et al., 2015; Noble et al., 2015; Bridgestock et al., 2018; Zurbrick et al., 2018).

1.5.1 Lead Isotope Variability of Anthropogenic Sources

Figure 1.2 illustrates the Pb isotope variability of major ore deposits used in Pb production and the atmospheric emissions from various relevant regions. The Pb isotope signatures of late 20th century atmospheric particles from different continental regions reflect, to a first order, the provenance of Pb ores used for the manufacturing of leaded petrol across those regions.

Aerosols from Eurasia (except East Asia), North Africa and most Southern Hemisphere regions (Southern Africa, Australia and Patagonian South America) exhibit low $^{206}Pb/^{207}Pb$ (1.06-1.16) and $^{208}Pb/^{207}Pb$ (2.33-2.45) ratios that define a well-defined linear array on a three isotope ($^{206}Pb/^{207}Pb$-$^{208}Pb/^{207}Pb$) plot. This reflects the common use of tetraethyllead additives sold by Associated Octel Ltd., which were manufactured with ores from Australia, Morocco, Sweden and Canada (Véron et al., 1999; Bollhöfer and Rosman, 2001). In particular, Australian (Broken Hill-type) ores accounted for ≥ 50% of the ore mixtures used in tetraethyllead production by the company (Véron et al., 1999), and these are characterised by very low $^{206}Pb/^{207}Pb$ (1.04) and $^{208}Pb/^{207}Pb$ (2.32) ratios (Doe and Stacey, 1974; Townsend et al., 1998). The high-$^{206}Pb/^{207}Pb$ (1.19-1.22) signatures of aerosols from the USA reflect use of tetraethyllead from Ethyl Corporation, which was produced with Mississippi Valley-type (MVT) ores from southeast Missouri and the Tri-State region of the USA (Sangster et al., 2000). Aerosols from other parts of the American continent, such as Canada, Mexico and Brazil, exhibit intermediate and wider ranges of $^{206}Pb/^{207}Pb$ (1.14-1.20) and $^{208}Pb/^{207}Pb$ (2.41-2.46), which reflects the mixing of diverse emission sources (tetraethyllead and other industrial sources) that employed MVT, Mexican-Peruvian and Broken Hill-type ores (Bollhöfer and Rosman, 2000, 2001). Chinese aerosols are characterised by distinctively low $^{206}Pb/^{207}Pb$ ratios for a given $^{208}Pb/^{207}Pb$, which reflects the Pb isotope signatures of domestic lead-zinc ores that dominate the emissions (Bi et al., 2017).

Whilst the Pb isotope compositions of aerosols from some continental regions overlap, the Pb signatures of many regions that border ocean basins are distinguishable. For example, among the key Pb input sources to the North Atlantic Ocean during the 1990s, North American (mainly USA) emissions with their high $^{206}Pb/^{207}Pb$ (1.19-1.22) fingerprints can be discriminated from European and North African emissions with lower $^{206}Pb/^{207}Pb$ (< 1.16) ratios. Hence, the relative contributions of Pb influxes from these two major source regions, which have distinct isotope fingerprints, can be determined from the measured $^{206}Pb/^{207}Pb$ and $^{208}Pb/^{207}Pb$ ratios in North Atlantic seawater.

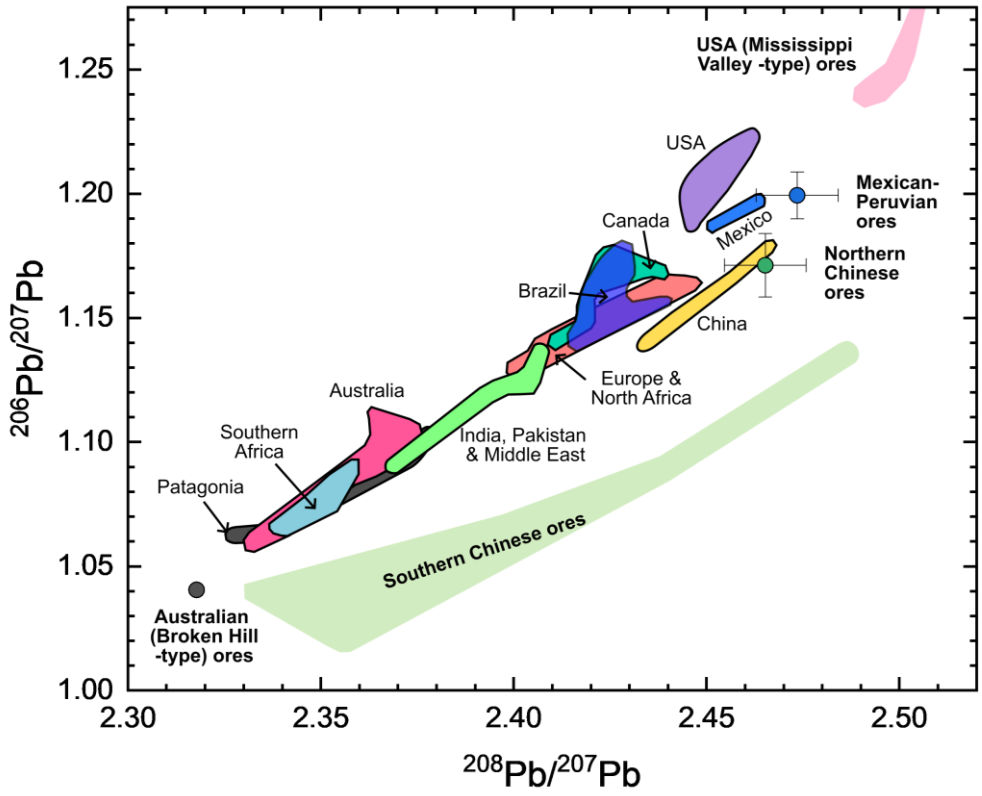


Figure 1.2. Plot of $^{206}Pb/^{207}Pb$ versus $^{208}Pb/^{207}Pb$ for aerosols sampled in different countries / regions and key Pb ore deposits. The compositional ranges of atmospheric aerosol leachates (Bollhöfer and Rosman, 2000, 2001) are shown as coloured fields with borders. The compositions of ore deposits (Sangster et al., 2000 and references therein) are shown as mean with 1 SD error bars and/or as borderless fields.

1.5.2 Spatiotemporal Variability in Anthropogenic Pb Emissions over the Past Century

Anthropogenic Pb emissions exhibit significant regional variations in time and magnitude, owing to the global disparities in the trends of socioeconomic development and implementation of environment policies. The inventories of anthropogenic Pb emissions for major continental regions were compiled for the period of 1930-2012 from published literature and reports and are summarised

in Figure 1.3. Across all continental regions, Pb emissions increased during the mid-20th century, with distinct regional peaks reached in the 1970s, followed by a decline towards the most recent decade.

1.5.2.1 Northern Hemisphere

The high historical Pb emissions from North America and Europe reflect the early industrialisation and economic development of these regions throughout the 20th century. The USA was the largest consumer of leaded petrol by country, which alone contributed to half of the global vehicular emissions of Pb (Fig. 1.3a). Between 1950 and 1980, anthropogenic Pb emissions in the USA exceeded 100 thousand metric tonnes per year (kt/yr; = 10^9 g/yr) and peaked at > 230 kt/yr in the early 1970s. Until the late 1970s, petrol Pb emissions in Mexico and Canada were estimated to each have amounted to less than 10% of the USA inventory. In Europe, peak Pb emissions (159 kt/yr in 1975) were lower than that in North America despite a similar population, due to the use of smaller and more efficient combustion engines (Fig. 1.3b) (Nriagu, 1990). The European part of the former USSR was the largest European Pb emitter during the late 20th century, contributing 30-50% of the European emissions during this period (Pacyna and Pacyna, 2000). Nearly 40% of the petrol Pb emissions in Europe in the 1970s were from the UK, Germany, France and Italy.

Lead emissions in North America and Europe began to decrease after about 1975. The USA was one of the earliest countries to limit the Pb content in petrol and introduce unleaded petrol (Nriagu, 1990). Consequently, Pb emission in the USA decreased drastically between the 1970s and 1990s, and by 1990, its Pb emission dropped to 5-10% of the 1970 level. Lead emissions in Mexico and Canada also decreased throughout the 1980s (Loranger and Zayed, 1994; Soto-Jimenez et al., 2006). Mexican emission reached a peak in 1980 (20 kt/yr for petrol Pb emission) and decreased thereafter, albeit at a slower pace compared to the USA. Hence, at about 1990, Mexico became the largest Pb emitter in North America, exceeding the USA (Pacyna and Pacyna, 2001). Most European countries only began to significantly reduce the Pb content in petrol in the 1980s (see review by von Storch et al., 2003). In 1990, Pb emissions in Europe (58 kt/yr) were still at about 37% of the peak level in 1975. As a result of the slower phasing-out of leaded petrol, Europe overtook North America as the dominant Pb-emitting continent bordering the North Atlantic Ocean in the 1980s. In the 2000s, anthropogenic Pb emissions in both North America and Europe diminished to less than 10 kt/yr and continued to decline.

Continent-wide emission inventories for Asia and Africa are only available from 1989 (Fig. 1.3c-d). Whilst the Asian inventory has an overall declining trend over the past three decades, Pb emissions in many Asian countries (especially China, India and various Southeast Asian countries) increased during the 1980s and 1990s, driven by their accelerating socioeconomic development and weaker environmental regulations (Fig. 1.3c) (Pacyna and Pacyna, 2001; Lee et al., 2014; Chen et al., 2016b). In China, anthropogenic Pb emission doubled from 1980 to 2000, followed by a sharp decline in 2001 as the phasing-out of leaded petrol in China was completed (Tian et al., 2015). Furthermore, Asian emissions were sustained by sources other than motor vehicles, particularly coal combustion and non-

ferrous and ferrous metal production, which continued to increase over the past decades (Pacyna and Pacyna, 2001; Zhu et al., 2020). As a result, Pb emission slowly increased in China even after the official cessation of leaded petrol consumption in 2001, regaining 70% of the year 2000 level by 2012. Asia has overtaken Europe as the largest Pb-emitting continent since the mid-1990s, accounting for 45% of the global Pb emission in 1995 (51 kt/yr) and rising to 61% in 2012 (29 kt/yr) (Zhu et al., 2020).

Historical Pb emissions from the African continent have been low relative to the other continental regions of the Northern Hemisphere (Fig. 1.3d). In 1990, the anthropogenic Pb emissions from the African continent and for Africa north of the Equator were 16 and 10 kt/yr respectively (Nriagu et al., 1996). The latter source, which contributes to the Pb budget of the North Atlantic atmosphere, contributed only a small proportion (17%) of the concurrent European emission. The African emissions have declined more slowly over the past three decades than the European and North American emissions. In 2012, the anthropogenic Pb emissions of the African continent were 5.6 kt/yr, which were similar to or slightly exceeded those of Europe (4.9 kt/yr) and North America (3.0 kt/yr), respectively (Zhu et al., 2020).

1.5.2.2 Southern Hemisphere

Anthropogenic Pb emissions from the continental regions of the Southern Hemisphere, encompassing Africa south of the Equator, South America and Oceania, have been low relative to those of the Northern Hemisphere. Over the last three decades, the anthropogenic Pb emissions of all three regions evolved roughly in sync, with each region having emissions of 6-15 kt/yr in 1990, which decreased by a factor of ~2 by the 2010s (Fig. 1.3d-f). South Africa was the largest Pb-emitting country in Africa in the late 20th century, contributing about 70% to the Pb emissions from across Africa south of the Equator in 1990 (Nriagu et al., 1996).

In South America, Pb emissions peaked at ≥ 13 kt/yr in 1980, falling short of the concurrent emissions of Mexico (20 kt/yr, petrol Pb emission only) (Fig. 1.3e). South American emissions began to decline in the 1980s, whilst their contribution to the global anthropogenic Pb inventory has grown. In particular, Chile was reported to be the fourth largest Pb-emitting country in 2012 (after China, Iraq and Afghanistan) with the highest Pb emission intensity, due to its non-ferrous metal production industry (Zhu et al., 2020).

The Pb inventory of Oceania is dominated by Australian emissions, which generally followed the trend defined by the USA and European countries (Fig. 1.3f). Petrol Pb emission in Australia plateaued between 1971 and 1984 at 7-8 kt/yr, followed by a decline. The initial decline in the 1980s was subtle, due to variable legislative schedules between different Australian state governments on the phasing-out of leaded petrol (Kristensen, 2015). A sharp decline in Australian Pb emissions occurred in the mid-1990s when a nationwide limit on petrol Pb concentration (of 0.2 g/L) was introduced, and in 2002 when leaded petrol was banned across the country (Kristensen, 2015).

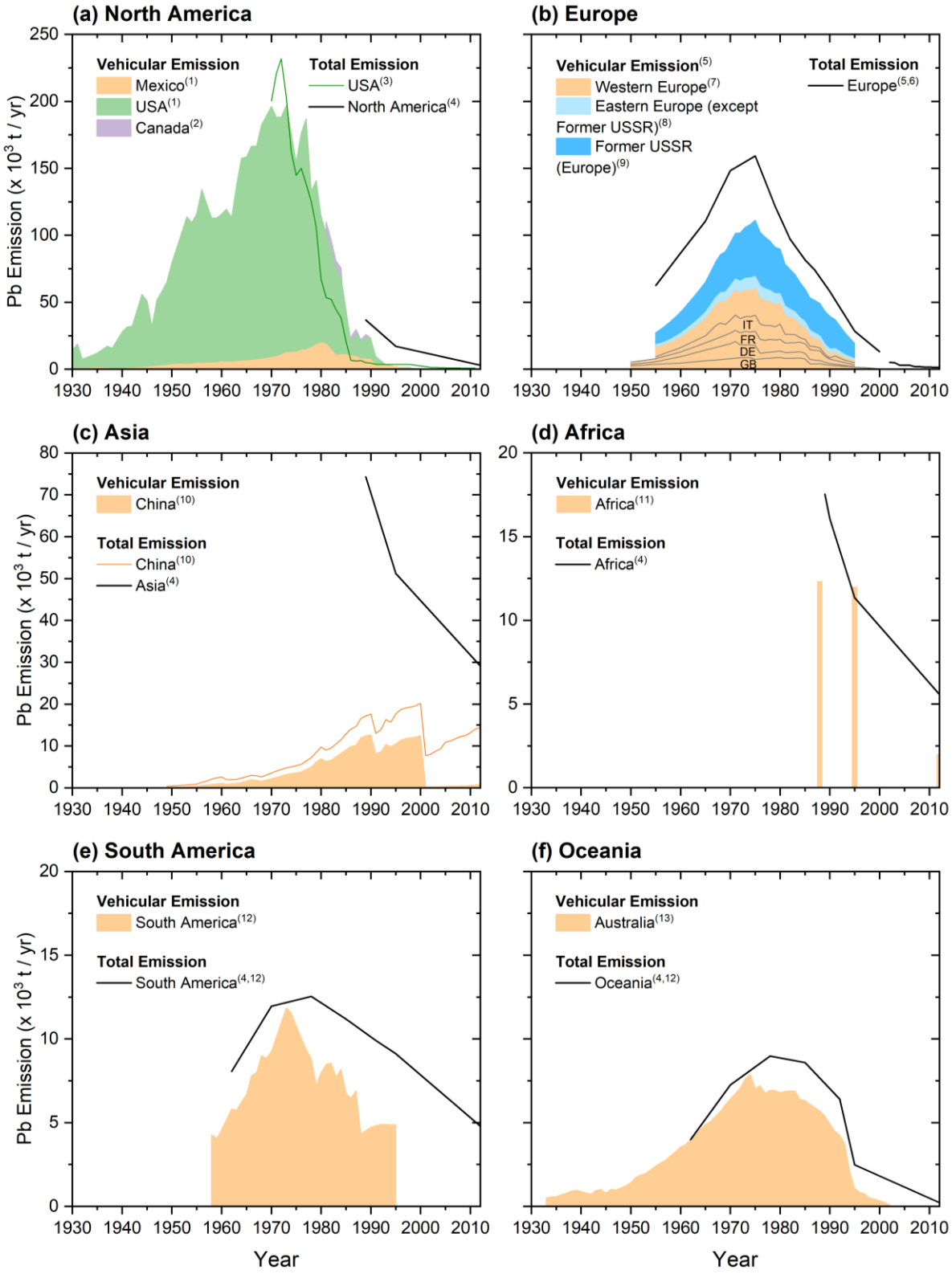


Figure 1.3. Historical trends of annual Pb emissions from road vehicles and all primary anthropogenic sources in various continental regions, 1930-2012. Vehicle emissions (predominantly from the combustion of leaded petrol) are shown as filled areas, where the trends for individual countries or sub-regions are stacked to reflect the cumulative emissions of a continental region. The total anthropogenic emissions for continental regions and/or some countries are shown as lines. Note the different scales of panels a-b, c, d-f. See notes and data sources on the following page.

Notes for Figure 1.3:

(1) Petrol Pb consumption data: USA (Nriagu, 1990) and Mexico (Soto-Jimenez et al., 2006). The annual Pb emission from petrol consumption is calculated using a conversion formula: *Annual petrol consumption* × *EF*, where EF denotes the emission factor of 0.75 (Hassel et al., 1987) for the proportion of Pb emitted from petrol combustion in vehicles.
(2) Loranger and Zayed (1994).
(3) Reported in the National Emission Inventory (NEI) by the U.S. Environmental Protection Agency (U.S. EPA, 2000). The total emission inventory reported by the USEPA falls slightly below the road source inventory reported by Nriagu (1990), due to discrepancy in the estimation method on consumption/emission between the two data sources.
(4) Except for Europe, all continent-wide total emission data during 1989-2012 are from Pacyna and Graedel (1995), Pacyna and Pacyna (2001) and Zhu et al. (2020).
(5) Pacyna, Pacyna and co-workers evaluated the petrol and total emission inventories for individual European countries during 1955-2000 at five-year or more frequent intervals (Pacyna, 1984; Pacyna and Munch, 1988; Olendrzyński et al., 1996; Pacyna and Pacyna, 2000; Pacyna et al., 2007). Additional annual emission data for various Western European countries are included (see below for data sources).
(6) Total emission inventory for Europe since 1996 is the sum of national estimates submitted to the European Monitoring and Evaluation Programme (EMEP/CEIP, 2023). Emission data for Russia unavailable in the English language literature since 2007.
(7) Individual petrol Pb inventories shown for the four countries that account for about 70% of the emission load across Western and Northern Europe: UK (GB - National Atmospheric Emission Inventory, 2023), Germany (DE - Dörr et al., 1990), France (FR - Nicolas et al., 1994) and Italy (IT - Wu and Boyle, 1997). Rest of the 'Western Europe' field encompasses: Austria, Belgium, Denmark, Finland, Iceland, Ireland, Luxembourg, the Netherlands, Portugal, Spain, Sweden and Switzerland.
(8) Albania, Bulgaria, the Czech Republic, Greece, Hungary, Poland, Romania, Slovakia and Former Yugoslavia.
(9) European part of the Former Soviet Union territories covered by the EMEP grid.
(10) Tian et al. (2015).
(11) Petrol Pb emission data covering the entire African continent is only available for the years 1989 (Pacyna and Graedel, 1995), 1995 (Pacyna and Pacyna, 2001) and 2012 (Zhu et al., 2020).
(12) Data for 1962-1989 from Barbante et al. (1997) and are likely minimum estimates.
(13) Kristensen (2015).

1.5.3 Fate of Anthropogenic Pb in the North Atlantic Ocean: the Bermuda Time Series

The North Atlantic Ocean was the region most impacted by Pb pollution from early industrialising countries and has by far received the most attention in the study of Pb and its isotopes (Boyle et al., 2014). At the Bermuda Atlantic Time Series (BATS) station in the North Atlantic Ocean, depth profiles of Pb concentrations and isotopes have been collected and analysed every few years since the late 1970s (Fig. 1.4a). Compilation of the data for seawater samples collected between 1984 and 2011 provides a time series of Pb distributions, which reveals the down-column shift of the anthropogenic spike in response to changes in anthropogenic Pb input fluxes from the surrounding continental regions (Boyle et al., 2014; Noble et al., 2015) (Fig. 1.4b, c).

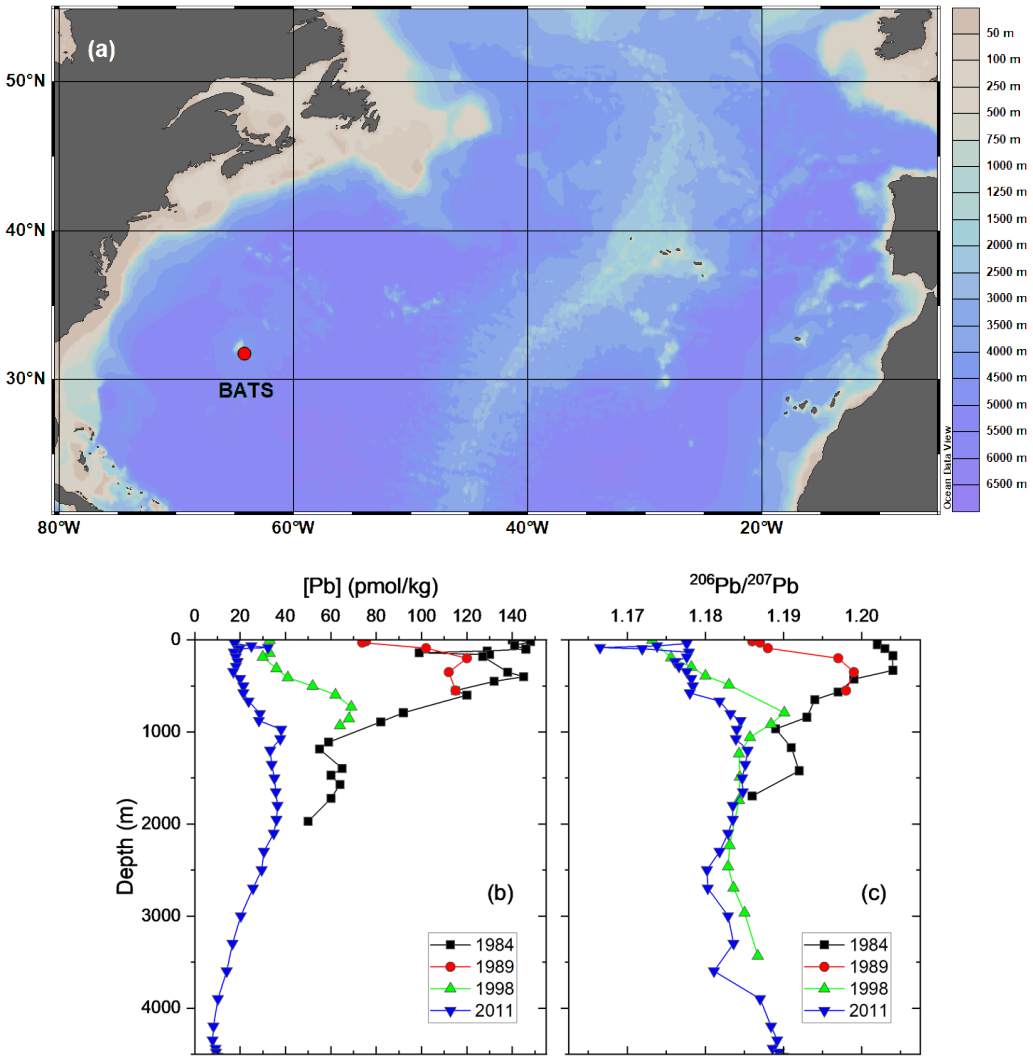


Figure 1.4. (a) Map of the North Atlantic Ocean showing the location of the Bermuda Atlantic Time Series (BATS) station, and vertical profiles of dissolved (b) Pb concentrations ([Pb]) and (c) $^{206}Pb/^{207}Pb$ isotope ratios at the BATS station between 1984 and 2011. Lead concentration data: 1984 (Boyle et al., 1986), 1989 (Véron et al., 1993) and 1998 and 2011 (Noble et al., 2015). Lead isotope data: 1984 (Shen and Boyle, 1988), 1989 (Véron et al., 1993), 1998 (Reuer, 2002) and 2011 (Noble et al., 2015). Map (a) was created using the Ocean Data View (ODV) software (Schlitzer, 2020), with ocean background colours indicating the bottom topography. Figures (b) and (c) were modified from Noble et al. (2015).

The Pb data obtained for the upper ocean at the BATS station for 1984-2011 reveal a dramatic decline in Pb concentrations, which is due to lower input fluxes of Pb as a consequence of the successive phasing-out of leaded petrol in the North American and European nations. In 1984, the high dissolved Pb levels of 130-150 pmol/kg in the upper 500 m reflect both the relatively high anthropogenic Pb inputs to the surface waters during the early 1980s and the subduction of high-[Pb] surface waters to thermocline depths (100-700 m). The high $^{206}Pb/^{207}Pb$ ratios of these upper water masses (of about 1.203) in 1984 reflect the overwhelming quantities of Pb with a high $^{206}Pb/^{207}Pb$ signature (≈ 1.20) emitted from the USA (Véron et al., 1992). From 1984 to 1998, the Pb concentrations of the surface water

decreased by a factor of four to about 33 pmol/kg, reflecting the decline of petrol Pb emissions during this period. The declining surface water [Pb] coincide with a decrease in $^{206}Pb/^{207}Pb$ ratios, due to the higher relative contributions of low-$^{206}Pb/^{207}Pb$ European emissions (1.11-1.15) (Véron et al., 1993 and references therein), in accord with the slower phasing-out of leaded petrol in the European nations compared to the USA (Wu and Boyle, 1997 and references therein). In 2011, surface water Pb concentrations as low as 18 pmol/kg were measured, reflecting the relatively low Pb emissions in the region since the beginning of the 21st century.

The BATS data for the ocean interior reveal the down-column transfer dynamics of the anthropogenic Pb influx. As anthropogenic Pb inputs decreased progressively from 1984 to 2011, the [Pb] maximum associated with the large anthropogenic influxes of the earlier decades (1950-1980) has been deepening and dissipating (Fig. 1.4). In 1984, a pronounced [Pb] maximum of about 145 pmol/kg occurred at a depth of 400 m, whilst in 2011, the [Pb] maximum was significantly attenuated (36 pmol/kg, at 1800 m depth) and it was dispersed across a broader, deeper range of depths between about 600 and 2500 m. This reflects the dispersion of the Pb influx by various oceanographic processes, including the subduction of Pb-enriched waters that were ventilated during the period of maximum anthropogenic Pb influx and their mixing with both older and younger water masses with lower Pb concentrations, as well as the removal of Pb from the water column by particle scavenging (Noble et al., 2015).

1.6 Tracing Natural Fluxes using Pb-Nd Isotopes

Identification of a naturally derived Pb isotope fingerprint in modern seawater and marine particles is impeded by the pervasive contamination of the global ocean by anthropogenic Pb. Fortunately, marine sediments provide an archive of naturally derived Pb in the ocean prior to the major anthropogenic perturbations of the recent centuries (Abouchami and Goldstein, 1995; von Blanckenburg et al., 1996). Lead isotopes have been applied to trace the terrestrial sources of both detrital inputs (Jones et al., 2000; Stancin et al., 2006; Fagel et al., 2014; Erhardt et al., 2021) and dissolved weathering inputs to the ocean (Abouchami and Goldstein, 1995; von Blanckenburg et al., 1996; van de Flierdt et al., 2003; Wilson et al., 2015). For the latter, the dissolved isotope signatures in pre-anthropogenic (deep) seawater can be recovered from authigenic Fe-Mn sediments, which formed by slow precipitation in the deep ocean (Abouchami and Goldstein, 1995; von Blanckenburg et al., 1996).

The sedimentary isotope signature of Pb can be combined with that of Nd, another trace metal with a radiogenic isotope from long-lived radioactive decay, to trace natural fluxes to the ocean. In particular, the large variations in terrestrial signatures when the two isotope systems are combined enable enhanced constraint on the source regions, whilst the two isotope systems offer complementary roles as tracers of dissolved weathering input. For the latter, the residence time of Pb in deep waters (< 400 years) is short

relative to the timescale of global water mass mixing (~10^3 years) (Broecker and Peng, 1982), which enables the tracing of regional gradients in local weathering inputs (von Blanckenburg et al., 1996 and references therein). In contrast, due to the longer oceanic residence time of Nd (500-1000 years) (Tachikawa et al., 2003), dissolved Nd isotope signatures are relatively well-mixed within an ocean basin and are, therefore, more suitable as a tracer of water mass mixing between major ocean basins (see review by Frank, 2002).

1.7 Neodymium Geochemistry

1.7.1 Chemical Properties and Isotope Systematics of Nd

Neodymium is one of the rare-earth elements (REEs). Similar to most REEs, Nd exists as the trivalent Nd^{3+} in natural environments. In a model surface seawater environment, the inorganic speciation of dissolved Nd is dominated by the formation of carbonate complexes ($Nd(CO_3)_2^-$; ≈ 90%) (Cantrell and Byrne, 1987). Organic complexation is also known to be important for the dissolved speciation of REEs in some types of natural waters (Tang and Johannesson, 2003; Marsac et al., 2021). For example, in river waters at pH > 5, complexes with humic substances account for ≥ 60% of the dissolved REE budgets (Pourret et al., 2007). Whilst little is known about the nature and significance of REE-binding ligands in seawater, organic complexation of REEs in seawater appears to be weaker than in freshwater (Christenson and Schijf, 2011; Schijf and Byrne, 2021). Furthermore, rare-earth elements exhibit high particle reactivity in the ocean, whereby metal oxyhydroxides and particulate organic matter are known to be important solid-phase carriers of REEs in seawater (Sholkovitz et al., 1994).

Neodymium has seven naturally occurring stable isotopes (^{142}Nd, ^{143}Nd, ^{144}Nd, ^{145}Nd, ^{146}Nd, ^{148}Nd and ^{150}Nd), of which ^{143}Nd is formed by the radioactive decay of ^{147}Sm. The relative abundance of radiogenic ^{143}Nd is generally expressed relative to primordial ^{144}Nd using the $^{143}Nd/^{144}Nd$ ratio. Due to the long half-life of ^{147}Sm of 106 Ga and the limited fractionation of Sm/Nd ratios in natural systems, natural variations in $^{143}Nd/^{144}Nd$ ratios among geological reservoirs are typically small. Therefore, Nd isotope compositions are commonly expressed in the epsilon notation (ε_{Nd}):

$$\varepsilon_{Nd} = \left(\frac{^{143}Nd/^{144}Nd_{sample}}{^{143}Nd/^{144}Nd_{CHUR}} - 1 \right) \times 10^4 \qquad (1.1)$$

The notation hence denotes the deviation of the measured $^{143}Nd/^{144}Nd$ of a sample from the $^{143}Nd/^{144}Nd$ ratio of the present-day Chondritic Uniform Reservoir (CHUR) (0.512638, Jacobsen and Wasserburg, 1980) in parts per ten thousand.

Lithological variations in $^{143}Nd/^{144}Nd$ are principally driven by Sm/Nd fractionation and age of the reservoir (DePaolo and Wasserburg, 1976). In detail, Nd is slightly more incompatible than Sm, and during partial melting of the mantle, a crustal melt is therefore enriched in Nd relative to Sm (lower

Sm/Nd), whilst the residual depleted mantle is depleted in Nd relative to Sm (higher Sm/Nd). Old continental crustal rocks evolved with low Sm/Nd ratios over geological time hence now have unradiogenic $^{143}Nd/^{144}Nd$ ratios (and low ε_{Nd} values). In contrast, the depleted mantle, which experienced progressive extractions of low-Sm/Nd crustal melts, evolved with a high time-integrated Sm/Nd ratio and hence now has a radiogenic $^{143}Nd/^{144}Nd$ ratio (and a high ε_{Nd} value). Young arc rocks and mid-ocean ridge basalts, which were recently derived from the depleted mantle, will therefore have higher $^{143}Nd/^{144}Nd$ ratios (and ε_{Nd} values) than older crustal rocks.

1.7.2 The Marine Nd Cycle

The principal sources of dissolved Nd in the global ocean are continental weathering products in the form of aeolian particles and the dissolved and particulate loads of rivers (Goldstein et al., 1984; Tachikawa et al., 1999; Frank, 2002), as well as continental margin sediments through boundary exchange (e.g. Lacan and Jeandel, 2005). Hydrothermal activities are a negligible source or even a net sink of dissolved oceanic Nd, due to the intense adsorption of dissolved Nd onto hydrothermal particles (chiefly Fe-Mn oxyhydroxides) (Michard et al., 1983; German et al., 1990). However, exchange of dissolved Nd and its isotopes between hydrothermal fluids and deep seawater is speculated to occur near hydrothermal vents (Jeandel et al., 2013).

The cycling of Nd in the ocean interior is driven by a combination of physical advection and vertical transport process mediated by particles (Siddall et al., 2008). In the open ocean, dissolved Nd concentrations typically exhibit a 'nutrient-like' distribution, with a depletion in the upper ocean and enrichments in the deep ocean and along thermohaline circulation pathways. This distribution highlights the importance of vertical processes, as dissolved Nd is scavenged by particles in the upper ocean and subsequently remobilised from particles in the deeper part of the water column (Bertram and Elderfield, 1993; Jeandel et al., 1995). In contrast, Nd isotope compositions in the open ocean exhibit a 'quasi-conservative' distribution and broadly track the movement and mixing of deep water masses (advective processes) (Siddall et al., 2008; Tachikawa et al., 2017). This decoupling between the Nd concentrations and isotope distributions is termed the 'Nd paradox' (Goldstein and Hemming, 2003). Nevertheless, modifications of deep water ε_{Nd} signatures relative to the basin-wide signature have been observed in regions with large influxes of lithogenic and volcanogenic particles (Singh et al., 2012; Grasse et al., 2012, 2017; Jeandel and Oelkers, 2015; Molina-Kescher et al., 2018).

1.8 Seawater Pb Concentration and Isotope Data, Analytical Challenges and Current Data Coverage

The determination of seawater Pb concentrations and isotope compositions poses significant analytical challenges. In particular, seawater samples have extremely low abundances (10^{-12} to 10^{-10} pmol/kg) of Pb and feature a highly saline seawater matrix with ~3.5% total dissolved solids, and the

analyses are furthermore hindered by the susceptibility of Pb to contamination during sampling and laboratory processing of seawater samples (Lee et al., 2011; Griffiths et al., 2020). Overcoming these challenges requires rigorous ultraclean protocols for sample collection and handling during analyses, efficient preconcentration and purification procedures, and high-sensitivity measurement techniques that are suitable for analyses of samples with extremely low Pb abundances. The first accurate results of seawater Pb concentrations and isotope compositions were presented in 1981 (Schaule and Patterson, 1981) and 1988 (Shen and Boyle, 1988) respectively, and these led to further studies which documented the pervasive anthropogenic perturbations of the global marine Pb budget. The introduction of automated sampling techniques in the 1990s (Wu and Boyle, 1997) and advances in analytical techniques (Reuer et al., 2003; Lee et al., 2011; Boyle et al., 2012; Paul et al., 2015; Griffiths et al., 2020) have substantially improved and simplified Pb concentration and isotope measurements for seawater, and as a result, significantly more observational data have become available in recent years.

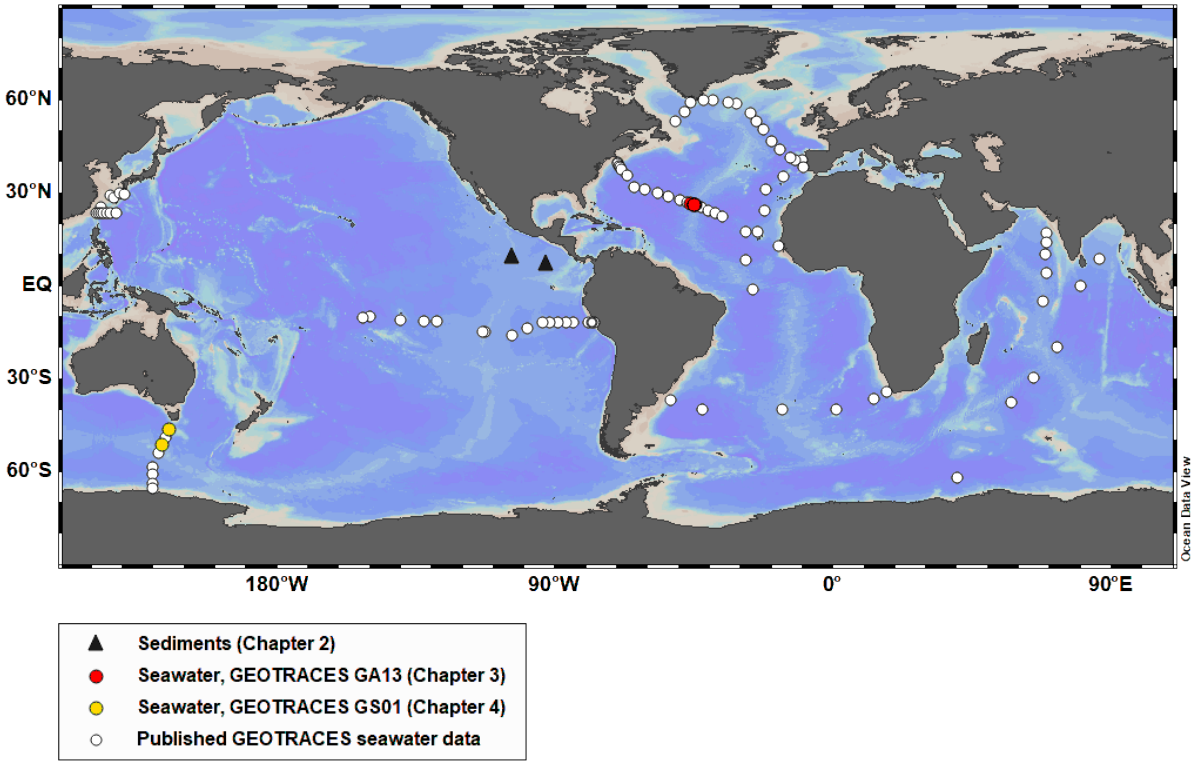


Figure 1.5. Global map showing the sampling locations with published GEOTRACES seawater Pb concentration and isotope data for depth profiles (white circles), as well as the sediment (black triangles) and seawater samples (red and yellow circles) that were analysed for this PhD thesis.

Since the launch of the GEOTRACES programme in 2006, high-resolution, full-depth transects of seawater Pb concentrations and isotope compositions have been obtained from many major ocean regions. Figure 1.5 shows a global compilation of GEOTRACES sampling locations for which coupled full-depth seawater Pb concentration and isotope data are either published or available in the latest 2021 GEOTRACES Intermediate Data Product (IDP) (GEOTRACES Intermediate Data Product Group, 2021). This figure highlights that the best data coverage by far is achieved for the North Atlantic Ocean, through the GEOTRACES sections GA01 (Zurbrick et al., 2018), GA03 (Noble et al., 2015) and GA06 (Bridgestock et al., 2018). For the Pacific Ocean, high-resolution data are available for the southeast sector (GEOTRACES GP16, Boyle et al., 2020) and the northwest sector (GEOTRACES GP06, Chien et al., 2017; Chen et al., 2023a). In contrast, only limited GEOTRACES Pb data are currently available for the South Atlantic Ocean (GEOTRACES GA10, data by Maxence Paul (Imperial College London) and available in the GEOTRACES IDP 2021 database; GEOTRACES Intermediate Data Product Group, 2021) and the Indian Ocean (GEOTRACES GI04; Lee et al., 2015). Coupled seawater Pb concentration and isotope data for the Southern Ocean was extremely limited, until the first partial dataset for the GEOTRACES section GS01 in the Southern Ocean sector south of Tasmania was reported in the PhD thesis of Griffiths (2019).

1.9 Research Objectives and Thesis Outline

The aim of this thesis is to improve understanding of the marine source and sink fluxes of Pb and the internal cycling of the element in the modern ocean, with focuses on the vicinity of high-temperature hydrothermal activities and the Southern Ocean, which remain poorly explored for Pb cycling. To this end, Pb concentration and isotope data are presented and discussed for seafloor sediment and seawater samples from various ocean regions (Fig. 1.5), in order to address three research aims:

1. **Identify key terrigenous fluxes in the Eastern Equatorial Pacific Ocean.**
2. **Characterise the fluxes and biogeochemical cycling of Pb in the vicinity of high-temperature hydrothermal systems.**
3. **Determine the relative significance of physical advection and particulate processes for the internal redistribution of Pb in the Southern Ocean.**

Notably, the results obtained in this study fill key gaps in the GEOTRACES database of dissolved Pb concentrations and isotope compositions in the global ocean. The analytical work was carried out in the MAGIC Laboratories in the Department of Earth Science and Engineering. The seawater analyses thereby benefitted from new methods that were recently developed in the MAGIC Group (Griffiths et al., 2020), which enable the acquisition of high-quality Pb concentration and isotope data with significantly improved sample throughput through the use of Nobias Chelate PA-1 resin for Pb preconcentration and multi-collector inductively coupled plasma mass spectrometry for data acquisition.

Chapter 2 presents Pb and Nd isotope data for metalliferous core-top sediments from two locations in the Guatemala Basin, Eastern Equatorial Pacific Ocean. A number of studies have previously investigated the aeolian dust flux in this ocean region to track changes in atmospheric circulation over various Cenozoic timescales (Xie and Marcantonio, 2012; Pichat et al., 2014; Höfig et al., 2016; Reimi and Marcantonio, 2016; Reimi et al., 2019). However, the modern detrital flux in this region is not well constrained. By comparing the isotope compositions of the detrital sediment components to the signatures of potential terrestrial source regions, the major sources of terrigenous detrital materials to the Guatemala Basin are identified. The relative significance of proximal and distal source regions and the environmental factors that favour the contribution of detrital materials from the identified source regions are assessed. In addition, the leachate sediment components provide an archive of the pre-anthropogenic seawater compositions. The latter results enable an assessment of the influence of local weathering inputs and hydrothermal activity on the marine Pb and Nd budgets at the two sampled sites, which are located at contrasting proximities (25 and 1300 km, respectively) to the fast-spreading East Pacific Rise.

Chapter 3 presents the dissolved Pb concentrations and isotope compositions for seawater samples from five depth profiles above and in the vicinity of the TAG Hydrothermal Field in the North Atlantic Ocean (26°N), collected during the GEOTRACES GA13 expedition (FRidge, 2017/18). These seawater profiles form a high-resolution, quasi-zonal transect across the crest of the Mid-Atlantic Ridge. This chapter serves as a case study to improve understanding of the fluxes and cycling of Pb in the vicinity of high-temperature hydrothermal vent sites. Possible anomalies in Pb signatures related to the hydrothermal activity are evaluated by comparing the results obtained for samples from the buoyant and neutrally buoyant hydrothermal plume with data for 'background' seawater unaffected by the hydrothermal activity, both from the current study and the GEOTRACES section GA03 (Noble et al., 2015). In particular, Pb concentration anomalies can help to constrain if hydrothermal plumes are a net source or sink of dissolved seawater Pb, whilst anomalies in Pb isotope compositions can reveal the sources of dissolved Pb in the hydrothermal plume and, in particular, the presence of mantle-derived Pb from hydrothermal fluids. The Pb isotope signatures of recent inputs to surface waters and the origins of the Pb distributions in the remaining water column unaffected by the TAG plume are also examined.

Chapter 4 presents dissolved Pb concentration and isotope data for seawater from two depth profiles collected in 2018 on the GEOTRACES section GS01 in the Subantarctic Zone (47-52°S) of the Southern Ocean south of Tasmania. The chapter complements the study of Griffiths (2019), which presented the GEOTRACES GS01 data for higher southern latitudes (52-65°S). The results from this chapter provide new constraints on the sources and cycling of Pb in the Subantarctic Zone, which is characterised by a complex water mass structure. Together with the results of Griffiths (2019), the complete GEOTRACES GS01 data provide the first meridional transect of dissolved Pb isotope

compositions across the Southern Ocean (Fig. 1.5). This dataset offers novel insights into the sources of dissolved Pb, water mass origins and vertical flux dynamics across the ocean region.

Finally, **Chapter 5** provides a summary of the research presented in the thesis. The key findings of each chapter are reviewed and key implications for marine geochemistry are synthesised. Research questions that deserve further attention are also discussed.

Chapter 2

Lead Isotope Compositions of Seafloor Sediments in the Guatemala Basin, Eastern Equatorial Pacific Ocean: Implications for Terrigenous and Hydrothermal Inputs

2.1 Introduction

The sources and provenance of external material fluxes into the ocean can be determined from the Pb and Nd isotope compositions of seafloor sediments and encrustations (Nakai et al., 1993; Jones et al., 1994, 2000; von Blanckenburg et al., 1996; Ling et al., 1997; Frank et al., 2006; Stancin et al., 2006; Ziegler et al., 2007; Erhardt et al., 2021). In the Eastern Equatorial Pacific Ocean (EEP), the sediment archive there offers diverse applications for studies of the ancient and modern oceans and climate.

One key application is to track past changes in atmospheric circulation using the provenance of detrital sediments. The EEP is surrounded by multiple terrigenous source areas with diverse geological histories, and thus, radiogenic isotope fingerprints. The isotope signatures of detrital sediments in the region are therefore sensitive to changes in atmospheric and ocean circulations over geological timescales. Since the pioneering Sr-Nd-Pb isotope studies on Pacific surface sediments (Nakai et al., 1993; Jones et al., 2000), multiple studies have utilised Pb and Nd isotopes to trace dust provenance in the EEP (Stancin et al., 2006; Xie and Marcantonio, 2012; Pichat et al., 2014; Höfig et al., 2016; Erhardt et al., 2021). These studies generally revealed strong hemispheric differentiation in dust sources and the dominance of proximal sources from the American continent on the terrigenous sediment budget. However, the source mixing models of these studies were not robust. In particular, mixing models that rely on volcanic rock compositions for the characterisation of source signatures (Pichat et al., 2014; Höfig et al., 2016) tend to be inconsistent with models that define the source signatures based on dust or soil samples (Erhardt et al., 2021). Furthermore, there are few isotope provenance studies that encompass the Guatemala and Panama Basins (Höfig et al., 2016; Erhardt et al., 2021), ocean regions that are proximal to the key Central and South American sources of terrigenous sediments to the Eastern Pacific Ocean.

Another application is to evaluate the susceptibility of seawater Pb and Nd isotope compositions to modification by various processes near ocean boundaries. The EEP is characterised by high particle loading, from both terrigenous particle influx and biogenic particles (Pennington et al., 2006), which potentially modify the deep water isotope budgets by reversible scavenging. Recent dissolved Nd isotope data for the Panama Basin in the EEP show that deep water Nd isotope composition can record significant modification, by 4–7 ε_{Nd} units relative to the advected, basin-wide signature of the South Pacific Ocean, due to the large influx of volcanic particles (Grasse et al., 2012, 2017). The pre-anthropogenic Pb isotope signatures of marginal regions of the EEP, however, are not yet constrained. Furthermore, the occurrence of high-temperature hydrothermal activities on the East Pacific Rise (EPR) could also impact the deep seawater compositions of the ocean region. The net influxes of both Nd and Pb from hydrothermal fluids to deep seawater have long been considered negligible, owing to efficient removal near hydrothermal vents (German et al., 1990; Halliday et al., 1992; Godfrey et al., 1994). However, unusual isotope compositions of Nd and Pb have been detected in a range of distances from

the EPR, and these were tentatively attributed to dissolved-particulate exchange processes with metals released from hydrothermal fluids or pelagic sediments (Barrett et al., 1987; van de Flierdt et al., 2004; Jeandel et al., 2013). In Pb isotope studies of marine sediments in the southern EEP (13°S), a basaltic isotope fingerprint of 20-30% was even traceable up to about 1000 km west of the EPR, which suggests the possibility of distal transport of hydrothermal Pb (Barrett et al., 1987; van de Flierdt et al., 2004). The influence of hydrothermal activities on the deep water isotope compositions of the EEP remains to be further tested.

The development of sequential extraction techniques for the isolation of various operationally defined fractions from a bulk marine sediment sample has enabled independent assessments of the origins of different sediment phases (e.g. Chester and Hughes, 1967; Ziegler et al., 2007). In acid-reductive leaching, the weak hydroxylamine hydrochloride (HH) leachate fraction is dominated by Fe-Mn oxyhydroxide phases, which form by slow precipitation in the water column or near the seafloor and therefore record the isotope compositions of deep and bottom waters (the 'authigenic signature') (Gutjahr et al., 2007; Wilson et al., 2013). The residual detrital fraction that remains after the leaching procedure is dominated by quartz and aluminosilicate materials that are typically derived from aeolian dust and riverine particles, which record a terrigenous isotope signature (e.g. Olivarez et al., 1991; Weber II et al., 1996). For Pb, the present-day deep waters across all major ocean basins are significantly contaminated by anthropogenic Pb (e.g. Lee et al., 2015; Noble et al., 2015; Zurbrick et al., 2017; Boyle et al., 2020), and the authigenic component in marine sediments hence constitutes the only archive of the pre-anthropogenic Pb isotope composition of seawater (e.g. Abouchami and Goldstein, 1995; von Blanckenburg et al., 1996).

This study presents the Pb and Nd isotope compositions of metalliferous sediments recovered from Sites H and M of the Manganese Nodule Project (MANOP) in the Guatemala Basin, a marginal basin in the EEP (Fig. 2.1). The isotope data are used to determine: (1) the provenance of terrigenous sediments in the Guatemala Basin, and (2) the influence of local weathering input and hydrothermal activities on the dissolved Pb and Nd isotope compositions of the EEP. Both aims are addressed with the aid of mixing models that apply the isotope fingerprints of potential source areas. For the terrigenous provenance, the contributing source areas are identified from the best-fit mixing model that explains the detrital isotope compositions of the sediment samples and which is compatible with known delivery pathways for aeolian dust and/or riverine particles. The large combined Pb-Nd isotope heterogeneities of terrestrial lithologies provide improved constraints on the source areas, compared to most previous isotope studies in the region that rely on Pb isotope data alone (e.g. Höfig et al., 2016; Erhardt et al., 2021). For the seawater Pb and Nd isotope compositions, the data for sediment leachates are compared with those of the source water in the Guatemala Basin. The identification of distinct isotope signatures reflects modification of the advected budgets of Pb and/or Nd, and the local source(s) that are responsible for the modification can be deduced from isotope mixing relationships. In particular,

hydrothermally derived Pb and Nd are characterised by distinct, mantle-derived isotope signatures relative to deep seawater. The presence of a mantle-derived isotope fingerprint in the leachate fraction indicates the distal transport of hydrothermally-derived elements across the open ocean, either in dissolved form or adsorbed to Fe-Mn oxyhydroxide particles. The two sites in this study are located at distances of 25 km (Site M) and 1300 km (Site H) from the EPR. This enables tracking of the impact of hydrothermal activities at these two locations with very different proximities to the ridge crest.

2.2 Setting and Samples

2.2.1 Atmospheric Circulation

The low-level atmosphere of the EEP is dominated by easterly trade winds (Fig. 2.1). At subtropical latitudes, equatorward westerlies blow along the coast of the Western USA and Mexico, while northerly winds blow along the Peruvian coast. Both wind belts deflect westward into the remote Pacific Ocean, forming the northeast and southeast trade winds respectively. The trade winds from both hemispheres converge and rise at a narrow latitudinal band close to the Equator called the Intertropical Convergence Zone (ITCZ), forming a region of maximum annual precipitation (Philander et al., 1996; Schneider et al., 2014). The westward deflections of trade winds away from the American continent leave the sector of the EEP proximal to the American continent as a 'shadow zone' of relatively weak wind (Lavín et al., 2006).

The strength of atmospheric circulation and the latitudinal position of the ITCZ exhibit seasonal fluctuations (Schneider et al., 2014). During boreal winter, northeast trades strengthen and the ITCZ shifts to its southernmost position at about 5°N, and strong easterly jets blow from the Caribbean Sea through mountain gaps in Southern Mexico and Central America into the EEP (Lavín et al., 2006). During boreal summer, southeast trades strengthen and the ITCZ shifts northward to about 10°N, creating a weaker wind field over the EEP (Lavín et al., 2006).

2.2.2 Hydrographic Setting

The circulation and water mass distribution in the EEP were reviewed in detail by Kessler (2006) and Fiedler and Talley (2006), respectively (Fig. 2.2). The Guatemala Basin is bordered by the continental margins of Southern Mexico – Central America to its northeast, and it is separated from the open Pacific Ocean to the west by the EPR, and the Panama and Peru Basins to the south by the Cocos Ridge and Galápagos Spreading Centre (GSC), respectively.

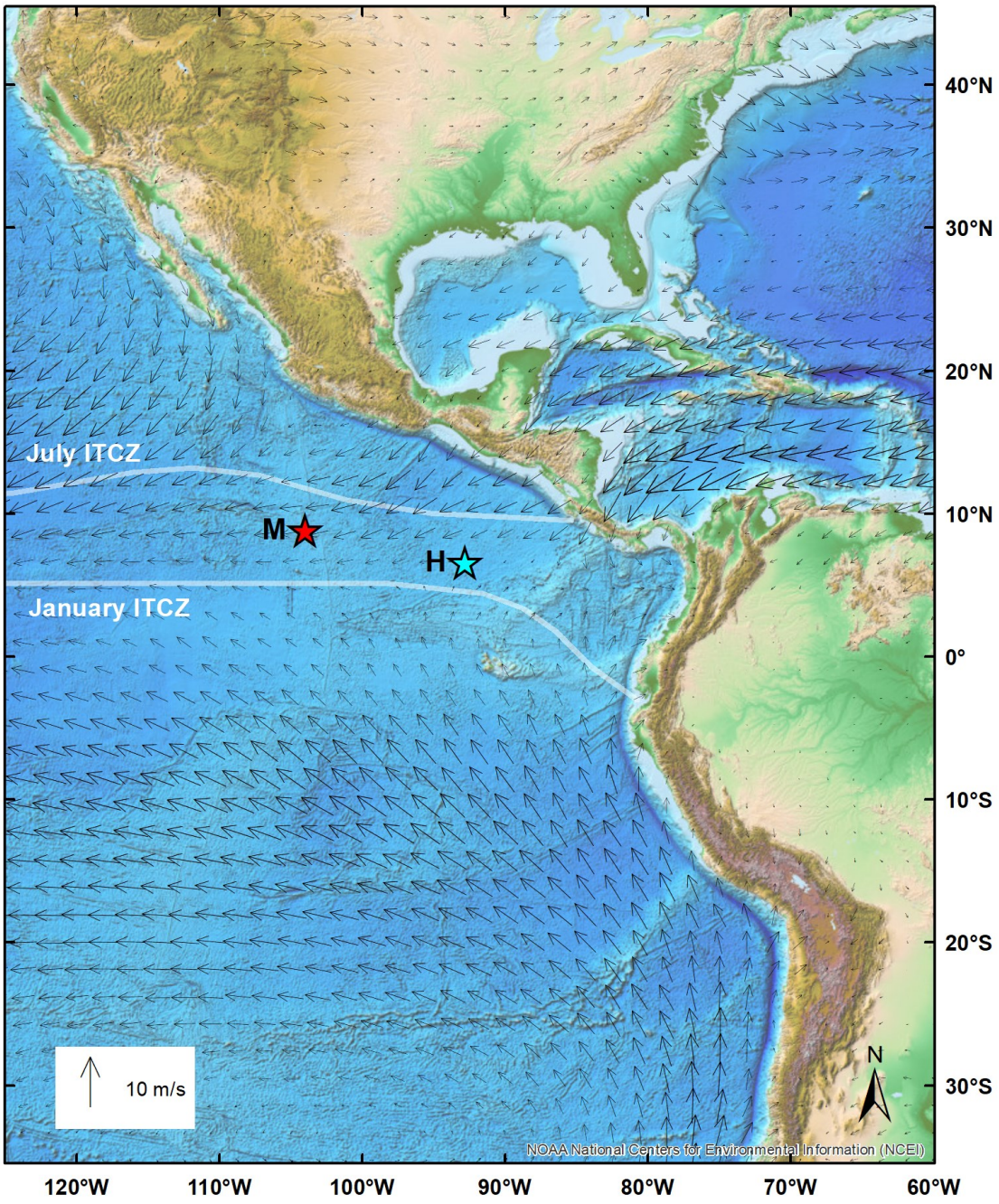


Figure 2.1. Overview map of the Eastern Pacific Ocean, showing the annual mean wind field and the locations of MANOP Sites H and M of this study. Wind vectors are generated using data from the NCEP/NCAR Reanalysis (Kalnay et al., 1996). Present-day January and July latitudinal positions of the Intertropical Convergence Zone (ITCZ) from Liu et al. (2015). Displayed elevation map was constructed from the ETOPO1 Global Relief Model, downloaded from the NOAA-NCEI data products (https://www.ncei.noaa.gov/products/etopo-global-relief-model).

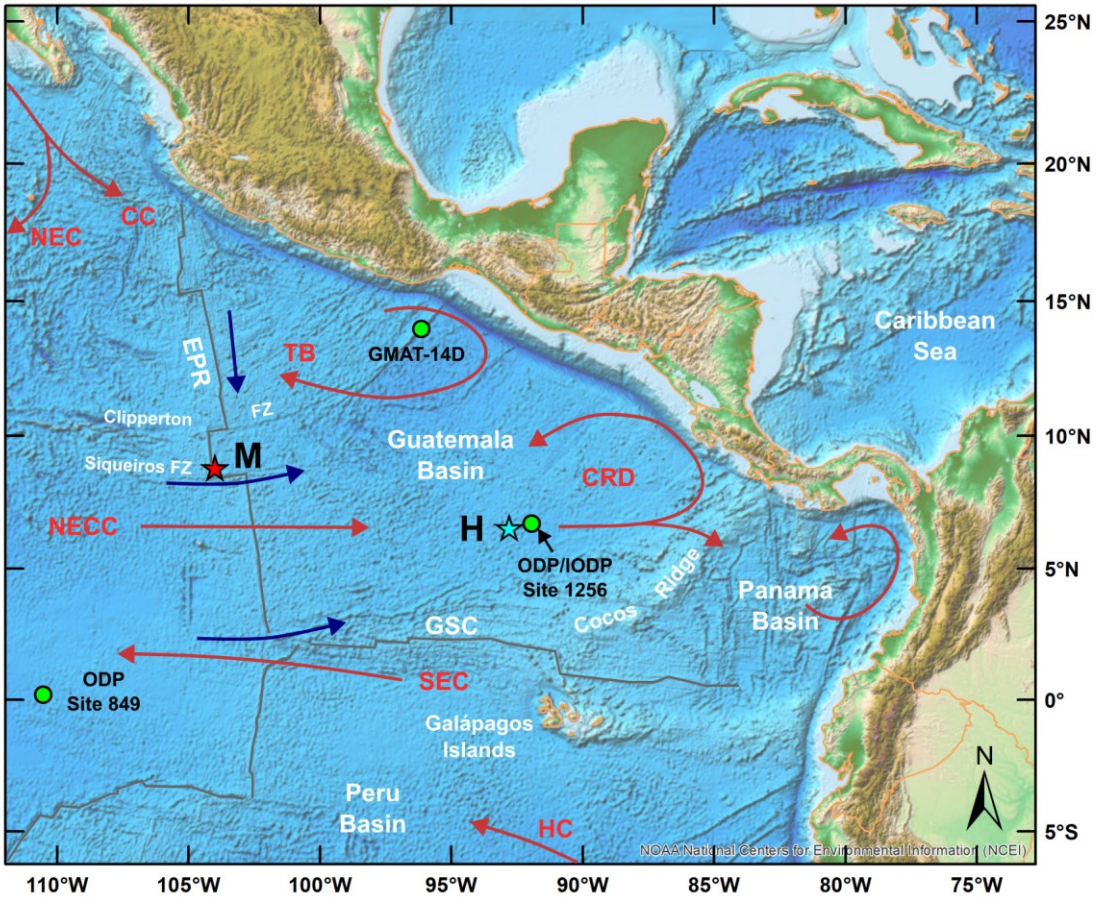


Figure 2.2. Map of the Eastern Equatorial Pacific Ocean showing the locations of the two MANOP sites of this study (stars), other sampled sites referred to in the text (green circles) and the ocean circulation regime. Mid-ocean ridges and fracture zones (FZ): East Pacific Rise (EPR), Galápagos Spreading Centre (GSC), Cocos Ridge and the Siqueiros and Clipperton Fracture Zones. Red arrows denote surface ocean currents and gyres according to Kessler (2006): North Equatorial Current (NEC), California Current (CC), North Equatorial Countercurrent (NECC), South Equatorial Current (SEC), Humbolt Current (HC), Tehuantepec Bowl (TB) and Costa Rica Dome (CRD). Navy arrows denote bottom water currents in the Guatemala Basin, including two eastward inflows across fracture zones in the EPR (Mantyla, 1975) and a southward flow along the western margin of the Guatemala Basin (Lyle, 1992).

The surface mixed layer of the Guatemala and Panama Basins is filled by Tropical Surface Water (TSW). The TSW is characterised by high temperatures (> 27.5°C) and low salinities (< 34) and forms the core of the eastern Pacific warm pool (Fiedler and Talley, 2006; Wang and Fiedler, 2006). Under strong trade wind forcing, the south-flowing California Current (CC) in the Northern Hemisphere detaches from the coast of Baja California, while the north-flowing Humboldt Current in the Southern Hemisphere detaches from the Peruvian coast, feeding the North Equatorial Current (NEC) and the South Equatorial Current (SEC), respectively. These west-flowing currents carry cold Eastern Pacific waters into the Central Pacific Ocean (Kessler, 2006). Between the NEC and SEC, the parallel North Equatorial Countercurrent (NECC) flows eastward underneath the ITCZ and carries warm water from the Central Pacific Ocean towards Central and South America (Kessler, 2006). In the Guatemala and

Panama Basins, the strongly zonal (east-west) flow regime breaks down underneath the wind shadow, and the surface ocean circulation in this region is instead characterised by smaller-scale, seasonally varying gyres (Kessler, 2006). A branch of the California Current continues to flow southeast-ward along the Western Mexican coast towards the Guatemala Basin, where this water is in turn circulated anticyclonically off the South Mexican coast, known as the Tehuantepec Bowl (TB) (Kessler, 2006). The east-flowing NECC weakens as it approaches the Central/South American coast, where a branch turns north to circulate cyclonically off the Central American Pacific coast, known as the Costa Rica Dome (CRD) (Kessler, 2006).

The intermediate depth (200-1500 m) of the Guatemala Basin is filled by Equatorial Pacific Intermediate Water (EqPIW), which is a mixture between Antarctic Intermediate Water (AAIW) from the Southeast Pacific Ocean and the underlying deep waters that upwell to shallower depths (Bostock et al., 2010). The deep portion of the Guatemala Basin (> 1500 m) is filled by deep water from the Northeast Pacific Ocean, which is composed predominantly of North Pacific Deep Water (NPDW) (Lonsdale, 1976; Peters et al., 2018). This deep water likely enters the Guatemala Basin as dispersed inflows through fracture zones in the EPR (Mantyla, 1975). A southward flow of bottom water was also found over the eastern flank of the EPR along the margin of the Guatemala Basin (Lyle, 1992).

2.2.3 Submarine Volcanism and Hydrothermal Activities

The western and southern margins of the Guatemala Basin are bounded by segments of the EPR and the Galápagos Spreading Centre (GSC), respectively (Fig. 2.2). Both ridge systems are characterised by mid-ocean ridge basalt (MORB) volcanism, which sustains fast (90-110 mm/a) (Langmuir et al., 1986) and intermediate (50 mm/a) (DeMets et al., 1990) full spreading rates, respectively, around the Guatemala Basin. Extensive high-temperature hydrothermal activity has been detected along the EPR segment that borders the Guatemala Basin (2-18°N) (Baker et al., 1994, 2001). At one of the studied sites (MANOP Site M) that is proximal to the EPR crest, hydrothermal plumes have been detected in the water column based on ^{222}Rn and Mn anomalies (Kadko et al., 1987a). In contrast, the GSC has a significantly lower incidence of high-temperature hydrothermal venting, a feature that is attributed to its unusually thick basaltic crust, which is a consequence of hotspot magmatism (Baker et al., 2008).

2.2.4 Studied Sites

Metalliferous sediment samples from two of the MANOP sites, ‘H’ and ‘M’, were selected for this study (Fig. 2.2). MANOP was a scientific project funded by the National Science Foundation (USA) to study sedimentation and formation processes of seafloor ferromanganese nodules at five sites in the Eastern Pacific Ocean (Dymond et al., 1984; Finney et al., 1988). Across these MANOP sites, the deposition processes, sediment compositions and post-depositional dynamics have been well-characterised. MANOP Site H (6°33’N, 92°48’W), located in the interior of the Guatemala Basin at a

seafloor depth of about 3600 m, was chosen to study hemipelagic sedimentation. MANOP Site M (8°48'N, 104°00'W), located about 25 km east of the EPR crest and at a seafloor depth of about 3100 m, was chosen to study hydrothermal sedimentation at a ridge flank location. Site M receives a considerable fraction of its sediment budget from hydrothermal activities, whilst Site H, located about 1300 km away from the EPR ridge axis, is characterised by purely hemipelagic sedimentation (Lyle et al., 1984). Therefore, the influence of hydrothermal activities on the sediment and seawater compositions of Pb and Nd of Site M can be compared to that of the hemipelagic Site H. Furthermore, the two MANOP sites are situated along different terrigenous sediment delivery pathways, whereby Site M is down-current of the elevated Mexican landmass along the anticyclonic circulation of North Equatorial Current – Tehuantepec Bowl (NEC-TB). In contrast, Site H is fed by the North Equatorial Countercurrent – Costa Rica Dome (NECC-CRD), which flows from the open ocean. Isotope data for these two sites hence enables determination of the spatial variability of the terrigenous sediment supply across the Guatemala Basin.

Core-top sediments (≤ 20 cm) at both sites consist of dark brown clay (Graybeal and Ross Heath, 1984). X-ray diffractometry reveals that the mineral assemblages of samples from both sites are dominated by smectite (49-60 wt%), followed by calcite (0.1-22 wt%), plagioclase (13-20 wt%), quartz (4-6 wt%), kaolinite (4-6 wt%), halite (4-5%), barite (1-3 wt%) and Fe-Mn oxyhydroxides (0.3-2 wt%) (Little et al., 2020). At Site M, muscovite (4 wt%) is additionally identified in the sediments (Little et al., 2020). Due to high fluxes of terrigenous detritus, biogenic particles and hydrothermal particles, Site M has a high flux of Al from terrigenous material (12 mg Al/cm^2/ka) and a high total sedimentation rate (1 cm/ka) (Kadko, 1981; Lyle et al., 1984). At Site H, the upper strata (< 10 cm) are relatively poor in calcite (< 5 %), which reflects that the seafloor depth is below the present-day calcite compensation depth (Lyle et al., 1984). In addition, the sediment cover at Site H contains up to 45% Mn-rich nodules (Graybeal and Ross Heath, 1984). Due to the dissolution of biogenic particles ($CaCO_3$) and the low terrigenous flux at Site H, both the Al flux (6 mg Al/cm^2/ka) and the total sedimentation rate (0.7 cm/ka) are only about half of those at Site M (Kadko, 1981; Lyle et al., 1984).

Both MANOP sites received high sedimentary fluxes of particulate organic matter (110 μg/cm^2/yr), which undergoes intense oxidation (Lyle et al., 1984). This results in a redox gradient of sub-oxic subsurface conditions underneath an oxygenated sediment-water interface, and consequently, the diagenetic redistributions of trace metals by reduction-oxidation and diffusive processes within the sediment core-top (Fig. 2.4) (Klinkhammer, 1980a; Emerson et al., 1980; Lyle et al., 1984). In particular, the reduction of Mn(IV) oxides to mobile Mn(II) at depth leads to the release of Mn into the pore waters, which diffuse upward. The Mn is thereby either re-precipitated as Mn(IV) oxides in the oxidised upper strata or it is released into the overlying water column. Strong, 2-fold enrichments in solid-phase Mn were observed in the upper 12 cm at both sites, but at Site M, the substantial loss of sedimentary Mn to the water column led to more subtle solid-phase Mn enrichments in the upper strata compared to Site

H. Similar redistribution processes also occur for Fe, through the reduction of Fe(III) oxyhydroxides to Fe(II) and the subsequent re-oxidation. The diagenetic redistribution of Fe at both sites are markedly more subtle, yielding solid-phase Fe enrichments of about 10% in the upper 14 cm (Site H) and 6 cm (Site M). In addition, both sites are affected by bioturbation in their uppermost ≤ 8 cm depth (Kadko and Heath, 1984; Kadko et al., 1987b).

2.2.5 Sampling

Sediment samples were collected during the VULCAN-1 and PLUTO-3 expeditions on the R/V Melville, which sailed in September 1980 and October 1981, respectively. Sediment cores were recovered using a 50 cm × 50 cm box corer and sub-sampled using a plastic core liner. The cores were then dried and stored at the Marine and Geology Repository at Oregon State University. For each site, three sub-samples from between 0 and 8 cm depths were retrieved from the sediment cores for isotope analyses. The selection of these young strata ensures that only samples deposited within the Holocene epoch (i.e. after the Last Glacial Termination) were included for analysis. Based on sedimentation rates of 0.7 cm/ka (Site H) and 1 cm/ka (Site M), samples from the top 8 cm would have deposition ages younger than 11,500 years before present, which fall within the Holocene epoch. Sub-sampling as deep as about 8 cm also ensures that pre-industrial strata, which are less likely to be contaminated by anthropogenic Pb, were used for the analyses.

2.3 Analytical Methods

Six sediment samples, three each from MANOP Sites H and M, were selected for processing in this study. Alongside the six bulk sediment samples, the leachate and detrital fractions were extracted from each of the bulk samples and processed for isotope analyses, resulting in a total of 18 samples.

All sample preparation work and determination of Nd and Pb isotope compositions were carried out at Imperial College London. Sample leaching, digestion and chromatographic procedures were performed in ISO Class 4 laminar flow hoods in ISO Class 6 clean rooms. The Nd and Pb concentrations were determined at the Eidgenössische Technische Hochschule Zürich (ETH Zürich). Milli-Q water with a resistivity of ~18.2 MΩ (Merk Millipore) was used throughout the procedures. The mineral acids used (HF, HNO_3, HCl and HBr) were purified by sub-boiling distillation (HBr was double-distilled) using quartz or Teflon distillation units, whilst Optima grade $HClO_4$ was purchased from Fisher Scientific.

2.3.1 Sediment Digestion and Determination of Nd and Pb Concentrations

Bulk sediment digestion and the determination of Nd and Pb concentrations were carried out by Susan H. Little, whereby the procedures are detailed in Little et al. (2020). For bulk sediment digestion, 49-103 mg of homogenised sediment powder were first decarbonated by treatment with 16 M HNO_3 and then digested in a 3+1 mixture of 28 M HF and 16 M HNO_3. Following evaporation of the solutions,

residual fluorides were removed by drying down the digestion residues three times with 16 M HNO_3. The digests were then dissolved in 6 mL 7 M HCl. Aliquots of bulk sediment digests were taken for multi-element analyses, including Nd and Pb, with a Thermo Scientific Element XR high-resolution inductively coupled plasma mass spectrometer. Further sample solution aliquots were used for the Nd and Pb isotope analyses.

2.3.2 Sequential Acid-Reductive Leaching

Sequential acid-reductive leaching was carried out by Rhian O'Callaghan to separate the authigenic leachate fractions and the detrital fractions from the bulk sediment samples. Similar procedures were developed and previously employed for the extraction of the authigenic signatures of Nd and Pb isotopes from marine sediments for palaeoceanographic reconstructions (e.g. Bayon et al., 2002; Gutjahr et al., 2007; Stumpf et al., 2010; Crocket et al., 2012; Wilson et al., 2013, 2015). In this study, the leaching procedure generally followed the method described by Haley et al. (2008), which was optimised for the extraction of Pb, Nd and strontium (Sr) isotope compositions of Fe-Mn oxyhydroxide leachates and detrital residues from pelagic sediment samples. Each sediment sample was first leached in a dilute, acid-reductive solution containing hydroxylamine hydrochloride (HH), acetic acid and Na_2-EDTA to extract a leachate fraction, which is presumed to be dominated by the acid-reducible Fe-Mn oxyhydroxides. Following two further leaching steps with more concentrated solutions of the acid mixture to ensure complete removal of the Fe-Mn oxyhydroxide phases, the solid residue that remained after the leaching procedure is the detrital fraction, which is dominated by refractory silicate phases.

In detail, 362-514 mg of homogenised sediment powder was taken for each sample, agitated in Milli-Q water, whereupon the water was decanted. To obtain the Fe-Mn oxyhydroxide leachates, the samples were agitated for 1 hour in 10 mL of an aqueous solution containing 0.005 M HH, 1.5% acetic acid and 0.03 M Na_2-EDTA, buffered to pH = 3.5-4.0 with NaOH. The remaining solids were further leached twice, for 3 and 17 hours, respectively, with 30 mL of a solution containing 0.05 M HH, 15% acetic acid and 0.03 M Na_2-EDTA, buffered to pH = 3.5-4.0 with NaOH, to remove any remaining Fe-Mn oxyhydroxide material. The remaining solids were the detrital fractions, which were triple-rinsed with Milli-Q water, dried and homogenised using a pestle and mortar. The Fe-Mn oxyhydroxide leachates were repeatedly dried and re-dissolved in 1 mL 16 M HNO_3, until the solutions were clear. For the detrital fractions, about 50 mg of each dried sample was digested by refluxing in 2 mL 28 M HF, 1 mL 16 M HNO_3 and 0.8 mL 11 M $HClO_4$ for two days. Both fractions were then dried and dissolved in 6 mL 6 M HCl.

Similar to the approach of Haley et al. (2008), a decarbonation step using buffered acetic acid prior to recovery of the Fe-Mn oxyhydroxide fraction was omitted. This is in light of leaching experiments by Wilson et al. (2013), which demonstrated that for sediment samples that are subjected to a decarbonation step, the subsequent HH leachates are more prone to release trace metals from the detrital phases and contaminate the recovered authigenic signature. Contrary to Haley et al. (2008), however,

Na_2-EDTA was included as a chelating agent in the leaching mixtures of the current study, as this helps to reduce re-adsorption of trace elements and to improve the selective extraction of Pb and REEs (Gutjahr et al., 2007; Wilson et al., 2013).

2.3.3 Purification and Isotope Analyses of Nd

The purification and isotope analyses of Nd were conducted by Rhian O'Callaghan. Neodymium was separated from the sample solutions using a two-stage chromatographic procedure, detailed in Table 2.1 and following an established method (Struve et al., 2016). Briefly, the rare earth elements (REEs) were first separated from matrix elements by cation exchange chromatography using Bio-Rad AGW50-X8 resin (200-400 mesh), whilst Nd was then separated from other REEs using Ln-Spec resin (50-100 μm bead size). Neodymium isotope analyses were then carried out with a Nu Instruments Nu Plasma HR multi-collector inductively coupled plasma mass spectrometer (MC-ICP-MS). A small (5%) aliquot was first taken from each sample and analysed by MC-ICP-MS to determine the total mass of Nd available for analysis. Another aliquot was then taken and diluted to 1 mL 0.1 M HNO_3 to obtain a Nd concentration of about 50 ng/mL for the isotope measurement. The MC-ICP-MS was operated in static multi-collection mode. Isotope analyses were conducted in three sessions in October and November 2018, alongside the standard reference materials BCR-2 and JNdi-1. A correction for the (negligible) isobaric interference of ^{144}Sm on ^{144}Nd was applied. To correct for instrumental mass fractionation, the measured $^{143}Nd/^{144}Nd$ ratios were corrected using the exponential law and relative to a $^{146}Nd/^{144}Nd$ ratio of 0.7219. Finally, the sample ratios were corrected for the mean offset between the $^{143}Nd/^{144}Nd$ ratios determined for the bracketing JNdi-1 standards and the reference value of 0.512115 ± 0.000007 (Tanaka et al., 2000).

The external precision of the $^{143}Nd/^{144}Nd$ measurements was assessed from replicate analyses of the JNdi-1 standard, which yielded within-session 2 SD (standard deviations) reproducibilities of 35-57 ppm. The basaltic USGS reference material BCR-2 was processed alongside the sediment samples, and yielded an average $^{143}Nd/^{144}Nd$ ratio of 0.512644 ± 0.000035 (uncertainty is 2 SD; n = 6). This result agrees with the previously published $^{143}Nd/^{144}Nd$ value of 0.512638 ± 0.000015 (Weis et al., 2006). Two procedural blanks of 30 and 28 pg were both negligible (at < 0.02%) compared to the indigenous Nd present in the processed sediment samples (130-5300 ng).

2.3.4 Purification and Isotope Analyses of Pb

The matrix element fractions, which were eluted from the cation exchange resin with 3 M HCl before elution of the rare earth elements, were collected for the separation of Pb. These fractions were dried and re-dissolved in 5 mL 6 M HCl. Following aliquoting, the sample solutions were dried and refluxed twice in 2 M HBr for conversion to the bromide form. Following drying, the sample residues were re-dissolved in 5 mL 2 M HBr for purification. For the separation of Pb from matrix elements, two identical stages of HBr-HNO_3 anion exchange column chromatography were carried out, which

followed established methods (Paul et al., 2015; Wilson et al., 2017) and are detailed in Table 2.2. Following purification, the Pb fractions were dried and re-dissolved in 1 mL 0.1 M HNO_3 for the isotope analyses.

Lead isotope analyses were conducted on a Nu Instruments Nu Plasma II MC-ICP-MS. A small (5%) aliquot was first taken from each sample and analysed by MC-ICP-MS to determine the total mass of Pb available for analysis. Another aliquot was then taken and doped with a NIST SRM 997 Tl solution. The Pb-Tl mixtures were immediately dried down, and then re-dissolved in 1.5 mL 0.1 M HNO_3 to obtain Pb and Tl concentrations of about 10 ng/mL. The isotope analyses followed the 'unspiked' protocol of Griffiths et al (2020). Within each measurement session, a set of NIST SRM 981 Pb – NIST SRM 997 Tl standard mixtures with Pb and Tl concentrations of ≈ 10 ng/mL were measured together with the samples to monitor within-run precision and to support correction of the instrumental mass fractionation. All sample measurements were conducted in two sessions in July and August 2020, respectively.

The measured isotope data was processed offline using the MATLAB program developed by Griffiths et al (2020) on a session-by-session basis. The isobaric interference of ^{204}Hg on ^{204}Pb was corrected based on the monitored ^{202}Hg ion beam intensity and a natural $^{204}Hg/^{202}Hg$ ratio of 0.22923 (Meija et al., 2010). To correct for instrumental mass fractionation, the Pb isotope ratios of the samples were externally normalised using an empirically optimised $^{205}Tl/^{203}Tl$ reference ratio based on the mass fractionation that was determined for the SRM 981 Pb – SRM 997 Tl standard mixtures (Rehkämper and Halliday, 1998). Finally, an offset correction was applied to the sample ratios using the residual deviations between the measured values and the reference values of Galer (1999) for SRM 981 Pb.

The external precision of the Pb isotope analyses was assessed from replicate analyses of the 10 ng/mL SRM 981 Pb – SRM 997 Tl standard mixtures in a measurement session. These runs yielded 2 SD reproducibilities of ~120 ppm for $^{206}Pb/^{204}Pb$, 100-170 ppm for $^{207}Pb/^{204}Pb$ and 110-190 ppm for $^{208}Pb/^{204}Pb$. To assess the accuracy of Pb isotope analyses, the USGS reference material BCR-2 was processed alongside each batch of six Pb samples, and this yielded results of $^{206}Pb/^{204}Pb = 18.749 \pm 0.003$, $^{207}Pb/^{204}Pb = 15.620 \pm 0.001$ and $^{208}Pb/^{204}Pb = 38.713 \pm 0.003$ (2 SD; $n = 3$). These data agree with previously published values of $^{206}Pb/^{204}Pb = 18.753 \pm 0.020$, $^{207}Pb/^{204}Pb = 15.625 \pm 0.004$ and $^{208}Pb/^{204}Pb = 38.724 \pm 0.041$ (Weis et al., 2006). Notably, the quoted precisions, of ~150 ppm for $^{206}Pb/^{204}Pb$, ~70 ppm for $^{207}Pb/^{204}Pb$ and ~80 ppm for $^{208}Pb/^{204}Pb$, are similar to the within-session reproducibilities that were obtained for replicate runs of SRM 981 Pb – SRM 997 Tl standard mixtures. Three procedural blanks for the anion exchange separation gave results of 5, 22 and 32 pg, which are all negligible (at < 0.01%) compared to the indigenous Pb present in the processed sediment samples (110-380 ng).

Table 2.1. Column chemistry procedure for the separation of Nd from sediment samples.

Purpose	Chemistry
Stage 1: Cation Exchange Chromatography	
1.4 mL Bio-Rad AG50W-X8 resin (200-400 mesh)	
Clean resin	1 × 10 mL 6 M HCl
Equilibrate resin	2 × 0.5 mL 1 M HCl
Load sample	2 × 0.5 mL sample in 1 M HCl
Elute matrix	2 × 0.5 mL 1 M HCl
	1 × 0.5 mL 3 M HCl
	2 × 3.25 mL 3 M HCl
Elute REE	1 × 6.5 mL 6 M HCl
Stage 2: Ln-spec Chemistry	
500 µL Eichrom Ln-Spec resin (50-100 µm bead size)	
Clean resin	1 × reservoir 6 M HCl
	2 × 1 mL Milli-Q water
Prepare sample	0.2 mL 0.2 M HCl to sample;
	30 minutes in ultrasonic bath
Equilibrate resin	2 × 1 mL 0.2 M HCl
Load sample	1 × 0.2 mL sample in 0.2 M HCl
Elute REEs	2 × 0.15 mL 0.2 M HCl
	1 × 4 mL 0.2 M HCl
Elute Nd	1 × 2.5 mL 0.2 M HCl

Table 2.2. Column chemistry procedure for the separation of Pb from sediment samples.

Purpose	Chemistry
Anion Exchange Chromatography, Two Identical Stages	
200 µL Eichrom AG1-X8 resin (100-200 mesh)	
Clean resin	3 × 3 mL 0.1 M HNO_3
Equilibrate resin	2 × 0.1 mL 2 M HBr
Load sample	5 mL sample in 2 M HBr
Elute matrix	2 × 0.1 mL 2 M HBr
	2 × 0.5 mL 0.2 M HBr – 0.5 M HNO_3
	1 × 0.2 mL 0.03 M HBr – 0.5 M HNO_3
Elute Pb	2 × 1.5 mL 0.03 M HBr – 0.5 M HNO3

Table 2.3. Isotope compositions and concentrations of Pb and Nd for the sediment samples from MANOP Sites H and M. Isotope measurements were conducted on the bulk sediment samples (-B) and the leachate (-L) and detrital (-R) fractions.

Fraction	Full sample name (cruise/core/stratum)	Short sample name	Depth (cm)	$^{206}Pb/^{204}Pb$	Within-run external 2sd[(a)]	$^{207}Pb/^{204}Pb$	Within-run external 2sd[(a)]	$^{208}Pb/^{204}Pb$	Within-run external 2sd[(a)]	ε_{Nd}[(b)]	Within-run external 2sd[(c)]	[Pb] (µg/g)	[Nd] (µg/g)
MANOP Site H													
Bulk	PLUTO 15MBC MP8950 AAZ	8950-B	3-4 cm	18.679	0.002	15.596	0.003	38.532	0.007	-1.5	0.3	12.2	27.9
	Repeat			18.676	0.002	15.595	0.002	38.530	0.004				
	Repeat			18.676	0.002	15.599	0.002	38.539	0.004				
	VULCAN 37BC MP5306 AAZ	MP6-B	5-7 cm	18.678	0.002	15.596	0.003	38.531	0.007	-1.3	0.6	13.6	31.2
	Repeat			18.676	0.002	15.596	0.002	38.530	0.004				
	Repeat			18.674	0.002	15.594	0.002	38.525	0.004				
	Repeat			18.678	0.002	15.596	0.002	38.529	0.004				
	VULCAN 37BC MP5307 AAZ	MP8-B	7-9 cm	18.679	0.002	15.595	0.003	38.526	0.007	-1.5	0.4	13.3	30.0
	Site H Mean			**18.68**		**15.60**		**38.53**		**-1.4**			
	SD			**0.00**		**0.00**		**0.00**		**0.1**			
Leachate	PLUTO 15MBC MP8950 AAZ (L)	8950-L	3-4 cm	18.643	0.002	15.592	0.002	38.503	0.004	-1.8	0.6		
	VULCAN 37BC MP5306 AAZ (L)	MP6-L	5-7 cm	18.645	0.002	15.598	0.002	38.516	0.004	-1.9	0.3		
	Repeat			18.647	0.002	15.595	0.002	38.512	0.004				
	VULCAN 37BC MP5307 AAZ (L)	MP8-L	7-9 cm	18.645	0.002	15.592	0.002	38.499	0.004	-1.8	0.6		
	Site H Mean			**18.64**		**15.59**		**38.51**		**-1.8**			
	SD			**0.00**		**0.00**		**0.01**		**0.1**			
Detrital	PLUTO 15MBC MP8950 AAZ (R)	8950-R	3-4 cm	18.843	0.002	15.623	0.002	38.703	0.004	0.7	0.6		
	VULCAN 37BC MP5306 AAZ (R)	MP6-R	5-7 cm	18.847	0.002	15.624	0.002	38.704	0.004	0.1	0.6		
	VULCAN 37BC MP5307 AAZ (R)	MP8-R	7-9 cm	18.851	0.002	15.623	0.002	38.707	0.004	0.2	0.6		
	Site H Mean			**18.85**		**15.62**		**38.70**		**0.3**			
	SD			**0.00**		**0.00**		**0.00**		**0.3**			

Table 2.3 (cont'd).

Fraction	Full sample name (cruise/core/stratum)	Short sample name	Depth (cm)	$^{206}Pb/^{204}Pb$	Within-run external 2sd[(a)]	$^{207}Pb/^{204}Pb$	Within-run external 2sd[(a)]	$^{208}Pb/^{204}Pb$	Within-run external 2sd[(a)]	ε_{Nd}[(b)]	Within-run external 2sd[(c)]	[Pb] (μg/g)	[Nd] (μg/g)
MANOP Site M													
Bulk	PLUTO 20BC MP8966 AAZ	8966-B	0.5-1 cm	18.526	0.002	15.557	0.003	38.213	0.007	-1.7	0.6	17.1	25.1
	PLUTO 20BC MP8967 AAZ	8967-B	1-3 cm	18.524	0.002	15.554	0.003	38.201	0.007	-1.7	0.6	19.1	27.4
	PLUTO 20BC MP8969 AAZ	8969-B	5-7 cm	18.533	0.002	15.559	0.003	38.220	0.007	-1.8	0.3	16.2	22.6
	Site M Mean			**18.53**		**15.56**		**38.21**		**-1.7**			
	SD			**0.00**		**0.00**		**0.01**		**0.1**			
Leachate	PLUTO 20BC MP8966 AAZ (L)	8966-L	0.5-1 cm	18.503	0.002	15.552	0.002	38.178	0.004	-1.7	0.6		
	PLUTO 20BC MP8967 AAZ (L)	8967-L	1-3 cm	18.503	0.002	15.551	0.002	38.174	0.004	-1.6	0.6		
	PLUTO 20BC MP8969 AAZ (L)	8969-L	5-7 cm	18.549	0.002	15.566	0.002	38.264	0.004	-1.5	0.6		
	Site M Mean			**18.52**		**15.56**		**38.21**		**-1.6**			
	SD			**0.03**		**0.01**		**0.05**		**0.1**			
Detrital	PLUTO 20BC MP8966 AAZ (R)	8966-R	0.5-1 cm	18.625	0.002	15.587	0.002	38.392	0.004	-2.5	0.3		
	PLUTO 20BC MP8967 AAZ (R)	8967-R	1-3 cm	18.621	0.002	15.587	0.002	38.392	0.004	-2.4	0.6		
	PLUTO 20BC MP8969 AAZ (R)	8969-R	5-7 cm	18.621	0.002	15.587	0.002	38.387	0.004	-2.5	0.6		
	Site M Mean			**18.62**		**15.59**		**38.39**		**-2.5**			
	SD			**0.00**		**0.00**		**0.00**		**0.1**			

(a) 2× standard deviations of repeated Pb isotope analyses of NIST SRM 981 – SRM 997 standard solutions (≈ 10 ng/g Pb, Tl) in each measurement session.

(b) ε_{Nd} values were calculated based on a $^{143}Nd/^{144}Nd$ ratio of 0.512638 for the Chondritic Uniform Reservoir (CHUR): $(^{143}Nd/^{144}Nd_{sample} / {}^{143}Nd/^{144}Nd_{CHUR} - 1) \times 10^4$.

(c) 2× standard deviations of repeated Nd isotope analyses of JNdi-1 standard solutions (≈ 50 ng/g Nd) in each measurement session.

2.4 Results

For the two MANOP sites of this study, Pb and Nd concentrations of 12-19 µg/g and 23-31 µg/g, respectively, are observed within the upper 8 cm of the sediment cores (Table 2.3; Fig. 2.3d, h). For both Pb and Nd concentrations, downcore variations in elemental abundances are less than about 10%, except for Nd concentrations at Site M (< 20%). At Site H, the sediment samples have relatively low Pb concentrations (12.7 ± 0.7 µg/g; 1 SD) and higher Nd abundances (29.7 ± 1.7 µg/g), which give low Pb/Nd ratios of around 0.4. In contrast, the sediment samples from Site M have higher Pb (17.2 ± 1.2 µg/g) and lower Nd abundances (25.0 ± 1.8 µg/g), giving higher Pb/Nd ratios of about 0.7.

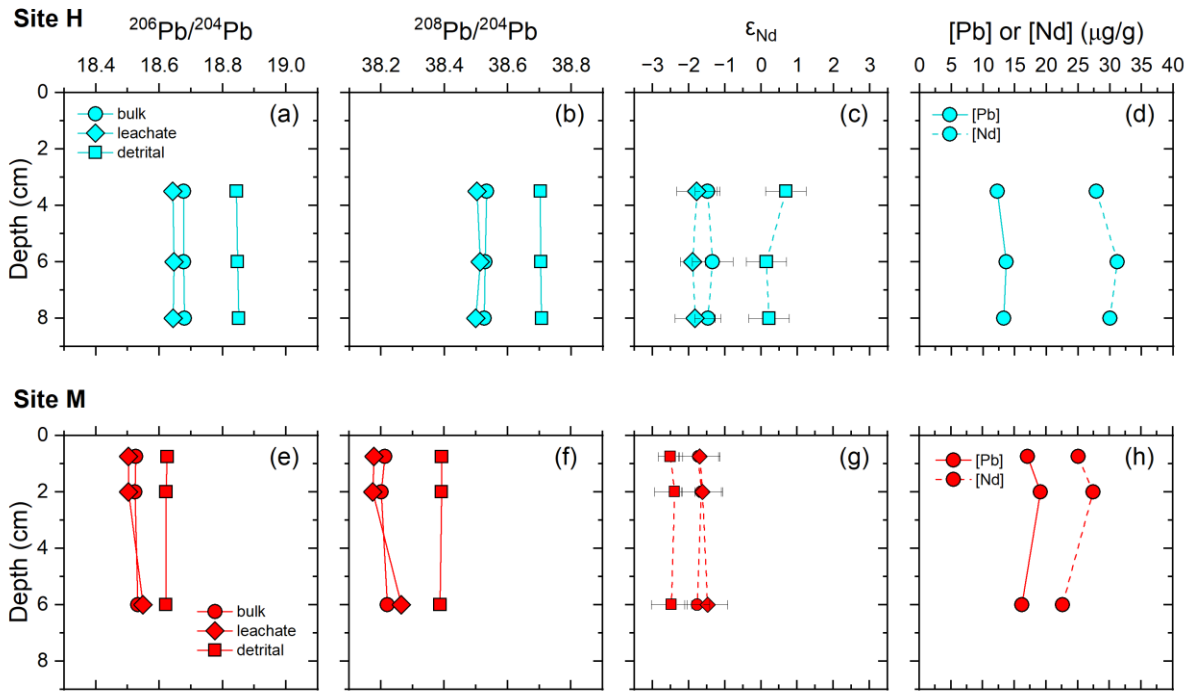


Figure 2.3. Vertical profiles of Pb and Nd isotope compositions and concentrations of sediments from MANOP Sites H (upper panels) and M (lower panels). From left to right: (a, e) $^{206}Pb/^{204}Pb$, (b, f) $^{208}Pb/^{204}Pb$; (c, g) Nd isotope compositions (in ε_{Nd}) and (d, h) bulk sedimentary concentrations of Pb and Nd. Trends for Pb and Nd are shown as solid and dashed lines, respectively. In the panels of isotope compositions (a-c, e-g), separate data for the bulk sediments (circles), leachate fractions (diamonds) and squares (squares) are shown. The distributions of $^{207}Pb/^{204}Pb$, not shown, are similar to $^{208}Pb/^{204}Pb$. Errors for the $^{206}Pb/^{204}Pb$ and $^{208}Pb/^{204}Pb$ ratios are smaller than the symbol sizes.

For both Pb and Nd, the isotope compositions of the bulk sediments and the leachate and detrital fractions show only limited downcore variations for the samples collected between 0 and 8 cm depths at each site (Table 2.3; Fig. 2.3a-c, e-g). Furthermore, within each site, the isotope compositions of the bulk sediments are consistently very similar or identical to the leachates but differ significantly from the detrital fractions. In detail, at Site H, the Pb isotope ratios of the leachate fractions ($^{206}Pb/^{204}Pb$ =

18.64, $^{207}Pb/^{204}Pb$ = 15.59, $^{208}Pb/^{204}Pb$ = 38.51) are very similar to the bulk sediment results (18.68, 15.60, 38.53), while the values for the detrital fractions (18.85, 15.62, 38.70) are consistently more radiogenic. Similar systematics are seen at Site M, but the Pb isotope compositions of the bulk sediments and the sediment fractions are less radiogenic than at Site H. In detail, the $^{20x}Pb/^{204}Pb$ ratios of the detrital fractions (18.62, 15.59, 38.39) are more radiogenic than the bulk sediments (18.53, 15.56, 38.21) and the leachates (18.52, 15.56, 38.21). The Nd isotope compositions of the leachate fractions from Site H (ε_{Nd} = –1.8) and Site M (ε_{Nd} = –1.6) are identical, within the 2 SD precision of the data, to the results obtained for the bulk sediments, with ε_{Nd} values of –1.4 and –1.7 for Sites H and M, respectively. In contrast, the detrital compositions are significantly different, with a higher ε_{Nd} value of +0.3 at Site H but a less radiogenic result of ε_{Nd} = –2.5 at Site M.

2.5 Discussion

2.5.1 Assessing Possible Analytical Artefacts in the Measured Pb-Nd Isotope Compositions

In this study, derivation of the radiogenic isotope compositions of deep seawater and detrital sediments relies on the laboratory extraction of operationally-defined authigenic and detrital fractions, respectively, from bulk marine sediment samples. Before making oceanographic interpretations on the measured isotope compositions, some potential issues need to be addressed, including: (1) effectiveness of the chosen extraction technique in isolating the authigenic and detrital signatures of radiogenic isotopes, (2) possible analytical artefacts due to bioturbation and diagenetic remobilisation, and (3) potential anthropogenic Pb contamination.

2.5.1.1 Efficacy in Isolating the Authigenic and Detrital Signatures

The first issue relates to the fidelity of the measured Pb and Nd isotope compositions towards the 'true' authigenic and detrital archives. The extraction method carries the inherent caveats that elements from phases other than Fe-Mn oxyhydroxides may dissolve in the first leachate fraction and therefore contaminate the authigenic signature, whilst elements from phases other than terrigenous particles may remain in the solid residue and therefore contaminate the detrital signature.

The detectable mineral phases in the MANOP sediment samples include clay minerals, calcite, feldspars, quartz, Fe-Mn oxyhydroxides and barite (halite is assumed to have completely dissolved during the water agitation step before the leaching step). During the initial acid leach, clay minerals (e.g. smectite) and calcite ($CaCO_3$) are possibly attacked to release their Pb and Nd budgets alongside Fe-Mn oxyhydroxides, the desired phases in the leachate fractions (Harlavan et al., 2010; Wilson et al., 2013). The use of a very dilute leach solution, with only 0.005 M HH, in this study already acts as a precaution to minimise the dissolution of clay minerals (e.g. Haley et al., 2008). Whilst the dissolution of $CaCO_3$ is inevitable, this will likely only have a very minor impact on the Pb and Nd isotope

compositions of the recovered leachate fractions. In particular, previous studies of hemipelagic sediments from various ocean basins found no significant differences in the Pb isotope signatures of decarbonated and non-decarbonated samples (Haley et al., 2008; Basak et al., 2011; Wilson et al., 2015). Furthermore, leaching experiments on Eastern Pacific pelagic sediments also confirmed that Pb was primarily present in Fe-Mn oxyhydroxide phases (40-65%), with only minor partitioning into $CaCO_3$ lattices (≤ 5%) (Koschinsky et al., 2001). Neodymium and other REEs are also known to be enriched in Fe-Mn oxyhydroxides (ΣREE ~ 10^3 ppm) by about an order of magnitude compared to $CaCO_3$ (ΣREE < 200 ppm) (Kato et al., 2011; Liao et al., 2019, 2022). Therefore, the extracted leachate fractions are likely to be dominated by Fe-Mn oxyhydroxide phases, and thus faithfully record the water mass signatures.

Chemically precipitated barite can survive the leaching steps and remain in the solid residues, alongside terrestrially derived quartz, feldspars and clays. For Nd, Martin et al. (1995) demonstrated that the element is significantly depleted in marine barites (< 4 ppm) compared to terrigenous particles (≈ 30 ppm, Winter et al., 1997), and that the Nd isotope compositions of marine barites are controlled by detrital grains that are trapped in the crystal lattices. Lead as a divalent cation, however, can substitute for barium (Ba) and may therefore be enriched in marine barites (Griffith and Paytan, 2012; Jewell et al., 2022). Without published data on typical Pb concentrations in marine barites, contamination of detrital fractions by barite-hosted Pb cannot be ruled out. Fortunately, potential artefacts in provenance tracing caused by contamination of the detrital signature by barite-hosted seawater Pb is minimised in this study, through the complementary use of the Nd isotope system, which is minimally affected by barite contamination.

2.5.1.2 Bioturbation and Diagenesis

The second issue relates to potential disturbances of the pristine, natural source signatures by post-depositional processes. Profiles of trace metals and their isotopes in sediment core-tops are especially prone to post-depositional redistribution processes, notably bioturbation and chemical diagenesis. For the former process, numerous faunal activities, from the development of burrows, ingestion and excretion of sediment particles to the infilling of abandoned cavities, can lead to physical stirring and mixing of sediment particles (Hülse et al., 2022). For the latter process, diagenetic dissolution and reprecipitation of redox-sensitive phases can result in the redistributions of many trace elements within the sediment column (e.g. Graybeal and Ross Heath, 1984). These processes could alter archives of sediment fluxes by mixing and homogenising potentially distinct signals of trace metals and their isotopes across strata, obscuring potential flux changes over time.

Bioturbation may have affected the acquired isotope data if the depth of biological mixing penetrated below the sediment profile of interest. The bioturbation profiles at both MANOP Sites H and M have been studied in detail (Kadko and Heath, 1984; Cochran, 1985; Kadko et al., 1987b) and are best illustrated with profiles of naturally occurring, short-lived radionuclides, such as ^{210}Pb (half-life =

22.3 years), whereby their depths of penetration approximate the bioturbation zone (Fig. 2.4e, j). At MANOP Site H, the excess ^{210}Pb profile shows physical mixing that is restricted to the upper 5 cm of the sediment column, therefore affecting only the uppermost of the three Pb-Nd isotope samples (3.5 cm). This argues against a bioturbation-related artefact on the observed downcore homogeneities in Pb and Nd isotope compositions at Site H. At Site M, the combination of ^{210}Pb observations and modelling reveals physical mixing down to about 8 cm depth, and this may have hence affected all Pb-Nd isotope samples at this site (0.5-7 cm). Therefore, the observed downcore homogeneities in Pb and Nd isotopes are potentially a consequence of physical mixing, rather than stable provenance over time. Nevertheless, physical mixing did not penetrate to below the Pleistocene-Holocene boundary at 12 cm at this site (Pleistocene-Holocene transition at 12 kyr; sedimentation rate ≈ 1 cm/kyr), such that the measured isotope signatures can still be treated to represent an average of inputs across the Holocene.

At the two MANOP sites, diagenetic remobilisation associated with Fe-Mn oxyhydroxides exert key controls over the solid-phase distributions of Mn, Fe and other trace metals (Co, Ni, Cu, Zn) in the top two decimetres of the sediments (Fig. 2.4c-d, h-i) (Klinkhammer, 1980a; Graybeal and Ross Heath, 1984; Lyle et al., 1984; Little et al., 2020). The potential diagenetic redistributions of Pb and Nd can be assessed from the coupling of their downcore solid-phase concentrations with Mn and Fe (Fig. 2.4b-d, g-i). At both studied sites, Pb and Nd exhibit clear, strong coupling in concentrations with Fe. In detail, these elements have similar profile shapes that are characterised by subtle downcore variations and slight enrichments in the upper 14 cm (Site H) and 6 cm (Site M). Furthermore, the Pb/Fe (Site H: 1.3×10^{-4}; Site M: 8×10^{-5}) and Nd/Fe (Site H: 7.4×10^{-4}; Site M: 4.6×10^{-4}) ratios remain constant with depth. In contrast, the Pb and Nd concentrations are decoupled from Mn. The observed close coupling with Fe is in accord with the affinities of Pb and Nd to Fe oxyhydroxides as compared to Mn oxides, based on leaching studies of hydrogenous Fe-Mn crusts (Koschinsky and Hein, 2003; Bau and Koschinsky, 2009). It is likely that Pb and Nd are released when Fe oxyhydroxides dissolve during diagenetic processes, whereupon they will diffuse upward to be re-scavenged by newly formed Fe oxyhydroxides phases at shallower depths. Hence, whilst diagenetic redistributions of Pb and Nd were likely associated with Fe cycling at the two MANOP sites, the redistributions were subtle, as these added only about 10-15% of the Pb and Nd budgets to the upper 7-9 cm of the studied cores. Given these mass balance considerations, the original Pb and Nd isotope compositions of the core-tops were likely altered only to a small extent by the minor diagenetic additions of the elements.

2.5.1.3 Anthropogenic Pb Contamination

The natural source signatures of Pb in sediment core-tops are additionally prone to contamination by anthropogenic Pb. Throughout the 20th century, the marine inputs of Pb were significantly elevated due to emissions associated with leaded petrol consumption, and these anthropogenic Pb fluxes were subsequently introduced into the sediment reservoir (Hamelin et al., 1990; Boyle et al., 2014). Possible anthropogenic Pb contamination of the MANOP sediment samples can be assessed by two means: (1)

identifying anomalies in Pb concentrations within contaminated horizons marked by the anthropogenic radionuclides $^{239, 240}$Pu and ^{137}Cs (Fig. 2.4); (2) comparing the isotope results with the compositions of major ore types associated with leaded petrol production and data for contaminated aerosols and sediment samples from the wider EEP (Fig. 2.5).

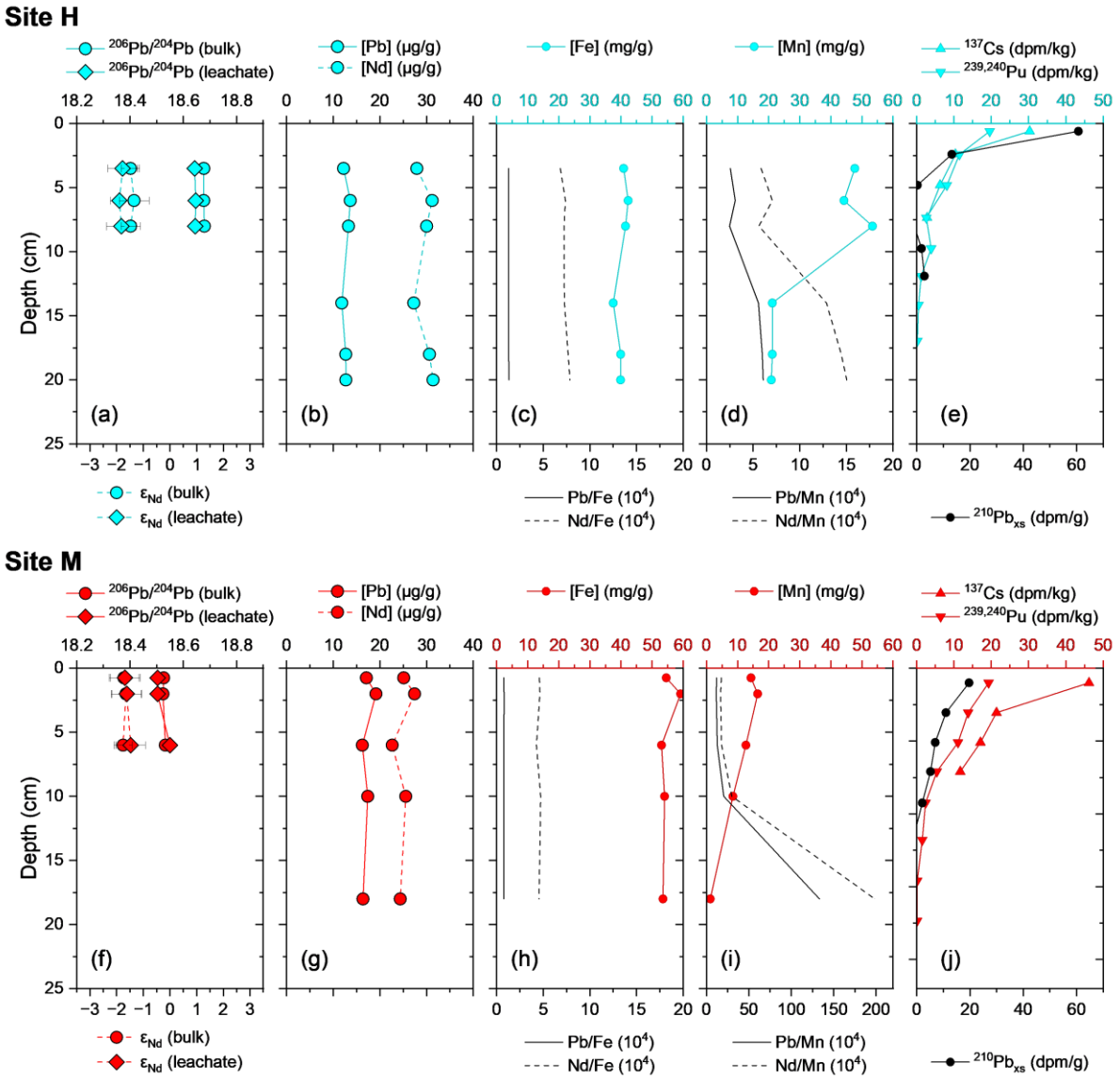


Figure 2.4. Vertical profiles of the solid phase concentrations, elemental ratios and/or isotope ratios of various trace elements (Pb, Nd, Fe, Mn) and radionuclides (^{210}Pb, ^{137}Cs, $^{239, 240}$Pu) for ≤ 20 cm sediment depth at MANOP Sites H and M. From left to right: (a, f) Pb and Nd isotope compositions; (b, g) Pb and Nd concentrations; (c, h) Fe concentrations and molar Pb/Fe and Nd/Fe ratios; (d, i) Mn concentrations and molar Pb/Mn and Nd/Mn ratios; (e, j) ^{210}Pb, ^{137}Cs and $^{239, 240}$Pu activities (Cochran, 1985). Excess ^{210}Pb (^{210}Pb$_{xs}$) was calculated by subtracting the ^{226}Ra activity from the ^{210}Pb activity. Unless stated otherwise, the data shown are bulk sedimentary compositions.

The radionuclides $^{239, 240}$Pu and ^{137}Cs were introduced into the global ocean by atmospheric fallout from nuclear weapon testing during the 1950s and early 1960s, and these nuclides were rapidly scavenged and deposited on the seafloor (Livingston and Povinec, 2000; Lee et al., 2005). Detectable levels of these radionuclides in sediment strata, therefore, serve as an age marker for recent sediment accumulation or physicochemical interactions with particles from the sediment-water interface during or after the 1950s (Livingston and Povinec, 2002). Notably, this timing coincides with the rapid increase in global Pb influxes to the ocean after World War II (Kelly et al., 2009; Boyle et al., 2014). At both MANOP sites, infiltrations of $^{239, 240}$Pu and ^{137}Cs were detected down to about 10 cm depth, and this encompasses all samples analysed for Pb and Nd isotopes in this study (Cochran, 1985) (Fig. 2.4e, j). However, Pb concentrations within the contaminated zones at both sites show no surface enrichment compared to the underlying strata – apart from the slight enrichments associated with Fe-phase diagenesis (Fig. 2.4b, g). The downcore variations in Pb concentrations are furthermore in accord with those of Nd, and the marine inventory of the latter element is not known for major anthropogenic perturbations. Therefore, any additions of anthropogenic Pb are likely insignificant relative to the natural Pb budgets of the sediment reservoirs.

The presence of anthropogenic Pb can be more accurately assessed with Pb isotope data (Fig. 2.5). For instance, Holocene (< 11 ka) sediment samples from a core obtained at Ocean Drilling Program (ODP) Site 849 (0°N, 110°W) in the EEP show clear perturbations by Mississippi Valley-type contamination with high ^{20x}Pb/^{204}Pb ratios (^{206}Pb/^{204}Pb = 21-23, ^{207}Pb/^{204}Pb = 15.9, ^{208}Pb/^{204}Pb = 40-42) (Sangster et al., 2000), which affected aerosols from the USA (Pichat et al., 2014). This is in accord with the overwhelmingly high Pb emissions from the USA compared to from other nations and regions across the American continent (see Section 1.5.2). In contrast, at MANOP Site H, the bulk sedimentary Pb isotope compositions fall within the ranges obtained for uncontaminated Quaternary sediments across the EEP (Pichat et al., 2014; Höfig et al., 2016; Erhardt et al., 2021). This suggests that any anthropogenic Pb contamination of the sediment samples from this site is negligible. The bulk sediments from MANOP Site M, however, have Pb isotope ratios that deviate from the compositions of most EEP sediments towards lower ^{20x}Pb/^{204}Pb values. Whilst these deviations could be a consequence of Broken Hill-type contamination (^{206}Pb/^{204}Pb = 16, ^{207}Pb/^{204}Pb = 15.4, ^{208}Pb/^{204}Pb = 36) (Doe and Stacey, 1974; Townsend et al., 1998) that affected South American (e.g. Colombian and Ecuadorian) aerosols, such contamination is very unlikely. This reflects the significantly lower historical levels of anthropogenic Pb emissions from the South American continent (≥ 13 kt/yr; year 1970) compared to North American nations (≥ 240 kt/yr from the USA and Mexico; year 1970) (Fig. 1.3, Chapter 1). As such, the relatively low ^{20x}Pb/^{204}Pb ratios observed at MANOP Site M are more likely a consequence of distinct natural inputs characterised by low ^{20x}Pb/^{204}Pb.

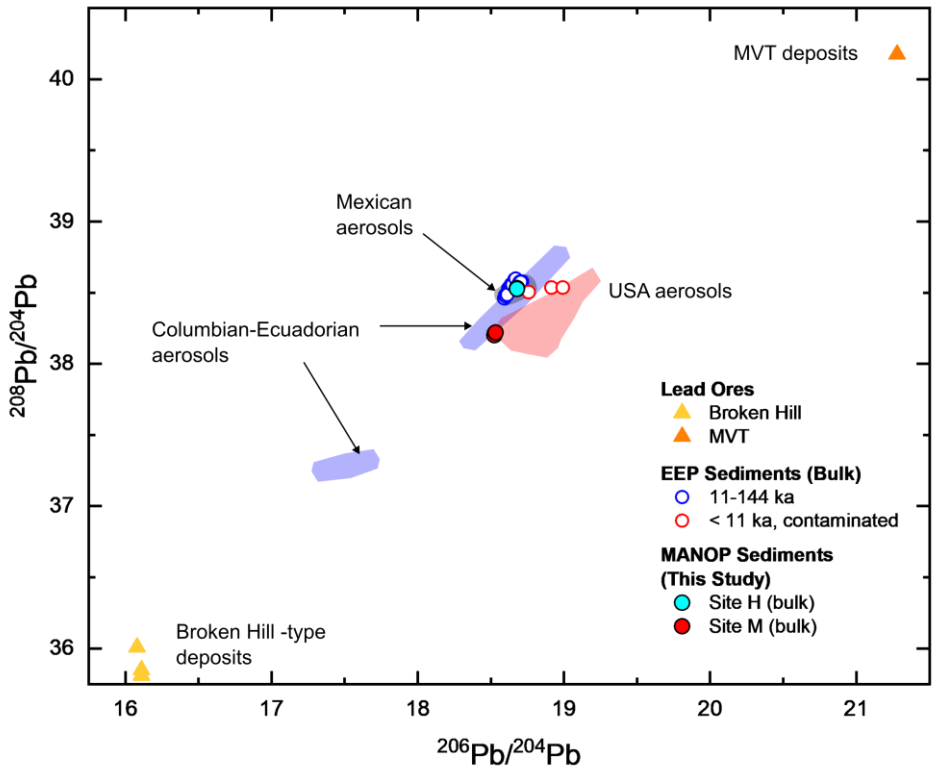


Figure 2.5. Plot of $^{208}Pb/^{204}Pb$ versus $^{206}Pb/^{204}Pb$ ratios for the bulk and leachate samples from MANOP Sites H and M and potential sources of anthropogenic contamination. The data for Quaternary bulk sediment samples from the EEP (open circles, errors smaller than the symbol sizes), with the contaminated core-top samples highlighted in red, are from Pichat et al. (2014) and Höfig et al. (2016). Coloured fields indicate the isotope ranges of aerosols from the continental regions surrounding the Guatemala Basin (Bollhöfer and Rosman, 2000, 2001). Also shown are the compositions of Broken Hill-type ores (Doe and Stacey, 1974; Townsend et al., 1998) and Mississippi Valley-type (MVT) ores (Sangster et al., 2000).

Based on the above consideration and discussion of Pb concentration and isotope compositions, as well as available results for anthropogenic radionuclides and Nd concentrations, the impact of anthropogenic Pb contamination on the measured Pb isotope data of the sediments is likely negligible. As such, the following discussion focuses on the natural sources of Pb in the detrital and leachate fractions of the MANOP sediments.

2.5.2 Detrital Sediments: Characterisation of Potential Source Areas

Possible sources of detrital materials in marine sediments include aeolian dust emitted from proximal or distal continental regions and hemipelagic materials delivered from relatively proximal continental regions. In order to identify the key source regions of detrital materials to the two MANOP sites, the Pb and Nd isotope signatures of potential terrestrial source areas are characterised using compiled literature data for bulk rocks, soils and dust from the major mountain sectors along the American Cordillera and other distal dust sources (Fig. 2.6). Details about the data compilation are provided in Appendix 1.

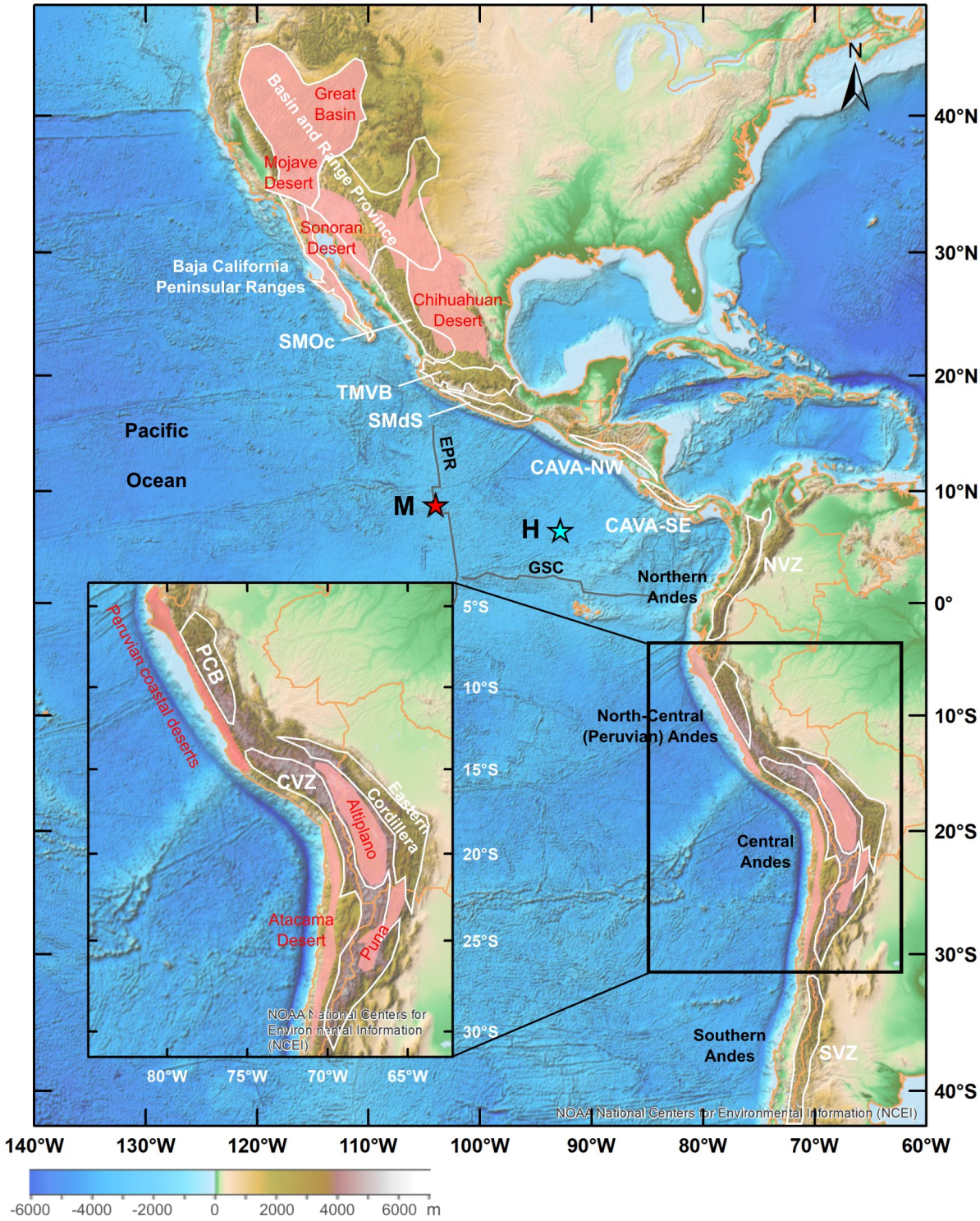


Figure 2.6. Map showing the major arid regions (pink shades) and mountain belts (white contours) used to characterise the Pb-Nd isotope signatures of the terrigenous sediment sources across the western side of the American continent. Mountain belts: Basin and Range Province of Western USA (eastern and western sectors), Baja California Peninsular Ranges, Sierra Madre Occidental (SMOc), Trans-Mexican Volcanic Belt (TMVB), Sierra Madre del Sur (SMdS), the Northwest and Southeast sectors of the Central American Volcanic Arc (CAVA-NW and CAVA-SE), Northern Volcanic Zone (NVZ), Peruvian Coastal Batholith (PCB), Central Volcanic Zone (CVZ), Eastern Cordillera of the Central Andes and Southern Volcanic Zone (SVZ). Inset shows an enlarged map of the mountain sectors and arid regions across the Peruvian and Central Andes.

2.5.2.1 Proximal terrestrial sources

Terrigenous materials from proximal source areas were shown to dominate the detrital fluxes to marginal regions of the Pacific Ocean (Lyle, 1992; Nakai et al., 1993; Jones et al., 2000). In the EEP, various South Mexican and Central American terranes along the northern margin of the ocean region, including the Trans-Mexican Volcanic Belt (TMVB), Sierra Madre del Sur (SMdS) and the northwest segment of the Central American Volcanic Arc (CAVA-NW), have been identified as key sources of terrigenous sediments (Saukel et al., 2011; Höfig et al., 2016; Erhardt et al., 2021). The southeast segment of the Central American Volcanic Arc (CAVA-SE) exhibits distinct Pb isotope signatures relative to the northwest segment and is hence included as a separate potential source area for provenance assessment. Höfig et al. (2016) also attributed hemipelagic input from the volcanic terranes of the Northern Andes (Northern Volcanic Zone, NVZ), a proximal source area along the eastern margin of the EEP, as a key source of terrigenous sediments to the Guatemala Basin.

2.5.2.2 Distal dust sources

Major dust-producing regions on the western side of the American continent are concentrated at northern and southern subtropical latitudes (Prospero et al., 2002; Ginoux et al., 2012). The North American Basin and Range Province encompasses a large swath of deserts and semi-desert terranes across the Western USA and Northern Mexico and receives very low annual rainfall (e.g. < 600 mm/a, Baja California; 150-300 mm/a, Great Basin) (Prospero et al., 2002; Amador et al., 2006; Ginoux et al., 2012). Dust emissions from the Sonoran and Chihuahuan Deserts are characterised by the bulk rock compositions of the Peninsular Ranges in Baja California and the Sierra Madre Occidental (SMOc), respectively. Lithologies within and bounding the USA portion of the Basin and Range Province (Great Basin, Mojave and Chihuahuan Deserts) span very large ranges of Pb and Nd isotope compositions (Fig. 2.8). The Pb isotope data obtained for silt from islands off the coast of Southern California (Erhardt et al., 2021) are hence taken to represent the average dust composition from the USA portion of the Basin and Range Province (Fig. 2.7).

The Andean Range traverses throughout the western margin of South America (Fig. 2.6). The arid coastal plains and slopes of the North-Central (Peruvian) and Central Andes encompass a continuous desert strip (8°S to 27°S) with strong dust emissions (Ginoux et al., 2012). In particular, the Atacama Desert in Northern Chile receives as little as ~20 mm/a of annual rainfall and is known as the driest place on Earth. Furthermore, the Puna and Altiplano plateaus of the Central Andes feature semi-arid conditions and are known to be significant dust sources (Prospero et al., 2002; Garreaud et al., 2003). Radiogenic isotope studies attributed terranes in the Central Andes as the major dust sources to the Eastern and Central Equatorial Pacific Ocean (92-158°W) (Pichat et al., 2014; Höfig et al., 2016; Reimi and Marcantonio, 2016; Reimi et al., 2019). Dust emissions from the Peruvian Andes are characterised based on the bulk compositions of the Peruvian Coastal Batholith (PCB), while the Central Andean dust sources are represented by analyses of surficial deposits from the Atacama Desert and the Puna-

Altiplano Plateau. Data of surficial deposits from the Puna-Altiplano Plateau overlap with the bulk rock compositions of samples from the Central Andes (Central Volcanic Zone, CVZ), whilst data from the Atacama Desert falls between the bulk rock compositions of samples from the CVZ and the Southern Andes (Southern Volcanic Zone, SVZ) (Fig. 2.7).

Dust from East Asia dominates the detrital sediment budget across the open North Pacific Ocean (e.g. Rea, 1994; Herman et al., 1997). Whilst previous isotope provenance studies showed a decline in Asian dust contributions east of 120°W in the easternmost sector of the Pacific Ocean (Nakai et al., 1993; Jones et al., 2000; Pettke et al., 2000; Reimi and Marcantonio, 2016; Erhardt et al., 2021), this source is nonetheless included for provenance assessment in the following.

2.5.3 Sources of Detrital Sediments

The source areas of the detrital sediments at the two MANOP sites are assessed based on comparisons of the sample isotope data with the signatures of potential source areas as well as with previously published Pb (Jones et al., 2000; Erhardt et al., 2021) and Nd (Nakai et al., 1993; Jones et al., 1994) isotope data for detrital core-tops from across the EEP.

2.5.3.1 Regional detrital isotope signatures in the EEP

Detrital sediments across the Central and Eastern Equatorial Pacific Ocean exhibit clear zonal gradients in Pb and Nd isotope signatures, consistent with the transition in dominant contributions from distal to proximal sources towards the Central/South American continent (Fig. 2.7; 2.9). In Pb-Pb isotope spaces, detrital compositions of the offshore region (120-140°W) have relatively high $^{207}Pb/^{204}Pb$ and $^{208}Pb/^{204}Pb$ for a given $^{206}Pb/^{204}Pb$, in accord with a mixed derivation from sources with signatures of surficial deposits from the Central Andes, East Asia and Western USA (Fig. 2.7a, b; 2.9a, b). These signatures hence reflect the dominant influence of dust inputs from some or all of these distal upwind regions. In contrast, the detrital compositions of more eastern sites (80-120°W) have lower $^{207}Pb/^{204}Pb$ and $^{208}Pb/^{204}Pb$ ratios for a given $^{206}Pb/^{204}Pb$, which likely indicate more dominant inputs from relatively proximal sources in Mexico (TMVB, SMdS, Peninsular Ranges and SMOc), Central America (CAVA-NW), the Northern Andes (NVZ) and the Peruvian Andes (PCB). Similarly, the zonal changes in Nd isotope compositions, from highly unradiogenic signatures in the offshore region ($\varepsilon_{Nd} \approx -10$, 120-140°W) to more radiogenic signatures east of 120°W ($\varepsilon_{Nd} = -6$ to -3), agree with the shifting dominance from Asian dust ($\varepsilon_{Nd} \approx -11$) to the more proximal Mexican, Central American and Northern Andean terranes ($\varepsilon_{Nd} > 0$) (Fig. 2.7c; 2.9c).

2.5.3.2 Detrital sources of MANOP Site H

At MANOP Site H, the detrital Pb isotope compositions ($^{206}Pb/^{204}Pb = 18.85$, $^{207}Pb/^{204}Pb = 15.62$, $^{208}Pb/^{204}Pb = 38.70$) are in accord with published data for detrital core-top sediments from proximal locations in the easternmost Equatorial Pacific Ocean (80-120°W; e.g. $^{206}Pb/^{204}Pb = 18.68$-$19.02$) (Fig.

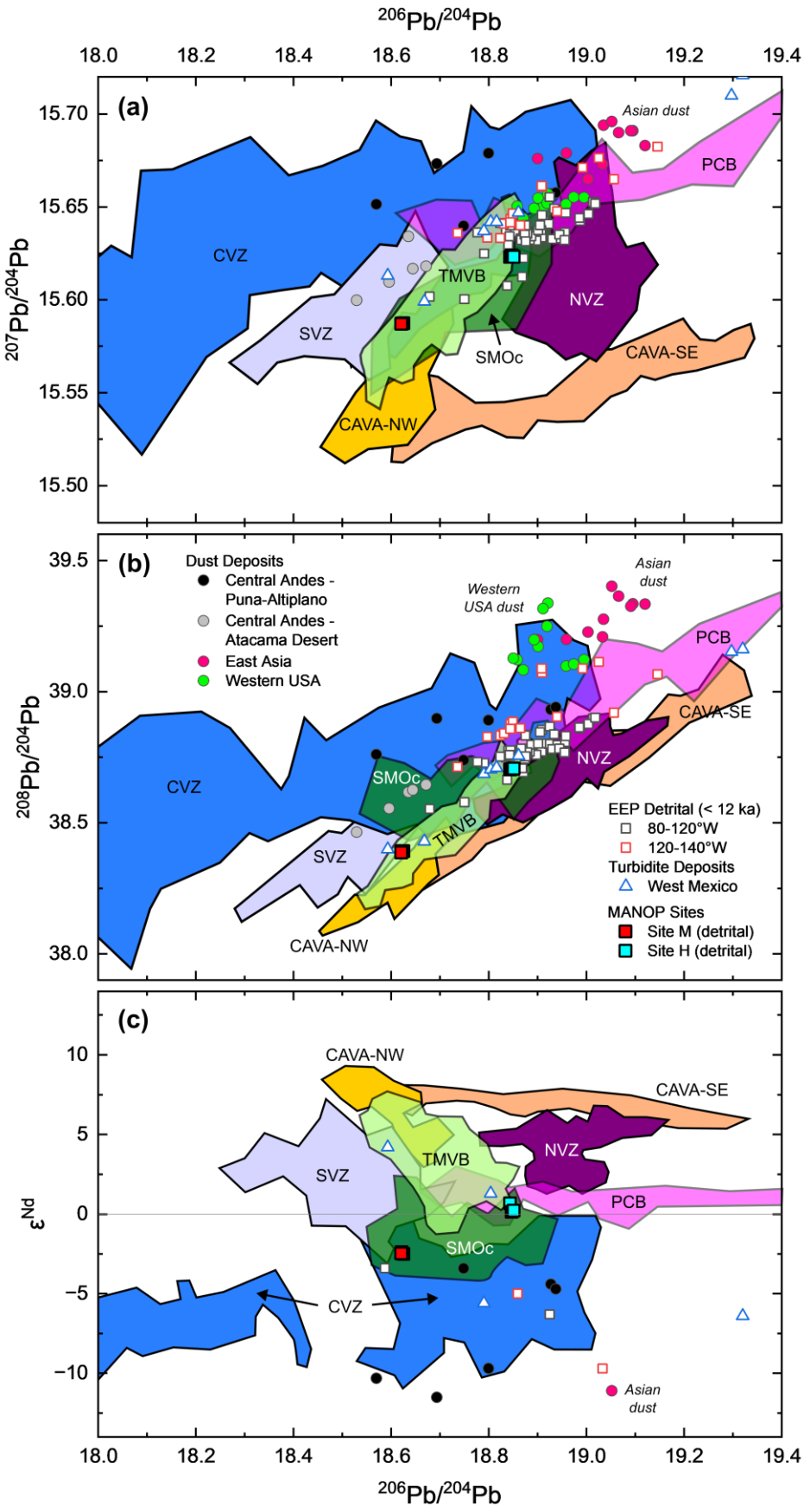

206Pb/204Pb
18.0
18.2
18.4
18.6
18.8
19.0
19.2
19.4
(a)
207Pb/204Pb
15.70
15.65
15.60
15.55
15.50
Asian dust
PCB
CVZ
TMVB
NVZ
SVZ
SMOc
CAVA-SE
CAVA-NW
(b)
208Pb/204Pb
39.5
39.0
38.5
38.0
Dust Deposits
Central Andes - Puna-Altiplano
Central Andes - Atacama Desert
East Asia
Western USA
Western USA dust
Asian dust
PCB
CAVA-SE
NVZ
CVZ
SMOc
TMVB
SVZ
CAVA-NW
EEP Detrital (< 12 ka)
80-120°W
120-140°W
Turbidite Deposits
West Mexico
MANOP Sites
Site M (detrital)
Site H (detrital)
(c)
εNd
10
5
0
−5
−10
CAVA-NW
CAVA-SE
NVZ
TMVB
SVZ
PCB
SMOc
CVZ
Asian dust
206Pb/204Pb

Figure 2.7.

Figure 2.7 (cont'd). Plots of (a) $^{207}Pb/^{204}Pb$, (b) $^{208}Pb/^{204}Pb$, and (c) ε_{Nd} versus $^{206}Pb/^{204}Pb$ for the detrital sediment fractions from the two MANOP sites in comparison to the isotope compositions of potential source areas and previously published marine sediment data for the Eastern Equatorial Pacific Ocean. Surficial terrestrial deposits (silt and loess) that characterise major dust sources (circles): Puna-Altiplano (Gili et al., 2016, 2017) and Atacama Desert (Erhardt et al., 2021) in the Central Andes, South America; East Asia (Chinese loess, Nakai et al., 1993; Jones et al., 2000); Western USA (Erhardt et al., 2021). Coloured fields indicate the bulk rock compositions of potential terrestrial source areas retrieved from the GEOROC database, each of which encompass the data points that fall within 2 SD of the mean composition of a source area (see Appendix 1 for details of compilation). The compositions of the TMVB, SMdS and the Peninsular Ranges are combined as a single field, labelled as 'TMVB'. Lithological compositions of the Western Cordillera (CVZ) and the Eastern Cordillera of the Central Andes are also grouped as a single field, labelled as 'CVZ'. The detrital sediment data in the EEP are divided between the proximal (80-120°W, grey open squares) and offshore (120-140°W, red open squares) sectors of the EEP; most Pb isotope data are from Erhardt et al. (2021) and the combined Pb-Nd isotope data are from Nakai et al. (1993) and Jones et al. (1994; 2000). Deep sea turbidite deposits off the West Mexican coast (open triangles) are from McLennan et al. (1990) and Hemming and McLennan (2001). Errors for the isotope compositions of the sediment samples are similar to or smaller than the symbol sizes.

2.7a, b; 2.9a, b). In contrast, the detrital ε_{Nd} values (+0.3) are higher than the values of –6 to –3 obtained for other sites in the EEP (Fig. 2.7c; 2.9c). The observed consistency in Pb isotope signatures suggest that the detrital sediments at Site H are likely affected by the same source mixing relationships that are relevant for the wider Guatemala and Panama Basins. The more radiogenic Nd isotope signature at Site H, however, indicates stronger contributions from terrestrial sources with higher ε_{Nd} values.

The various terranes along the Pacific coast of Mexico ($^{206}Pb/^{204}Pb$ = 18.5-18.9, $^{207}Pb/^{204}Pb$ = 15.52-15.67, $^{208}Pb/^{204}Pb$ = 38.2-38.8) likely define the low-$^{20x}Pb/^{204}Pb$ mixing endmember that contributes to the terrigenous sediments at Site H, through a combination of aeolian and hemipelagic materials. Significant dust emissions were identified for the Sonoran Desert of Northwest Mexico (Prospero et al., 2002; Ginoux et al., 2012). Dust storms were also identified in Southern Mexico, which features dry winters and wet summers and was naturally covered by subtropical dry forests until large-scale deforestations in recent centuries (Prospero and Bonatti, 1969; Griscom and Ashton, 2011). Prospero and Bonatti (1969) found elevated winter dust loads in the atmosphere above the Guatemala and Panama Basins (0.68 $\mu g/m^3$, compared to 0.14 $\mu g/m^3$ south of the Equator) and attributed the 'dustier' atmosphere to those two Mexican regions with frequent occurrences of dust storms. Dust from these source regions can be delivered to the Guatemala Basin by prevailing north westerly and northerly winds (Fig. 2.1).

The Central American land bridge is, in principle, an alternative source of detrital sediments to Site H, based on terrigenous sedimentation mapping for the EEP during ODP Leg 138. Notably, the mapping revealed a sediment wedge extending from the Pacific coast of Central America into the interior of the Guatemala Basin (Lyle, 1992). However, the Nd isotope signatures of both CAVA-NW (ε_{Nd} = +6 ± 2, 1 SD) and CAVA-SE ($\varepsilon_{Nd} \approx +7$) are too high for these sources to provide significant contributions to the detrital sediments at Site H (ε_{Nd} = +0.3) or other sites in the EEP ($\varepsilon_{Nd} < -3$) (Fig. 2.7c). This may

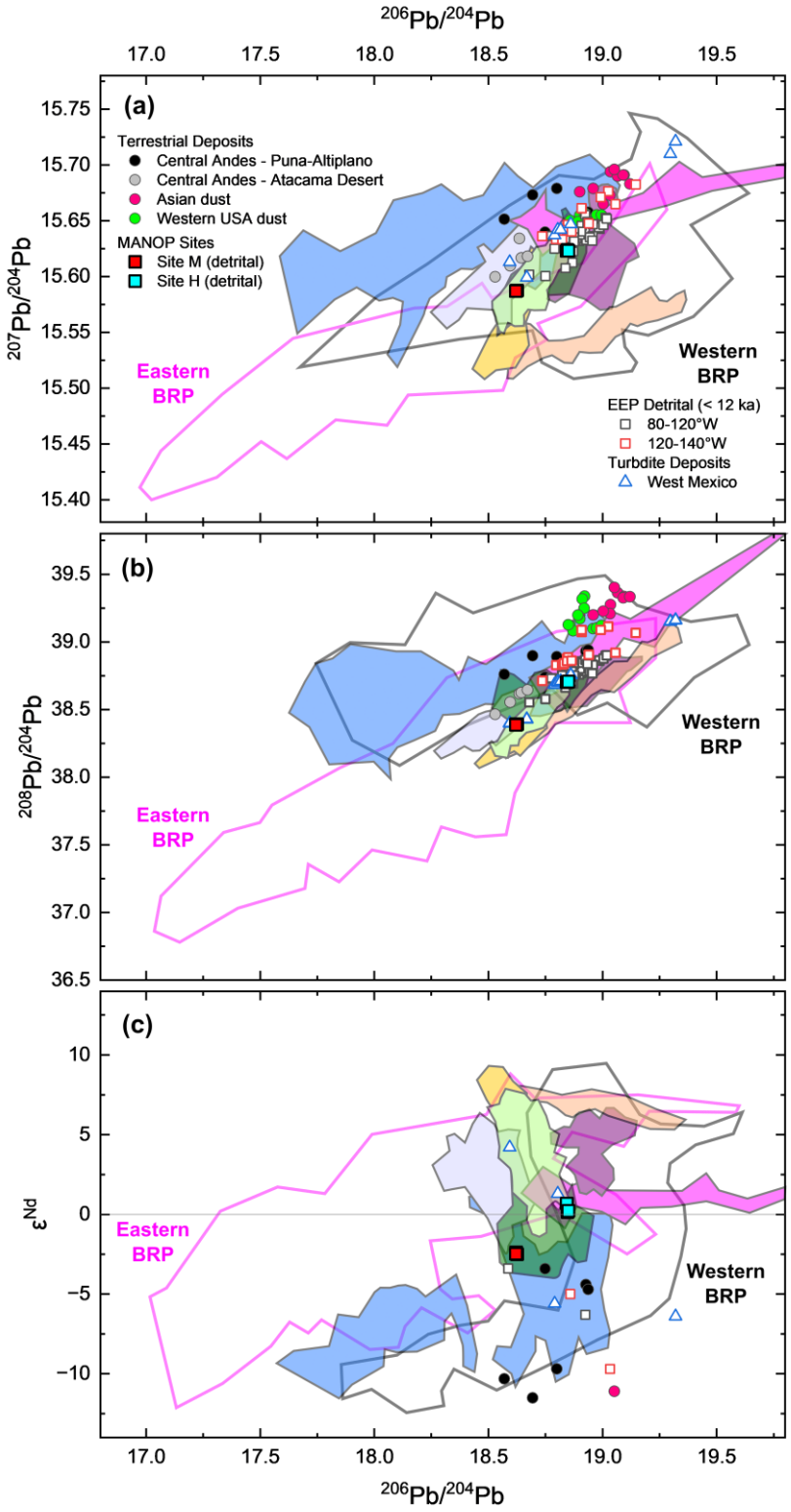


Figure 2.8. Plots of (a) $^{207}Pb/^{204}Pb$, (b) $^{208}Pb/^{204}Pb$, and (c) ε_{Nd} versus $^{206}Pb/^{204}Pb$ for the detrital sediment fractions from the two MANOP sites in comparison to the bulk rock isotope compositions from the western (grey contours) and eastern (pink contours) sectors of the North American Basin and Range Province (BRP), retrieved from the GEOROC database. Contoured fields encompass the data points that fall within 2 SD of the mean composition of each source area. The isotope ranges of other terrestrial source areas in Figure 2.7 are overlain for comparison. Errors for the isotope compositions of the sediment samples are similar to or smaller than the symbol sizes. Note the extended scales for the Pb isotope ratios in comparison to Figure 2.7.

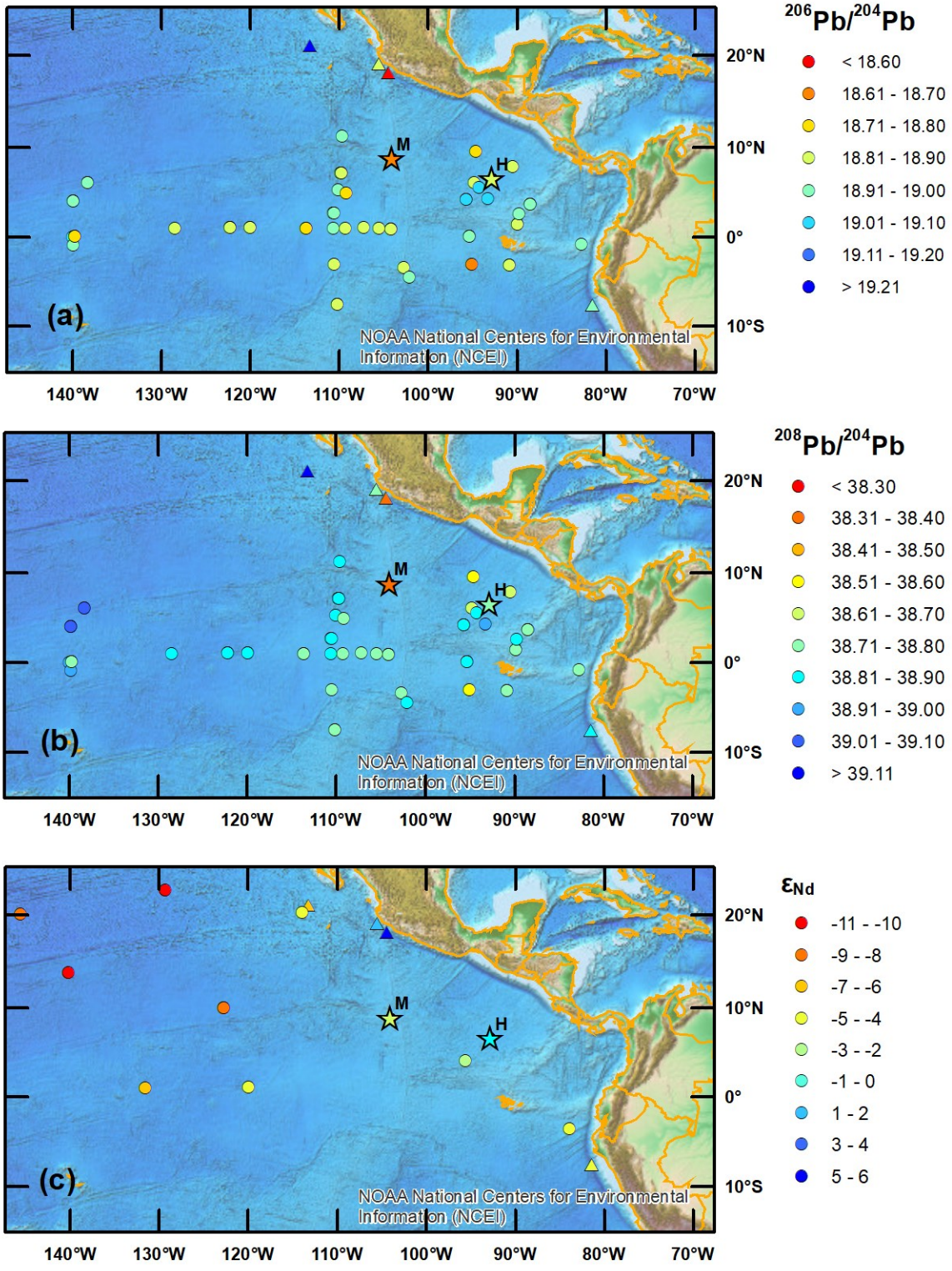


Figure 2.9. Maps of (a) $^{206}Pb/^{204}Pb$, (b) $^{208}Pb/^{204}Pb$, and (c) ε_{Nd} data for the detrital sediment fractions of MANOP Sites H and M (stars, this study) and published values for other sediment samples in the Eastern Equatorial Pacific Ocean. Published data: core-top detrital sediments (circles) (Nakai et al., 1993; Jones et al., 1994, 2000; Erhardt et al., 2021); deep sea turbidites (triangles) (McLennan et al., 1990; Hemming and McLennan, 2001). Symbols are colour-coded based on their Pb or Nd isotope values.

reflect the limited relief and geographical extent of the Central American land bridge, which restricts the production of detritus from this region (Höfig et al., 2016). Instead, hemipelagic input from the Central American land bridge may be overwhelmed by the larger quantities of detritus that are derived from the neighbouring Southern Mexican terranes (TMVB and SMdS). This conclusion reflects that the latter are characterised by ε_{Nd} values of between –1 and +7 (with a mean of +3.4), and which are thus closer to the detrital signatures observed at Site H. Hemipelagic sediments from Southern Mexico can be transported eastward along the Central American coast and carried offshore by the anticyclonic Tehuantepec Bowl (Fig. 2.2).

Proximal hemipelagic input from the Northern Andes ($^{206}Pb/^{204}Pb$ = 18.8-19.15, $^{207}Pb/^{204}Pb$ = 15.57-15.70, $^{208}Pb/^{204}Pb$ = 38.5-38.9; NVZ) and dust input from the Peruvian Andes ($^{206}Pb/^{204}Pb$ = 18.7-19.8, $^{207}Pb/^{204}Pb$ = 15.62-15.70, $^{208}Pb/^{204}Pb$ = 38.7-39.8; PCB) are two potential candidates for the high-$^{20x}Pb/^{204}Pb$ mixing endmember that contributes to terrigenous sediments at Site H (Fig. 2.7a, b). Lyle (1992) showed another sediment wedge extending westward from the Northern Andean coast into the interior of the Guatemala Basin. This coast features a humid tropical climate, with exceptionally high orographic rainfall of 8-13 m/a on the Pacific coast of Colombia (Poveda and Mesa, 2000), conducive to high continental runoff. While Western South America lacks large drainage basins, small mountainous rivers draining into this active margin could carry large sediment loads to the offshore region, due to the combined conditions of frequent turbidite discharges from mass wasting events and poor sediment trapping by the narrow continental shelves (Milliman and Syvitski, 1992; Höfig et al., 2016). Furthermore, the Colombia Trench bordering the Northern Andes is shallower and narrower than the Peru-Chile Trench to the south (Fig. 2.2) (e.g. Lonsdale and Klitgord, 1978). The hemipelagic sediments from this part of the Andean Cordillera are, therefore, more likely to escape the ocean trench and reach offshore regions of the Panama Basin. Surface ocean gyres could further distribute the Northern Andean detritus from the Panama Basin into the Guatemala Basin (Fig. 2.2). Alternatively, elevated dust loads from the Peruvian coastal deserts may be delivered by the prevailing southeast trades to the Guatemala Basin (Fig. 2.1).

The Nd isotope signatures of most of the proximal sources, including most Mexican terranes ($\varepsilon_{Nd} \approx$ +3, TMVB, SMdS and Peninsular Ranges), the Northern Andes (+4) and the Peruvian Andes (+1), are more radiogenic than the detrital signature at site H (ε_{Nd} = +0.3) (Fig. 2.7c). This requires the addition of material with less radiogenic Nd isotope signatures. Dust contribution from Northern Mexico (e.g. Chihuahuan Desert) that is characterised by the slightly negative ε_{Nd} values of the Sierra Madre Occidental (SMOc) (–1 ± 2), and Pb isotope signatures that resemble other Mexican terranes, could hence explain the detrital signature at Site H. Alternatively, mixing of proximal sources (TMVB and NVZ) with a small proportion of distally transported Central Andean dust (ε_{Nd} = –12 to –3, Puna-Altiplano) could also account for the detrital Nd isotope signature observed at Site H. Nevertheless, any contributions from Central Andean dust are likely minor, in line with the observed northward trend of increasing ε_{Nd} values defined by core-top sediments from the EEP (Fig. 2.9c) and the lower dust load

over the Southeast Pacific Ocean (Prospero and Bonatti, 1969). Significant additions of Southern Andean materials (SVZ) to the detrital sediments at Site H or the wider Guatemala Basin can also be ruled out. In particular, the limited contributions of Central Andean materials to Guatemala Basin sediments render large dust inputs from the more remote South Andean coast with its relatively minor dust emissions very unlikely.

The Pb isotope compositions of bulk sediments from Ocean Drilling Program / Integrated Ocean Drilling Program (ODP/IODP) Site 1256 (6°44'N, 91°56'W), which is proximal to MANOP Site H (6°33'N, 92°48'W) (Fig. 2.2), suggest that the Pliocene-Quaternary terrigenous sedimentation in the region reflects mixing between Southern Mexican materials with low $^{20x}Pb/^{204}Pb$, and Northern and Central Andean materials with high $^{20x}Pb/^{204}Pb$ (Höfig et al., 2016). The Holocene provenance model of the current study for MANOP Site H is hence largely in accord with the palaeoceanographic model developed from the ODP/IODP Site 1256 record. However, based on the additional Nd isotope constraints, only minor contributions are attributed to Central Andean dust, as the large, proximal sediment fluxes from Mexico and the Northern Andes will likely overwhelm the distal dust input.

2.5.3.3 Detrital sources of MANOP Site M

The Pb isotope compositions of detrital sediments from Site M ($^{206}Pb/^{204}Pb$ = 18.62, $^{207}Pb/^{204}Pb$ = 15.59, $^{208}Pb/^{204}Pb$ = 38.39) are distinctively less radiogenic than at Site H and most other detrital sediment samples in the EEP east of 120°W ($^{206}Pb/^{204}Pb$ = 18.68-19.02, $^{207}Pb/^{204}Pb$ = 15.60-15.65, $^{208}Pb/^{204}Pb$ = 38.55-38.90) (Fig. 2.7a, b; 2.9a, b). This suggests stronger influence of terrestrial sources with low $^{20x}Pb/^{204}Pb$ signatures.

Dominance of terrigenous detritus from Mexico can explain the detrital $^{20x}Pb/^{204}Pb$ signature at Site M, as this falls within the compositional range of the various Mexican terranes ($^{206}Pb/^{204}Pb$ = 18.5-18.9, $^{207}Pb/^{204}Pb$ = 15.52-15.67, $^{208}Pb/^{204}Pb$ = 38.2-38.8) (Fig. 2.9a, b). Site M is situated about 1000 km from the South Mexican coast in the northwest area of the Guatemala Basin and favourable transport pathways are present between the South Mexican margin and the latter (Fig. 2.1; 2.2). In particular, the prevailing northeast trade wind and the anticyclonic surface ocean gyre of the Tehuantepec Bowl can efficiently deliver dust and hemipelagic fluxes, respectively, from offshore Mexico to dominate the detrital sediment budget at Site M. The delivery of Southern Mexican detritus is further enhanced by the southward flow of bottom water along the western margin of the Guatemala Basin. The similarity of the detrital Pb isotope signature at Site M to results obtained for some deep sea turbidite samples from off the West Mexican coast, which also exhibit relatively low $^{20x}Pb/^{204}Pb$ ratios ($^{206}Pb/^{204}Pb$ = 18.59, 18.67, $^{208}Pb/^{204}Pb$ = 38.40, 38.43), supports the dominance of hemipelagic input from Mexico at Site M (Fig. 2.7a, b; 2.9a, b). This conclusion is further supported by the terrigenous sedimentation mapping for the EEP, as this shows a thick sediment wedge extending from the southwest corner of Mexico along the eastern flank of the EPR to the location of Site M (Lyle, 1992).

The detrital ε_{Nd} value of –2.5 for Site M is slightly less radiogenic than the compositions of coastal Mexican sources (ε_{Nd} = –1 to +8 for TMVB, SMdS and Peninsular Ranges), suggesting the involvement of one or several sources with lower ε_{Nd}. Dust samples from East Asia and the Central Andes have very low ε_{Nd} values of –12 to –3. However, significant contributions from either source can be ruled out. In particular, East Asian dust has much higher $^{20x}Pb/^{204}Pb$ (e.g. $^{206}Pb/^{204}Pb$ > 18.9) than the detrital signature at Site M (Fig. 2.7a, b). In the context of the southeast trades, Site M is situated downwind of Site H, but the latter shows little evidence for significant contribution of a detrital Central Andean dust component with low ε_{Nd} (Fig. 2.1; 2.9c). This observation hence argues against a significant presence of Central Andean dust in the detritus of Site M.

Alternatively, dust emitted from the Chihuahuan Desert of Northern Mexico can contribute detrital sediments with low ε_{Nd} signatures to Site M. The SMOc is a key dust source area for the Chihuahuan Desert and has ε_{Nd} values (–4 to +2, 1 SD) that are suitably unradiogenic to account for the Nd isotope signature at Site M (ε_{Nd} = –2.5). Furthermore, the Eastern Basin and Range Province, another potential dust source area for the Chihuahuan and Sonoran Deserts, has highly variable Pb and Nd isotope compositions (with $^{206}Pb/^{204}Pb$ = 17.0-19.3 and ε_{Nd} = –12 to +7), which could impact the average composition of dust emitted from the two deserts and help account for the detrital signatures seen at Site M (Fig. 2.6; 2.8). A better characterisation of the compositions of dust from these sources would enable an improved assessment of their significance in the terrigenous sedimentation in the EEP.

2.5.4 Water Mass Signatures and Hydrothermal Sedimentation

In the following, the Pb and Nd isotope compositions of the sediment leachates from the two MANOP sites are compared to the compositions of sediment leachates and the surface layers of Fe-Mn crusts and nodules from the surrounding ocean regions (Fig. 2.10; 2.11), whereby the latter are thought to represent the average deep water compositions over the Late Quaternary (< 300 ka) (von Blanckenburg et al., 1996; Ling et al., 1997, 2005; Frank et al., 1999; Pichat et al., 2014; Höfig et al., 2016). For Nd isotopes, the sediment leachate records are also compared with available seawater data for the Pacific Ocean (Fig. 2.11) (Piepgras and Jacobsen, 1988; Amakawa et al., 2009; Haley et al., 2021).

Deep water in the Guatemala Basin is fed by inflows from the open North Pacific Ocean across the EPR (Mantyla, 1975; Lonsdale, 1976). The surfaces of Fe-Mn crusts and nodules from the open North Pacific Ocean exhibit small ranges of $^{20x}Pb/^{204}Pb$ ratios: $^{206}Pb/^{204}Pb$ = 18.66-18.70, $^{207}Pb/^{204}Pb$ = 15.62-15.66 and $^{208}Pb/^{204}Pb$ = 38.6-38.8 (Fig. 2.10a, b). For Nd, the North Pacific crusts and nodules exhibit homogeneous isotope signatures with ε_{Nd} values of –4 to –3 (Fig. 2.10c). Notably, these ε_{Nd} results are in accord with ε_{Nd} values of between –6 and –3 obtained for NPDW from stations in the open Pacific Ocean west of the EPR (Fig. 2.11) (Piepgras and Jacobsen, 1988; Amakawa et al., 2009; Haley et al., 2021). In the EEP east of 120°W, Late Quaternary (< 160 ka) sediment leachates and Fe-Mn crusts exhibit slight shifts in Pb isotope compositions from the North Pacific crust and nodule values towards

lower $^{207}Pb/^{204}Pb$ (15.59-15.62) and $^{208}Pb/^{204}Pb$ (38.5-38.6) ratios (Fig. 2.10a, b). The surface Nd isotope composition of Fe-Mn crust GMAT-14D from the Guatemala Basin is also slightly more radiogenic, with $\varepsilon_{Nd} = -2.4$, than Fe-Mn sediments and seawater samples from the open North Pacific Ocean (Fig. 2.10c; 2.11) (Frank et al., 1999).

In this study, sediments from both MANOP sites exhibit leachate Nd isotope compositions, of $\varepsilon_{Nd} = -1.7 \pm 0.6$, which are identical within uncertainty to that of crust GMAT-14D (Fig. 2.10c; 2.11). At Site H in the basin interior, the leachate Pb isotope composition ($^{206}Pb/^{204}Pb = 18.64$, $^{207}Pb/^{204}Pb = 15.59$, $^{208}Pb/^{204}Pb = 38.51$) is within the range of published results for the EEP, whilst at Site M near the EPR, the $^{20x}Pb/^{204}Pb$ ratios ($^{206}Pb/^{204}Pb = 18.50\text{-}18.55$, $^{207}Pb/^{204}Pb = 15.55\text{-}15.57$, $^{208}Pb/^{204}Pb = 38.17\text{-}38.26$) are significantly lower (Fig. 2.10a, b).

The distinct Pb and Nd isotope provinces in the EEP reflects modification of the deep water advected from the open Pacific Ocean by local sources characterised by lower $^{207}Pb/^{204}Pb$ and $^{208}Pb/^{204}Pb$ and higher ε_{Nd}. Potential sources include sediment fluxes from the proximal Mexican and Central American terranes, as well as hydrothermal effluents from the EPR. Higher ε_{Nd} values of –1.6 to +1.3 (with a mean of –0.1) were obtained for deep water from the neighbouring Panama Basin, and these were interpreted to reflect the impact of Central American and Northern Andean dissolved fluxes with ε_{Nd} values > 0 (Fig. 2.11) (Grasse et al., 2012, 2017). Large hemipelagic fluxes and poor ventilation likely facilitate the preservation of distinct deep water Pb and Nd isotope signatures for the Guatemala and Panama Basins relative to the open Pacific Ocean (Lonsdale, 1976; Grasse et al., 2012).

At MANOP Site M, the leachate $^{20x}Pb/^{204}Pb$ signatures deviate from those of other sites in the EEP by trending towards the average composition of MORBs from the EPR segment near the site ($^{206}Pb/^{204}Pb = 18.2\text{-}18.4$, $^{207}Pb/^{204}Pb = 15.45\text{-}15.50$, $^{208}Pb/^{204}Pb = 37.8\text{-}38.1$) (Fig. 2.10a-c). This compositional shift is best explained by the presence of Pb of hydrothermal origin. Along mid-ocean ridges, hydrothermal fluids undergo exchange with the basaltic substrate, and they inherit the Pb isotope signature of MORB (e.g. Chen, 1987). As the emitted hydrothermal fluids mix with ambient seawater, hydrothermally derived Pb can be transported by the laterally spreading plume either in dissolved form and/or in hydrothermal particles, including Fe-Mn oxyhydroxides (Dymond and Roth, 1988; German et al., 1991a; Godfrey et al., 1994). At Site M, which is situated only 25 km from the EPR crest, hydrothermal plumes have been detected in the water column (Kadko et al., 1987a). Settling of precipitates that are enriched in hydrothermal Pb can therefore explain the MORB signature of the leachable sediment fraction of Site M. This conclusion is in accord with previous sediment studies of the Southeast Pacific Ocean, which found a significant MORB component in the Pb isotope compositions of Fe-Mn sediments more than 1000 km away from mid-ocean ridges (Barrett et al., 1987; van de Flierdt et al., 2004).

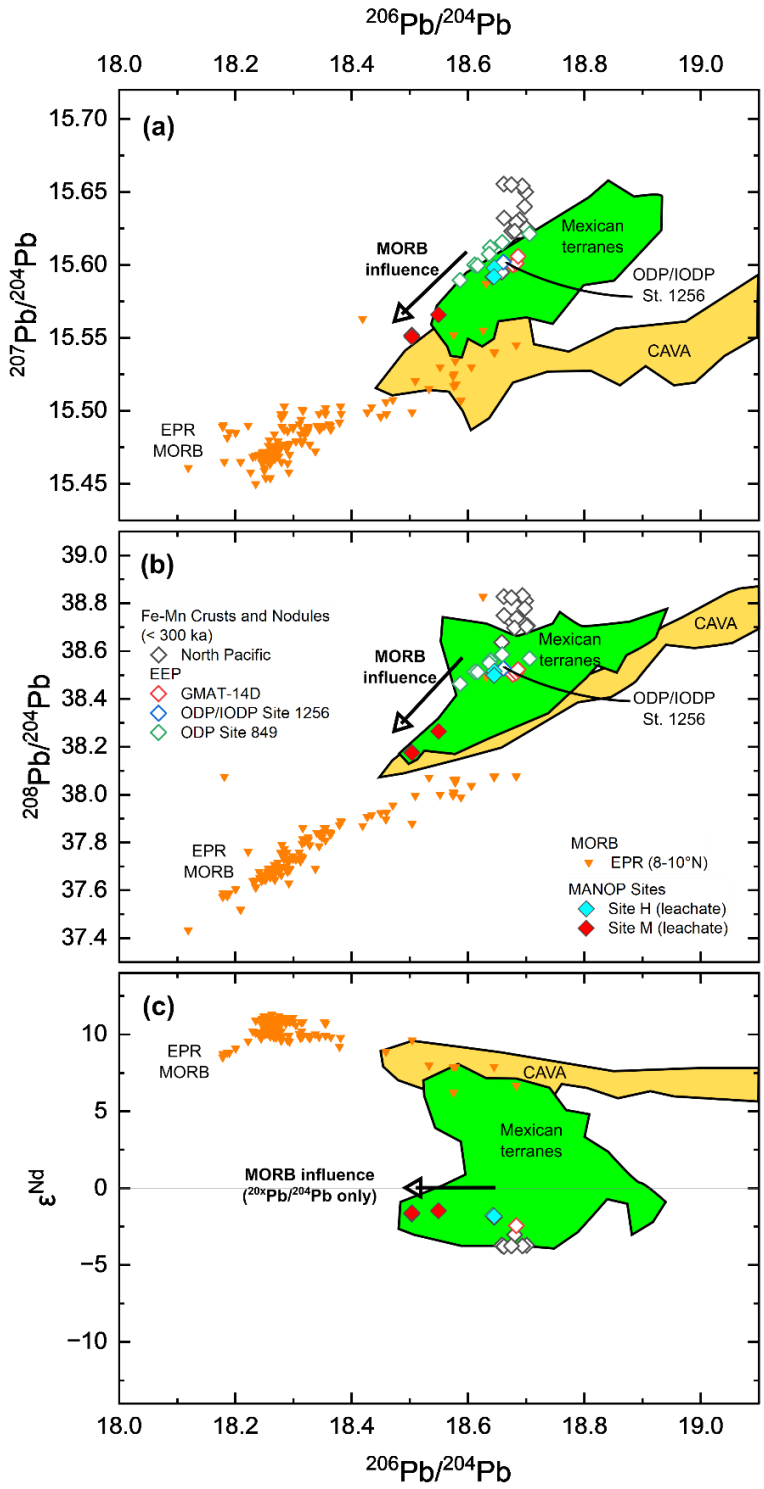


Figure 2.10. Plots of (a) $^{207}Pb/^{204}Pb$, (b) $^{208}Pb/^{204}Pb$, and (c) ε_{Nd} versus $^{206}Pb/^{204}Pb$ for the leachate fractions from the two MANOP sites in comparison to literature values of Fe-Mn sediments in the Pacific Ocean and potential lithological sources. Fe-Mn sediments (open diamonds): crust GMAT-14D (Frank et al., 1999); crusts and nodules from the North Pacific Ocean (von Blanckenburg et al., 1996); sediment leachates at ODP/IODP Site 1256 (Höfig et al., 2016) and ODP Site 849 (Pichat et al., 2014). MORB from the EPR segment 8-10°N (orange triangles) were retrieved from the PetDB database. Green and yellow fields denote the bulk rock compositions of Mexican and Central American terranes, each of which encompasses the data points that fall within 2 SD of the mean composition of a terrane (refer to Appendix 1 and the caption of Figure 2.7 for details). Errors for the isotope compositions of the sediment samples are similar to or smaller than the symbol sizes.

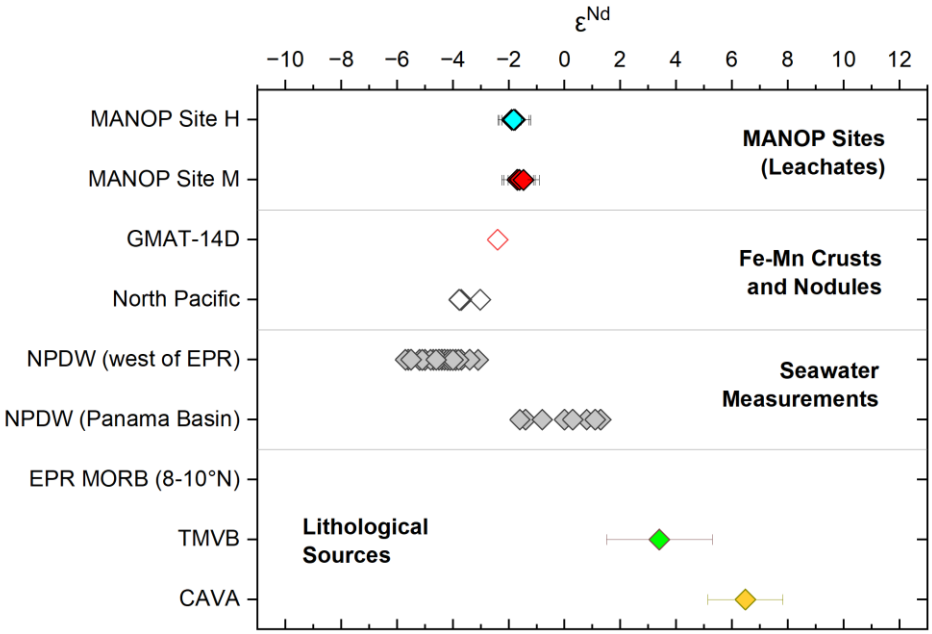


Figure 2.11. Plot of ε_{Nd} values for the leachate fractions from the MANOP sites in comparison to literature values of Fe-Mn sediments, potential lithological sources and present-day deep water measurements of dissolved Nd isotopes. Measurements of North Pacific Deep Water (NPDW; grey diamonds): open Pacific Ocean west of EPR (Piepgras and Jacobsen, 1988; Amakawa et al., 2009; Haley et al., 2021); Panama Basin (Grasse et al., 2012, 2017). Refer to the caption of Figure 2.10 for the other data sources. Error bars denote the 2 SD precisions and compositional ranges of the sediment leachates and lithological sources, respectively.

In contrast, the Nd isotope compositions of Site M sediment leachates, of $\varepsilon_{Nd} = -1.6 \pm 0.6$, are indistinguishable from results obtained for the MANOP Site H sediment leachates ($\varepsilon_{Nd} = -1.8$) and the surface layer of Fe-Mn crust GMAT-14D ($\varepsilon_{Nd} = -2.4$). The lack of a hydrothermal impact on the Nd isotope signature of the Site M sediment leachates corroborates previous observations, which suggest the rapid recycling of hydrothermally derived Nd near the source (German et al., 1990; Halliday et al., 1992). As such, the contrasting observations made for Pb and Nd in proximity to the hydrothermal activities indicate that their behaviours are decoupled (Fig. 2.10c; 2.11). This decoupled behaviour most likely reflects differences in the adsorption of the two elements to hydrothermal particles and/or differences in their marine speciation. For example, whilst both dissolved Pb and Nd predominantly form carbonate complexes in seawater (pH ≈ 8), Pb additionally forms chloride complexes, which increase in abundances as the pH decreases (Powell et al., 2009). Stabilisation of dissolved Pb by the formation of chloride complexes might therefore facilitate more distal transport of the element in the more acidic environment of a hydrothermal plume in comparison to Nd. Additional studies on the speciation and adsorption of Pb and Nd in hydrothermal plumes and the deep ocean environment are required, however, to better constrain the decoupled behaviour of the two elements.

2.6 Conclusions

Lead and Nd isotope compositions are presented for bulk samples as well as leachate and detrital fractions of sediments from MANOP Sites H and M in the Guatemala Basin, Eastern Pacific Ocean.

The isotope signatures of the detrital sediment fractions indicate the predominance of proximal terrigenous inputs from the American continent. The results reinforce the significance of Mexican terrigenous inputs, through the combination of elevated dust emissions from arid and semi-arid regions and hemipelagic input. The results also highlight the significance of South American hemipelagic and dust inputs from the northern (Colombian-Ecuadorian) and/or north-central (Peruvian) sectors, respectively, of the Andean Range. In addition, dust emissions from desert regions in subtropical North and/or South America are likely minor contributors to the detrital sediment budgets of the Guatemala Basin. In contrast, detrital sediment contribution from the Central American land bridge appears to be minimal despite its proximity to the studied sites, most likely as the limited relief restricts the production of detritus.

The ability to constrain terrestrial source areas of detrital sediments in the Guatemala Basin is restricted by the overlapping Pb and Nd isotope signatures of many potential source areas. Notably, the currently available data do not unambiguously constrain the relative significance of dust fluxes from arid regions in North America (Mexico and Western USA) on the one hand and South America (Central Andes) on the other. An improved characterisation of the isotope compositions of relevant terrigenous sources through the analyses of direct erosional products (e.g. dust and river sediments), especially for the North American source areas, would provide improved constraints on the contributing source areas to the ocean region and enable quantitative source apportionment.

The analyses of the sediment leachates indicate that the deep water Pb and Nd isotope signatures of the EEP largely reflect mixing of North Pacific Deep Water with elemental inputs derived from proximal terrestrial sources. In addition, at MANOP Site M, which is situated only 25 km from the EPR crest, the leachate Pb isotope composition contains a significant hydrothermally derived MORB component. Detection of significant MORB components in the sedimentary Pb budget, at this site and other East Pacific localities up to about 1000 km from the EPR, highlights the significance of hydrothermal inputs for sedimentary Pb budget in the vicinity of mid-ocean ridges in this ocean region. In contrast, the Nd isotope compositions of sediment leachates from Site M do not show evidence for the presence of a MORB component, in accord with the results of previous studies which concluded that Nd is efficiently lost from hydrothermal plumes close to vent sites (German et al., 1990; Halliday et al., 1992).

2.7 Researcher Contributions

The Pb isotope compositions of the sediment samples presented in this study were obtained by the author. Digestion of bulk sediment samples and measurements of Nd and Pb concentrations were

conducted by Susan H. Little. Rhian O'Callaghan carried out the sediment leaching procedure for the leachate and detrital fractions. Rhian O'Callaghan was also responsible for obtaining the Nd isotope compositions presented in this study. The author led the interpretations of the results presented in this study, with insightful comments from Tina van de Flierdt and Mark Rehkämper.

Chapter 3

Lead and Hydrothermal Plumes in the Ocean: A Study at the TAG Hydrothermal Field, Mid-Atlantic Ridge

3.1 Introduction

3.1.1 Submarine Hydrothermal Activities and Metal Flux to the Ocean

Submarine hydrothermal activities represent major sites of material exchange between the ocean and the lithosphere and are known for important influences on the ocean biogeochemical cycles of various elements (Von Damm, 1990; Elderfield and Schultz, 1996; Saito et al., 2013; Resing et al., 2015; German et al., 2016; Roshan et al., 2016; Fitzsimmons et al., 2017; Pavia et al., 2018; Jenkins et al., 2018). At some magmatic and/or tectonic regions along mid-ocean ridges, seawater percolates through fractures into the oceanic crust, is heated by an internal heat source and is subsequently emitted back into the deep ocean (German and Seyfried, 2014). Upon intrusion into the cold, dense seawater, this fluid rises as a buoyant plume, entrains ambient seawater and spreads laterally as it reaches a neutral density level within the water column (Lupton et al., 1985; Speer and Rona, 1989).

High-temperature vent fluids are significantly enriched in many dissolved trace metals relative to ambient seawater (Edmond et al., 1979). For example, dissolved Fe and Mn can be enriched by ~10^6 in vent fluids (e.g. Von Damm et al., 1985; German et al., 1991a). The hydrothermal influx of these trace metals can potentially be transported over long distances by the spreading hydrothermal plume, thus acting as a net source of dissolved metals to the ocean (Klinkhammer, 1980b; German et al., 1991a; Lupton, 1995; Saito et al., 2013; Resing et al., 2015). However, the net flux depends on the deep ocean circulation and, particularly, the physicochemical stability of individual trace metals in the hydrothermal plume. At the most studied vent type, high-temperature black smokers, the large physicochemical gradient between the intruding hot (350-400°C), reducing vent fluid and the cold, oxic bottom seawater often triggers intense precipitation of sulphide and oxyhydroxide phases (Feely et al., 1987; Dymond and Roth, 1988; German et al., 1991a; Lilley et al., 1995). For some trace metals, such as the rare earth elements (German et al., 1990, 2002; Rudnicki and Elderfield, 1993; Stichel et al., 2018) and particle-reactive Th (German et al., 1991b; Hayes et al., 2015; Pavia et al., 2018), hydrothermal activity can act as net sink of these elements in the deep ocean through enhanced elemental scavenging by plume particles.

3.1.2 Hydrothermal Activities and Marine Pb Cycling

High-temperature vent fluids are known to be enriched in total dissolvable Pb – the sum of dissolved (< 0.2 μm) and particulate (> 0.2 μm) Pb, by 3 to 4 orders of magnitude relative to ambient seawater (Von Damm et al., 1985; Chen et al., 1986; Hinkley and Tatsumoto, 1987; Douville et al., 2002). However, the net effect of hydrothermal activities on the dissolved Pb budget of seawater remains elusive. Various early studies (Trocine and Trefry, 1988; Mottl and McConachy, 1990; German et al., 1991a; Elderfield et al., 1993; Godfrey et al., 1994) assessed the fate of Pb at black smoker vent systems using the plume particulate concentration ratios between Pb and Fe, the latter being a key element that

was assumed to have only a negligible net hydrothermal flux to the open ocean (see review by German and Seyfried, 2014). These studies revealed a co-enrichment of Pb and Fe in plume particles, which suggests that like most chalcophile elements (e.g. Cu, Co, Zn, Cd), dissolved Pb in vent fluids is quantitatively removed by intense adsorption or incorporation onto/into Fe sulphide and oxyhydroxide particles, therefore yielding no net Pb flux to the ocean. However, as pointed out by Godfrey et al. (1994), particulate Pb/Fe relationships in hydrothermal plumes exhibit considerable scatter, which potentially indicates that biogeochemical processes other than interactions with Fe phases are dictating the fate of Pb in plumes. In the same work, pioneering Pb isotope data for plume particles from the TAG (Transatlantic Geotraverse) Hydrothermal Field at the Mid-Atlantic Ridge were also presented. These results provide evidence for scavenging of dissolved Pb from the ambient seawater in the TAG plume, pointing to hydrothermal activity acting as a net sink for dissolved Pb in the deep ocean. However, other Pb isotope studies on sedimentary archives of past seawater Pb, such as ferromanganese crusts and metalliferous sediments, reveal the possibility of distal transport of hydrothermal Pb (Barrett et al., 1987; van de Flierdt et al., 2004). For example, metalliferous sediments located more than 1000 km west of the East Pacific Rise appear to contain 20-30% of a hydrothermal component (Barrett et al., 1987).

Recent observations that emerge from the GEOTRACES programme have led to major reassessments of the biogeochemical processes and fates of many trace metals in hydrothermal plumes, especially for Fe and Mn. It was traditionally assumed that hydrothermal activity yielded a negligible net flux of dissolved Fe to the open ocean (German et al., 1991a; German and Seyfried, 2014). However, recent measurements and modelling studies on the marine distribution of dissolved Fe were able to reveal distal transport of hydrothermally sourced Fe, to distances up to 2000 km from the vent sources and across different major basins of the global ocean (Klunder et al., 2011, 2012; Nishioka et al., 2013; Saito et al., 2013; Resing et al., 2015; Fitzsimmons et al., 2017). These observations were attributed to various physicochemical mechanisms and dynamics that stabilise the dissolved Fe output from hydrothermal vents, including complexation with dissolved organic ligands (Bennett et al., 2008; Toner et al., 2009; Sander and Koschinsky, 2011; Lough et al., 2019), precipitation as or incorporation into colloidal-sized particles (‘colloids’, 0.02-0.2 μm) (Yücel et al., 2011; Gartman et al., 2014; Findlay et al., 2015), reversible dissolved-particulate exchange processes (Fitzsimmons et al., 2017), interactions with organic particles (Fitzsimmons et al., 2017; Hoffman et al., 2018) and microbial activities (Li et al., 2014). In contrast, the hydrothermal outputs of dissolved Mn, which were originally thought to behave more conservatively than Fe in hydrothermal plumes, were shown to undergo more rapid removal compared to Fe (Middag et al., 2011; Resing et al., 2015). Previous hydrothermal flux models for chalcophile elements have also been revised. For example, recent observations revealed the distal transport of hydrothermally sourced Zn in the Southeast Pacific Ocean (Roshan et al., 2016), whilst

modelling work for Cu highlighted the role of organic complexation in stabilising the dissolved load against precipitation in hydrothermal plumes (Sander and Koschinsky, 2011).

The above findings necessitate a reassessment of the existing understanding on the flux balance of Pb in hydrothermal plumes and its transport in the deep ocean (Trocine and Trefry, 1988; German et al., 1991a; Godfrey et al., 1994), which up to now was largely based on the assumption of limited dispersal of hydrothermal Fe in the open ocean. For example, given the observed coupling of Pb and Fe in plume environments (e.g. Elderfield et al., 1993), the complex physicochemical mechanisms involved in the distal transport of hydrothermally derived Fe could also affect the cycling of Pb. Organic complexation, which is known to dominate (> 50%) the speciation of dissolved Pb in marine environments such as estuaries and surface waters (e.g. Capodaglio et al., 1990; Maring and Duce, 1990; Kozelka and Bruland, 1998), could contribute to the stabilisation of Pb in hydrothermal plumes. These hypotheses require testing with observational data for dissolved Pb and its isotopes in the deep ocean, which remain scarce at present. The deep ocean has extremely low Pb concentrations, and it is only until recent years that methods for precise and accurate measurements of Pb concentrations and isotope compositions in seawater at these concentrations have become available (Reuer et al., 2003; Lee et al., 2011; Boyle et al., 2012; Paul et al., 2015; Griffiths et al., 2020).

Analyses of seawater samples collected in 2011 from the GEOTRACES section GA03 (Noble et al., 2015) provided the first high-resolution and full-depth dissolved Pb isotope profiles across the North Atlantic Ocean. In particular, this dataset includes the first Pb isotope measurements from within a hydrothermal plume, a single seawater profile over the TAG Hydrothermal Field at the Mid-Atlantic Ridge. Further measurements for the hydrothermal plume emanating from the East Pacific Rise (15°S) were obtained on samples collected in 2013 from the GEOTRACES section GP16 in the Southeast Pacific Ocean (Boyle et al., 2020). Both studies revealed the net removal of dissolved Pb in the hydrothermal plumes, agreeing with the suggestion by Godfrey et al. (1994) based on plume particle isotope data. Despite rapid removal of Pb in the hydrothermal plume, Boyle et al. (2020) showed that hydrothermally derived Pb constitutes a small fraction (~1%) of the dissolved Pb budget within the hydrothermal plume emanating from the East Pacific Rise. With the results of more recent studies (Bridgestock et al., 2018; Zurbrick et al., 2018), which provide an improved characterisation of the ambient Pb signatures of the North Atlantic, there is now sufficient background data, to conduct a detailed investigation of Pb cycling in the vicinity of hydrothermal systems in the North Atlantic ocean basin.

3.1.3 This Study

This chapter presents the dissolved Pb concentrations, [Pb], and isotope compositions of five seawater depth profiles at and in the vicinity of the TAG Hydrothermal Field in the North Atlantic, collected during the GEOTRACES GA13 section cruise (FRidge) (Fig. 3.1). This locality hosts the most extensively sampled and studied hydrothermal field in the Atlantic Ocean (Humphris et al., 2015

and references therein). Its geochemistry and hydrothermal activities are well-known (Trocine and Trefry, 1988; German et al., 1990, 1991a, b; Elderfield et al., 1993; Metz and Trefry, 2000). In addition, the Pb isotope signatures of ambient seawater from the vicinity of the TAG Field was constrained at high resolution based on samples from the zonal GEOTRACES GA03 transect (Noble et al. 2015). In this study, new seawater Pb concentration and isotope data are presented and examined, which aim to investigate the processes that control the distribution of Pb in the TAG hydrothermal plume, both above the vent field and at more distal locations in the open Atlantic Ocean.

3.2 Setting

3.2.1 Hydrographic Setting

3.2.1.1 Hydrography of the North Atlantic Ocean

The anticyclonic, wind-driven North Atlantic Subtropical Gyre dominates the surface water of the North Atlantic Ocean between 10°N and 40°N (e.g. Talley et al., 2011) (Fig. 3.1a). Upper water from the Equatorial Atlantic exits the Strait of Florida and propagates northward along the western boundary in the Gulf Stream. At ~40°N, the Gulf Stream splits into the Azores Current and the North Atlantic Current (NAC) (e.g. Talley et al., 2011). The Azores Current propagates east, circulates around the subtropical Atlantic in other currents and returns to the Caribbean Sea at ~20°N, completing the subtropical gyre (Fig. 3.1a; see also Figure 8 of Schmitz and McCartney, 1993).

Intermediate and deep waters in the subtropical North Atlantic are influenced by advected water masses originating from higher latitudes in both hemispheres (Fig. 3.1a; Table 3.1). Cold dense water forms in the Nordic Seas, overflows into the subpolar Iceland Basin and Irminger Sea and forms the Iceland-Scotland Overflow Water (ISOW) and Denmark Strait Overflow Water (DSOW) respectively, which then propagate westward into the Labrador Sea (Swift, 1984; Schmitz and McCartney, 1993). In the Labrador Sea, deep water convection during boreal winter forms the Classical Labrador Sea Water (CLSW) (e.g. McCartney and Talley, 1982; Talley and McCartney, 1982) and the overlying Upper Labrador Sea Water (ULSW) (Pickart, 1992; Pickart et al., 1996). These newly formed water masses join the ISOW and DSOW, forming the North Atlantic Deep Water (NADW) (Schmitz and McCartney, 1993; Talley et al., 2011). The NADW dominates the deeper portion of the water column in the subpolar North Atlantic and advects southward along the western boundary in the Deep Western Boundary Current (DWBC), towards the Southern Ocean where it upwells (e.g. Rhein et al., 2015). The northward flowing Gulf Stream in the upper ocean and the southward flowing DWBC in the deep ocean form the upper cell of the Atlantic Meridional Overturning Circulation (Buckley and Marshall, 2016). Near its point of export from the Labrador Sea at ~55°N, the NADW encompasses four principal components with different potential densities: ULSW (σ_θ = 27.68-27.74 kg/m^3), CLSW (σ_θ = 27.74-27.80 kg/m^3),

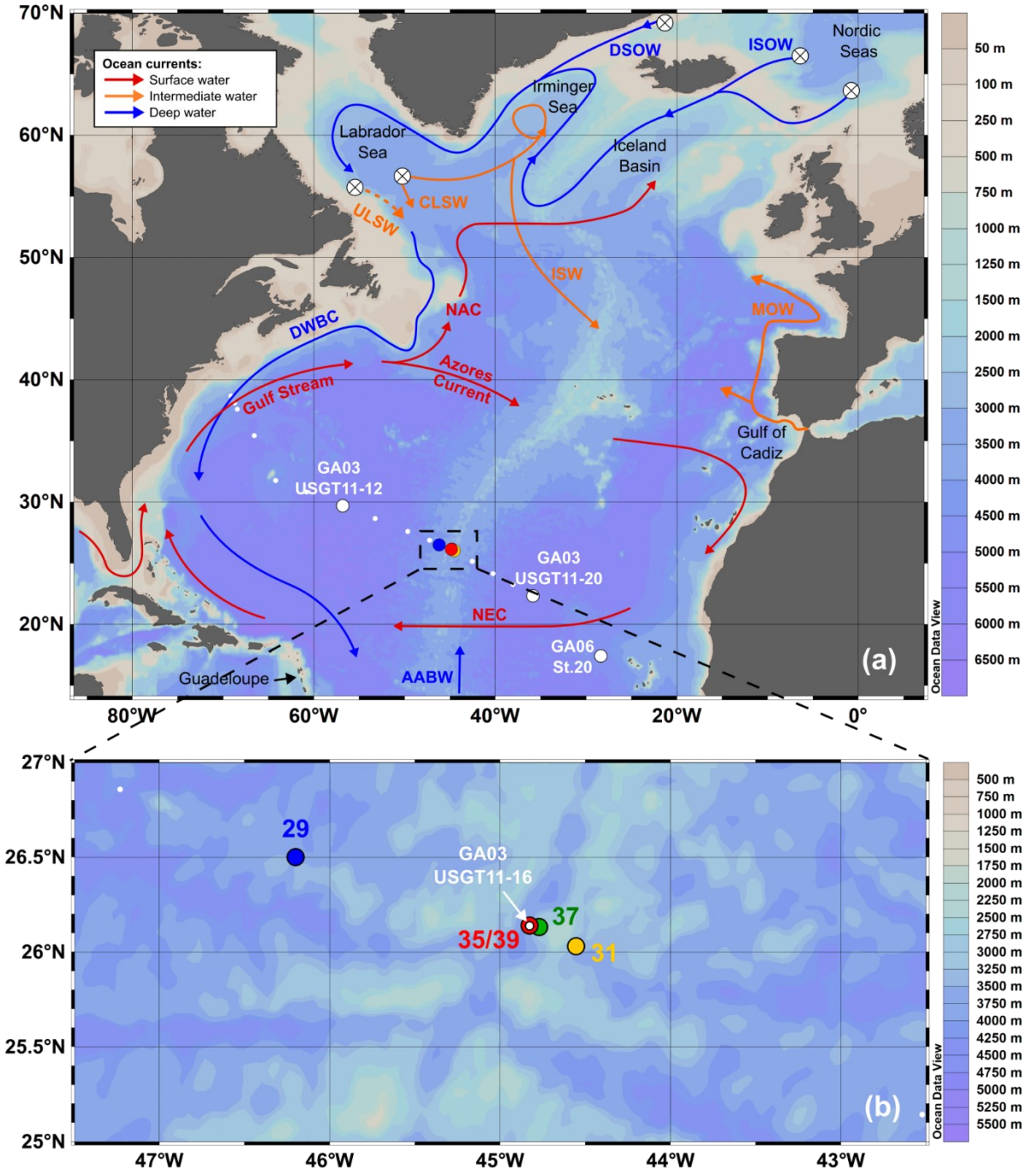


Figure 3.1. (a) Map of the North Atlantic Ocean, showing the locations of the GEOTRACES GA13 sampling stations near the TAG vent site that are relevant for this study (coloured circles) and of other stations with previously published seawater Pb isotope data (white circles). Shown are stations of the GEOTRACES GA03 (Noble et al., 2015) and GA06 (Bridgestock et al., 2018) expeditions, whereby large, white circles denote stations with full-depth measurements of Pb isotope compositions. The schematic large-scale circulation pattern is adapted from Daniault et al. (2016). Arrows denote the flow directions of surface waters (red arrows), intermediate depth water masses (orange arrows; σ^{θ} = 27.3-27.7) and deep water masses (blue arrows; σ^{θ} > 27.7). Water mass abbreviations as in Table 3.1. **(b) Enlargement of map (a) for the TAG Hydrothermal Field region and the GA13 seawater stations relevant for this study.** Station USGT11-16 from the GA03 section nearly coincides with station 35/39 of this study. The maps were created using Ocean Data View (ODV) software (Schlitzer, 2020), with ocean background colours indicating the bottom topography.

Table 3.1. Summary of the major endmember water masses and their potential density (σ_θ) ranges in the subtropical North Atlantic Ocean. Density ranges according to Jenkins et al. (2015b) and references therein.

	Water Mass	σ_θ (kg/m^3)
NACW	North Atlantic Central Water	25.8-27.3
MOW	Mediterranean Outflow Water	27.3-27.7
ISW	Irminger Sea Water	27.3-27.7
ULSW	Upper Labrador Sea Water	27.68-27.74
CLSW	Classical Labrador Sea Water	27.74-27.80
ISOW	Iceland-Scotland Overflow Water	27.81-27.88
DSOW	Denmark Strait Overflow Water	> 27.88
AABW	Antarctic Bottom Water	~27.9

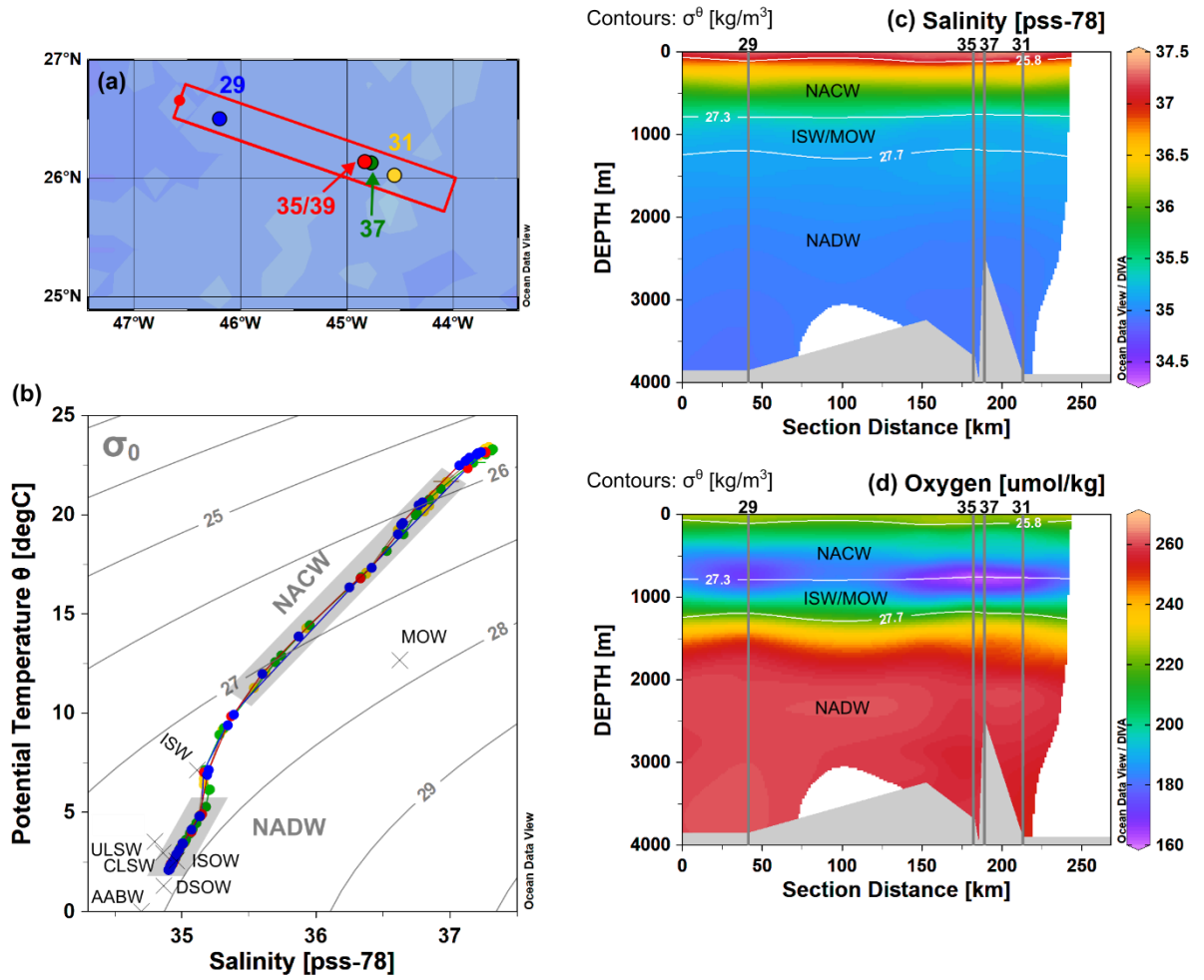


Figure 3.2. Hydrographic data for stations from the TAG hydrothermal area, sampled during the GEOTRACES GA13 expedition. (a) Locations of stations sampled for Pb concentrations and isotope compositions. (b) Potential temperature and salinity data for the GA13 stations relevant to this study as well as endmember water mass compositions (crosses) following Jenkins et al. (2015b); the water mass abbreviations are defined in Table 3.1. (c-d) Quasi-zonal section plots of salinity and oxygen concentration across the Mid-Atlantic Ridge in the TAG hydrothermal area. Contours denote the potential density (σ^θ) isopycnals that correspond to the boundaries of major water masses. Grey surfaces denote the bottom topography. All plots were created using the ODV software (Schlitzer, 2020).

ISOW (σ_θ = 27.81-27.88 kg/m^3, often referred to as the Northeast Atlantic Deep Water), and DSOW (σ_θ > 27.88 kg/m^3) (Jenkins et al., 2015b; Rhein et al., 2015 and references therein for the water type compositions and density ranges).

Intermediate depths of the subtropical North Atlantic Ocean are predominantly filled by the Irminger Sea Water (ISW) and the Mediterranean Outflow Water (MOW) (Jenkins et al., 2015b). During winter, cold subsurface waters in the subpolar Irminger and Labrador Seas subduct to intermediate depths, forming the relatively fresh, oxygenated ISW (potential temperature (θ) = 7.1, salinity (S) = 35.2, σ_θ = 27.30-27.65 kg/m^3) (Harvey and Arhan, 1988; Tanhua et al., 2005; Jenkins et al., 2015b), also known as the Subarctic Intermediate Water (Arhan, 1990; van Aken, 2000b). Saline water from the Mediterranean Sea exits through the Strait of Gibraltar and descends in the Gulf of Cadiz. In the Western Gulf of Cadiz (~36°N), the MOW is defined by a potential temperature (θ) of 12.65°C, a salinity (S) of 36.62 (WOCE A03 1993, Jenkins et al., 2015b) and potential densities (σ_θ) of between 27.3 and 27.7 kg/m^3 (Baringer and Price, 1997). Once in the open North Atlantic, the core of the MOW moves mainly north along the eastern boundary of the ocean basin, but also dissipates westward into the wider North Atlantic (Harvey and Arhan, 1988; Richardson et al., 1991; van Aken, 2000b and references therein).

Antarctic Bottom Water (AABW) forms along the Antarctic continental margin in the Southern Ocean, propagating northward into all ocean basins as dense, bottom flows (Orsi et al., 1999). Along its northward journey, this cold Antarctic water becomes warmer, upwells to shallower isopycnals and mixes with the overlying NADW (Schmitz and McCartney, 1993; van Aken, 2000a). This modified AABW (θ = 2.0°C, S = 34.90, σ_θ = 27.9 kg/m^3 at ~36°N) (van Aken, 2000a) is sometimes referred to as the Lower Deep Water in the literature (McCartney, 1992). The AABW and its return flow within the Lower Deep Water form the lower cell of the Antarctic Meridional Overturning Circulation (Marshall and Speer, 2012). In the modern ocean, both cells are interwoven, often described as a 'Figure Eight Loop' (e.g. Ferrari et al., 2014).

Any east-west exchange of deep and bottom waters in the subtropical North Atlantic is restricted by the Mid-Atlantic Ridge, which forms a quasi-meridional topographic barrier between the eastern and western basins. Deep water mass exchange is only possible through advection across deep fracture zones in the ridge or diapycnal mixing with water masses occupying shallower density levels above the ridge topography.

3.2.1.2 Water masses in the vicinity of the TAG Hydrothermal Field

The uppermost ~100 m of the water column is occupied by well-mixed, high salinity surface waters (θ = 22-24°C, S = 37.1-37.4, σ_θ < 25.8 kg/m^3) (Fig. 3.2). Below the mixed layer, the North Atlantic Central Water (NACW; σ_θ = 25.8-27.3 kg/m^3) occupies depths between about 100 and 700 m and is characterised by decreasing temperature (from 16°C and 10°C) and salinity (from 36.2 to 35.4) with depth (Sverdrup et al., 1942). The intermediate depth range (700-1200 m, σ_θ = 27.3-27.7 kg/m^3) is

filled predominantly by a mixture of ISW and MOW from the north (Jenkins et al., 2015b). The deep portion of the water column (about 1200 m to bottom depth, σ_θ > 27.7) is dominated by NADW (Tsuchiya et al., 1992), characterised by high salinity (> 34.9) and high oxygen levels (> 250 μmol/kg). Optimal multi-parameter (OMP) analysis (Jenkins et al., 2015b) suggests the presence of up to 25-30% AABW at the deepest sampled depth of about 4000 m.

Small but systematic differences in deep water compositions exist between the two sides of the Mid-Atlantic Ridge. Below 1500 m depth, hydrographic stations at the western flank of the ridge show consistently higher oxygen levels (247-262 μmol/kg) than those at the eastern flank (239-255 μmol/kg) (Fig. 3.2d). Such observations agree with data from the zonal GApr08 transect further south (~22°N) (Fig. 3c of Artigue et al., 2020) and, at least in part, that the deep western basin is filled by more recently ventilated NADW from the DWBC, while the deep eastern basin is filled by older, less oxygenated NADW (Jenkins et al., 2015b; Holzer et al., 2018).

3.2.2 Geological Setting

The TAG Hydrothermal Field (26.13°N, 44.83°W) is located in a slow-spreading segment of the Mid-Atlantic Ridge (half-spreading rate: 9-13 mm/a), between the Atlantis (30°N) and Kane (24°N) Fracture Zones (Lattimore et al., 1974; McGregor et al., 1977). The field is hosted in basaltic crust that is displaced over a major detachment fault, which lies above a field of gabbroic intrusions (Tivey et al., 1998; Canales et al., 2007; DeMartin et al., 2007; McCaig et al., 2007; Zhao et al., 2012). The crustal block is further dissected by intersecting ridge-parallel (NNE) and ridge-oblique (ENE) faults systems (Karson and Rona, 1990; Kleinrock and Humphris, 1996; Bohnenstiehl and Kleinrock, 1999). The presence of a heat source underneath the heavily fissured crust fuels a significant volume of hydrothermal circulation through the crust.

The TAG Field spans a total area of 25 km^2 over the east-bounding wall of the axial valley of the ridge (Rona, 1980) and has been hydrothermally active over the last 125,000 years (Lalou et al., 1998). High-temperature venting is centred over a circular-shaped sulphide mound known as the 'TAG mound', which lies at seafloor depths between 3625 and 3670 m (Rona et al., 1993a, b; White et al., 1998). At the TAG mound, high-temperature venting began in 50-40 ka and occurred in cycles of focussed venting and quiescence every 4000-6000 years, which continues till the present-day (Lalou et al., 1990, 1998; Lalou, 1993; You and Bickle, 1998).

Evidence of venting from the TAG Hydrothermal Field was first detected during the Trans-Atlantic Geotraverse project (1972-73) (M. R. Scott et al., 1974; R. B. Scott et al., 1974; Rona et al., 1975). The active high-temperature vent site was discovered in 1985 (Rona et al., 1986) and first sampled in 1986 by the submersible *Alvin* (Campbell et al., 1988; Thompson et al., 1988). The emitted black smoker fluids are characterised by high temperatures (347-369°C), acidic pH (3.0-3.8), high chlorinity (≈ 640 mmol/kg) and elemental compositions that reflect subsurface interactions of seawater with basaltic

rocks, including enrichment trends in transition metals (e.g. Fe, Mn, Zn) and rare earth elements (Campbell et al., 1988; German and Seyfried, 2014). Compared to other major localities of hydrothermal activities, the black smoker fluids from the TAG Field feature low Fe/H_2S (~2), indicating relatively oxidising subsurface condition (e.g. Foustoukos and Seyfried, 2005).

Above the TAG mound, the initially buoyant hydrothermal plume rises to neutral buoyancy heights of 300-450 m above the seafloor, where the plume spreads laterally (Klinkhammer et al., 1986; Nelsen and Forde, 1991; Rudnicki et al., 1994). Bounded by tall walls of up to 2 km above the valley floor (Rona et al., 1986; Zonenshain et al., 1989) and in the absence of strong bottom currents, the dispersal of plume materials away from the TAG Field is likely to be restricted by the steep topography (German et al., 1991b; German and Sparks, 1993; Rudnicki et al., 1994).

3.3 Methods

3.3.1 Samples

The GEOTRACES GA13 section cruise ("FRidge" expedition) on the *RRS James Cook* (JC156) sailed between 20th December 2017 and 1st February 2018, from Southampton, UK to Pointe-à-Pitre, Guadeloupe. Five seawater profiles above and in the vicinity of the TAG Hydrothermal Field were collected during the FRidge expedition for dissolved Pb concentrations and isotopes, each at between six and twelve depths throughout the water column (Fig. 3.1b; Table 3.2). Profiles were collected directly above the active vent site (station 35/39, 'vent site station'), 6 km east of the vent site above the east valley wall (station 37, 'valley wall station') as well as 31 km ESE (station 31, 'proximal E station') and 142 km WNW (station 29, 'distal W station') of the vent site. Following initial sampling at vent site station 35, most samples from shallower depths (< 2000 m) at this location were collected during a second visit, termed station 39. Stations 35 and 39 are therefore treated as a single station in the following. All stations form a quasi-zonal (WNW-ESE) transect across the ridge crest. Vent site station 35/39 is located within 1 km of station USGT11-16 of the GEOTRACES quasi-zonal GA03 transect, enabling a direct comparison of the new data in the current study with the results published by Noble et al. (2015) for GA03 seawater samples collected in 2011.

Seawater sample collection during the FRidge expedition was conducted using trace metal clean 10 L OTE (Ocean Technology Equipment) bottles mounted on a titanium frame CTD rosette. The CTD system was fitted with electrical potential (Eh) and light scattering sensors to aid the detection of the hydrothermal plume, the main target of the expedition. Upon recovery, the OTE bottles were transferred to a shipboard clean sampling laboratory. Seawater samples were filtered, under pressurised (~7 psi) filtered air and using 0.2 µm Sartobran® 300 (Sartorius) filter capsules. For Pb concentration and isotope measurements, the filtered seawater was collected in two acid-cleaned 1 L LDPE sample bottles, whereby the bottles and caps were rinsed three times with the filtered seawater before being filled. The

filtered samples were then triple-bagged for storage until they were analysed onshore (i.e. at Imperial College London).

Table 3.2. Information about the five GEOTRACES GA13 stations that were sampled for the determination of Pb concentrations and isotope compositions.

Station	Location	Lat (°N)	Long (°W)	Date of Sampling (dd/mm/yyyy)
29	Distal W	26.50	46.20	19/01/2018
31	Proximal E	26.03	44.55	21/01/2018
35	Vent site	26.14	44.83	25/01/2018
39*				26/01/2018
37	Valley wall	26.13	44.77	27/01/2018

*Station 39 was a revisit of station 35 above the TAG Hydrothermal Field.

3.3.2 Dissolved Pb Concentrations and Isotopes

The measurements of Pb concentrations and isotope compositions of the seawater samples were carried out at Imperial College London, following the analytical protocols described in detail in Griffiths et al. (2020).

3.3.3.1 Lead concentrations

All samples were acidified to 0.024 M HCl (pH ≤ 2.0) using distilled 6 M HCl at least two weeks before further sample preparation for the determination of Pb concentrations by isotope dilution. A ^{207}Pb-^{204}Pb double spike was added to a 50 mL aliquot of each seawater sample to achieve an optimal spike to sample-derived Pb (S/N) ratio of ≈ 2.6. After at least 10 days of equilibration, Pb was pre-concentrated by $Mg(OH)_2$ co-precipitation using 0.6-0.8 mL of purified ammonia solution. Following centrifugation, the Pb in the samples was separated with a single-stage of HBr-HNO_3 anion exchange chromatography using AG1-X8 (100-200 mesh) resin and shrink-fit Teflon columns with 20 µL resin reservoirs. The Pb fractions were then doped with a NIST SRM 997 Tl standard solution to obtain a Tl/Pb ratio of 3, dried and re-dissolved in 0.1 M HNO_3 to be analysed on a Nu Plasma II multi-collector inductively coupled plasma mass spectrometer (MC-ICP-MS; Nu Instruments). The measurements were corrected for instrumental mass fractionation by external normalisation to a constant ^{205}Tl-^{203}Tl ratio = 2.3888 based on the exponential law, followed by isotope dilution data reduction to obtain the Pb concentrations.

The procedural Pb blanks during 17 months of concentration measurements were 5.6 ± 3.0 pg (1 SD; n = 18; 2 to 13 pg), representing 0.1-22% of the indigenous Pb in the aliquots across the sample set. The Pb concentrations of all samples were corrected for the average blank value. The long-term

external precision, determined from replicate analyses of two in-house seawater quality control materials, was ± 0.5 pmol/kg (1 SD) or better (Table 3.3).

At least two aliquots of all samples were analysed for Pb concentrations, with at least one aliquot taken from each of the two 1 L sample bottles, in order to check for spurious blank contributions from the sample bottles and/or the analytical procedure. Unless specified, all reported concentration values are averages of all valid measurements from across the two bottles. For the 3000 m sample from station 29, a single analysis yielded a Pb concentration that was about 4 pmol/kg higher compared to latter results obtained for both bottles (Table 3.4). The higher value was discarded as it was most likely affected by a spurious blank. Where the uncertainty of valid replicate [Pb] measurements was poorer than that calculated for the in-house reference materials (± 0.5 pmol/kg), the former uncertainty is reported and this is generally less than ± 1.5 pmol/kg, with a few notable exceptions (see Section 3.4.2).

3.3.3.2 Lead isotope compositions

All samples were acidified to 0.024 M HCl (pH ≤ 2.0) between 2 and 20 weeks before further sample preparation for the Pb isotope measurements. For analysis, 1-2 L of seawater was processed to obtain 1-5 ng of Pb for the isotope measurements. The samples were first treated with 0.01 M H_2O_2 to achieve 0.01 mmol / L seawater. After approximately 24 hours, 2 mL / L seawater of 5 M ammonium acetate solution was added as a buffer, followed by adjustment of the sample pH to 4.8 ± 0.1 by the addition of purified ammonia solution. After setting the pH, Pb was pre-concentrated from the seawater by solid phase extraction with Nobias Chelate PA-1 resin using the procedure of Griffiths et al. (2020). Following elution of Pb from the Nobias PA-1 resin with 30 mL 3 M HNO_3, the eluates were dried, and the residues were refluxed with 0.4 mL of a 15 M HNO_3 – 9 M H_2O_2 mixture in a 9:1 ratio at 140°C for at least 2 hours to remove any traces of organic matter. After drying, the sample residues were treated with 1 mL of 2 M HBr and refluxed at 120°C to convert the Pb into bromide form and dried again. The sample residues were then re-dissolved in 5 mL of 2 M HBr and purified with two stages of HBr-HNO_3 anion exchange chromatography using AG1-X8 (100-200 mesh) resin and shrink-fit Teflon columns with 150 µL resin reservoirs. The chromatography procedure followed the revised protocol of Griffiths et al. (2020), with the only modification being that no HF was added during the first stage of chromatography. The HF addition was first introduced by Paul et al. (2015) to prevent silica gel formation during anion exchange chromatography of Si-rich seawater samples after $Mg(OH)_2$ co-precipitation. However, the highly selective Nobias PA-1 resin used in this study yields minimal recovery for Si and most other metalloid elements (Sohrin et al., 2008). Furthermore, the samples from the subtropical North Atlantic Ocean had relatively low Si concentrations (≤ 40 µmol/kg). Therefore, the decision was made to omit HF for this sample set, and as expected, silica gel formation was not observed in any of the analysed samples during chromatography. After purification, a 1/3 aliquot of the Pb fractions was separated and mixed with the ^{207}Pb-^{204}Pb double spike (S/N ≈ 1.23) for spiked measurements, while the remaining 2/3 aliquot was left for the unspiked measurements. Prior to isotope

measurements, both the spiked and unspiked aliquots were doped with a NIST SRM 997 Tl standard solution to obtain a Tl/Pb ratio of 3, dried and re-dissolved in 1-1.5 mL of 0.1 M HNO_3.

All isotope measurements were conducted using a Nu Plasma II MC-ICP-MS (Nu Instruments). For each batch of 7 to 14 samples, unspiked measurements were first conducted, followed by spiked measurements on a subsequent day in the same order of samples. A set of NIST SRM 981 Pb – NIST SRM 997 Tl standard mixtures with a Tl/Pb ratio of 3 and 1-5 ng/g Pb were measured together with the samples during each measurement session to monitor within-run precision and to support correction for instrumental mass fractionation. The measurements were processed offline by a MATLAB program which encompasses the following steps (Griffiths et al., 2020). The isobaric interference of ^{204}Hg on ^{204}Pb was corrected based on the measured ^{202}Hg ion beam intensity and a ratio of $^{204}Hg/^{202}Hg = 0.22923$ (Meija et al., 2010). To correct for instrumental mass fractionation, the unspiked measurements were first corrected by external normalisation using an empirically optimised $^{205}Tl/^{203}Tl$ ratio based on the mass fractionations of the measured NIST Pb-Tl standard mixtures (Rehkämper and Halliday, 1998). This dataset was then combined with the double spiked measurements to generate the double spike corrected data by iteratively solving a set of non-linear equations (Rudge et al., 2009). A final standardisation step was carried out, to correct for any deviations of the measured values for the NIST Pb-Tl standard mixtures from the reference data (Galer, 1999).

The precision of the Pb isotope measurements was assessed by replicate analyses of two in-house seawater reference materials, 'EP-78' (n = 6, measured Pb ≈ 4 ng) and 'SO-151' (n = 6, measured Pb ≈ 2 ng), alongside the samples (Table 3.3). Over the course of 12 months of sample measurements, the Pb isotope data for EP-78 displayed 2 SD precisions of ~200 ppm for $^{206}Pb/^{207}Pb$ and $^{208}Pb/^{207}Pb$, and ~700 ppm for $^{206}Pb/^{204}Pb$. With this, the precisions were similar to or better than those achieved by Griffiths et al. (2020) and Paul et al. (2015), respectively, in seawater analyses that used about 4-10 ng Pb. The precision was poorer for SO-151, which was analysed using run solutions that had Pb concentrations of only ≈ 2 ng/mL. In this case, 2 SD precisions of ~1400 ppm for $^{206}Pb/^{207}Pb$, ~400 ppm for $^{208}Pb/^{207}Pb$ and ~2200 ppm for $^{206}Pb/^{204}Pb$ were achieved, when one anomalous result, which indicated significant contamination, was omitted. The precision for $^{206}Pb/^{204}Pb$ was nearly two times worse than that obtained by Griffiths et al. (2020). This is most likely due to the 1.5- to 2-fold reduction in instrumental sensitivity (800-1000 V/ppm Pb) during some measurement sessions of this study compared to the analyses of Griffiths et al. (2020) (~1500 V/ppm), and this will have most severely impacted monitoring of the small ^{204}Pb ion beam. For $^{206}Pb/^{207}Pb$ and $^{208}Pb/^{207}Pb$, the precisions obtained were similar to those of Griffiths et al. (2020) for analyses of ≤ 2 ng of Pb. Notably, multiple analyses of EP-78 (with ≈ 4 ng Pb) and SO-151 (with ≈ 2 ng Pb) yielded precisions for the latter that are about 2× poorer for $^{208}Pb/^{207}Pb$ but 7× worse for $^{206}Pb/^{207}Pb$. Similar observations were present in previous studies that reported seawater Pb isotope data from analyses at different Pb concentrations (Paul et al., 2015; Zurbrick et al., 2018; Griffiths et al., 2020).

Table 3.3. Lead concentration and isotope data obtained for two in-house seawater reference materials and the GEOTRACES intercalibration sample GSP.

Sample	Remarks	n-ID[(a)]	[Pb] (pmol/kg)	1sd[(b)]	n-IC[(c)]	IC sample size (L)	Meas. Pb[(d)] (ng)	$^{206}Pb/^{207}Pb$	2sd[(e)]	$^{208}Pb/^{207}Pb$	2sd[(e)]	$^{206}Pb/^{204}Pb$	2sd[(e)]
In-house reference samples													
EP-78		4	55.7	0.5	6	1.5-1.9	~4	1.1572	0.0002166	2.4348	0.0006249	18.057	0.012652
SO-151		10	9.7	0.3	5	~0.7	~2	1.1958	0.0017411	2.4499	0.0010410	18.730	0.0402157
GEOTRACES intercalibration sample (GSP)													
GSP	This study[(f)]				1	0.5	~4	1.1589	0.0002166	2.4471	0.0006249	18.066	0.012652
	Griffiths et al. (2020)[(g)]				9	0.2-0.7	~3.5	1.1584	0.0003280	2.4476	0.0006230	18.075	0.010530

(a) Number of individual sample aliquots analysed for Pb concentrations.
(b) 1sd is the standard deviation of the Pb concentrations calculated from the results of *n* individual analyses.
(c) Number of individual sample aliquots analysed for Pb isotope compositions.
(d) Average mass of Pb available in the unspiked sample aliquot for MC-ICP-MS measurements.
(e) 2sd is 2× standard deviation of Pb isotope ratios determined from the results of *n* individual analyses; this is denoted as the 'long-term external precision'. Relative 2sd values in parts per million (ppm) are given below.
(f) As $n = 1$, 2sd precision determined for the in-house reference sample EP-78 was assigned to this sample.
(g) Results of Griffiths et al. (2020) obtained using Pb separation with Nobias PA-1 resin and double spike data reduction.

The precisions obtained for EP-78 were applied to samples which yielded MC-ICP-MS run solutions with Pb concentrations of ≥ 4 ng/mL, while the precisions determined for SO-151 were applied to samples with Pb concentrations of less than 4 ng/mL in the run solutions. The trueness of Pb isotope data was verified by analysis of the GEOTRACES intercalibration sample GSP, which yielded results that agree well with the published values of Griffiths et al. (2020) (Table 3.3).

The sample preparation procedure consistently achieved near-quantitative Pb yields of 94 ± 3% (1 SD; 86% to 102 %). The total procedural Pb blank during the measurement period was 31 ± 10 pg (1 SD; n = 6; 27 to 48 pg), representing 0.2-1.7% of the indigenous sample Pb. Repeated Pb isotope measurements of the procedural blanks yielded poorly reproducible data, due to the low beam intensities and variable blank compositions. However, in the worst-case scenario, the blank corrections to the sample Pb isotope ratios would be similar to or smaller than the analytical errors. No blank corrections were therefore applied to the sample isotope data.

3.3.3 Other parameters

Additional geochemical parameters were determined by members of the FRidge expedition team, in order to aid detection of the hydrothermal plume. Electrical potential and light scattering were measured using shipboard sensors attached to the titanium frame CTD rosette. The dissolved He isotope compositions ($^{3}He/^{4}He$) and Fe concentrations were determined at Woods Hole Oceanographic Institution (MA, USA) and the shipboard laboratories, respectively, and retrieved from the GEOTRACES Intermediate Data Product (IDP) 2021 (GEOTRACES Intermediate Data Product Group, 2021). The dissolved Mn concentrations were also measured in the shipboard laboratories and they are unpublished results provided by Joseph A. Resing (personal communication). Together, these data are used in the following to identify the hydrothermal plume at the stations sampled for Pb concentrations and isotopes.

3.4 Results

3.4.1 Distributions of Dissolved Pb Concentrations and Isotopes

The Pb concentration and isotope data for the seawater samples analysed in this study are displayed as vertical profiles (Fig. 3.3) and quasi-zonal sections (Fig. 3.4) and are shown in Table 3.4. The dissolved Pb concentrations range between 5.5 and 48.2 pmol/kg. The vertical distributions of Pb concentration are characterised by an intermediate depth maximum at 800-1000 m and relatively low levels in the upper and deeper water column. Dissolved $^{206}Pb/^{207}Pb$ and $^{208}Pb/^{207}Pb$ ratios vary between 1.166-1.183 and 2.440-2.453 respectively, except for an anomalous sample at 3236 m depth at vent site station 35/39. Across the sampled stations, the Pb isotope compositions are relatively homogeneous between depths of 700 m and 2500 m but show larger variabilities within the uppermost 400 m depths and deeper depths of ≥ 2500 m.

The uppermost 400 m of the water column (σ_θ < 27.0 kg/m^3) is characterised by low Pb concentrations (17-26 pmol/kg) and relatively low $^{206}Pb/^{207}Pb$ (1.171 ± 0.004) and $^{208}Pb/^{207}Pb$ (2.445 ± 0.003) signatures. Lead concentrations increase with depth between 400 m and 800 m (σ_θ = 27.0-27.3 kg/m^3) and attain a maximum of 46-48 pmol/kg at 800-1000 m depth (σ_θ = 27.3-27.5 kg/m^3) where ISW and MOW dominate. The downward increase in Pb concentrations coincides with a shift towards maximum $^{206}Pb/^{207}Pb$ (≈ 1.183) at a relatively constant $^{208}Pb/^{207}Pb$ ratio of about 2.448.

Within NADW (> 1200 m, σ_θ > 27.7), Pb concentrations decrease markedly with depth, from 44-46 pmol/kg at 1500 m depth, to 14-16 pmol/kg for the deepest samples at 3500-4000 m depths. At vent site station 35/39, the samples between 3100 and 3544 m depths show unusually low Pb concentrations, down to 5.5 pmol/kg at 3322 m depth, the lowest value obtained in this study. Between depths of about 1500 and 2500 m, relatively homogeneous $^{206}Pb/^{207}Pb$ (1.180-1.181) and $^{208}Pb/^{207}Pb$ (2.449-2.450) ratios are observed across the sampled stations. For depths ≥ 2500 m that are sampled by three stations

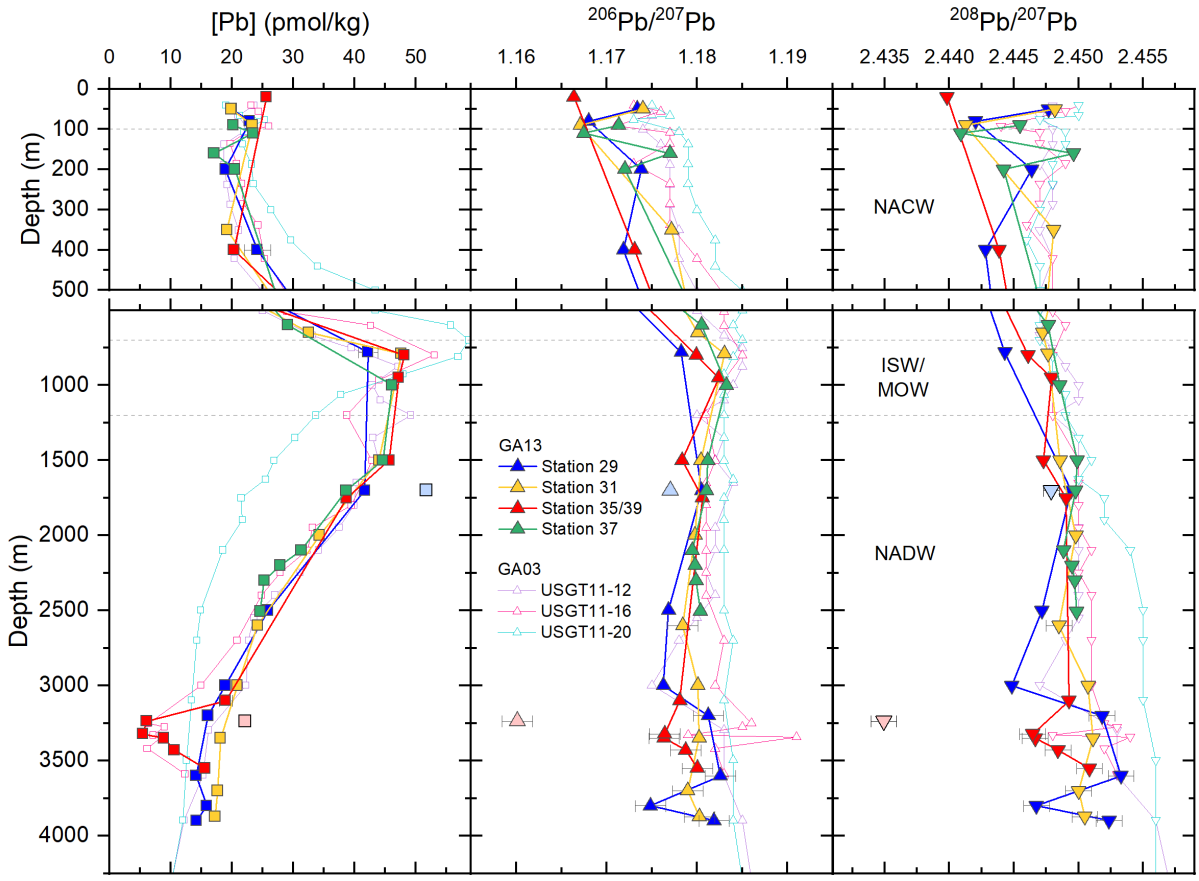


Figure 3.3. Vertical profiles of Pb concentrations ([Pb]), $^{206}Pb/^{207}Pb$, and $^{208}Pb/^{207}Pb$ for the four GA13 stations sampled for Pb concentrations and isotope compositions (large solid symbols). Also shown are previous results for GA03 stations USGT11-12, USGT11-16 and USGT11-20 (small open symbols). GA03 station USGT11-16 is a crossover station with GA13 station 35/39 of the present study. The isolated filled symbols denote Pb concentration and isotope data for possibly contaminated samples that are not discussed in the text. These samples are from 1700 m depth at station 29 (pale blue symbols) and 3236 m depth at station 35/39 (pale red symbols). Horizontal dashed lines mark the boundaries of major water masses. Errors bars denote the 2sd external precisions of the Pb isotope data; these are only shown if larger than the symbol size.

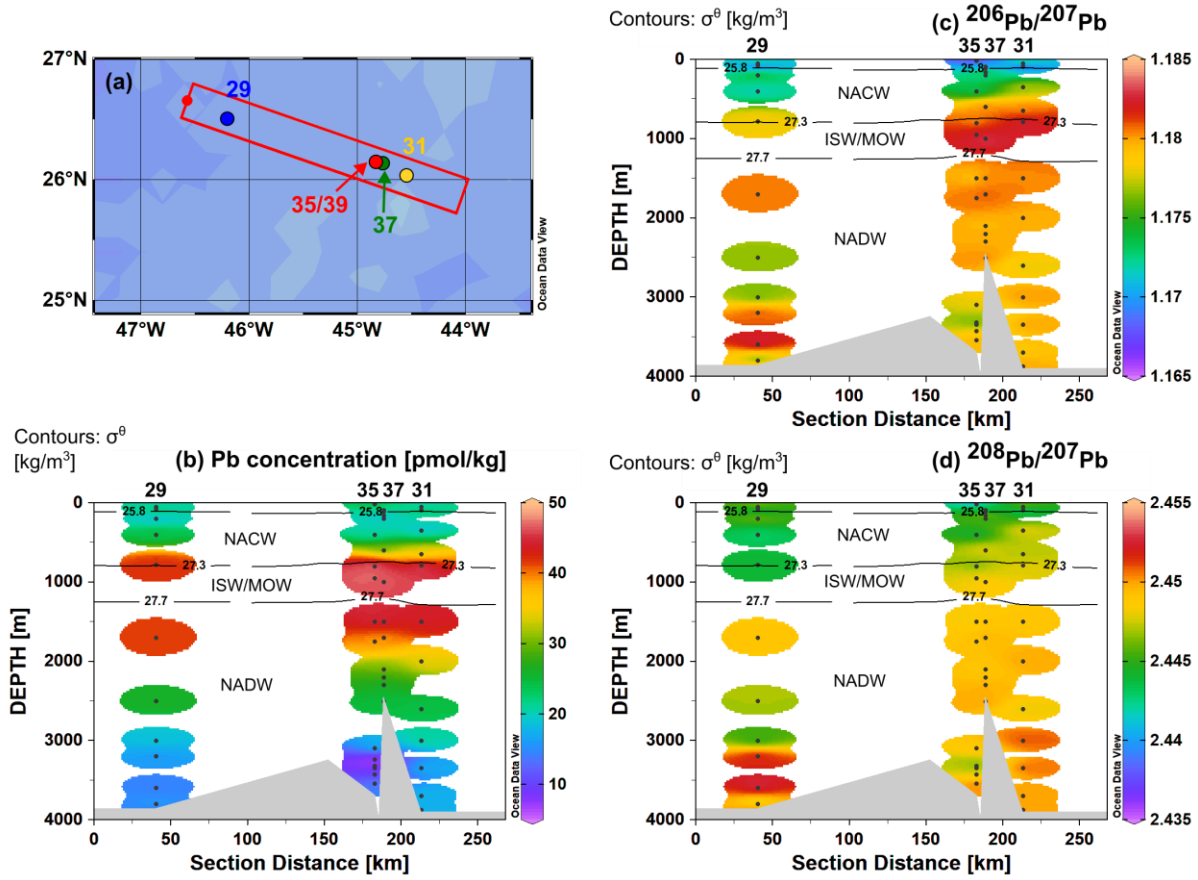


Figure 3.4. (a) Map showing the four GA13 sampling stations relevant to this study and (b-d) quasi-zonal section plots of (b) Pb concentrations, (c) $^{206}Pb/^{207}Pb$ ratios and (d) $^{208}Pb/^{207}Pb$ ratios. The location of the quasi-zonal sections is highlighted in map (a). Black dots on the section plots denote the locations and depths of the samples analysed for Pb concentrations and isotope compositions. Contours denote potential density (σ^{θ}) isopycnals that correspond to the boundaries of major water masses. The plots were created using the ODV software (Schlitzer, 2020).

in this study (stations 29, 31 and 35/39), remarkably variable Pb isotope compositions are observed. At proximal E station 31, the five samples from depths ≥ 2500 m have $^{206}Pb/^{207}Pb$ (1.178-1.180) and $^{208}Pb/^{207}Pb$ (2.449-2.451) ratios that are very similar to values obtained at shallower depths of 1500-2500 m, hence resulting in vertically homogeneous isotope distributions throughout the NADW layer. Therefore, most deep water variabilities in Pb isotope compositions stem from stations 29 and 35/39. At vent site station 35/39, the samples that are markedly depleted in Pb concentrations between depths of 3100 and 3544 m show unusually low $^{208}Pb/^{207}Pb$ ratios beyond analytical error, where a minimum of $^{208}Pb/^{207}Pb = 2.446$ coincides with the minimum [Pb] at 3322 m depth. Even lower $^{206}Pb/^{207}Pb$ (2.435) and $^{208}Pb/^{207}Pb$ (1.160) ratios were determined for the sample collected at 3236 m depth, about 100 m above the [Pb] minimum. At distal W station 29, low $^{206}Pb/^{207}Pb$ (1.175-1.177) and $^{208}Pb/^{207}Pb$ (2.445-2.447) ratios were determined for two samples from 2500 and 3000 m depths and for the near-bottom sample from 3800 m depth. Notably, the sample collected at 3800 m has a slightly higher Pb concentration (15.9 pmol/kg) compared to the samples from adjacent depths (≈ 14 pmol/kg). The low

$^{206}Pb/^{207}Pb$ and $^{208}Pb/^{207}Pb$ ratios of the 3800 m sample furthermore stand in contrast to the relatively high $^{206}Pb/^{207}Pb$ (1.181-1.183) and $^{208}Pb/^{207}Pb$ (2.452-2.453) ratios determined for the three other deep water samples from station 29, which were collected at depths of 3200 m, 3600 m and 3899 m.

Table 3.4. Lead concentration and isotope data for filtered seawater samples from five depth profiles collected during the GEOTRACES GA13 section cruise.

Depth (m)		n-ID[(a)]	[Pb][(b)] (pmol/kg)	1sd	$^{206}Pb/^{207}Pb$	2sd[(c)]	$^{208}Pb/^{207}Pb$	2sd[(c)]	$^{206}Pb/^{204}Pb$	2sd[(c)]
Station 29 (26.50°N, 46.20°W; 19/01/2018; distal W)										
50		2	20.0	1.3	1.1734	0.0002	2.4477	0.0006	18.348	0.012
80		3	22.9	0.9	1.1680	0.0002	2.4420	0.0006	18.250	0.012
200		2	18.9	0.8	1.1738	0.0002	2.4464	0.0006	18.354	0.012
400		2	24.2	2.2	1.1719	0.0002	2.4428	0.0006	18.310	0.012
780		3	42.2	1.6	1.1783	0.0002	2.4443	0.0006	18.416	0.012
1700[(d)]	B1	2	41.7	0.5	1.1805	0.0002	2.4494	0.0006	18.458	0.012
	B2	2	{51.7}	{0.5}	{1.1770}	{0.0002}	{2.4479}	{0.0006}	{18.392}	{0.012}
2500		2	25.9	0.5	1.1768	0.0002	2.4472	0.0006	18.397	0.012
3000		2	18.9*	0.8	1.1763	0.0002	2.4448	0.0006	18.353	0.012
3200		2	16.1	0.5	1.1813	0.0017	2.4518	0.0010	18.464	0.040
3600		2	14.2	0.5	1.1826	0.0017	2.4533	0.0010	18.481	0.040
3800		2	15.9	0.5	1.1748	0.0017	2.4467	0.0010	18.359	0.040
3899		2	14.2	0.5	1.1819	0.0017	2.4524	0.0010	18.470	0.040
Station 31 (26.03°N, 44.55°W; 21/01/2018; proximal E)										
50		2	19.9	0.5	1.1740	0.0002	2.4482	0.0006	18.357	0.012
90		2	23.3	0.5	1.1671	0.0002	2.4413	0.0006	18.233	0.012
350		2	19.2	0.5	1.1772	0.0002	2.4481	0.0006	18.407	0.012
650		2	32.5	0.5	1.1801	0.0002	2.4472	0.0006	18.459	0.012
790		2	47.6	0.5	1.1830	0.0002	2.4476	0.0006	18.499	0.012
1500		2	44.0	0.5	1.1804	0.0002	2.4486	0.0006	18.445	0.012
2000		2	34.3	0.5	1.1798	0.0002	2.4498	0.0006	18.447	0.012
2600		2	24.2	0.5	1.1784	0.0017	2.4485	0.0010	18.391	0.040
3000		2	20.9	0.9	1.1801	0.0002	2.4507	0.0006	18.440	0.012
3350		2	18.1	0.7	1.1802	0.0002	2.4511	0.0006	18.445	0.012
3700		2	17.7	0.5	1.1790	0.0017	2.4500	0.0010	18.415	0.040
3872		2	17.3	0.6	1.1802	0.0017	2.4505	0.0010	18.434	0.040
Station 35 (26.14°N, 44.83°W; 25/01/2018; vent site)										
1500		2	45.7	0.5	1.1784	0.0002	2.4473	0.0006	18.415	0.012
3100		4	19.0	1.1	1.1781	0.0002	2.4493	0.0006	18.409	0.012
3236[(d)]	B1	2	6.1	0.5						
	B2	2	{22.2}	{0.5}						
	B1+B2				{1.1601}	{0.0017}	{2.4349}	{0.0010}	{18.110}	{0.040}
3322		4	5.5	0.5	1.1764	0.0017	2.4464	0.0010	18.367	0.040
3350		2	8.9	0.5	1.1763	0.0017	2.4466	0.0010	18.360	0.040
3429		2	10.6	0.5	1.1787	0.0017	2.4484	0.0010	18.405	0.040
3550		2	15.6	0.6	1.1800	0.0017	2.4509	0.0010	18.437	0.040
Station 39 (26.14°N, 44.83°W; 26/01/2018; vent site)										
20		2	25.6	0.5	1.1664	0.0002	2.4398	0.0006	18.215	0.012
400		2	20.3	0.6	1.1731	0.0002	2.4438	0.0006	18.343	0.012
800		2	48.1	0.5	1.1799	0.0002	2.4461	0.0006	18.460	0.012
950		2	47.2	0.8	1.1824	0.0002	2.4479	0.0006	18.491	0.012
1750		2	38.7	0.5	1.1806	0.0002	2.4490	0.0006	18.443	0.012

Table 3.4 (cont'd).

Depth (m)	n-ID[(a)]	[Pb][(b)] (pmol/kg)	1sd	$^{206}Pb/^{207}Pb$	2sd[(c)]	$^{208}Pb/^{207}Pb$	2sd[(c)]	$^{206}Pb/^{204}Pb$	2sd[(c)]
Station 37 (26.13°N, 44.77°W; 27/01/18; valley wall)									
90	2	20.2	0.6	1.1713	0.0002	2.4455	0.0006	18.302	0.012
110	2	23.4	0.6	1.1675	0.0002	2.4409	0.0006	18.236	0.012
160	2	17.1	0.9	1.1770	0.0002	2.4496	0.0006	18.412	0.012
200	2	20.5	0.5	1.1720	0.0002	2.4442	0.0006	18.320	0.012
600	2	29.2	0.5	1.1805	0.0002	2.4477	0.0006	18.463	0.012
1000	2	46.1	0.5	1.1833	0.0002	2.4486	0.0006	18.501	0.012
1500	2	44.6	0.5	1.1812	0.0002	2.4499	0.0006	18.468	0.012
1700	2	38.7	0.5	1.1811	0.0002	2.4498	0.0006	18.454	0.012
2100	2	31.3	0.5	1.1795	0.0002	2.4488	0.0006	18.432	0.012
2200	2	27.9	0.5	1.1798	0.0002	2.4495	0.0006	18.437	0.012
2300	2	25.3	0.5	1.1799	0.0002	2.4497	0.0006	18.442	0.012
2506	2	24.6	0.9	1.1804	0.0002	2.4498	0.0006	18.442	0.012

(a) Number of individual sample aliquots analysed for Pb concentration.
(b) Reported Pb concentrations are calculated from the average of all valid measurements for each sample.
(c) 2sd precision assigned based on the data obtained for replicate analyses of the in-house seawater reference material with a comparable Pb concentration in the unspiked MC-ICP-MS run solution as the seawater sample.
(d) Samples with significant discrepancies in measured Pb concentrations for the two 1 L sample bottles. The measured Pb concentrations for bottle 1 (B1) and bottle 2 (B2) are reported separately. For the sample from 1700 m depth at station 29, the isotope compositions of the two sample bottles were measured and reported separately. Curly brackets indicate Pb concentration and isotope data that were potentially affected by contamination.

* Denote a sample with one of the replicate values being removed from the calculation of the average Pb concentrations, due to significantly higher values (> 4 pmol/kg) from the other replicate values (i.e. potential contamination).

3.4.2 Anomalous Samples

Two seawater samples showed significant (> 10 pmol/kg) discrepancies in the Pb concentrations that were determined for each of the two 1 L bottles of each sample. These are (i) the sample from 3236 m depth at vent site station 35 with unusually low $^{206}Pb/^{207}Pb$ (1.160) and $^{208}Pb/^{207}Pb$ (2.435) ratios, and (ii) the sample from 1700 m depth at distal W station 29 (Table 3.4; Fig. 3.3). For both samples, the higher measured Pb concentrations were anomalous compared to results obtained for samples from adjacent depths. For the latter sample, the $^{206}Pb/^{207}Pb$ (1.177) and $^{208}Pb/^{207}Pb$ (2.448) ratios determined for the bottle with the higher Pb concentration (Bottle 2) are markedly lower than the values that were obtained for the other bottle (Bottle 1) and samples from the same depth range (1700-1750 m) collected at neighbouring stations (≈ 1.181; ≈ 2.449). The above observations suggest that a non-indigenous dissolved Pb component with low $^{206}Pb/^{207}Pb$ and $^{208}Pb/^{207}Pb$ ratios was present in the sample bottles that exhibit anomalously high Pb concentrations. This component is most likely of anthropogenic origin, with a Pb signature similar to European and North African aerosols, which was added to the samples during sample collection or handling. Alternatively, the anthropogenic Pb may have been remobilised

from aerosol particles that were present in the seawater samples and which released Pb during the prolonged filtration process, in accord with the findings of a previous study (Chen et al., 2016a).

Based on the above conclusions, for the sample from 1700 m depth at station 29, only the results determined for the bottle with the lower Pb concentration (Bottle 1, Table 3.4) are considered. For the sample from 3236 m depth at station 35, only the Pb concentration that was obtained for the bottle with the lower Pb concentration (Bottle 1, Table 3.4) is used. While the extremely low $^{206}Pb/^{207}Pb$ and $^{208}Pb/^{207}Pb$ ratios determined for the latter sample are in accord with the isotope trends defined by other samples from similar depths at this station, they are disregarded in the following as they may also be an analytical artefact.

3.4.3 Distributions of Dissolved δ^3He, Mn and Fe

The vertical distributions of dissolved helium isotopes and Mn and Fe concentrations at NADW depths of ≥ 1500 m for the stations considered in this study are displayed in Figure 3.5. The He isotope compositions are expressed in the δ^3He notation, which denotes the relative deviation of the $^3He/^4He$ ratio of a sample from the atmospheric ratio (1.384×10^{-6}) in parts per 100 (Jenkins et al., 2015a):

$$\delta\ ^3\mathrm{He} = \left(\frac{^3\mathrm{He}/\ ^4\mathrm{He}_{\mathrm{sample}}}{^3\mathrm{He}/\ ^4\mathrm{He}_{\mathrm{atmosphere}}} - 1 \right) \times 100\% \qquad (3.1)$$

Slightly elevated δ^3He values of 6-9% are detected in the upper portion of NADW (1500-2500 m) across stations 29 and 35/39. In the lower portion of NADW (> 3000 m), the δ^3He values in the vicinity of the vent site are relatively low (3-5%; stations 29 and 31), while a pronounced excursion towards elevated δ^3He is evident directly above the vent site (station 35/39) at between 3150 m and 3500 m depths, with a maximum δ^3He of 43% at 3249 m.

For both Mn and Fe, dissolved concentrations are generally low (Mn < 0.2 nmol/kg; Fe < 0.7 nmol/kg) at depths ≥ 1500 m but with notable excursions. At vent site station 35/39, strong (~100-fold) enrichments in dissolved Mn and Fe are identified between 3000 and 3600 m depths, with maxima of 67 nmol/kg for Mn (3334 m) and 90 nmol/kg for Fe (3236 m) respectively, which coincide broadly with the δ^3He maxima. At the other sampled stations in the vicinity of the vent field, small excursions in dissolved Mn (0.3 nmol/kg) are identified between depths of 2000 and 3000 m. At the two stations to the east of the vent site, small Mn and Fe enrichments at 2100-2400 m depths coincide with each other. At distal W station 29, there are markedly high Fe concentrations (up to 2.6 nmol/kg) between depths of 2000 and 3400 m that are coupled with much more subtle Mn enrichments (0.3 nmol/kg).

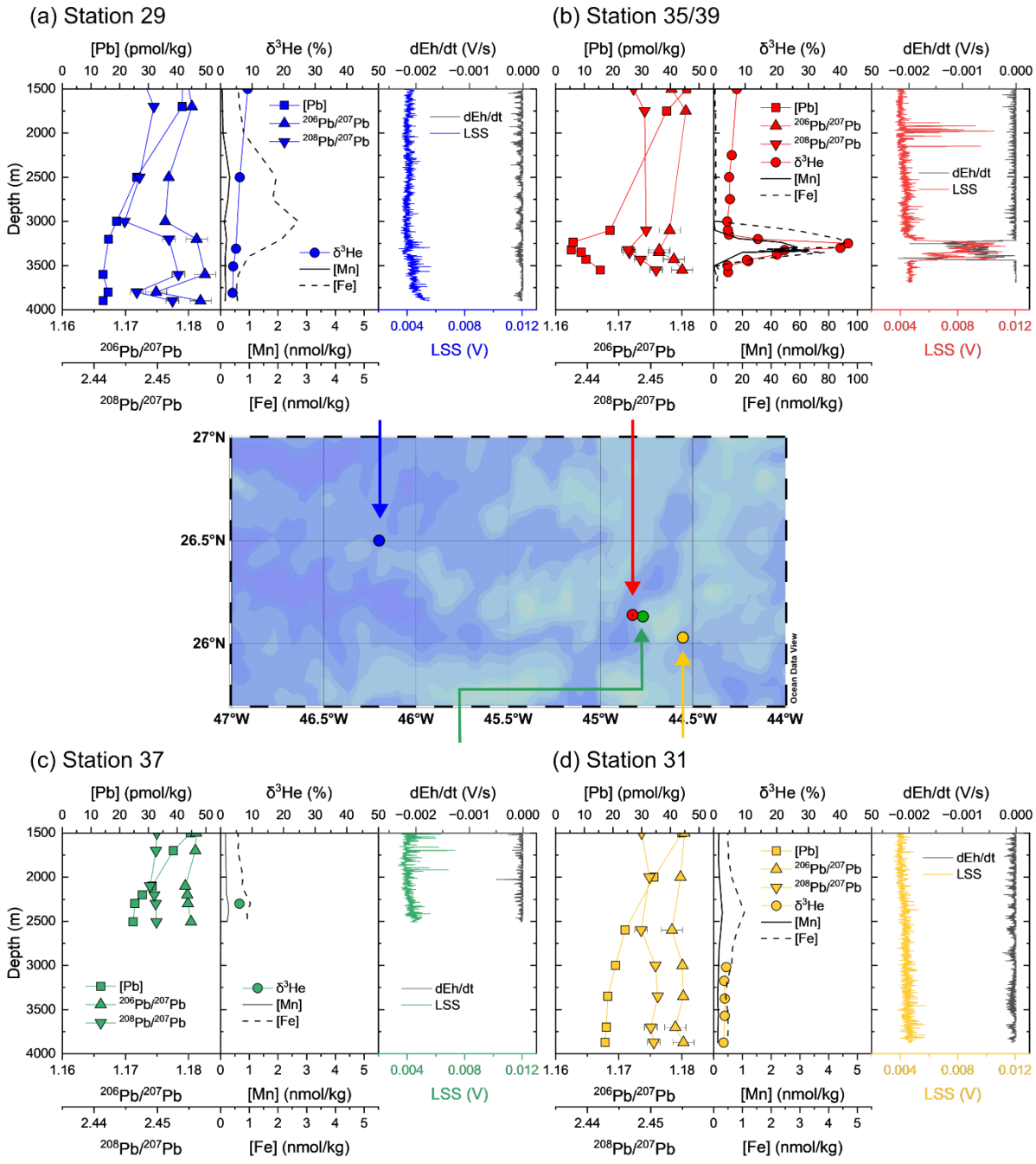


Figure 3.5. Vertical profiles of dissolved element concentrations and isotope compositions as well as sensor data for samples collected from depths > 1500 m at the four GA13 stations in the TAG hydrothermal area: (a) distal W station 29, (b) vent site station 35/39, (c) valley wall station 37 and (d) proximal E station 31. For each station: the left panel shows the dissolved Pb concentrations (squares), $^{206}Pb/^{207}Pb$ (upright triangles) and $^{208}Pb/^{207}Pb$ ratios (inverted triangles); the middle panel shows the dissolved δ^3He values (circles) and Mn (black solid lines) and Fe concentrations (black dashed lines); the right panel shows the Eh values (electrode potential, black lines) and LSS (light scattering sensor, coloured lines) anomalies. The map of the TAG hydrothermal area in the centre of the figure shows the station locations. Note the different scales for Mn and Fe concentrations in panel (b) compared to the other stations.

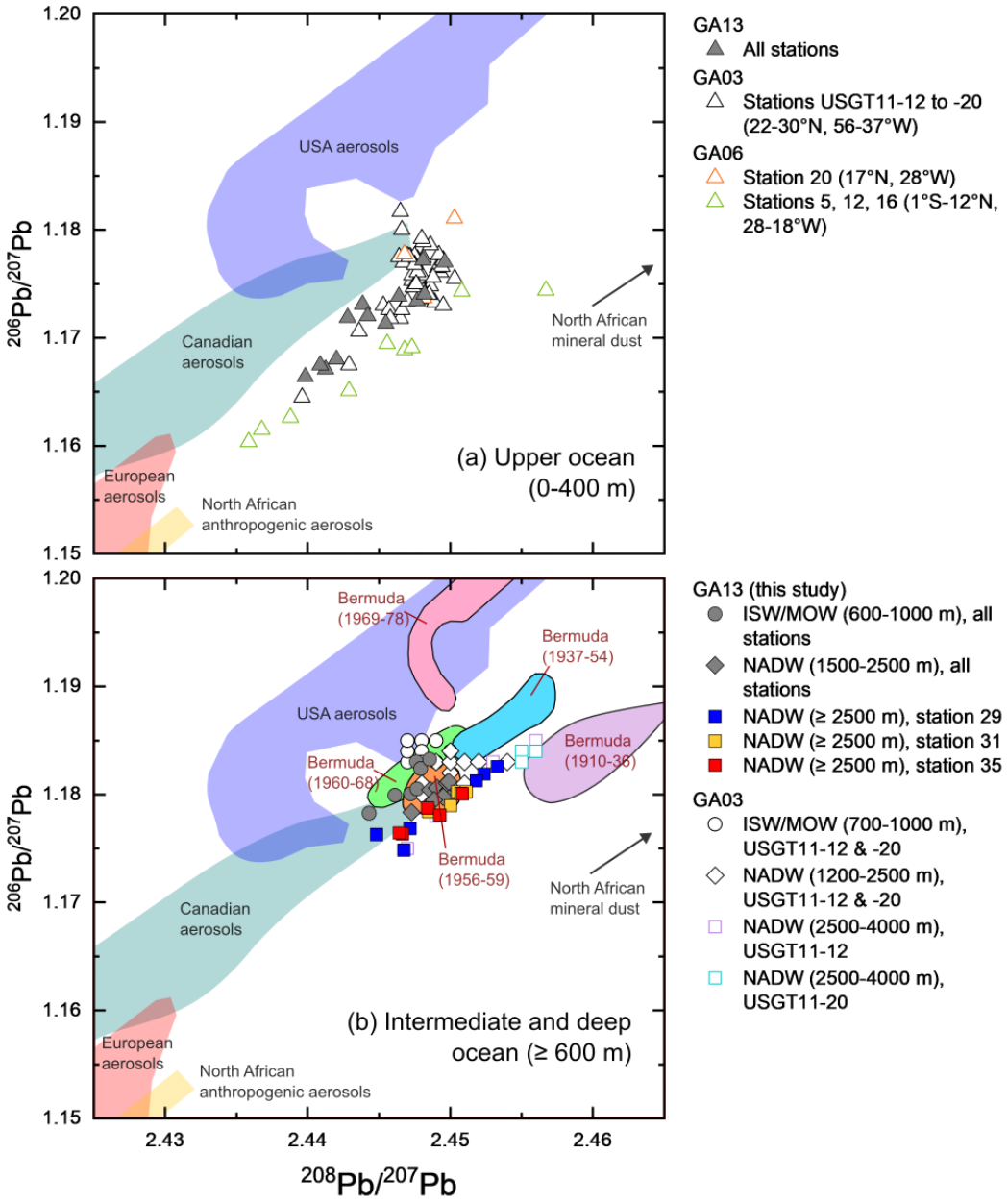


Figure 3.6. Plots of $^{206}Pb/^{207}Pb$ versus $^{208}Pb/^{207}Pb$ ratios for GA13 seawater samples (a) from depths ≤ 400 m and (b) from depths ≥ 600 m (solid symbols), in comparison to relevant literature results (open symbols) for seawater, potential sources of atmospheric aerosols for the study area (coloured fields without borders, enclosing mean ± 2 SD), and archive data of historic surface seawater compositions (coloured fields with borders, enclosing mean ± 2 SD). The seawater samples are classified according to depth ranges and distinguished by symbol shapes: upper ocean (≤ 400 m, triangles), intermediate depth ISW/MOW (600-1000 m, circles), shallower NADW (1200-2500 m, diamonds) and deeper NADW (2500-4000 m, squares). Previously published seawater data for the GA03 section in the subtropical North Atlantic (Noble et al., 2015): full-depth data from stations USGT11-12 and USGT11-20 and additional data for the upper water column for stations between USGT11-12 and USGT11-20. Seawater data for the GA06 section in the tropical Eastern Atlantic (Bridgestock et al., 2016, 2018): upper water column samples from station 20 (17°N) and stations 5, 12 and 16 at lower latitudes (1°S-12°N). Aerosol data: urban aerosol digests from Southwest Europe and North Africa (Bollhöfer and Rosman, 2001), the USA (Bollhöfer and Rosman, 2001; Sherman et al., 2015) and Canada (Bollhöfer and Rosman, 2001; Simonetti et al., 2003). Historic surface seawater compositions were reconstructed by Kelly et al. (2009) from coral data for the Bermuda Atlantic Time Series Station in the Northwest Atlantic for various 20th century periods; each field is labelled with 'Bermuda' and the relevant age range.

3.5 Discussion

In the following, the Pb concentration and isotope results for samples from the TAG area are discussed in the context of published data for the subtropical North Atlantic Ocean from the GEOTRACES sections GA03 (Noble et al., 2015) and GA06 (Bridgestock et al., 2016, 2018). In particular, station USGT11-16 from the GA03 section is a crossover station at the TAG vent site and thus enables a direct comparison with the results of the current study. The data of the current study are also compared in detail to results obtained for the North Atlantic stations USGT11-12 (57°W, 30°N) and USGT11-20 (36°W, 22°N) from the GA03 section, which are located at about 1000 km west and east of the TAG vent site, respectively. The results obtained for seawater samples that are clearly not impacted by the TAG hydrothermal plume are discussed first. This is followed by a detailed discussion of the variations in dissolved Pb concentrations and isotope compositions for seawater from depths ≥ 2500 m, which appear to be largely linked to the presence of the TAG plume.

3.5.1 Variabilities of Pb Concentrations and Isotope Compositions in the Upper Water Column

The dissolved Pb isotope compositions in the mixed surface layer of the subtropical North Atlantic Ocean reflect the impacts of atmospheric deposition and redistribution of dissolved seawater Pb by wind-driven surface currents, within the Pb residence time in oligotrophic surface waters of < 2 years (Schaule and Patterson, 1981; Flegal and Patterson, 1983; Boyle et al., 1986; Véron et al., 1994; Hamelin et al., 1997). Across the stations in the present study, significant variabilities for both the dissolved Pb concentrations (17-26 pmol/kg) and isotope ratios ($^{206}Pb/^{207}Pb$ = 1.168-1.174, $^{208}Pb/^{207}Pb$ = 2.441-2.450) are observed in the uppermost 400 m depths, which encompass the surface mixed layer and upper NACW. These data for the samples of the present study, which were collected in 2018, thereby agree well with the Pb concentrations (17-30 pmol/kg) and isotope compositions ($^{206}Pb/^{207}Pb$ = 1.168-1.179, $^{208}Pb/^{207}Pb$ = 2.443-2.450) that were determined for samples from the same depth range in the subtropical North Atlantic during the GA03 section cruise in 2011 (Fig. 3.3; 3.6a) (Noble et al., 2015). This suggests relatively stable Pb sources and input fluxes for this ocean region over the last decade.

On a $^{206}Pb/^{207}Pb$ versus $^{208}Pb/^{207}Pb$ plot, the samples from ≤ 400 m depth of this study define a linear correlation (Fig. 3.6a). Notably, low $^{206}Pb/^{207}Pb$ and $^{208}Pb/^{207}Pb$ ratios are also correlated with high Pb concentrations, such that the data also define linear correlations in plots of $^{206}Pb/^{207}Pb$ (r^2 = 0.77) and $^{208}Pb/^{207}Pb$ (r^2 = 0.85) versus 1/[Pb] (Fig. 3.7). These correlations suggest that the dissolved Pb budget in the upper water of the TAG area is largely controlled by two-component mixing. The mixing endmembers are most likely anthropogenic Pb with low $^{206}Pb/^{207}Pb$ and $^{208}Pb/^{207}Pb$ ratios, as determined for European and North African aerosols, and natural Pb with higher $^{206}Pb/^{207}Pb$ and $^{208}Pb/^{207}Pb$ ratios, as found in mineral dust from the Sahara Desert (Fig. 3.6a). This conclusion is in accord with air mass

back trajectories (Fig. A3 in the Appendix) (Draxler and Rolph, 2003), which show that the TAG area is affected by prevailing northeasterly trade winds that transport aerosols from Europe and North Africa. Furthermore, a detailed Pb source apportionment was previously carried out for surface waters of the tropical Eastern Atlantic Ocean (GEOTRACES GA06 section, Fig. 3.1a; Bridgestock et al. (2016)) and this revealed Pb fluxes that were dominated by anthropogenic aerosols and mineral dust delivered from North Africa via the northeasterly trades. In the $^{206}Pb/^{207}Pb$ versus $^{208}Pb/^{207}Pb$ plot, the trend defined by the seawater samples from ≤ 400 m depth of this study largely overlaps with the results obtained for samples from the northernmost GA06 station (station 20, 17°N) but is shifted to higher $^{206}Pb/^{207}Pb$ ratios in comparison to the trend defined by GA06 samples from more tropical latitudes (≤ 12°N) (Fig. 3.6a). These parallel trends suggest that similar sources largely dominate the Pb inputs into the tropical Eastern Atlantic Ocean and the TAG area. Surface and near-surface seawater from more northern latitudes, including the samples of the current study (from 26°N), the GA03 stations at 22-30°N and GA06 station 20 (at 17°N), are thereby shifted towards higher $^{206}Pb/^{207}Pb$ ratios. This signature most likely reflects a larger impact of anthropogenic aerosols originating from North America and/or Europe on the subtropical surface ocean, as both sources typically have higher $^{206}Pb/^{207}Pb$ ratios than North African anthropogenic Pb.

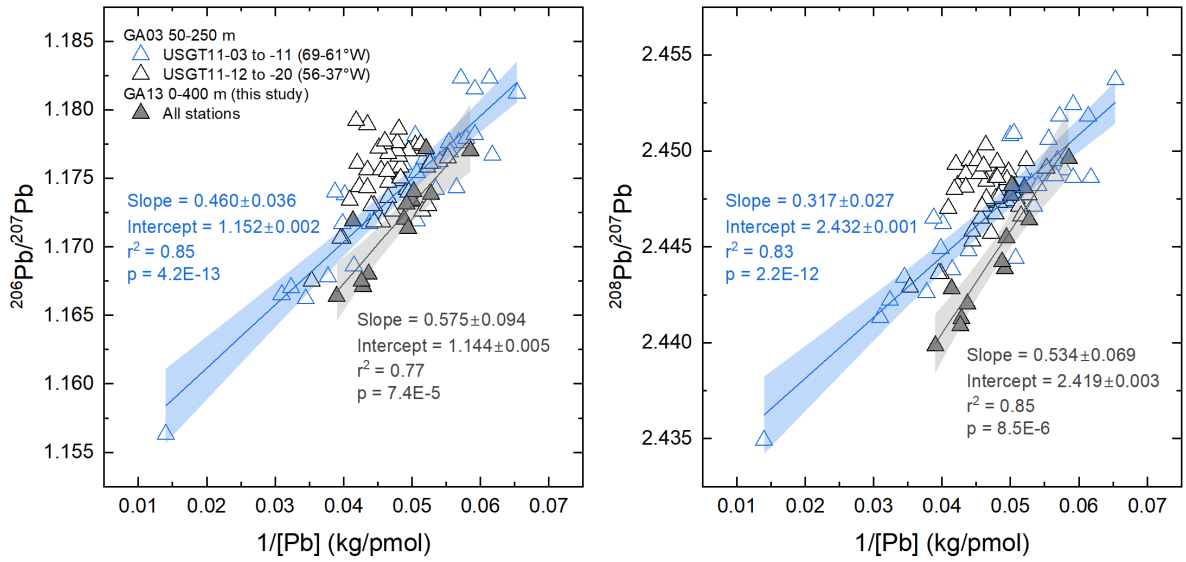


Figure 3.7. Plots of $^{206}Pb/^{207}Pb$ and $^{208}Pb/^{207}Pb$ versus the inverse of [Pb] for seawater samples collected at depths ≤ 400 m from the GA13 stations in the TAG hydrothermal area (solid triangles) and the GA03 stations across the subtropical North Atlantic Ocean (open triangles) from Noble et al. (2015). The GA03 data for more western stations (blue open triangles, 69-61°W) are distinguished from results obtained for stations in the central and eastern parts of the subtropical North Atlantic (black open triangles, 56-37°W). Simple linear regression lines with associated 95% confidence intervals (shades) are fitted to the GA13 samples of this study and the GA03 samples from western stations.

The variable Pb concentrations and isotopes observed in seawater from ≤ 400 m depth in this study corroborate previous observations in the subtropical North Atlantic Ocean by Noble et al. (2015) and Bridgestock et al. (2018). In detail, the latter investigations both observed significant variations in Pb concentrations and isotope compositions in the uppermost water column down to depths of 150 to 200 m, whereby higher Pb levels were correlated with lower $^{206}Pb/^{207}Pb$ and $^{208}Pb/^{207}Pb$ ratios. Compared to these previous studies in the ocean region, the current GA13 data reveals significant vertical variabilities in Pb signatures that extend to depths of up to 400 m, and which hence clearly extend from the mixed layer into NACW (Fig. 3.3; 3.4). In addition, the current results also document significant lateral variability in Pb signatures for closely spaced stations, which are separated by distances of only 6-170 km. Together, these observations reveal that heterogeneous Pb isotope signatures are widespread in the upper water column of the subtropical North Atlantic Ocean, and that the observed heterogeneities persist on vertical and lateral scales of less than 20 m and less than a few kilometres, respectively.

The data of Noble et al. (2015) demonstrate, for their GA03 seawater samples collected at depths ≤ 200 m to the west of station USGT11-12 (from 69°W to 61°W), statistically significant ($p << 0.05$), strong linear correlations of $^{206}Pb/^{207}Pb$ ($r^2 = 0.85$) and $^{208}Pb/^{207}Pb$ ($r^2 = 0.83$) with 1/[Pb] (blue open triangles and lines, Fig. 3.7). Notably, such correlations were not observed for shallow seawater samples that were collected in the Central North Atlantic Ocean (encompassing the TAG area) during the GA03 cruise (black open triangles, Fig. 3.7a, b). It is of interest in this context, that the results of the current study for seawater from ≤ 400 m depth yield strong linear correlations of $^{206}Pb/^{207}Pb$ ($r^2 = 0.77$) and $^{208}Pb/^{207}Pb$ ($r^2 = 0.85$) with 1/[Pb] (solid triangles and black lines, Fig. 3.7) that are both statistically significant ($p << 0.05$), which are also sub-parallel to the trends defined by the upper ocean samples from 69°W to 61°W of the GA03 section. Both Noble et al. (2015) and Bridgestock et al. (2018) attributed the observed upper ocean variabilities in Pb signatures to the advection of and mixing with the Subtropical Underwater (STUW). This conclusion was based on the observation that many samples with high Pb concentrations and low $^{206}Pb/^{207}Pb$ and $^{208}Pb/^{207}Pb$ ratios also had higher salinities, as salinities exceeding 37 are a characteristic of STUW (O'Connor et al., 2005). In the current study, however, the elevated Pb concentrations and lower $^{206}Pb/^{207}Pb$ and $^{208}Pb/^{207}Pb$ ratios were observed as deep as 400 m within NACW and for water samples with lower salinities (36.2-36.9) that are not indicative for the presence of STUW (Fig. 3.2c; 3.4). This suggests that the variable Pb signatures in the upper water column may have a different origin, and this may be the release of dissolved Pb from the sinking anthropogenic aerosols of European and/or North African origin. Notably, such a mechanism was previously shown to contribute to elevated levels of dissolved [Pb] in the deep North Pacific Ocean (Wu et al., 2010).

3.5.2 Intermediate and Deep Waters

Dissolved Pb concentrations increase sharply, from an average of 21 pmol/kg in the upper water column at less than 400 m depth, to peak levels of 46-48 pmol/kg at intermediate depths between 800

and 1000 m, where ISW and MOW dominate (Fig. 3.3). This increase in [Pb] is accompanied by an increase in $^{206}Pb/^{207}Pb$, from 1.172-1.177 at 400 m depth to ratios up to 1.183 at depths of 800-1000 m within the [Pb] peak. In contrast, the $^{208}Pb/^{207}Pb$ ratios of about 2.448 within the [Pb] peak are similar to the highest values observed within the upper water column (2.445 ± 0.003). The results of this study are thereby similar to the $^{206}Pb/^{207}Pb$ (1.183-1.185) and $^{208}Pb/^{207}Pb$ (2.447-2.450) ratios that were previously determined for GA03 samples from similar depths in the subtropical North Atlantic Ocean (Noble et al., 2015) (Fig. 3.3; 3.6b).

Irminger Sea Water is formed by the subduction of surface waters in the subpolar Irminger and Labrador Seas and is the dominant intermediate water mass in the TAG area (Jenkins et al., 2015b). Hence, the close match in Pb isotope compositions between the intermediate depth samples from the current study (collected in 2018) and surface waters from the Western North Atlantic in the 1960s, suggests ventilation ages of 50-60 years for the former, when the Pb input to the North Atlantic was still approaching its maximum in the 1970s (Fig. 3.6b) (Kelly et al., 2009; Boyle et al., 2014). This ventilation age estimate agrees with that of Bridgestock et al. (2018) for intermediate depth waters from the subtropical Eastern North Atlantic but is slightly older than the ventilation ages of about 40 years (the 1970s) that were determined for intermediate depth waters of the Western and Central North Atlantic using SF_6 (Noble et al., 2015) and tritium-^{3}He (Jenkins et al., 2015a). The presence of a small fraction of MOW, characterised by high historic inputs of anthropogenic Pb (Laumond et al., 1984; Copin-Montegut et al., 1986; Lambert et al., 1991) with a slightly lower $^{206}Pb/^{207}Pb$ ratio of about 1.179 (Noble et al., 2015) will, however, add some uncertainty to the Pb isotope -based ventilation ages.

Below 1200 m depth, NADW is the dominant water mass and this originates from sinking surface waters at subpolar latitudes. Notably, samples at 1500 m depth retain high Pb concentrations (> 44 pmol/kg), most likely due to diapycnal mixing with the overlying intermediate depth ISW/MOW (Fig. 3.3; 3.4). Below 1500 m depth, the declining Pb concentrations reflect the presence of older water masses that were ventilated well before the maximum Pb inputs in the mid-20th century and the loss of dissolved Pb to particle scavenging (Noble et al., 2015). The [Pb] trends that were observed for the NADW layer in the current study agree well with that observed in the Western North Atlantic at station USGT11-12 of the GA03 section (Fig. 3.3). The notable exceptions are the water samples from between 3100 and 3544 m depths at vent site station 35/39, which are discussed below.

The $^{206}Pb/^{207}Pb$ (1.175-1.183) and $^{208}Pb/^{207}Pb$ (2.446-2.453) ratios of the GA13 samples from ≥ 1750 m depth are markedly lower than the results obtained for the Eastern North Atlantic station USGT11-20 ($^{206}Pb/^{207}Pb$ = 1.183-1.184, $^{208}Pb/^{207}Pb$ = 2.452-2.456) within depths of 1750-4000 m, and are closer to the results for the Western North Atlantic station USGT11-12 (1.180-1.183, 2.450-2.453) within the same depth range (Fig. 3.3; 3.6b). This reflects the westward decrease in deep water ventilation ages across the subtropical Atlantic Ocean (Jenkins et al., 2015b; Noble et al., 2015). In detail, the Pb isotope data for the NADW samples from 1500-2500 m depths in the current study are

thereby akin to North Atlantic surface waters from the late 1950s (Kelly et al., 2009), in accord with a ventilation age of about 60 years (Fig. 3.6b). This estimate is significantly younger than the minimum ventilation ages of 80-100 years (pre-1930) that were estimated for NADW in the Eastern North Atlantic Ocean based on Pb isotope signatures (Noble et al., 2015; Bridgestock et al., 2018). Notably, the unusually low $^{206}Pb/^{207}Pb$ (1.175-1.177) and $^{208}Pb/^{207}Pb$ (2.446-2.448) ratios that were observed for some samples from ≥ 2500 m depths at stations 29 and 35/39 fall outside the range of compositions observed for NADW samples from GA03 stations and historic North Atlantic surface waters from the 20th century. These unusual variations are also discussed below.

3.5.3 Identification of the TAG Hydrothermal Plume

3.5.3.1 Tracers of hydrothermal plumes

Dissolved δ^3He is a key tracer of hydrothermal plumes. Helium rich in primordial ^3He is emitted from hydrothermal vents, which is then diluted conservatively in the spreading hydrothermal plume (Clarke et al., 1969; Jenkins et al., 1978). In the western and central parts of the subtropical North Atlantic Ocean, waters at depths between 700 and 3000 m are characterised by higher ambient δ^3He values (5-8%) than waters from > 3000 m depth (< 5%) (Jenkins et al., 2015a). The high ambient δ^3He values of the shallower waters reflect the dominance of tritium-rich water masses (MOW, ULSW and CLSW), which have excess ^3He from radioactive decay of ^3H (Jenkins et al., 2015a). The extent of the TAG plume can hence be defined by the detection of δ^3He values that exceed the ambient signatures, which implies δ^3He > 8% for ISW/MOW and NADW from depths of 700-3000 m, and δ^3He > 5% for NADW from > 3000 m depth.

Recent work in the study area (Tagliabue et al., 2022b; Lough et al., 2023) and in the South Atlantic Ocean (Saito et al., 2013) demonstrated the presence of plumes enriched in dissolved Mn and Fe at distances of up to 250-1100 km from the Mid-Atlantic Ridge. These plumes were interpreted to be of hydrothermal origin even though the implicated off-axis regions showed background levels of ^3He. Enrichments in dissolved Mn and Fe above NADW background concentrations, of ~0.2 nmol/kg for Mn and ~0.7 nmol/kg for Fe in the central subtropical North Atlantic (Hatta et al., 2015), are therefore also employed in the following for detection of the TAG plume. In addition, hydrothermal plumes can be identified by their negative Eh anomalies, which indicate reducing conditions, as well as positive light scattering anomalies that reflect elevated particle concentrations.

3.5.3.2 Locations of the TAG hydrothermal plume

The strongest plume signals were detected above vent site station 35/39, where high δ^3He values of 10 to 43% between depths of 3150 m and 3500 m delineate the buoyant TAG hydrothermal plume (Fig. 3.5b). This coincides with the ~100-fold enrichments in dissolved [Mn] (1-67 nmol/kg) and [Fe] (1-90 nmol/kg) between depths of 3000 m and 3600 m. The ^3He enrichments also coincide with negative Eh anomalies and elevated particle concentrations at the same depths. At shallower depths of < 3000 m,

dissolved δ^3He at this station (< 7%) was within the background range of NADW, even though a particle-rich horizon was detected between depths of 1800 m and 2200 m.

Across the three sampled stations in the vicinity of the vent site, δ^3He values throughout the NADW layer were at ambient levels (Fig. 3.5a, c, d). However, small deep ocean enrichments in dissolved Mn and Fe above the background concentrations were detected at these stations, which indicate the lateral spreading of the neutrally buoyant TAG plume. At the two stations to the east of the vent site, ~1.5-fold enrichments in dissolved [Mn] (0.3 nmol/kg) and [Fe] (1 nmol/kg) were observed between depths of 2000 m and 3000 m (proximal E station 31) and below 2000 m (valley wall station 37), which indicate very dilute plume solutions (Fig. 3.5c, d). At distal W station 29, the more pronounced enrichment in dissolved Fe (2.6 nmol/kg, ~5-fold above the background level) is attributed to preferential spreading of the neutrally buoyant TAG plume towards the western basin (Fig. 3.5a) (Tagliabue et al., 2022b). Furthermore, at valley wall station 37, a particle-rich zone was detected between 1500 m and 1900 m depths, which broadly matches with the depth of the shallow particle-rich zone above the vent site (Fig. 3.5b, c).

3.5.4 Hydrothermal Scavenging of Pb in the TAG Plume

3.5.4.1 Buoyant TAG plume

At vent site station 35/39, water samples within the buoyant TAG plume exhibit lower dissolved Pb concentrations (5.5-10.6 pmol/kg) compared to the seawater collected above and below the plume (16-19 pmol/kg) (Fig. 3.5b; 3.8a). The minimum in dissolved [Pb] (5.5 pmol/kg, 3322 m) was observed at broadly the same depth as the maxima in δ^3He (at 3249 m) and dissolved [Mn] (at 3334 m). As a consequence, dissolved [Pb] in the buoyant plume exhibits a statistically significant ($p < 0.05$), well-defined negative correlation with the plume-enriched dissolved [Mn] ($r^2 = 0.80$, Fig. 3.9a). These findings agree well with previous observations at station USGT11-16 from the GA03 section, which also showed deficits in dissolved [Pb] for samples collected in the buoyant hydrothermal plume (7.1 ± 0.8 pmol/kg) compared to samples from above and below the plume (12.1 and 14.1 pmol/kg) (Noble et al., 2015) (Fig. 3.8b).

Together, these observations reinforce the conclusion that despite significant enrichments of dissolved Pb in the TAG vent fluids, intense particle scavenging in the hydrothermal plume generates a net deficit in the dissolved Pb budget (Godfrey et al., 1994; Noble et al., 2015). As such, the buoyant hydrothermal plume at the TAG vent site is a net sink for dissolved marine Pb. Net removal of dissolved Pb in the buoyant hydrothermal plume was also observed at the southern East Pacific Rise (~15°S) for samples from the GEOTRACES section GP16 (Boyle et al., 2020). The similar dissolved [Pb] distributions found in the buoyant plumes of both the fast-spreading East Pacific Rise and the slow-spreading Mid-Atlantic Ridge suggest that the net removal of dissolved Pb is a common phenomenon at mid-ocean ridge hydrothermal systems.

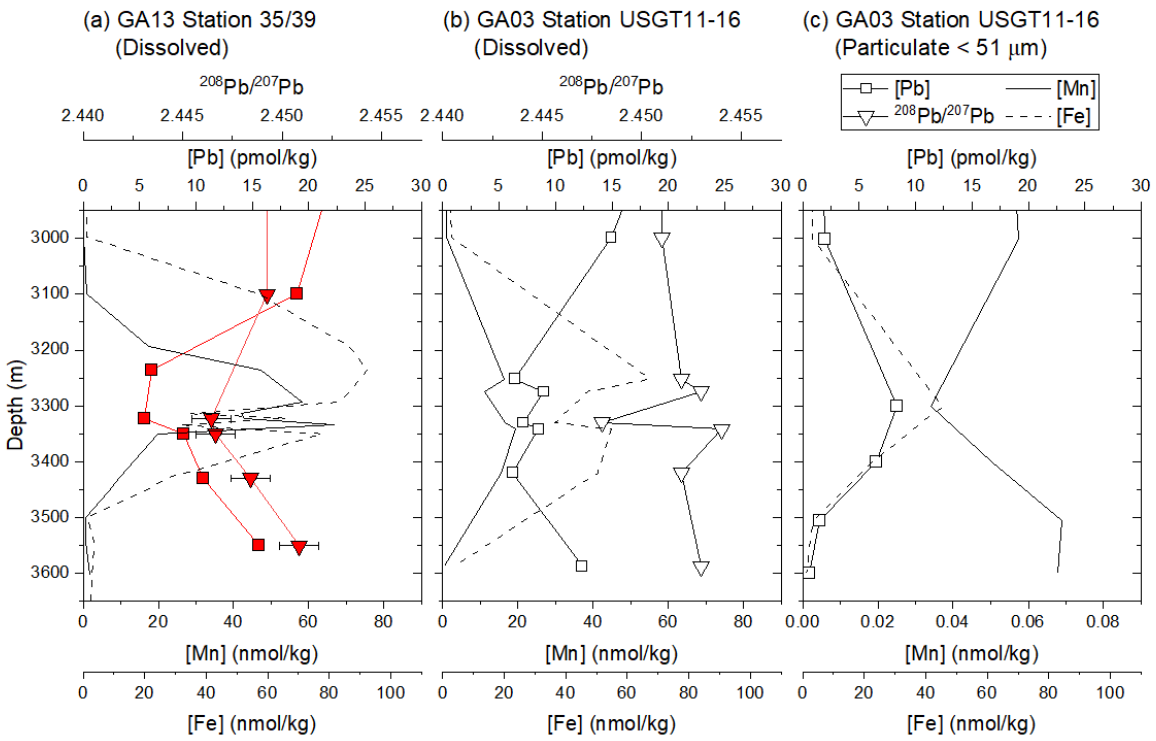


Figure 3.8. Vertical profiles of dissolved and particulate Pb, Mn and Fe concentrations and $^{208}Pb/^{207}Pb$ ratios in the buoyant TAG plume for samples from the GA13 and GA03 section cruises. (a) Data for the dissolved phase at vent site station 35/39 of the GA13 section (filled symbols, this study). Data for the (b) dissolved and (c) small particulate (< 51 μm) phases for samples from the crossover station USGT11-16 of the GA03 section (open symbols, Noble et al., 2015). Symbols: Pb concentrations – lines with squares; $^{208}Pb/^{207}Pb$ ratios – lines with inverted triangles; Mn concentrations – solid lines; Fe concentrations – dashed lines.

Observations from both the vent site station 35/39 of this study and the crossover station USGT11-16 of the GA03 section support the conclusion that enhanced particle scavenging is responsible for the net loss of Pb in the buoyant TAG plume. At station 35/39 of this study, excess suspended particulate concentrations were detected throughout the buoyant plume (Fig. 3.5b), whilst results for station USGT11-16 revealed excess particulate Pb concentrations within the plume that coincided with the deficits in dissolved [Pb] and enrichments in particulate [Fe] (Fig. 3.8b, c). The compositions of suspended particles collected in the buoyant TAG plume during the GA03 expedition showed 10-15-fold and 4-fold enrichments in Fe oxyhydroxides and opal, respectively, compared to NADW background concentrations, whilst Mn oxide levels were slightly depleted (Lam et al., 2015). These observations indicate that Fe oxyhydroxide particles were primarily responsible for the enhanced scavenging of Pb within the buoyant TAG plume. This finding is in accord with the strong affinity of Pb to Fe oxyhydroxide phases, based on leaching studies of hydrogenous Fe-Mn crusts (Koschinsky and Hein, 2003).

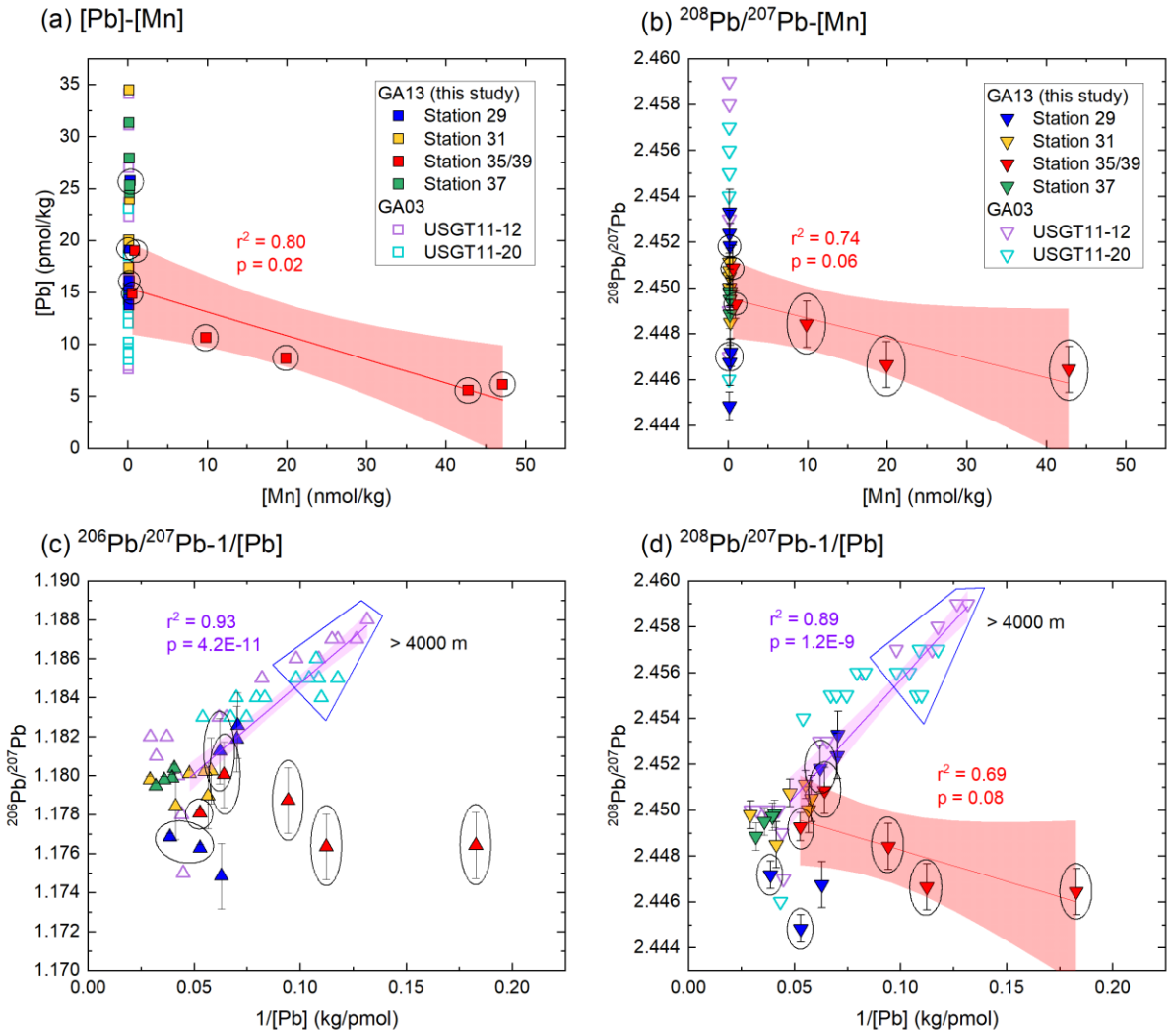


Figure 3.9. Cross plots of dissolved [Pb], [Mn] and Pb isotope ratios for the GA13 samples collected at depths > 2000 m from this study (solid symbols) and GA03 stations USGT11-12 and USGT11-20 (open symbols) from Noble et al. (2015). (a-b) Dissolved [Pb] and $^{208}Pb/^{207}Pb$ ratios versus dissolved [Mn]. (c-d) $^{206}Pb/^{207}Pb$ and $^{208}Pb/^{207}Pb$ versus the inverse of [Pb], with samples from depths > 4000 m at stations USGT11-12 and USGT11-20 enclosed by blue boxes. Ellipses indicate samples which show plume-related enrichments in dissolved [Mn] (> ~0.2 nmol/kg) and [Fe] (> ~0.7 nmol/kg); for clarity, samples from stations 31 and 37 with very small enrichments in dissolved [Mn] and [Fe] levels are not highlighted with ellipses. Simple linear regression lines with associated 95% confidence interval (shades) are fitted to: (i) the samples collected in the buoyant TAG plume at station 35/39 with large enrichments in dissolved [Mn] and [Fe] (red lines), and (ii) the deep water samples at station 29 with relatively high $^{20x}Pb/^{207}Pb$ and the samples from depths > 4000 m at stations USGT11-12 and USGT11-20 (purple lines); no regression line is shown for the plume samples in panel (c) as the samples have identical $^{206}Pb/^{207}Pb$ ratios within error.

3.5.4.2 Neutrally buoyant TAG plume

In contrast to the notable deficits in dissolved [Pb] in the buoyant plume near the vent site, samples with smaller plume-associated enrichments in dissolved [Mn] and [Fe] from locations more distal to the vent site (about 6 km to 140 km away) display no detectable anomalies in Pb concentrations (Fig. 3.5a, c, d). Most likely, this reflects the lack of plume-associated particle enrichments and hence weaker

Pb scavenging in the distal regions of the TAG plume. However, whilst slightly elevated particle concentrations were observed at 1500 m to 1900 m depth at valley wall station 37, the Pb concentrations were close to the background values (Fig. 3.3a; 3.5c). It is conceivable that the lack of resolvable Pb scavenging at station 37 is a consequence of the only marginally enriched particle levels at this site.

These results contrast with observations at the southern East Pacific Rise, which showed a deficit in dissolved Pb concentrations within the westward extending neutrally buoyant plume, up to about 1500 km from the ridge (Boyle et al., 2020). This is despite broadly similar enrichments in dissolved [Mn] (0.5-1.0 nmol/kg) and in [Fe] (1.0-1.7 nmol/kg) in the distal part of the plume at the East Pacific Rise (300-1500 km off-axis, Hatta et al., 2015) compared to the stations in the vicinity of the TAG Field at the Mid-Atlantic Ridge ([Mn] ≈ 0.3 nmol/kg; [Fe] = 1.0-2.6 nmol/kg). Measurements of suspended particle concentrations and compositions in the off-axis regions of the TAG plume are required to assess the cause of the different scavenging behaviours observed at the two sites.

3.5.5 Lead Isotope Variability Below 2500 m Depth – TAG Plume and Beyond

3.5.5.1 Lead isotope signatures

At vent site station 35/39, the low $^{208}Pb/^{207}Pb$ ratios between depths of 3100 m and 3544 m, with a minimum value of 2.446, mirror the strong plume-associated enrichments in ^{3}He and dissolved [Mn] and [Fe] and coincide with the pronounced deficits in [Pb] (Fig. 3.5b). These few samples, which were collected from within the buoyant TAG plume, also hint at an apparent negative linear correlation in a plot of $^{208}Pb/^{207}Pb$ versus dissolved [Mn] (Fig. 3.9b). Whilst the latter trend lacks a clear statistical significance with $p = 0.06$, it resembles the negative correlation of dissolved [Pb] with dissolved [Mn] ($p = 0.02$; Fig. 3.9a). Together, these observations suggest that the observed isotope excursions are likely tied to the buoyant TAG plume.

The Pb isotope signatures of samples from ≥ 2500 m depth at stations in the vicinity of the vent site show a more complex link with the TAG plume. At distal W station 29, the deep seawater samples display highly variable $^{206}Pb/^{207}Pb$ (1.175-1.183) and $^{208}Pb/^{207}Pb$ (2.445-2.453) ratios (Fig. 3.3; 3.5a). Three samples from ≥ 3200 m depth thereby show relatively high $^{206}Pb/^{207}Pb$ (1.181-1.183) and $^{208}Pb/^{207}Pb$ (2.452-2.453), which exceed the values that were observed at similar depths at proximal E station 31 (1.178-1.180, 2.449-2.451) but overlap with the NADW compositions determined for samples from the GA03 stations USGT11-12 and USGT11-20 (1.180-1.185, 2.450-2.456). In contrast, the shallower station 29 samples from depths of 2500 and 3000 m display markedly lower $^{206}Pb/^{207}Pb$ (1.176-1.177) and $^{208}Pb/^{207}Pb$ (2.445-2.447) ratios, which coincide with an enrichment in dissolved [Fe] (2.6 nmol/kg) associated with the neutrally buoyant TAG plume. These isotope excursions are similar in magnitude to those observed within the buoyant TAG plume at vent site station 35/39, but at station 29 there are no negative excursions in Pb concentrations, and the plume-associated enrichments in dissolved [Fe] are considerably lower. Furthermore, similarly low $^{206}Pb/^{207}Pb$ and $^{208}Pb/^{207}Pb$ ratios of

1.175 and 2.447, respectively, were seen at 3800 m depth of station 29, where the TAG plume is absent. In contrast, no notable Pb isotope excursions were detected for NADW samples from stations 31 and 37 to the east of the vent site, even at depths where minor plume signals were detected (Fig. 3.5c, d).

3.5.5.2 Covariations of Pb concentration and isotope composition: stable isotope fractionation versus mixing relationships

In plots of $^{206}Pb/^{207}Pb$ and $^{208}Pb/^{207}Pb$ versus 1/[Pb] (Fig. 3.9c, d), many samples from depths ≥ 2500 m of stations 29 and 35/39 appear to define distinct excursion patterns from a NADW endmember, characterised by a composition akin to that of water samples from ≥ 2000 m depth at stations 31 and 37 ($^{206}Pb/^{207}Pb \approx 1.180$ and $^{208}Pb/^{207}Pb \approx 2.450$, termed 'background NADW' in the following), towards lower Pb concentrations and distinct $^{208}Pb/^{207}Pb$ and $^{206}Pb/^{207}Pb$ values.

Most of the deepest samples from station 29 (depths of 3200 m, 3600 m and 3899 m) define statistically significant ($p < 0.05$), positive linear correlations in plots of $^{206}Pb/^{207}Pb$ ($r^2 = 0.93$) and $^{208}Pb/^{207}Pb$ ($r^2 = 0.89$) versus 1/[Pb], with compositions that are intermediate between background NADW and the GA03 samples from depths > 4000 m of stations USGT11-12 and USGT11-20 (Fig. 3.9c, d). These trends are most likely a consequence of mixing with an older water mass characterised by higher $^{206}Pb/^{207}Pb$ and $^{208}Pb/^{207}Pb$, such as a NADW component that was ventilated before the late 1930s (Fig. 3.6b).

In contrast, the water samples from the buoyant hydrothermal plume at station 35/39 and from depths of 2500 m, 3000 m and 3800 m at station 29 hint at lower $^{206}Pb/^{207}Pb$ and $^{208}Pb/^{207}Pb$ ratios with increasing 1/[Pb], although the apparent relationships have limited statistical significance ($p = 0.08$ for $^{208}Pb/^{207}Pb$ versus 1/[Pb]) due to the small numbers of samples (Fig. 3.9c, d). Two possible mechanisms could be responsible for these apparent covariations: (1) stable isotope fractionation between the dissolved and particulate phases during scavenging of Pb in the plume, and (2) mixing of background NADW with other isotopic endmember(s) that are characterised by relatively low Pb concentrations and lower $^{206}Pb/^{207}Pb$ and $^{208}Pb/^{207}Pb$.

Equilibrium isotope fractionation during particle scavenging of dissolved trace metals could lead to coupled depletions in elemental concentrations and changes in stable isotope compositions. For many elements, the partitioning of trace metals between a dissolved phase and particles is associated with an enrichment of heavy or light isotopes (depending on the element and the particulate phase) in either phase (e.g. Rehkämper et al., 2002; Pokrovsky et al., 2005; Lough et al., 2017; Yan et al., 2021). Notably, such mass-dependent isotope fractionation will produce opposing effects of similar magnitude for the dissolved $^{206}Pb/^{207}Pb$ and $^{208}Pb/^{207}Pb$ ratios, for example, an increase of the dissolved $^{206}Pb/^{207}Pb$ ratio by stable isotope fractionation will be matched by a similar decrease of dissolved $^{208}Pb/^{207}Pb$. However, the observed $^{206}Pb/^{207}Pb$ and $^{208}Pb/^{207}Pb$ ratios of the buoyant TAG plume at station 35/39 do not exhibit such opposing shifts relative to the background NADW composition but rather trend in the same direction (Fig. 3.5b). In particular, the $^{206}Pb/^{207}Pb$ (≈ 1.176) and $^{208}Pb/^{207}Pb$ (≈ 2.446) ratios of station

35/39 samples with large plume-associated enrichments in dissolved [Mn] and [Fe] are both lower compared to the background NADW signature ($^{206}Pb/^{207}Pb \approx 1.180$, $^{208}Pb/^{207}Pb \approx 2.450$; station 31). Therefore, stable isotope fractionation can confidently be ruled out as the cause for the observed deep water Pb isotope signatures at station 35/39.

The observed lower $^{206}Pb/^{207}Pb$ and $^{208}Pb/^{207}Pb$ ratios at stations 29 and 35/39 are more viably explained by mixing relationships. This interpretation is supported by the statistically significant ($p << 0.05$), linear correlation ($r^2 = 0.87$) of the deep water data in a plot of $^{206}Pb/^{207}Pb$ versus $^{208}Pb/^{207}Pb$, which is indicative of a mixing relationship between background NADW and at least one other isotopic endmember with lower $^{206}Pb/^{207}Pb$ and $^{208}Pb/^{207}Pb$ ratios (red line, Fig. 3.10). The most obvious additional component is mantle-derived Pb from TAG hydrothermal fluids, which are enriched in dissolved Pb from the local MORB substrate (Godfrey et al., 1994). In Figure 3.10, the data of MORBs from the ridge segment of the TAG Field form a trend roughly parallel to that defined by the samples from ≥ 2500 m depth of stations 29 and 35/39 but at significantly higher $^{206}Pb/^{207}Pb$ ratios. This suggests that mantle-derived Pb most likely plays only a subordinate role in generating the low $^{206}Pb/^{207}Pb$ and $^{208}Pb/^{207}Pb$ values, even for samples collected from the buoyant TAG plume. The most probable origin for the low $^{206}Pb/^{207}Pb$ and $^{208}Pb/^{207}Pb$ ratios is, therefore, anthropogenic Pb with an isotope signature similar to that of European and North African aerosols (Fig. 3.10). The presence of such Pb in the deep waters of the TAG region is surprising, as the release of Pb from aerosols is normally expected to only impact the uppermost water column. However, the release of anthropogenic Pb in the deep ocean from sinking particles was previously reported by Wu et al. (2010) and Lanning et al. (2023) for the North Pacific Ocean.

There are two further observations that support and extend the above conclusions. First, Noble et al. (2015) identified even larger Pb isotope variations ($^{206}Pb/^{207}Pb = 1.179\text{-}1.191$, $^{208}Pb/^{207}Pb = 2.448\text{-}2.454$) for GA03 water samples collected in the buoyant TAG plume at station USGT11-16 (Fig. 3.8; 3.10). Notably, some of their plume samples show $^{206}Pb/^{207}Pb$ ratios (1.185-1.191) that are significantly higher than any of the values that were determined for samples from ≥ 2500 m in this study (Fig. 3.10). These results of Noble et al. (2015) are in accord with mixing between NADW and anthropogenic Pb of North American origin characterised by high $^{206}Pb/^{207}Pb$ ratios, with the latter most likely originating from sinking particles. Second, suspended particles that were collected in the neutrally buoyant TAG plume at a distance of up to 1.5 km from the vent site (Godfrey et al., 1994) define a $^{206}Pb/^{207}Pb$ versus $^{208}Pb/^{207}Pb$ correlation ($r^2 = 0.86$, $p << 0.05$) that is sub-parallel to the trend of the water samples from ≥ 2500 m depth at stations 29 and 35/39, and which also trends towards the isotope signature of Eurafrican aerosols (blue line, Fig. 3.10). This suggests that the Pb isotope compositions of the plume particles were also impacted by anthropogenic Pb of European or North African origin, and this was most likely delivered into the deep water via particles.

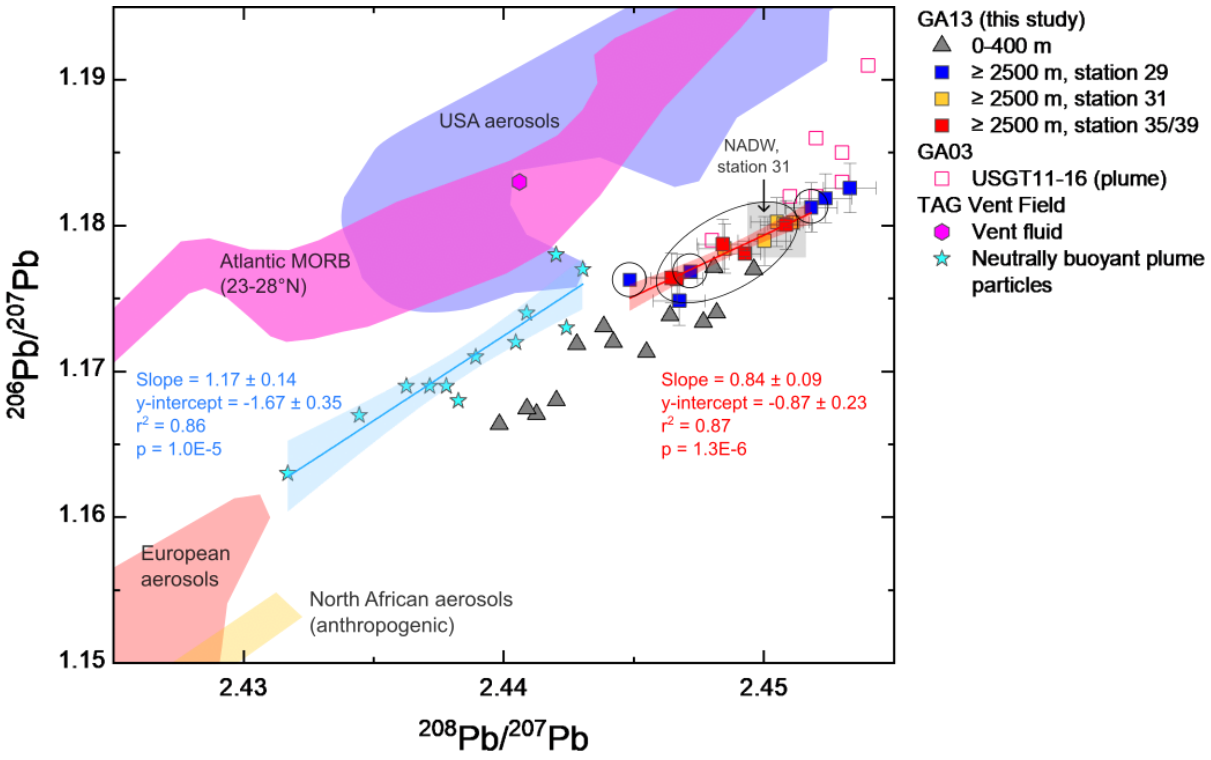


Figure 3.10. Plot of $^{206}Pb/^{207}Pb$ versus $^{208}Pb/^{207}Pb$ ratios for the GA13 seawater samples collected at depths ≥ 2500 m for this study (filled squares), in comparison to literature data of the potential sources of dissolved Pb for the deep water samples. Ellipses encircle seawater samples that coincide with plume-associated enrichments in dissolved [Mn] (> ~0.2 nmol/kg) and [Fe] (> ~0.7 nmol/kg). Simple linear regression lines with associated 95% confidence intervals (shades) are fitted for: (1) all seawater samples from stations 29 and 35/39 that show plume-associated enrichments in dissolved [Mn] and [Fe] and that are encircled by ellipses; (2) particles collected in the neutrally buoyant TAG plume by Godfrey et al. (1994) (blue line). Data obtained for seawater from the buoyant TAG plume at station USGT11-16 during the GA03 expedition are shown for comparison (open squares; Noble et al., 2015). The magenta field encompasses Pb isotope data for MORBs from the ridge segment of the TAG Hydrothermal Field (23-28°N) and were compiled from the PetDB database (www.earthchem.org/petdb, accessed on 18th May 2022). Other literature data: vent fluid from the TAG vent site (magenta hexagon) and neutrally buoyant TAG plume particles (stars) (Godfrey et al., 1994); urban aerosols from Western Europe, North Africa and the USA (Bollhöfer and Rosman, 2001; Sherman et al., 2015).

3.5.5.3 Dissolved-particulate exchange processes in the deep ocean

The finding of anthropogenic Pb with a European and/or North African origin in old (> 60 years) NADW is unambiguous. The most reasonable origin of this anthropogenic Pb are aerosol particles, from which anthropogenic Pb was released whilst they sank into the deep ocean. Such sinking particles can release either their indigenous inventories of natural and anthropogenic Pb as well as any additional Pb that was scavenged from seawater following deposition in the ocean (Schaule and Patterson, 1981; Flegal and Patterson, 1983). Notably, a number of studies have shown that anthropogenic Pb is preferentially released into seawater from aerosol particles in comparison to natural Pb associated with mineral dust, which reflects that anthropogenic Pb emissions from high-temperature processes are primarily present in the particles in the form of more labile species (e.g. halide, carbonate, sulphate and

oxide species), whilst Pb in mineral dust is bound in more stable silicate minerals (Chester et al., 1989; Koçak et al., 2007; Fishwick et al., 2018).

Simple release of Pb from particles alone, however, cannot be responsible for the observed Pb systematics, as this would generate lower $^{206}Pb/^{207}Pb$ and $^{208}Pb/^{207}Pb$ ratios coupled with higher Pb concentrations, contrary to the observations (Fig. 3.9c, d). Hence, reversible exchange of Pb and its isotopes between dissolved and particulate phases is most likely responsible for the unusually low $^{206}Pb/^{207}Pb$ and $^{208}Pb/^{207}Pb$ ratios of the deep water samples analysed in this study. This conclusion is supported by seawater profiles from the Western Atlantic Ocean, which revealed isotopic equilibration between dissolved Pb and Pb adsorbed to small (< 50 μm) suspended particles (Shen and Boyle, 1988; Sherrell et al., 1992), a phenomenon that is further confirmed by isotope exchange experiments in the laboratory (Chen et al., 2016a).

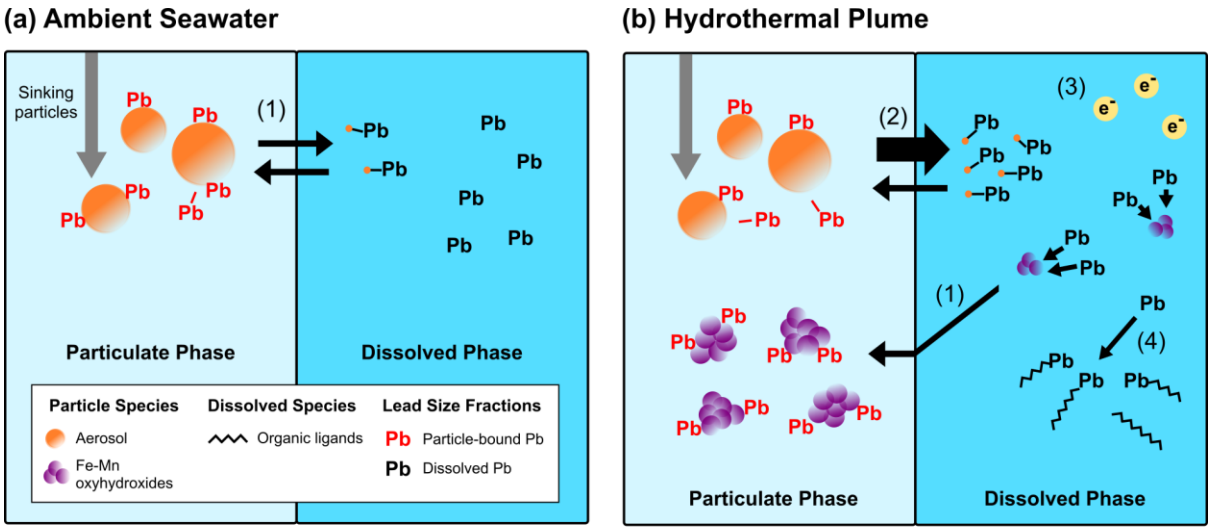
For the sample from 3800 m depth at distal W station 29, the distinctively low $^{206}Pb/^{207}Pb$ (1.175) and $^{208}Pb/^{207}Pb$ (2.447) ratios were most likely impacted by Pb released from resuspended seafloor sediments. At this station, a nepheloid layer was detected by light scattering measurements in the bottom 150 m of the water column (Fig. 3.5a) and this encompassed the depth at which the sample was collected. The resuspended seafloor sediments will contain particles that recently settled from the surface and are hence enriched in Pb with a current anthropogenic signature. Release of Pb from such sediments and exchange with dissolved Pb in the nepheloid layer can thus explain the slightly enriched Pb concentration and the lower $^{206}Pb/^{207}Pb$ and $^{208}Pb/^{207}Pb$ ratios of this seawater sample. Notably, along the GA03 section, the deepest samples from three Eastern Atlantic stations also show excursions towards lower $^{206}Pb/^{207}Pb$ and $^{208}Pb/^{207}Pb$ ratios alongside [Pb] enrichments, which were attributed to the release of Pb from sediment particles in the nepheloid layer (Noble et al., 2015).

The other deep water samples with distinctively low $^{206}Pb/^{207}Pb$ and $^{208}Pb/^{207}Pb$ ratios from vent site station 35/39 (3100-3544 m) and distal W station 29 (2500 m and 3000 m) display plume-associated enrichments in dissolved [Fe] and [Mn], which linked with the TAG hydrothermal activity (Fig. 3.5a, b). Given this, the observations most likely reflect enhanced exchange of anthropogenic Pb present in sinking particles with dissolved Pb at the distinct physicochemical conditions within the buoyant and neutrally buoyant TAG plume. Various physicochemical mechanisms presumably facilitated the exchange processes, including intense scavenging of dissolved Pb from the plume by hydrothermal particles, the reducing plume conditions, and stabilisation of dissolved Pb due to elevated concentrations of Pb-binding organic ligands (Fig. 3.11).

The intense scavenging of dissolved Pb by Fe-Mn oxyhydroxides in the buoyant TAG plume may be coupled with enhanced remobilisation of anthropogenic Pb adsorbed to sinking particles. Assuming equilibrium control on the partitioning of trace metals between the dissolved and particulate phases (e.g. Balistrieri et al., 1981), the rapid removal of dissolved Pb from the hydrothermal plume due to adsorption onto Fe-Mn oxyhydroxides may support the release of anthropogenic Pb from particles that

have sunk from the surface, to replenish the dissolved Pb pool. Furthermore, the reducing conditions in the buoyant TAG plume may also aid in the dissolution of the labile Pb phases present in the sinking particles.

Organic complexation is known to exert important controls on the speciation of dissolved Pb in seawater. In surface seawater of the open ocean, organic Pb complexes exhibit conditional stability constants on the order of ~10^8 to ~10^{12} and can account for up to half of the dissolved Pb budget (Capodaglio et al., 1990; Kozelka et al., 1997; Wells et al., 1998; Ren et al., 2023). In addition, the laboratory study of Maring and Duce (1990) demonstrated that the dissolution of Pb from aerosols is enhanced in surface waters that are enriched in dissolved organic carbon. It is hence conceivable that elevated organic ligand concentrations in the TAG hydrothermal plume also supported and increased the remobilisation of Pb from the sinking particles. Previous studies revealed the presence of Fe-complexing organic ligands in hydrothermal plumes, which were either entrained from the open ocean and/or produced around the vents (Bennett et al., 2008; Toner et al., 2009; Lough et al., 2019). Furthermore, laboratory studies have identified specific Pb-binding organic compounds that are released by vent microbes (Loaëc et al., 1998). The presence of such complexing organic compounds in the TAG plume can, therefore, help to account for the enhanced release of anthropogenic Pb from sinking aerosol particles.



(1) Background level of remobilisation of anthropogenic Pb from sinking particles.

(1) Loss of dissolved Pb to scavenging by Fe-Mn oxyhydroxides.
(2) Enhanced remobilisation of anthropogenic Pb from sinking particles under equilibrium metal-particle partitioning.
(3) Enhanced remobilisation of Pb from particles under reducing buoyant plume condition.
(4) Stabilisation of dissolved Pb by an elevated level of dissolved organic ligands.

Figure 3.11. Conceptual illustration that summarises physicochemical mechanisms that drive reversible dissolved-particulate exchange of Pb in ambient seawater and in hydrothermal plumes.

3.6 Conclusions

This study presents new dissolved Pb concentration and isotope data for seawater samples from five stations at and in the vicinity of the TAG Hydrothermal Field on the Mid-Atlantic Ridge. The key findings of this study relate to (i) variabilities in dissolved Pb concentrations and isotope compositions in samples from depths exceeding 2500 m, which largely appear to be linked with the hydrothermal plume, and (ii) further variations in the uppermost water column, which are not connected to the hydrothermal activity.

In the upper ocean at ≤ 400 m depth, significant vertical and lateral heterogeneities in dissolved Pb signatures were observed on spatial scales of less than 20 m and a few kilometres, respectively. These heterogeneities most likely reflect the release of anthropogenic Pb from aerosol particles in the upper water column.

In the deep ocean (≥ 2500 m), pronounced deficits in dissolved Pb concentrations were observed in the buoyant TAG plume, in agreement with the results of previous studies. This is despite the strong enrichment of dissolved Pb in vent fluids. These deficits reflect intense scavenging of Pb by hydrothermal particles in the buoyant plume. In contrast, no dissolved Pb deficits were observed in the neutrally buoyant plume, most likely due to the significantly lower ambient particle concentrations.

Whilst the hydrothermal activity contributes to an overall net sink for dissolved Pb in the deep water column, significant and unexpected Pb isotope variations were detected at depths ≥ 2500 m. In particular, unusually low $^{206}Pb/^{207}Pb$ and $^{208}Pb/^{207}Pb$ ratios were determined for samples from the buoyant hydrothermal plume at station 35/39 as well as for samples from the non-buoyant plume and the nepheloid layer at station 29. The observed isotope signatures predominantly reflect mixing between background NADW and anthropogenic Pb of European and/or North African origin. This result is surprising, considering that the release of anthropogenic Pb is normally expected to be restricted to the uppermost water column. The isotope heterogeneities are thought to be caused by exchange of anthropogenic Pb from either sinking particles or modern resuspended sediments with ambient dissolved seawater Pb. These exchange reactions may be enhanced by distinct physicochemical conditions within the TAG plume, including (i) rapid initial scavenging of dissolved Pb from the hydrothermal plume by Fe oxyhydroxide phases; (ii) reducing plume conditions, which may enhance the dissolution of labile anthropogenic Pb from sinking aerosol particles; and (iii) higher concentrations of dissolved organic ligands, which may help to stabilise dissolved anthropogenic Pb by complexation.

Additional sampling and Pb concentration and isotope analyses of seawater from other hydrothermal vent sites and plumes are desirable to better constrain how the flux balance and cycling of Pb is affected by hydrothermal activity. Furthermore, combined Pb concentration and isotope studies of filtered seawater and particles are required to improve understanding of how Pb and other trace

metals are exchanged between dissolved and particulate phases and in what manner hydrothermal activity impacts such exchange processes.

3.7 Researcher Contributions

The dissolved seawater Pb concentration and isotope data that are presented and discussed in this chapter were obtained by the author. The dissolved Fe and Mn concentrations and He isotope compositions of the samples were obtained by Alastair J. M. Lough (University of Leeds, UK), Joseph A. Resing (University of Washington, USA) and William J. Jenkins (Woods Hole Oceanographic Institution, USA), respectively. The author led the interpretations of the results presented in this study, with insightful comments from Mark Rehkämper and Tina van de Flierdt. Maeve C. Lohan (University of Southampton, UK) and all the participants of the GEOTRACES GA13 expedition are thanked for collecting the seawater samples that were analysed in this study.

Chapter 4

Lead Concentrations and Isotope Compositions along Southern Ocean GEOTRACES Section GS01

4.1 Introduction

The distributions of Pb and its isotopes in the global ocean reflect the interplay between their input at ocean boundaries and internal redistribution processes. Since the beginning of the last century, atmospheric deposition of anthropogenic Pb from leaded petrol consumption and other industrial activities have dominated the input of Pb into the global ocean (Boyle et al., 2014). The dynamic input of Pb is in turn redistributed in the ocean interior through the advection and mixing of water masses (Boyle et al., 1986; Alleman et al., 1999; Noble et al., 2015; Zurbrick et al., 2017, 2018; Bridgestock et al., 2018), as well as particulate redissolution / remineralisation processes (Wu et al., 2010; Echegoyen et al., 2014; Lee et al., 2015; Zurbrick et al., 2017).

One of the most remote areas from sources of anthropogenic Pb pollution is the Southern Ocean. The Southern Ocean is defined as the ocean area south of 35 or 40°S and north of Antarctica. Due to the absence of land barriers in the Southern Ocean, strong winds drive the vigorous, east-flowing Antarctic Circumpolar Current (ACC), one of the most powerful ocean current systems on Earth (see review by Rintoul, 2018). The Southern Ocean is where deep water masses from all ocean basins upwell along tilted isopycnals to contribute to Antarctic surface waters, which in turn sink close to the Antarctic continent and ultimately return to the meridional ocean basins as Antarctic Bottom Water (AABW) (Fig. 4.1) (Marshall and Speer, 2012; Talley, 2013). Further north in the Southern Ocean, Subantarctic Mode Water (SAMW) and Antarctic Intermediate Water (AAIW) sink, which also spread north and fill shallower depths of the meridional ocean basins (McCartney, 1977, 1982; Hanawa and Talley, 2001). An additional feature of the Southern Ocean is that both the hydrography and biogeochemistry exhibit north-south gradients that occur not gradually, but as sharp transitions denoted as fronts (Deacon, 1982). These fronts demarcate latitudinal zones of outcropping/subducting water masses (e.g. Rintoul and Bullister, 1999) and biogeochemical properties (e.g. Sarmiento et al., 2004) and are locations of major zonal currents (e.g. Orsi et al., 1995; Belkin and Gordon, 1996).

All of the above make the Southern Ocean an interesting area to study for any trace element or isotope system that does not behave conservatively in the ocean. An additional angle of interest for studying Pb is that the remoteness of the area might offer an opportunity to observe a significant natural Pb signature, in contrast to other heavily polluted parts of the global ocean (i.e. Boyle et al., 2014). However, existing studies indicate that significant perturbations by anthropogenic Pb might still be found in remote Southern Ocean waters or in water masses that were ventilated in the Southern Ocean (Flegal et al., 1993; Alleman et al., 2001; Paul et al., 2015; Ndungu et al., 2016; Bridgestock et al., 2018). This observation in part reflects the significant Pb pollution of the Antarctic atmosphere and snow (McConnell et al., 2014 and references therein). Yet, understanding of such Pb signals, as well as the cycling of Pb in the Southern Ocean, is limited by the scarcity of dissolved Pb concentration and isotope data in the region. Only three studies have been published to date, which comprise studies of

surface waters from the Weddell and Scotia Seas, Atlantic sector of the Southern Ocean (Flegal et al., 1993), four depth profiles in the Amundsen Sea, Pacific sector of the Southern Ocean (Ndungu et al., 2016), and one depth profile from the Indian Ocean sector of the Southern Ocean (Lee et al., 2015). In addition, Griffiths (2019) reported in his PhD thesis a first partial dataset of dissolved Pb concentrations and isotope compositions from the Australian sector of the Southern Ocean, which consists of six seawater depth profiles (49 to 65°S) collected along a meridional section between Tasmania and Antarctica during the GEOTRACES GS01 expedition (IN2018_V01).

This study completes the partial dataset presented by Griffiths (2019) by adding seawater depth profiles of dissolved Pb concentrations and isotope compositions from the GEOTRACES GS01 expedition in the Subantarctic Zone south of Tasmania. The complete GS01 dataset allows a thorough analysis of inter-laboratory precision of the dissolved Pb concentration measurements (Imperial College London and the University of Tasmania) and an assessment of the relative significance of advection and particulate processes in the area, with a focus on processes in the Subantarctic Zone.

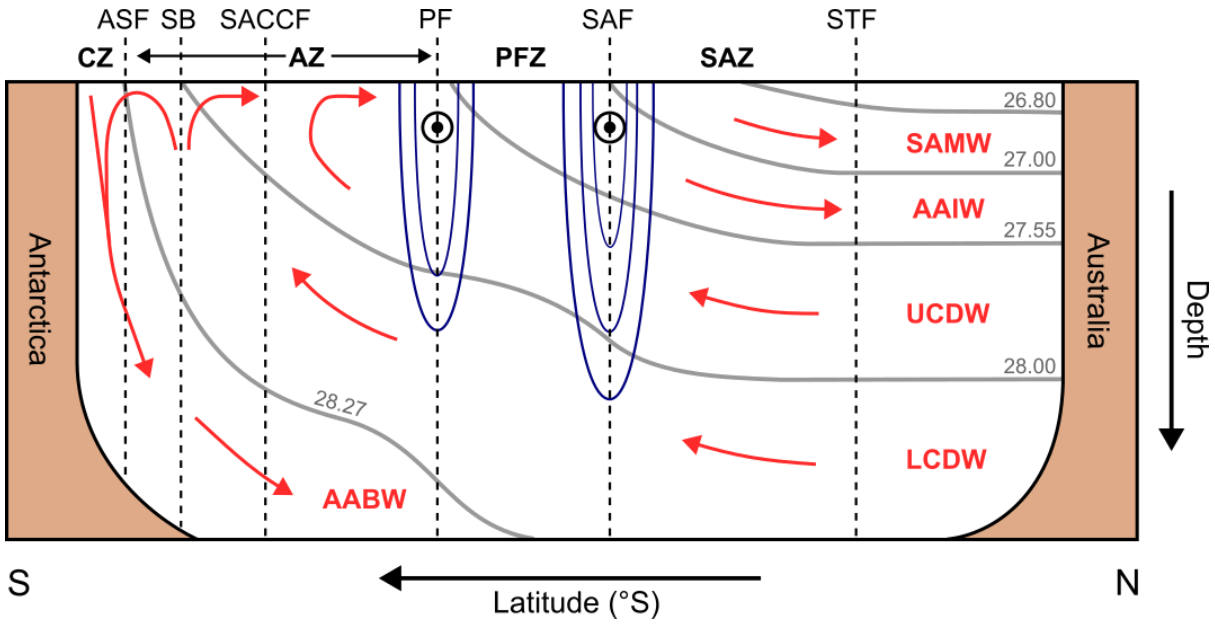


Figure 4.1. Schematic illustration of the hydrography of the Southern Ocean between Australia and Antarctica. Solid grey lines indicate the neutral density (γ^n) horizons that demarcate the major water masses across the transect, labelled with γ^n values in kg/m^3. Water mass abbreviations are defined in Table 4.3; red arrows show the directions of water mass movement. Vertical dashed lines indicate the fronts that separate the oceanographic zones, abbreviated as in Table 4.1. Blue contours indicate the principal flows of the Antarctic Circumpolar Current along the Subantarctic Front (SAF) and the Polar Front (PF); the flow direction is towards the east (⊙ as opposed to ⊗). The figure was modified from Rintoul (2018) and Anderson et al. (2009).

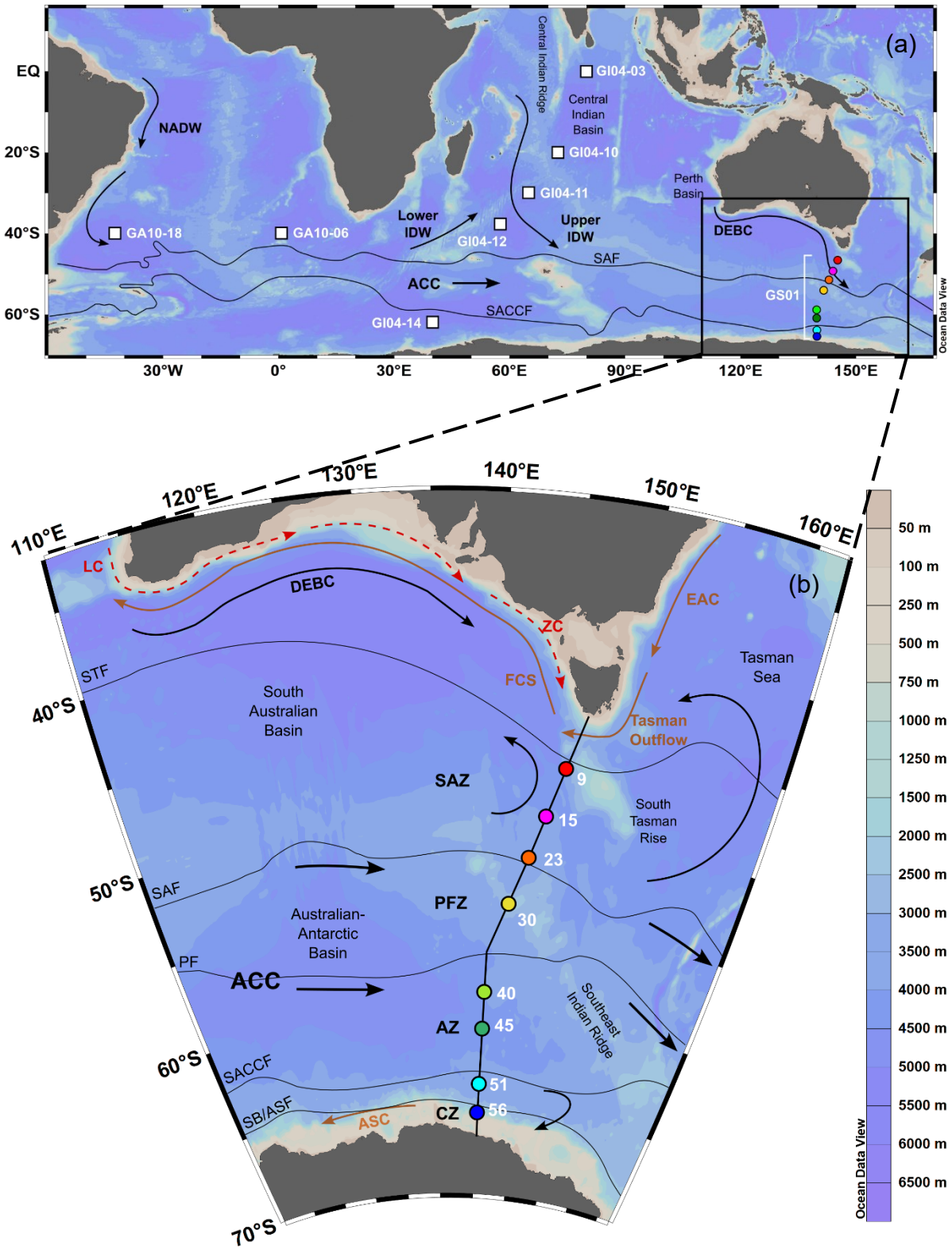

(a)
EQ
20°S
40°S
60°S
30°W
0°
30°E
60°E
90°E
120°E
150°E
NADW
GA10-18
GA10-06
Lower IDW
GI04-12
Upper IDW
GI04-03
Central Indian Ridge
Central Indian Basin
GI04-10
GI04-11
Perth Basin
DEBC
SAF
ACC
SACCF
GI04-14
GS01
Ocean Data View
110°E
120°E
130°E
140°E
150°E
160°E
70°S
(b)
LC
DEBC
ZC
EAC
STF
FCS
Tasman Sea
South Australian Basin
Tasman Outflow
SAZ
9
15
23
South Tasman Rise
PFZ
30
Australian-Antarctic Basin
PF
ACC
40
AZ
45
Southeast Indian Ridge
SACCF
51
SB/ASF
ASC
CZ
56
50 m
100 m
250 m
500 m
750 m
1000 m
1250 m
1500 m
2000 m
2500 m
3000 m
3500 m
4000 m
4500 m
5000 m
5500 m
6000 m
6500 m
Ocean Data View

Figure 4.2

Figure 4.2 (cont'd). (a) Map of the Atlantic Ocean, Indian Ocean and the Southern Ocean (Atlantic, Indian and Australian sectors), showing the locations of seawater sampling along the GEOTRACES GS01 transect (coloured circles; Griffiths (2019) and this study) and reference stations (white squares) along the GEOTRACES section GI04 in the Indian Ocean and section GA10 in the South Atlantic Ocean. Black arrows indicate major deep water currents / movement in the Southern Ocean: Antarctic Circumpolar Current (ACC), Indian Deep Water (IDW) inflow and outflow, Deep Eastern Boundary Current (DEBC) and North Atlantic Deep Water (NADW) flow along the deep western boundary. Thin black lines indicate the Subantarctic Front (SAF) and Southern ACC Front (SACCF) of the ACC. **(b) Enlargement of map (a) showing the study area, the GS01 cruise track along the WOCE SR3 line and the stations sampled for dissolved Pb concentrations and isotopes during the expedition (coloured circles).** Red dashed arrows indicate surface water currents: Leeuwin Current (LC) and Zeehan Current (ZC). Brown solid arrows indicate intermediate depth slope currents: East Australian Current (EAC), Tasman Outflow, Flinders Current System (FCS) and Antarctic Slope Current (ASC). Black arrows indicate deep water currents (DEBC) or currents that extend from the surface to the deep water (ACC and the associated gyres). Thin black lines indicate the major fronts identified along the GS01 transect. Abbreviations of the major oceanographic fronts and zones are defined in Table 4.1. The maps were created using the Ocean Data View (ODV) software (Schlitzer, 2020), with ocean background colours indicating the bottom topography.

4.2 The GS01 Expedition and Setting

4.2.1 The GEOTRACES GS01 Expedition and the SR3 Line

The GEOTRACES GS01 section cruise ('IN2018_V01' expedition) aboard the *RV Investigator* sailed between Hobart, Tasmania and Antarctica (11th January - 21st February 2018), with the scientific objectives to study Southern Ocean hydrography and marine trace elements and their isotopes, as well as atmospheric parameters (Fig. 4.2b). The expedition featured a reoccupation of the World Ocean Circulation Experiment (WOCE) meridional SR3 line (between 44°S, 146°E and 65.7°S, 140°E), a repeat section that is well-studied for its hydrography (e.g. Rintoul and Bullister, 1999; Sokolov and Rintoul, 2002). Eight seawater profiles were collected along the meridional SR3 line for dissolved Pb concentrations and isotopes, sampling between eight and nine depths throughout the water column.

4.2.2 Geographical and Hydrographic Setting

4.2.2.1 Geographical setting

The Australian sector of the Southern Ocean defines the ocean region between the South Pacific and Indian Oceans, bounded by the Southern Australian – Tasmanian coastlines to the north and the Wilkes-Adélie Land Coast of Antarctica to the south (Fig. 4.2). The Southeast Indian Ridge forms a quasi-zonal topographic barrier across the region. It rises to a bottom depth of ~2500 m and divides the South Australian Basin to the north and the Australian-Antarctic Basin to the south. Just south of Tasmania, the South Tasman Rise forms an isolated topographic saddle that rises to ~2000 m depth. The region represents the key (deep) gateway for the exchange of water between the Indian and Pacific Oceans.

4.2.2.2 Frontal structure and oceanographic zones

The frontal structure along the SR3 line had been mapped and described in detail by Sokolov & Rintoul (2002, 2007) (Fig. 4.1, 4.2; Table 4.1). The Subtropical Front (STF, 47°S) marks the northern limit of the Subantarctic Zone (SAZ), which can be identified by sharp southward decreases in potential temperature (from > 14°C to < 12°C) and salinity (from > 35.0 to < 34.6) in the surface mixed layer. The Subantarctic Front (SAF, ~52°S) separates the SAZ from the Polar Frontal Zone (PFZ) and marks the northern limit of the ACC belt. This front is characterised by pronounced hydrographic gradients and strong vertical mixing throughout the water column (e.g. Rintoul, 2018). The Polar Front (PF, ~56°S) demarcates the transition from the PFZ into the Antarctic Zone (AZ). It is identified by the northern limit of cold subsurface water (< 2°C, 100-300 m), and is another area of intense vertical mixing and strong ACC flow (e.g. Rintoul, 2018). The Southern Antarctic Circumpolar Current Front (SACCF) at ~64°S lies within the AZ and delimits the southern limit of a 1.8°C potential temperature maximum in the Upper Circumpolar Deep Water (UCDW) layer. The Southern Boundary (SB) of the ACC and the Antarctic Slope Front (ASF) are two closely spaced southern fronts at ~65°S, which demarcate the AZ to the north and the Continental Zone (CZ) to the south. The SB represents the southern limit of the ACC belt.

Table 4.1. Summary of the major oceanographic fronts and zones along the SR3 line during the GEOTRACES GS01 section cruise in January/February 2018.

	Front	Lat (°S)		Oceanographic Zone
STF	Subtropical Front	47		
			SAZ	Subantarctic Zone
SAF	Subantarctic Front	52		
			PFZ	Polar Frontal Zone
PF	Polar Front	56		
			AZ	Antarctic Zone
SACCF	Southern Antarctic Circumpolar Current Front	64		
SB	Southern Boundary	65		
ASF	Antarctic Slope Front	65		
			CZ	Continental Zone

4.2.2.3 Regional circulation

The regional circulation regime is dominated by the east-flowing ACC (Fig. 4.2b), the largest oceanic current on Earth with estimated volume transport between 120 and 184 Sverdrup (Sv; 1 Sv = 10^6 m^3 s^{-1}) (Donohue et al., 2016 and references therein). The ACC belt spans a broad latitudinal range

between the SAF (~52°S) and SB (~65°S) (i.e. encompassing the PFZ and AZ) and represents the principal zonal pathway for the advection of upper ocean waters and Circumpolar Deep Water (CDW) in the Southern Ocean (Sokolov and Rintoul, 2007 and references therein). Most of the flow of the ACC can be observed along its two major fronts, the SAF and PF (e.g. Rintoul and Sokolov, 2001). North of the ACC belt, the SAZ is characterised by a confluence of meridional and zonal flows. A branch of the East Australian Current (EAC) flows southward along the east coast of Tasmania, which turns at the southern tip of Tasmania to flow westward, forming the Tasman Outflow (Rintoul and Sokolov, 2001; Speich et al., 2002). The Tasman Outflow, together with a north-flowing branch of the ACC and mode waters off the west coast of Tasmania, feed the intermediate depth Flinders Current System (FCS), which flows westward along the Southern Australian continental slope (Middleton and Cirano, 2002; Middleton and Bye, 2007; Richardson et al., 2019). The east-flowing ACC and the west-flowing FCS form the major anticyclonic gyre in the South Australian Basin (Rintoul and Sokolov, 2001; Davis, 2005; McCartney and Donohue, 2007). Above the FCS, the Zeehan Current (ZC) forms part of the surface Leeuwin Current System, which flows from the Southeast Indian Ocean and eastward along the Southern Australian shelf, reaching the west of Tasmania (Cresswell, 2000; Ridgway and Condie, 2004). Below the FCS, the Deep Eastern Boundary Current (DEBC) flows eastward and allows Indian Deep Water (IDW) to enter the Australian sector of the Southern Ocean (Tamsitt et al., 2019). South of the ACC belt, the Antarctic Slope Current (ASC) flows westward along the Antarctic continental slope (Thompson et al., 2018). Branches of the ACC veer south and join the ASC, forming cyclonic gyres on the southern side of the ACC (McCartney and Donohue, 2007).

4.3 Methods

4.3.1 Sample Locations and Collection

The eight stations along the GEOTRACES GS01 section sampled for Pb concentrations and isotopes span across all major fronts of the Southern Ocean (Table 4.2; Fig. 4.2b). Station 9 was located near the STF (46.7°S, 'northern SAZ station'), and stations 15 (49.3°S, 'mid-SAZ station') and 23 (51.6°S, 'southern SAZ station') were sampled on the northern flank of the SAF in the SAZ. Station 30 (54.1°S, 'PFZ station') was located in the PFZ. Stations 40 (58.9°S, 'northern AZ station'), 45 (60.8°S, 'mid-AZ station') and 51 (63.9°S, 'southern AZ station') were located between the PF and SB in the AZ. The CZ was sampled by the southernmost station 56 (65.4°S, 'CZ station').

Seawater sample collection was conducted using an aluminium trace metal rosette system (TMR, Seabird) mounted with 12 × 12 L trace metal clean Niskin bottles (OTE). Upon recovery, the Niskin bottles were immediately transferred to a clean laboratory environment onboard the vessel (ISO class 5), where seawater was filtered using 0.2 µm Acropak® 200 (Pall) filter capsules into two acid-cleaned 1 L LDPE bottles for each sample. Following this, the samples were acidified with 6 M HCl to pH ≈

1.8. The filtered, acidified samples were then double-bagged and stored at room temperature until they were processed back on shore (i.e. at Imperial College London and the University of Tasmania).

Table 4.2. Information about the eight stations with seawater depth profiles collected for Pb isotope analysis during the GEOTRACES GS01 section cruise. Asterisk (*) indicates the stations for which Pb concentration and isotope results were presented by Griffiths (2019).

Station	TMR Number	Location	Lat (°S)	Long (°E)	Bottom depth (m)	Date(s) of sample collection (dd/mm/yyyy)
9	5, 6	Northern SAZ	46.65	145.25	3344	14/01/2018-15/01/2018
15*	9, 10	Mid-SAZ	49.27	144.09	4292	17/01/2018
23	13, 14	Southern SAZ	51.55	143.00	3628	19/01/2018-20/01/2018
30*	17, 18	Northern PFZ	54.07	141.60	2563	22/01/2018
40*	23, 24	Northern PFZ	58.85	139.84	3929	25/01/2018-26/01/2018
45*	26, 27	Mid-AZ	60.85	139.85	4405	27/01/2018
51*	30, 31	Southern AZ	63.86	139.87	3729	29/01/2018-30/01/2018
56*	33, 34	CZ	65.40	139.85	2386	31/01/2018

4.3.2 Determination of Dissolved Pb Concentrations and Isotopes

Measurements of dissolved Pb concentrations and/or isotope compositions were carried out for 70 samples at Imperial College London (ICL). 53 samples from south of the SAF (stations 30, 40, 45, 51 and 56) and a shallow water (< ~1000 m) profile from the SAZ (station 15) were analysed by Alex Griffiths for Pb concentrations and/or isotope compositions (Griffiths, 2019). The remaining 17 seawater samples from stations 9 and 23 from the SAZ were analysed during this study following the protocols published by Griffiths et al. (2020).

Lead concentrations were determined on 50 mL aliquots of seawater samples by isotope dilution. Following equilibration with a ^{207}Pb-^{204}Pb double spike, Pb was pre-concentrated by $Mg(OH)_2$ co-precipitation and purified by a single stage of anion exchange chromatography. Measurements were conducted on a Nu Plasma II MC-ICP-MS (Nu Instruments), followed by data reduction to obtain the Pb concentrations. The average procedural blank during Pb concentration measurements was at 5.6 ± 3.0 pg (1 SD; n = 18; Chapter 3 of this thesis), representing 2-20% of the indigenous Pb in the sample aliquots. Lead concentrations of all samples were corrected for the average procedural blank. Three aliquots were processed and measured for Pb concentrations for all samples in this study. For two of the samples (station 9, 987 m and station 23, 493 m; Table 4.4), one replicate measurement yielded Pb concentration that differed from the two other measurements by > 2 pmol/kg, and the spurious value was discarded. The triplicate uncertainties (1 SD) in Pb concentrations were applied to individual samples, which were generally similar to or better than the long-term external precision from replicate analyses of the in-house seawater reference material SO-151 (± 0.5 pmol/kg; Chapter 3 of this thesis).

Lead isotope compositions were determined on 1-4 ng of Pb. Briefly, Pb was preconcentrated from approximately 2 L of seawater samples by solid phase extraction with Nobias Chelate PA-1 resin and purified by two stages of anion exchange chromatography (see Griffith et al. (2020) for details). Isotope measurements were conducted using a Nu Plasma II MC-ICP-MS (Nu Instruments). For every batch of 6-8 samples, unspiked aliquots were first measured, followed by double spiked aliquots in a subsequent measurement session. The two sets of measurements were then combined to generate the final data through various correction steps, including (1) correction for the isobaric interference of ^{204}Hg on ^{204}Pb, (2) external normalisation of the unspiked measurements using an empirically optimised ^{205}Tl/^{203}Tl ratio, (3) iteration through a set of non-linear double spike equations, and (4) standardisation with the bracketing NIST SRM 981 Pb – NIST SRM 997 Tl standard measurements. Lead yields from the sample preparation procedure were consistently near-quantitative at 96 ± 4% (1 SD; 87 to 102%). The total procedural blanks during the period of measurements were 63, 69 and 110 pg respectively, representing 2-7% of the indigenous sample Pb. No blank correction was applied to the isotope data. The long-term external precisions (2 SD) for replicate isotope analyses of SO-151 (n = 6; ≈ 2 ng Pb), i.e. ~1400 ppm for ^{206}Pb/^{207}Pb, ~400 ppm for ^{208}Pb/^{207}Pb and ~2200 ppm for ^{206}Pb/^{204}Pb (Chapter 3), were applied to all samples of this study, which were measured at Pb concentrations of 1-4 ng/mL in the MC-ICP-MS run solutions. Isotope measurement of an aliquot of the GEOTRACES intercalibration sample GSP yielded ^{206}Pb/^{207}Pb = 1.1584 ± 0.0017, ^{208}Pb/^{207}Pb = 2.4475 ± 0.0010, and ^{206}Pb/^{204}Pb = 18.09 ± 0.04. These results were identical within error to the GSP results published by Griffiths et al. (2020) (^{206}Pb/^{207}Pb = 1.1584 ± 0.0003, ^{208}Pb/^{207}Pb = 2.4476 ± 0.0006, ^{206}Pb/^{204}Pb = 18.08 ± 0.01).

4.3.3 Determination of the Dissolved Concentrations of Pb and Other Trace Metals at the University of Tasmania (UTAS)

Measurements of the dissolved Pb concentrations of seawater samples from the same locations were separately carried out by Andrew Bowie et al. as part of the multi-elemental analysis effort at the University of Tasmania (UTAS), and the data was made available in the GEOTRACES Intermediate Data Product (IDP) 2021 (GEOTRACES Intermediate Data Product Group, 2021). Multi-elemental analyses at UTAS followed the protocol as described in Wuttig et al. (2019). Briefly, trace metals were preconcentrated offline from 10-50 mL of seawater samples using an automated, commercially available sea*FAST* system (S2 pico; Elemental Scientific, USA), in which samples were passed through two 200 µL columns filled with Nobias PA-1 resin, and the targeted trace metals were extracted with 10% HNO_3. The preconcentrated samples were analysed using a sector-field inductively coupled plasma mass spectrometer (SF-ICP-MS; ELEMENT 2; Thermo Fisher Scientific). Elemental concentrations were calculated using a combination of external calibration and standard addition internal calibration and corrected with the mean procedural blank from each preconcentration batch. The uncertainties on these Pb concentration measurements were generally better than ± 0.6 pmol/kg.

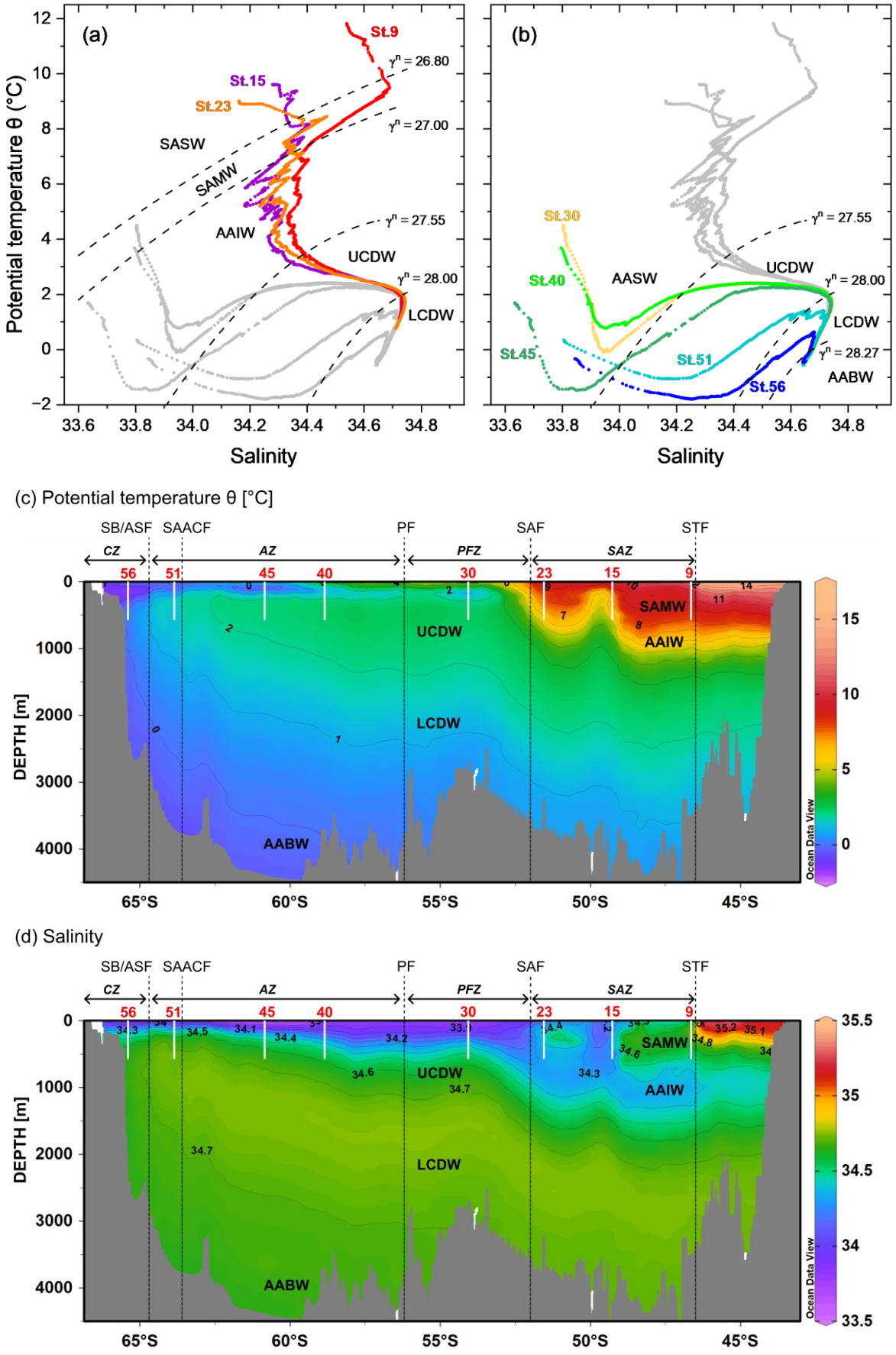

(a)
(b)
Potential temperature θ (°C)
Salinity
St.9
St.15
St.23
St.30
St.40
St.45
St.51
St.56
SASW
SAMW
AAIW
AASW
UCDW
LCDW
AABW
γn = 26.80
γn = 27.00
γn = 27.55
γn = 28.00
γn = 28.27
(c) Potential temperature θ [°C]
(d) Salinity
SB/ASF
SAACF
PF
SAF
STF
CZ
AZ
PFZ
SAZ
56
51
45
40
30
23
15
9
DEPTH [m]
65°S
60°S
55°S
50°S
45°S
Ocean Data View

Figure 4.3.

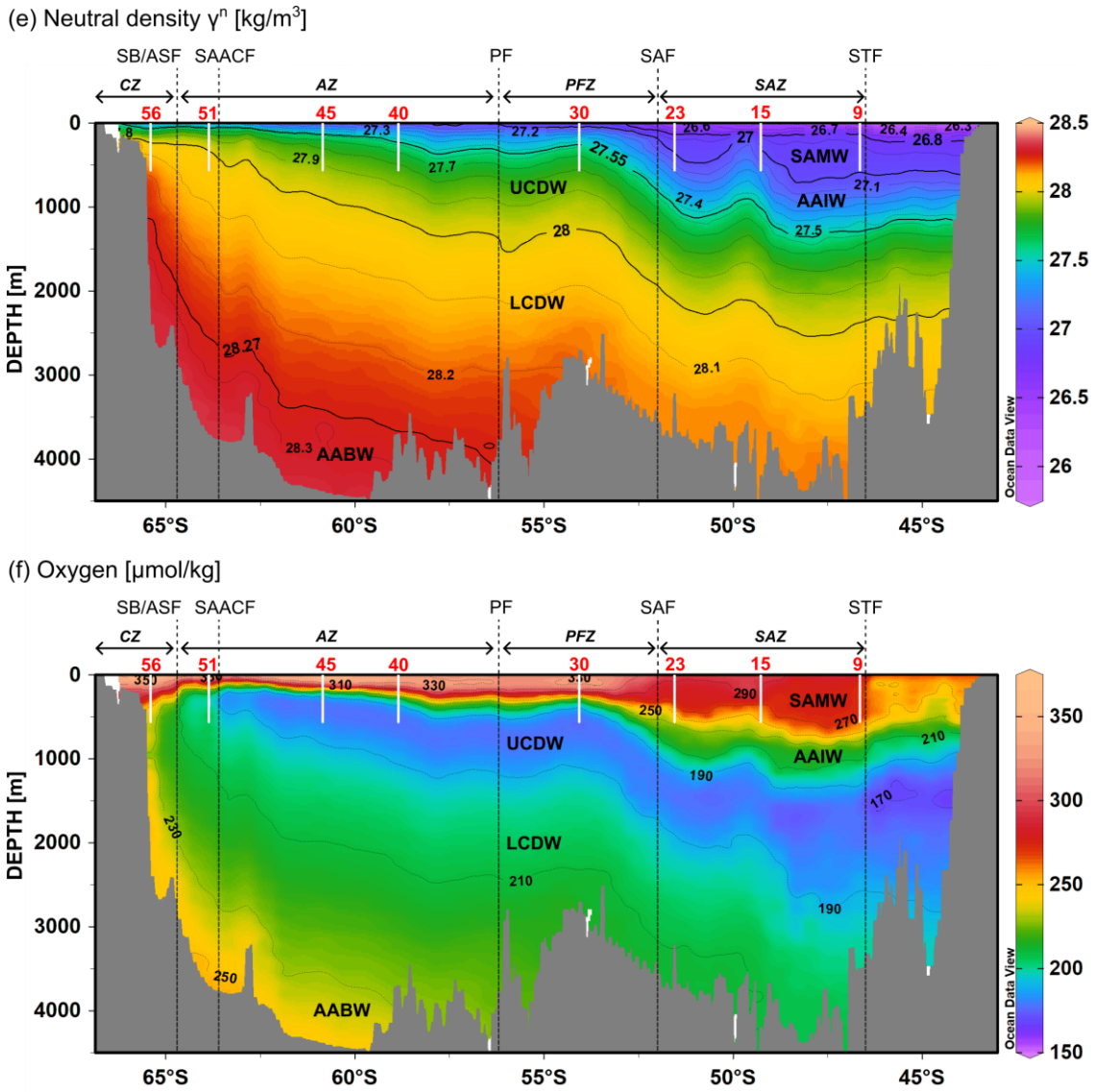


Figure 4.3. (cont'd). Hydrography of the study area, sampled during the GEOTRACES GS01 expedition. (a-b) Potential temperature and salinity data for the stations measured for Pb concentrations and isotopes. Black dashed lines indicate the neutral density isopycnals that separate the major water masses. (c-f) Meridional section plots of potential temperature (c), salinity (d), neutral density (e) and oxygen concentration (f) along the GS01 transect. In panel (e), thick, solid lines denote the neutral density horizons that demarcate the major water masses across the transect. The locations of stations sampled for Pb (texts in red) and the oceanographic zones and fronts (texts in black) are indicated at the top of each panel. Grey surface denotes bathymetry generated by the GEBCO 2014 6×6 min grid. The section plots were created using the ODV software (Schlitzer, 2020).

Table 4.3. Summary of the water masses and characteristics along the SR3 line.

	Water Mass	γ^n (kg/m^3)
SASW	Subantarctic Surface Water	26.3-26.8
AASW	Antarctic Surface Water	26.7-27.5
SAMW	Subantarctic Mode Water	26.85-27.00
AAIW	Antarctic Intermediate Water	27.00-27.55
UCDW	Upper Circumpolar Deep Water	27.55-28.00
LCDW	Lower Circumpolar Deep Water	28.00-28.27
AABW	Antarctic Bottom Water	> 28.27

4.4 Results

4.4.1 Water Mass Distributions

Major water masses encountered along the SR3 line during the GS01 expedition are identified according to potential temperature (θ), salinity (S), neutral density (γ^n) and oxygen concentration (Fig. 4.3; Table 4.3).

Upper waters (0 to 150 m) are characterised by a poleward trend of decreasing temperature and salinity towards the Antarctic margin. The STF (~47°S) separates the warm and saline subtropical surface waters (θ = 12-16°C, S = 35.1-35.3, γ^n < 26.3 kg/m^3) to the north from the relatively cool and fresh Subantarctic Surface Water (SASW) (θ = 8-12°C, S = 34.1-34.7, γ^n = 26.3-26.8 kg/m^3) in the SAZ to the south. The supply of subtropical waters north of the STF vary seasonally with the flow regime. During the GS01 expedition in austral summer, the surface water north of the STF was dominated by Subtropical Lower Water from the Tasman Sea, which flows westward along the Tasman Outflow (Sokolov and Rintoul, 2002; Ridgway, 2007). South of the SAF (~52°S), the surface layer is occupied by the Antarctic Surface Water (AASW) (γ^n = 26.8-27.5 kg/m^3), which is characterised by low temperatures (between -2 and 5°C), as well as the lowest salinities (33.6-34.0) and highest oxygen concentrations (320-373 μmol/kg) across the entire GS01 section.

North of the SAF, a body of relatively warm, fresh and low-density water occupies the subsurface and intermediate depths, which corresponds to SAMW and the underlying AAIW. SAMW in this region forms by deep winter convection of local surface water within the SAZ (McCartney, 1977, 1982; Hanawa and Talley, 2001), which is identified by a pycnostad (γ^n = 26.85-27.00 kg/m^3) across subsurface/intermediate depths of 150-500 m and a linear θ-S trend for the SAZ station 9. AAIW fills intermediate depths of 500-1100 m (γ^n = 27.00-27.55 kg/m^3) north of the SAF and is identified by a salinity minimum of < 34.4. Across the three sampled stations in the SAZ, AAIW is principally fed by cool, fresh mode waters that subducted in the Southwest Atlantic Ocean (θ < 8°C, S < 34.4) and spread eastward along the ACC (Rintoul and Bullister, 1999; Sokolov and Rintoul, 2000; Sloyan and Rintoul, 2001; Herraiz-Borreguero and Rintoul, 2010; Koch-Larrouy et al., 2010).

Circumpolar Deep Water dominates the deeper portion of the water column (γ^n = 27.55-28.27 kg/m^3) (Orsi et al., 2002). The Upper Circumpolar Deep Water (UCDW) (γ^n = 27.55-28.0 kg/m^3) originates from the poorly ventilated deep waters in the Pacific and Indian Oceans, characterised by an oxygen minimum (< 190 μmol/kg) that extends up to the Southern Boundary of the ACC (~65°S) (Callahan, 1972; Tamsitt et al., 2019). The oxygen minimum associated with UCDW dissipates south of the SB, and the shallower depth (< 300 m) of the CZ station 56 is replaced by cold, oxygen-rich Antarctic shelf waters. The Lower Circumpolar Deep Water (LCDW) (γ^n = 28.00-28.27 kg/m^3) originates principally from the saline North Atlantic Deep Water (NADW) and is identified by a deep salinity maximum (> 34.70) that extends up to the Antarctic margin (Callahan, 1972). The depth ranges of both CDW layers

shoal progressively towards the Antarctic margin. UCDW occupies a deeper range of 1100-2300 m in the SAZ (stations 9-23) below the deeper isopycnals of SAMW and AAIW, and fills intermediate depths in the PFZ/AZ to the south (e.g. 200-1100 m, AZ station 40). LCDW occupies the deepest part of the water column in the SAZ, from about 2300 m depth down to the seafloor, and fills shallower depth ranges at stations 30-56 further south (e.g. 1100-3500 m, AZ station 40).

Along various regions of the Antarctic continental slope, sinking of cold, dense Antarctic shelf waters and the upwelled LCDW form dense AABW ($\gamma^n > 28.27$ kg/m^3) (Orsi et al., 1999; Talley, 2013). In the Australian sector of the Southern Ocean, AABW is fed by two main sources, the Adélie Land Bottom Water and Ross Sea Bottom Water (Orsi et al., 1999; Rintoul and Bullister, 1999), and during the GS01 cruise, the low salinity (< 34.7) of AABW indicates dominant influence by the former source from the Wilkes-Adélie Land Coast at the time of sampling. AABW is characterised by sub-zero bottom temperatures and relatively high oxygen concentrations (> 225 μmol/kg). The presence of the dense AABW along the section is confined to stations 40-56 within the Australian-Antarctic Basin, south of the Southeast Indian Ridge.

4.4.2 Dissolved Pb Concentrations and Isotopes

All the dissolved Pb concentration and isotope results along the GS01 transect are reported in Table 4.4 and Appendix Table A4, and the along-section and vertical distributions of dissolved Pb concentrations and isotope compositions are shown in Figures 4.4 and 4.5, respectively.

4.4.2.1 Subantarctic Zone (SAZ)

Across the three SAZ stations (9, 15 and 23), Pb concentrations range between 4.1 and 15.3 pmol/kg. The highest Pb concentrations of 15.1 and 15.3 pmol/kg were obtained at intermediate water depths of 296 and 987 m respectively at station 9, whilst the lowest Pb concentrations of 4.1 and 4.7 pmol/kg were obtained at the near-bottom depths of 3200 m at station 9 and 3097 m at station 23 respectively. In detail, the Pb concentration profiles are characterised by maximum levels of 10.8-15.3 pmol/kg in the subsurface and intermediate depth layers of SAMW and AAIW (100-1100 m, γ^n = 26.8-27.55), overlain by slightly lower Pb concentrations of 10.1-11.9 pmol/kg in the surface mixed layer (< 100 m, γ^n = 26.3-26.8, SASW). Lead concentrations decrease with depth through CDW (> 1100 m, $\gamma^n > 27.55$), where the lowest Pb concentration across the SAZ (4.1 pmol/kg) were obtained in the deepest LCDW sample (3200 m) at station 9. One exception is an outlier at 2953 m depth at station 23 with a Pb concentration of 11.8 pmol/kg. Latitudinally across the SAZ, Pb concentrations in the subsurface and intermediate depths (100-1100 m) decrease slightly towards the Subantarctic Front at the south, whilst no clear spatial trends in Pb concentrations are apparent in the CDW range across the SAZ.

The Pb isotope compositions at the three SAZ stations – $^{206}Pb/^{207}Pb$ = 1.147-1.163 and $^{208}Pb/^{207}Pb$ = 2.423-2.440, show relatively little vertical variability. The relatively high Pb concentrations in the upper and intermediate waters (SASW, SAMW and AAIW) coincide with relatively low $^{206}Pb/^{207}Pb$

(1.149 ± 0.002) and $^{208}Pb/^{207}Pb$ (2.425 ± 0.002) ratios. In the underlying CDW, in which Pb concentrations are lower, slightly higher $^{206}Pb/^{207}Pb$ (1.154-1.163) and $^{208}Pb/^{207}Pb$ (2.430-2.440) ratios are observed. While LCDW contains lower levels of Pb (4.7-6.5 pmol/kg) than the overlying UCDW (7.4-11.0 pmol/kg), the average Pb isotope compositions across LCDW ($^{206}Pb/^{207}Pb \approx 1.160$, $^{208}Pb/^{207}Pb \approx 2.438$) are identical within error to UCDW (≈ 1.159, ≈ 2.435). The LCDW sample at station 23 with anomalously high Pb concentration (11.8 pmol/kg; 2953 m) also shows lower $^{206}Pb/^{207}Pb$ (1.150) and $^{208}Pb/^{207}Pb$ (2.426) ratios compared to the samples at adjacent depths (1.163, 2.440). This Pb concentration value has been verified by triplicate measurements and is in agreement with the result reported by the UTAS laboratory (see Fig. 4.6a and Section 4.5.1). Across the SAZ, $^{206}Pb/^{207}Pb$ and $^{208}Pb/^{207}Pb$ ratios within each water mass are homogeneous.

Table 4.4. Lead concentration and isotope data for seawater samples from the GEOTRACES section GS01 presented in this study.

Depth (m)	[Pb][(a)] (pmol/kg)	1sd[(b)]	$^{206}Pb/^{207}Pb$[(c)]	$^{208}Pb/^{207}Pb$[(c)]	$^{206}Pb/^{204}Pb$[(c)]	Neutral Density (kg/m^3)	Water Mass
Subantarctic Zone (SAZ)							
Station 9 (46.65°S, 145.25°E; bottom depth: 3344 m)							
14	10.7	0.3	1.149	2.424	17.92	26.31	SASW
49	11.9	0.5	1.147	2.423	17.90	26.40	SASW
97	13.6	0.1	1.153	2.427	17.98	26.86	SAMW
296	15.1	0.2	1.149	2.426	17.95	26.93	SAMW
987	15.3*	0.3	1.147	2.423	17.88	27.32	AAIW
1480	9.6	0.4	1.154	2.430	18.00	27.69	UCDW
2457	6.1	0.2	1.159	2.437	18.09	28.01	LCDW
3200	4.1	0.2	1.159	2.438	18.09	28.11	LCDW
Station 23 (51.55°S, 143.00°E; 3628 m)							
14	10.3	0.2	1.150	2.426	17.94	26.52	SASW
49	10.1	0.1	1.149	2.425	17.92	26.52	SASW
96	10.1	0.2	1.153	2.430	18.01	26.60	SASW
295	12.9	0.4	1.150	2.427	17.95	26.95	SAMW
493	11.5*	0.3	1.151	2.427	17.97	27.09	AAIW
984	10.8	0.1	1.151	2.426	17.95	27.53	AAIW
1972	7.4	0.1	1.163	2.440	18.17	27.96	UCDW
2953	11.8	0.3	1.150	2.426	17.94	28.12	LCDW
3097	4.7	0.4	1.163	2.440	18.14	28.14	LCDW

(a) Reported Pb concentrations are the averages of triplicate measurements.
(b) 1× standard deviation of triplicate measurements of Pb concentration in pmol/kg.
(c) Precisions of Pb isotope measurements are given by the 2× standard deviations from replicate analyses of in-house reference materials, which correspond to ~1400 ppm, ~400 ppm and ~2200 ppm for $^{206}Pb/^{207}Pb$, $^{208}Pb/^{207}Pb$ and $^{206}Pb/^{204}Pb$ respectively.

* Denote samples with one of the triplicate values being removed from the calculation of the average Pb concentrations, due to significant discrepancies (> ~2 pmol/kg) from the other replicate values (i.e. potential contamination).

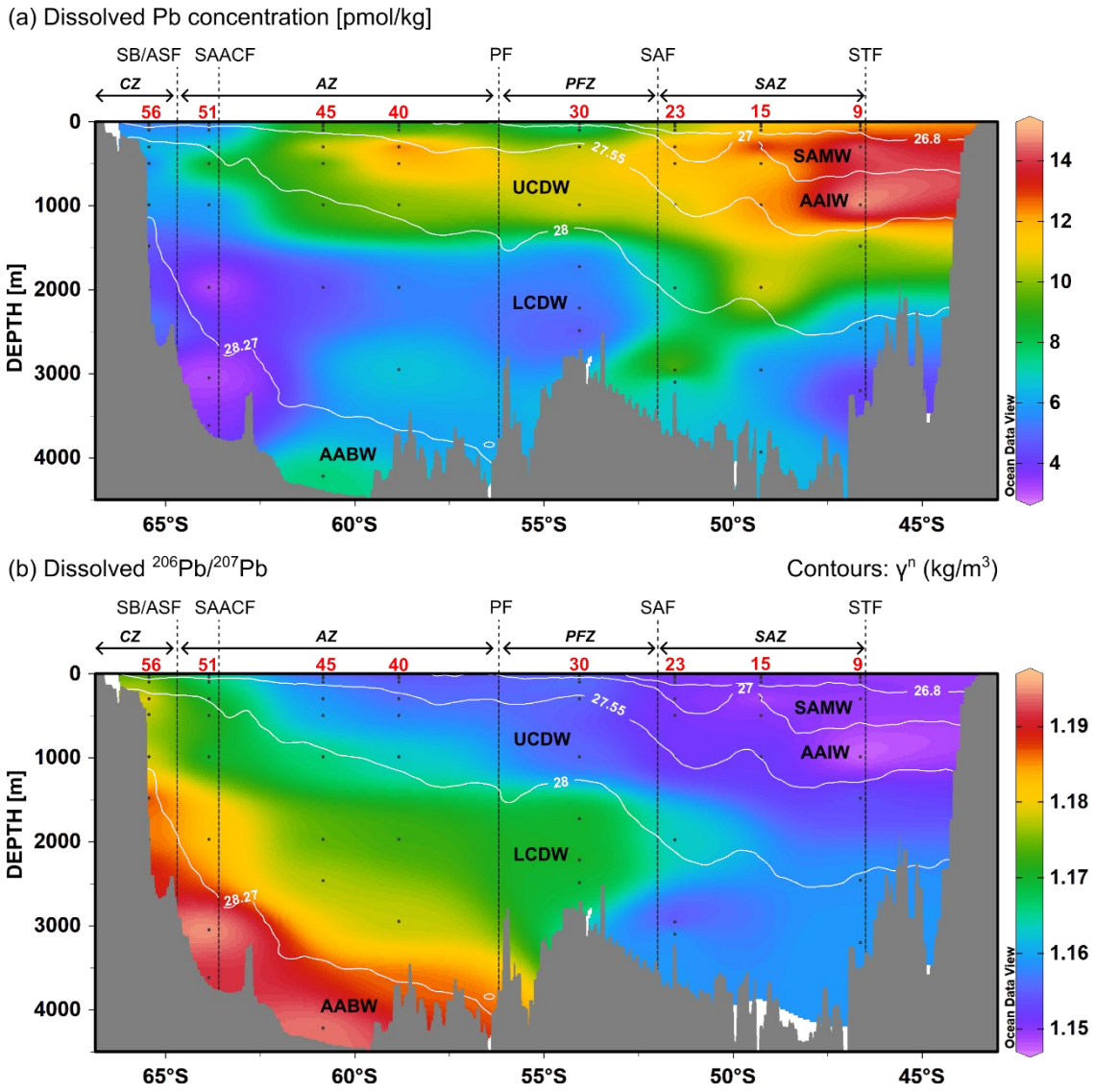


Figure 4.4. Meridional section plots of measured (a) Pb concentrations and (b) $^{206}Pb/^{207}Pb$ ratios along the GS01 transect. Sampling locations and depths are shown as black dots; white contours denote the neutral density horizons that demarcate the major water masses. The anomalous Pb concentration data at station 45 is omitted from plot (a). Graphics were created using the ODV software (Schlitzer, 2020).

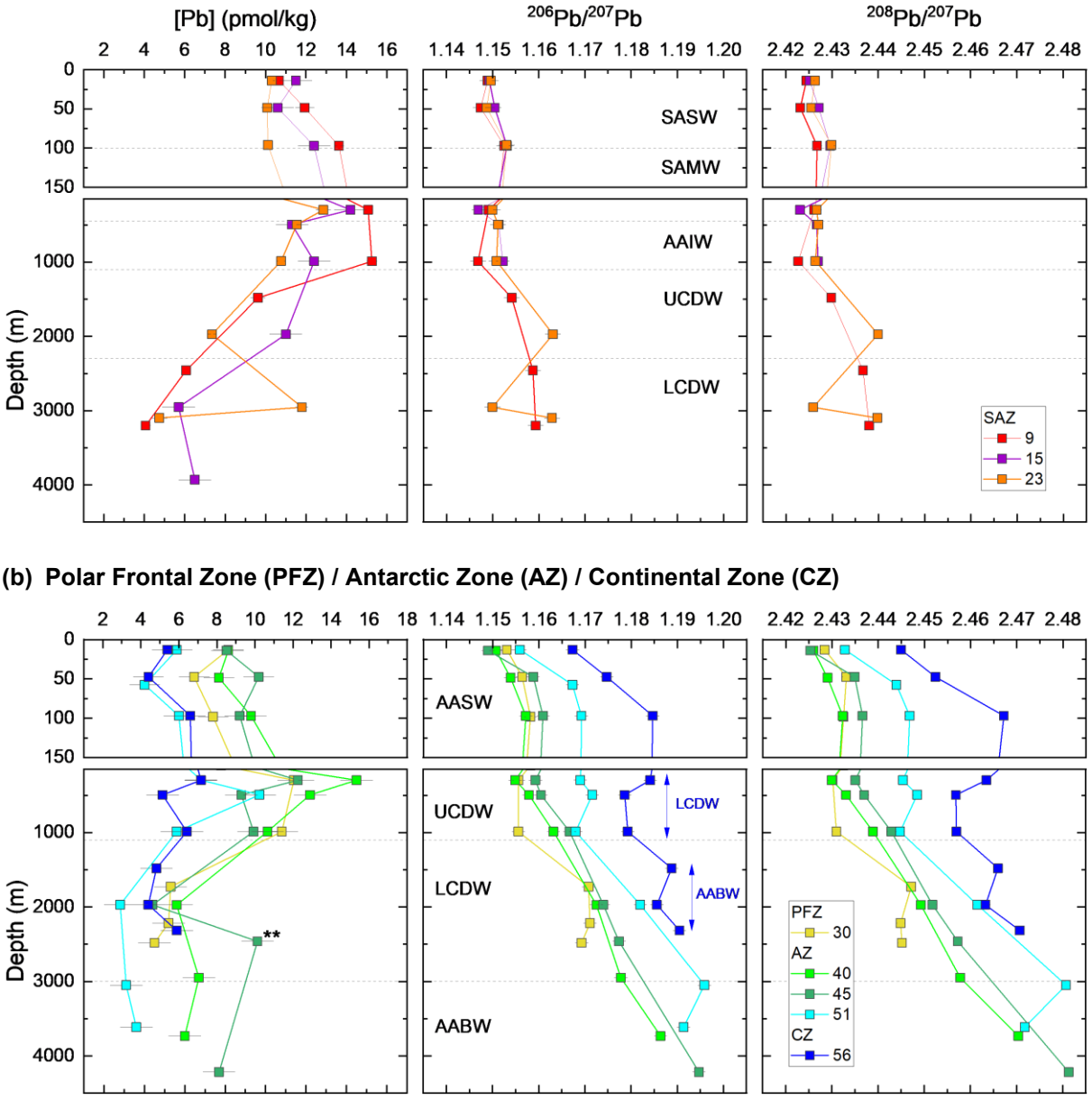


Figure 4.5. Vertical depth profiles of Pb concentrations ([Pb]), $^{206}Pb/^{207}Pb$ and $^{208}Pb/^{207}Pb$ ratios for the eight stations sampled for Pb concentrations and isotopes from the GS01 transect. Upper panels (a) show results for the SAZ, north of the SAF (< ~52°S); lower panels (b) show results for the PFZ, AZ and CZ, south of the SAF. Double asterisk (**) denotes the Pb concentration value from station 45 that is flagged as anomalous. Horizontal lines mark the average boundary depths of major water masses (refer to Table 4.3 for the full names of water masses and exact density horizons). The distinct water mass distributions at the CZ station 56 are indicated by the water mass labels next to its $^{206}Pb/^{207}Pb$ profile (lower middle panel). Error bars denote the precisions of Pb concentration (1 SD) and isotope (2 SD) measurements; these are only shown if larger than the symbol size.

4.4.2.2 Latitudinal variations in Pb concentrations and isotopes across the GS01 transect

The new data from the GS01 transect allow, for the first time, description of the first-order large-scale variations in Pb concentration and isotope composition across the Southern Ocean (Fig. 4.4; 4.5). In general, the GS01 transect is characterised by low Pb concentrations (3-15 pmol/kg) and large variations in $^{206}Pb/^{207}Pb$ (1.15-1.20) and $^{208}Pb/^{207}Pb$ (2.42-2.48) ratios. Across the surface mixed layer (SASW and AASW), Pb concentrations decrease steadily poleward, from 10-12 pmol/kg in the SAZ close to Tasmania (stations 9-23), to 4-7 pmol/kg at the southern end of the transect close to Antarctica (stations 51 and 56). Decreasing Pb concentrations in surface and subsurface waters southwards are accompanied by increasing $^{206}Pb/^{207}Pb$ and $^{208}Pb/^{207}Pb$ ratios, from ≈ 1.150 and ≈ 2.426 at the SAZ stations 9-23, to ≈ 1.170 and ≈ 2.447 respectively at stations 51 and 56 (southern AZ and CZ). As described for the SAZ in the previous section, Pb concentrations decrease and $^{206}Pb/^{207}Pb$ and $^{208}Pb/^{207}Pb$ ratios increase with depth. The most elevated Pb concentrations (15 pmol/kg) and lowest $^{206}Pb/^{207}Pb$ (≈ 1.147) and $^{208}Pb/^{207}Pb$ (≈ 2.423) ratios are observed in SAMW and AAIW that occupy the subsurface and intermediate depths in the SAZ. Deep and bottom waters (AABW and LCDW) close to the Antarctic margin (e.g. station 51) are the most depleted in Pb (≈ 3 pmol/kg) and have the highest $^{206}Pb/^{207}Pb$ (1.189 ± 0.005) and $^{208}Pb/^{207}Pb$ (2.471 ± 0.007) ratios. UCDW samples across the transect are characterised by relatively elevated Pb concentrations (7-12 pmol/kg) as well as intermediate and relatively homogeneous $^{206}Pb/^{207}Pb$ (1.159 ± 0.005) and $^{208}Pb/^{207}Pb$ (2.435 ± 0.005) ratios. Across the LCDW layer, Pb concentrations are generally low across the transect (3-7 pmol/kg), while $^{206}Pb/^{207}Pb$ and $^{208}Pb/^{207}Pb$ ratios in the SAZ are distinctively lower (1.160 ± 0.002, 2.438 ± 0.002) than in the ACC belt (1.175 ± 0.005, 2.452 ± 0.007) south of the Subantarctic Front, which appears to mark a dividing line in LCDW isotope compositions.

4.5 Discussion

4.5.1 Inter-laboratory Comparison of Dissolved Pb Concentration Data

Figure 4.6 and Table A5 in the Appendix show the Pb concentration results obtained by the laboratories at ICL and at UTAS for GS01 seawater samples from the same stations. Whilst sampling at sea followed the same protocol for all samples, subsequent processing for Pb concentrations at ICL and UTAS differed as outlined in Sections 4.3.2 and 4.3.3 respectively.

Across all eight stations, similar Pb concentration profiles are obtained based on the data determined in both laboratories (Fig. 4.6a). Three results, two from UTAS and one from ICL, are henceforth omitted from a detailed comparison of the data. The excluded UTAS data were flagged in the GEOTRACES IDP 2021 as 'bad values' and encompass the anomalously high Pb concentration of 17.0 pmol/kg at 984 m depth of station 23, and the anomalously low Pb concentration of 3.4 pmol/kg at 3928 m depth of station 15 (GEOTRACES Intermediate Data Product Group, 2021). The omitted ICL result is the Pb concentration of 9.6 pmol/kg measured for 2461 m depth at station 45. Notably, this result is

significantly higher than the Pb concentration of 4.1 pmol/kg that was determined at UTAS for the same sample. Furthermore, the ICL value significantly exceeds the Pb concentrations of deep water samples from adjacent depths at the same station (4.4 pmol/kg, 1970 m; 7.7 pmol/kg, 4216 m), and the sample does not coincide with any unusual hydrographic features or anomalous concentrations of other dissolved trace metals (e.g. Mn, Fe, Figure A6 in the Appendix). The significantly higher ICL value was therefore most likely impacted by contamination during sample handling and was hence not further considered.

Excluding the three outliers, the majority (80%) of the 67 samples analysed in both laboratories display Pb concentrations that agree to within 2.4 pmol/kg. In detail, the measured values for samples from station 9 show the best inter-laboratory agreement, as the results agree to within 1 pmol/kg or 10% of the Pb concentrations. As such, the results largely agree within the quoted intra-laboratory precisions (0.1-0.8 pmol/kg). Most data for samples from station 15 agree to within 2 pmol/kg or 20% of the Pb concentrations. For most samples from stations 23, 30 and 51, the ICL Pb concentrations are 0.4-2.4 pmol/kg (7-33%, average 21%) lower than the data obtained at UTAS. In contrast, for most samples from stations 40, 45 and 56, the ICL values are 0.4-4.2 pmol/kg (6-61%, average 33%) higher than the Pb concentrations obtained at UTAS.

The overall agreement between the Pb concentrations determined in the two laboratories is furthermore assessed by a linear regression analysis (Fig. 4.6b). The linear regression fitted for the UTAS versus the ICL data exhibits a statistically significant ($p << 0.05$) correlation with $r^2 = 0.51$, a slope of 0.68 ± 0.01 and a y-intercept of 1.2 ± 0.6. The slope of < 1 indicates an overall bias of the ICL data towards higher Pb concentrations, which is most apparent for samples with lower Pb concentrations. In particular, a significant proportion of the samples with UTAS-measured Pb concentration of less than 8 pmol/kg plot close to a 1:2 correlation line and these results are dominated by samples from stations 40, 45 and 56 at more southern latitudes, which show the lowest Pb concentrations, whereby the ICL values are conspicuously higher (Fig. 4.6a).

Measurements of seawater Pb concentrations at levels as low as those encountered in the GS01 transect (8 ± 3 pmol/kg) are extremely challenging. Both laboratories are rigorous in the control and correction of Pb blanks but contamination during sample processing cannot be ruled out as the origin of the discrepancies. Procedural Pb blanks for the analyses of the GS01 samples are only available for the ICL laboratory, and these were 20.2 ± 11.3 pg (1 SD, $n = 18$) for the 2017/2018 data for stations 15, 30, 40, 45, 51 and 56 and 5.6 ± 3.0 pg (1 SD, $n = 18$) for the 2021 analyses of samples from stations 9 and 23. However, low Pb procedural blanks of 2-7 pg, converted from published values of 0.2-0.6 pmol/kg, were reported for earlier analyses at the UTAS laboratory (Wuttig et al., 2019). As such, it is conceivable that the slightly higher ICL Pb concentrations are a consequence of insufficient blank corrections, as the ICL sample preparation procedure is more elaborate and blank contamination may hence be more variable. However, other analytical issues, such as Pb loss during sample preparation at

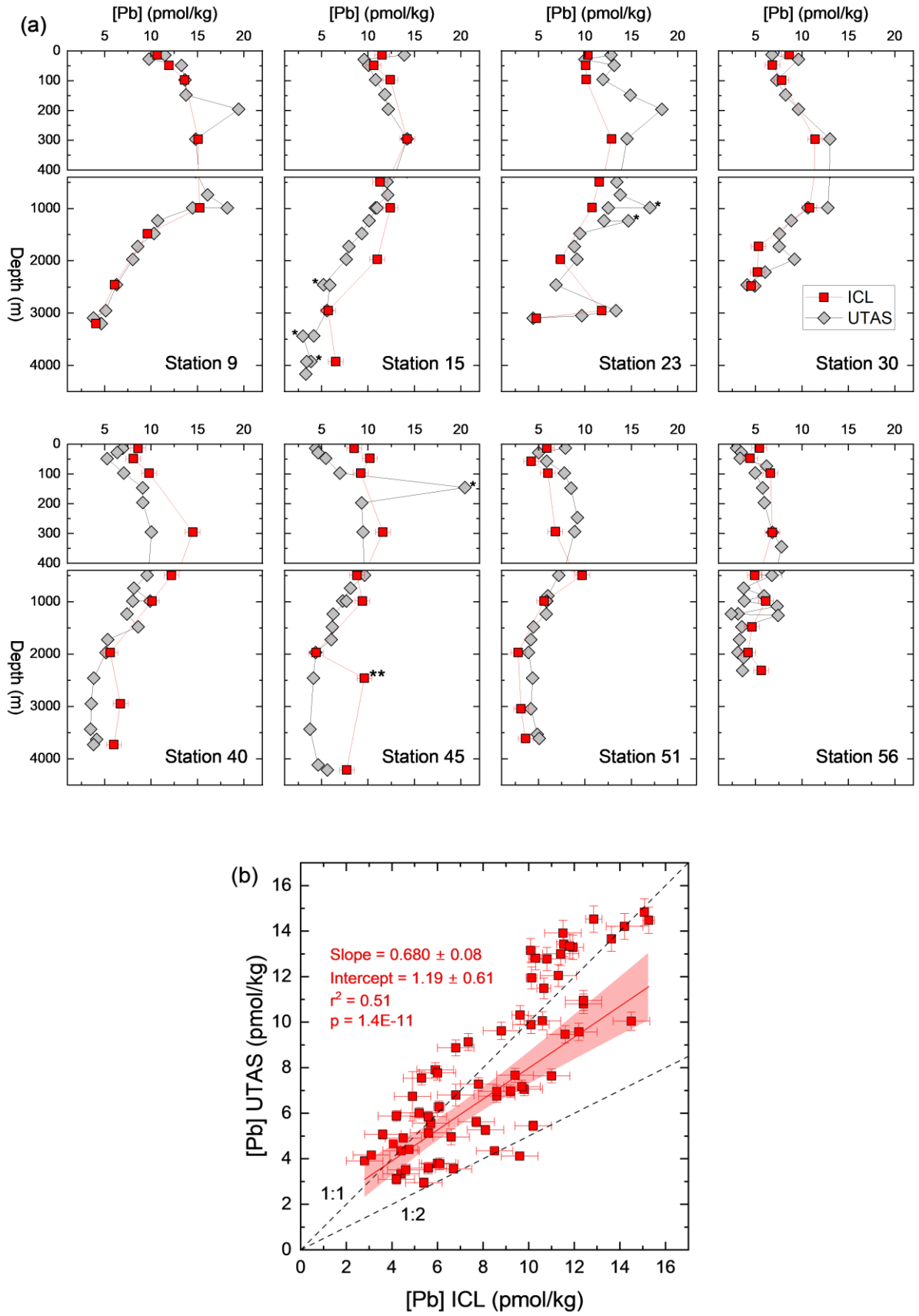

(a)
[Pb] (pmol/kg)
Depth (m)
ICL
UTAS
Station 9
Station 15
Station 23
Station 30
Station 40
Station 45
Station 51
Station 56
(b)
Slope = 0.680 ± 0.08
Intercept = 1.19 ± 0.61
r2 = 0.51
p = 1.4E-11
1:1
1:2
[Pb] UTAS (pmol/kg)
[Pb] ICL (pmol/kg)

Figure 4.6.

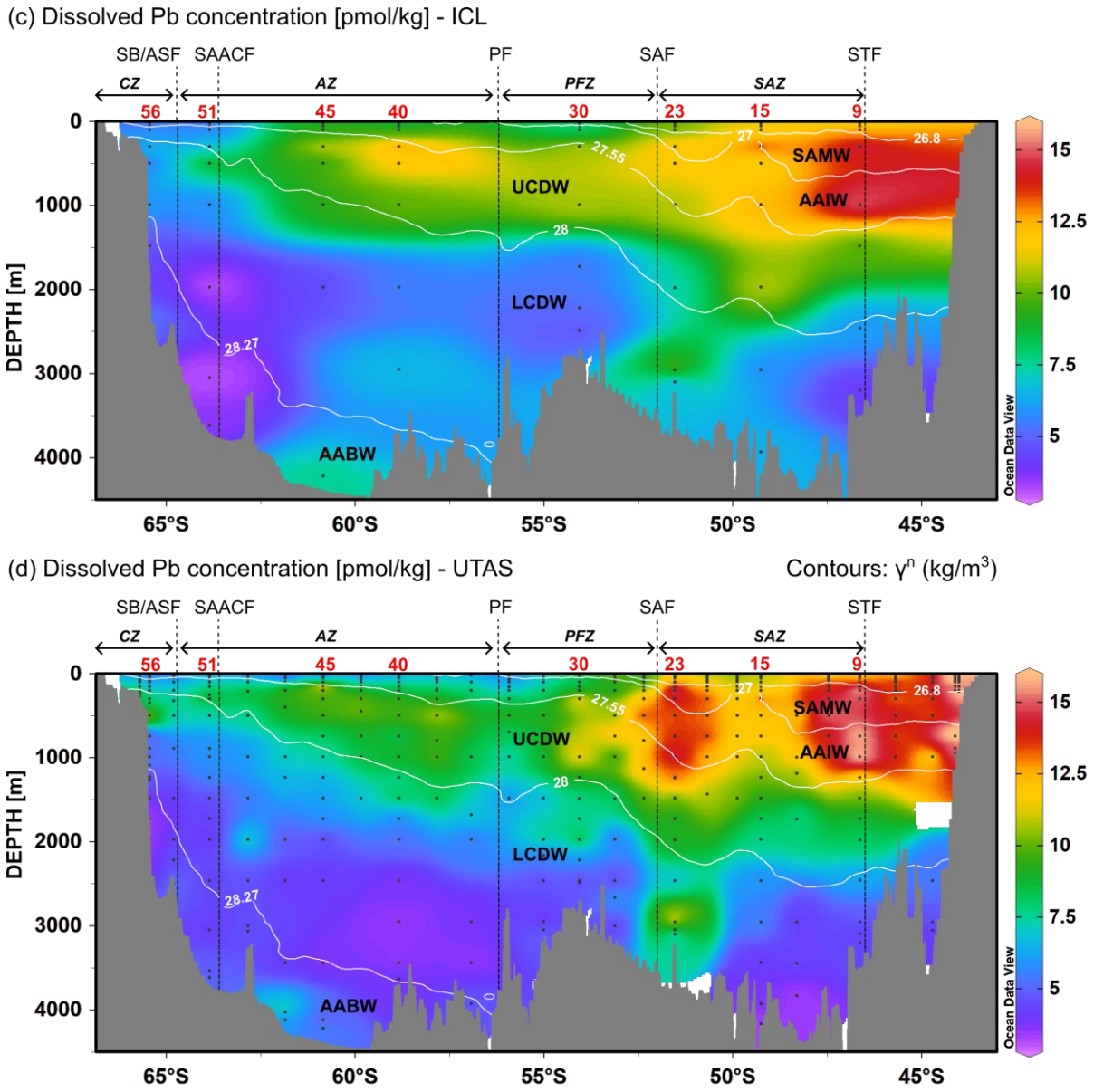


Figure 4.6 (cont'd). Inter-laboratory (ICL and UTAS) comparison of measured Pb concentrations along the GS01 transect. (a) Vertical depth profiles of Pb concentration data from ICL (Griffiths, 2019 and this study) and UTAS (data by Andrew Bowie et al.; GEOTRACES Intermediate Data Product Group 2021) for the eight stations with measurements from both laboratories. Single (*) and double (**) asterisks denote flagged values from the UTAS and ICL laboratories respectively (see text for the criteria of data quality). Error bars indicate the 1 SD precisions reported by each laboratory; shown only if they exceed the symbol size. (b) A correlation plot of Pb concentration values of UTAS versus ICL. Black dashed lines denote 1:1 and 1:2 correlations. Red solid line denotes the correlation line from weighted linear regression analysis, with shade indicating the 95% confidence interval. An outlier from the UTAS dataset that lies beyond the scale is not shown. (c, d) Meridional section plots of measured Pb concentrations along the GS01 transect obtained by the UTAS (c) and ICL (d) laboratories, respectively.

the UTAS laboratory (where no Pb spike that corrects for such losses is added to samples), cannot be ruled out at present.

With the majority of the ICL and UTAS Pb concentration data agreeing to within 2.4 pmol/kg for measured Pb concentrations of 8 ± 3 pmol/kg (1 SD), the bias between the results is typically 33% or better. Notably, this is similar to the agreement of 20-30% that was reported for a recent intercomparison of Pb concentration data (Boyle et al., 2020). The latter investigation evaluated repeated analyses of samples with Pb concentrations of 11 ± 8 pmol/kg (n = 861), as determined in different laboratories from GEOTRACES section GP16 in the Southeast Pacific Ocean. As such, the differences found here between the Pb concentrations of the ICL and UTAS laboratories are not unusual and a currently unavoidable consequence of the extremely challenging analyses. Notably, a superior inter-laboratory agreement of better than 15% was reported for an earlier GEOTRACES intercalibration effort (Zurbrick et al., 2012), but investigated samples with much higher Pb concentrations of 60 ± 22 pmol/kg (n = 33), and where the measurements are hence less prone to analytical artefacts.

Despite the identified limitations in the accuracy of the Pb concentration results, the data quality is readily sufficient to resolve key vertical gradients and the spatial heterogeneities within and between major water masses along the transect. This is highlighted by Fig. 4.6c, d, which shows along-section plots of the dissolved Pb concentrations determined in the two laboratories. In particular, both plots reveal relatively high Pb concentrations of > 12 pmol/kg at subsurface and intermediate depths in the SAZ, where SAMW and AAIW are present, with maximum concentrations at the northern SAF station 9. A tongue of intermediate Pb concentrations (10-11 pmol/kg) can be observed for UCDW in both plots, with both diagrams also delineating the southward thinning of this water mass. The data from both laboratories also highlight that the lowest Pb concentrations of 2-7 pmol/kg are present in the deep and bottom water masses of LCDW and AABW, and within the water columns of the southernmost stations 51 and 56. Furthermore, both laboratories found unusually high Pb concentration in the near-bottom samples from station 23.

4.5.2 Natural and Anthropogenic Sources of Pb to the Southern Ocean Sector South of Tasmania

The Pb isotope signatures of potential source areas to the studied region are assessed by compiling the relevant literature data, including (1) loess deposits representing the natural mineral dust from Australia (Vallelonga et al., 2010), (2) volcanic emissions from Antarctica (Mount Erebus, Sims et al., 2008), (3) anthropogenic aerosols from the urban areas of Australia, southern Africa and Patagonia (Bollhöfer and Rosman, 2000), and (4) river sediments from mainland Australia (De Deckker et al., 2010) and Tasmania (Townsend and Seen, 2012) (Fig. 4.7a). The Pb isotope compositions of seafloor Fe-Mn crusts from the vicinity of the GS01 transect, which act as archives of the pre-anthropogenic compositions of local deep and bottom waters, are compiled for comparison (Abouchami and Goldstein,

1995). In general, natural sources exhibit high $^{206}Pb/^{207}Pb$ (> 1.19) and $^{208}Pb/^{207}Pb$ (> 2.47) ratios, while anthropogenic aerosols are characterised by low $^{206}Pb/^{207}Pb$ (1.06-1.16) and $^{208}Pb/^{207}Pb$ (2.33-2.43) ratios. The latter is attributed to historic consumptions of 'Broken Hill -type' leaded petrol across the Southern Hemisphere nations that was manufactured principally with Pb ores from Australian mines such as Broken Hill and Mount Isa (Bollhöfer and Rosman, 2000), which exhibit very low $^{206}Pb/^{207}Pb$ (≈ 1.04) and $^{208}Pb/^{207}Pb$ (≈ 2.32) ratios (Doe and Stacey, 1974; Townsend et al., 1998). The compositions of Australian/Tasmanian river sediments lie between natural mineral dust and anthropogenic aerosols from Australia, suggesting the combined influence of local weathering products as well as transported mineral dust and anthropogenic aerosols.

In the triple isotope space ($^{206}Pb/^{207}Pb$-$^{208}Pb/^{207}Pb$), the dissolved Pb isotope data across the GS01 transect define a linear mixing array (r^2 = 0.99, n = 67) between two endmembers: (1) a natural endmember defined by the Australian loess and local Fe-Mn crusts, and (2) an anthropogenic endmember defined by the various aerosol sources in the Southern Hemisphere (Fig. 4.7a). In a plot of $^{206}Pb/^{207}Pb$ versus Pb concentration, the GS01 data define a mixing array between a low-$^{206}Pb/^{207}Pb$ endmember with an elevated Pb concentration, and a high-$^{206}Pb/^{207}Pb$ endmember that has a lower Pb concentration (Fig. 4.7b). This suggests that the anthropogenic endmember, characterised by lower $^{206}Pb/^{207}Pb$ (and $^{208}Pb/^{207}Pb$), is enriched in Pb compared to the natural endmember. Data from the Subantarctic Zone show the lowest $^{206}Pb/^{207}Pb$ (and $^{208}Pb/^{207}Pb$) isotope ratios and highest Pb concentrations of the GS01 array, suggesting relatively strong anthropogenic influence throughout the water column in this region (red symbols). GS01 samples on the other end of the mixing array are mainly those associated with LCDW and AABW close to Antarctica, indicating the most natural Pb signatures in those samples (green inverted triangles and pentagons).

The overlap between Australian mineral dust and local Fe-Mn crust (Fig. 4.7a) suggests that Australian mineral dust could form a key source of Pb to the ancient deep and bottom waters of the region, and hence contribute to the natural Pb signature that is most strongly present in the LCDW and AABW samples. This finding corroborates with mineral dust dispersal modelling in the Southern Ocean (Li et al., 2008), which suggested that Australian mineral dust dominates the natural dust input (≥ 80%) to the Southern Ocean region between Tasmania and Antarctica. For the anthropogenic endmember, potential candidates are SE Australian / Tasmanian aerosols, Tasmanian river sediments, and Southern African and Patagonian anthropogenic aerosols. If anthropogenic aerosols are assumed to have similar dispersal behaviour as mineral dust as modelled by Li et al. (2008), aerosols from SE Australia and Tasmania are likely the major source of the anthropogenic endmember in the GS01 samples.

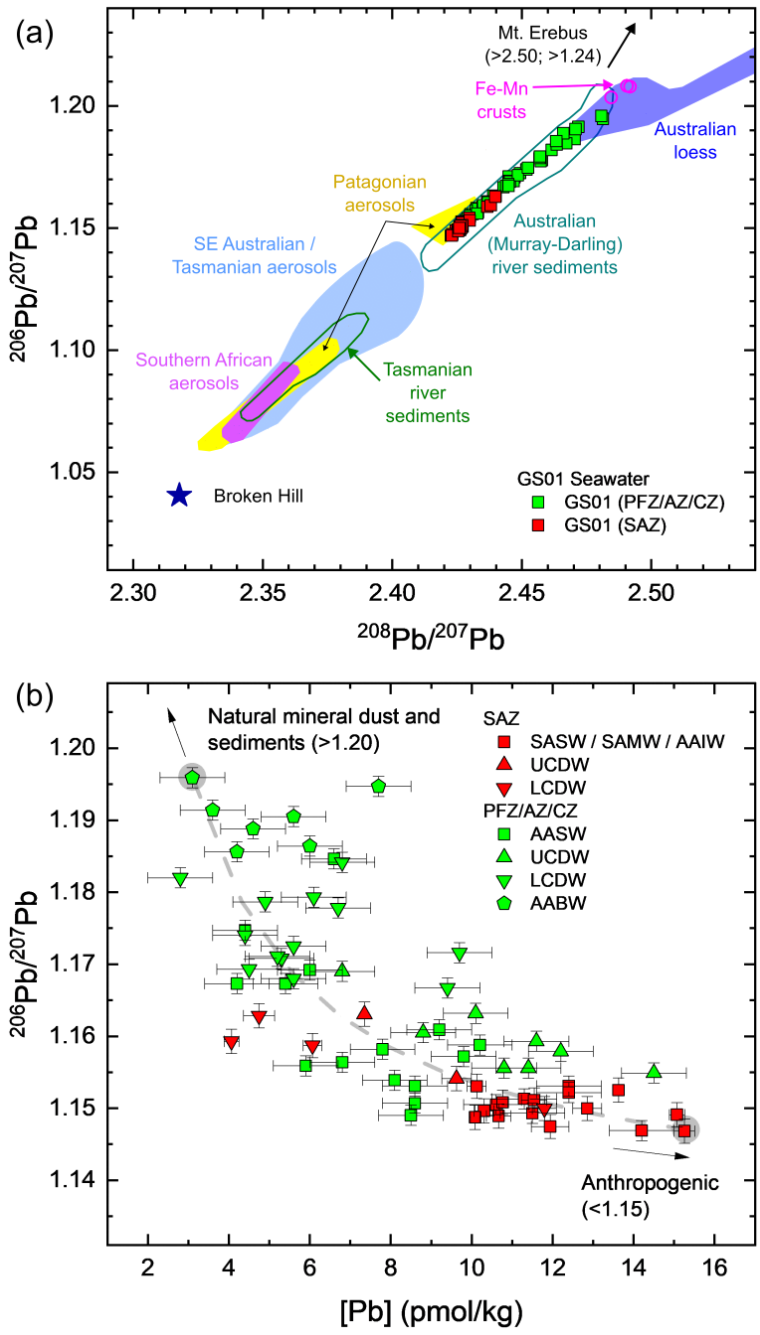


Figure 4.7. (a) $^{206}Pb/^{207}Pb$ versus $^{208}Pb/^{207}Pb$ ratios for all seawater samples from the GS01 transect in comparison to literature data. Colour-filled fields indicate the literature data of potential sources of atmospheric input: aerosols from Tasmania and the southeastern part of Australia (Bollhöfer and Rosman, 2000; Wu et al., 2016), southern Africa and Patagonia (Bollhöfer and Rosman, 2000); Quaternary loess from southern Australia defining the natural mineral dust source (Vallelonga et al., 2010). Open fields indicate the literature data of river sediments from Australia: Murray-Darling Basin, southeastern Australia (De Deckker et al., 2010); Derwent River, Tasmania (Townsend and Seen, 2012). Lead ores from the Broken Hill mine in Australia characterise the compositions of the leaded petrol consumed across large parts of the Southern Hemisphere (Doe and Stacey, 1974; Townsend et al., 1998). Seafloor Fe-Mn crusts from south of Tasmania and New Zealand characterise the ancient deep and bottom water compositions in the region (Abouchami and Goldstein, 1995). Lava samples from Mount Erebus characterise the volcanic emissions from Antarctica's Ross Sea region (Sims et al., 2008). **(b) $^{206}Pb/^{207}Pb$ ratios versus Pb concentrations for all seawater samples from the GS01 transect.** The grey dotted line shows the calculated mixing curve between two endmembers defined by the samples with the lowest and highest $^{206}Pb/^{207}Pb$ respectively.

4.5.3 Sources and Cycling of Pb in the Upper and Intermediate Waters of the SAZ (SASW, SAMW and AAIW)

The upper and intermediate waters of the Subantarctic Zone are characterised by the highest Pb concentrations (10.1-15.3 pmol/kg) and lowest $^{206}Pb/^{207}Pb$ (1.147-1.153) and $^{208}Pb/^{207}Pb$ (2.423-2.430) ratios across the GS01 transect (Fig. 4.5; 4.7b). The dissolved Pb budget in the surface mixed layer of the SAZ (SASW) is below discussed in terms of atmospheric input and lateral advection within a typical mixed layer residence time of less than 2 years for Pb (Schaule and Patterson, 1981; Flegal and Patterson, 1983; Boyle et al., 1986). The dissolved Pb budget at the subsurface and intermediate depths (SAMW and AAIW) is discussed in terms of the transfer of historic input through advection and potential modification by the vertical transport and redissolution / remineralisation of particles.

4.5.3.1 Surface mixed layer (SASW)

Across the mixed layer of the GS01 transect, relatively high Pb concentrations ([Pb] = 10-12 pmol/kg) and low $^{206}Pb/^{207}Pb$ ($\approx$ 1.150) and $^{208}Pb/^{207}Pb$ ($\approx$ 2.426) ratios are found in the SAZ relative to the ACC region south of the Subantarctic Front ([Pb] < 10 pmol/kg; $^{206}Pb/^{207}Pb$ = 1.158 $\pm$ 0.006, $^{208}Pb/^{207}Pb$ = 2.434 $\pm$ 0.007) (Fig. 4.5). Mineral dust dispersal modelling by Li et al. (2008) showed significantly higher dust flux of Australian origin to the SAZ ($10^{-5.6}$ to $10^{-5.1}$ kg/m^2) than to the ACC region ($10^{-6.5}$ to $10^{-5.7}$ kg/m^2). The observed increase in surface water Pb concentrations from the ACC region to the SAZ could therefore reflect the larger flux of atmospheric particles to the latter region. However, the lower surface water $^{206}Pb/^{207}Pb$ and $^{208}Pb/^{207}Pb$ ratios in the SAZ indicate that the enhanced Pb input into this region is coupled with increasing influence of anthropogenic (i.e. polluted) Pb, rather than natural Pb from mineral dust. This could reflect the heavy pollution of atmospheric particles from Australia, which results in stronger anthropogenic perturbations to the surface waters of the SAZ where the atmospheric particle flux is higher. Alternatively – or additionally – a similar signal could arise from southward advection of polluted subtropical surface waters along the EAC – Tasman Outflow and the Zeehan Current (Clementson et al., 1998; James et al., 2002), which are likely to have accumulated elevated levels of dissolved Pb as they propagate along the Australian-Tasmanian shelf.

4.5.3.2 Subsurface and intermediate depth layers (SAMW and AAIW)

Across the subsurface and intermediate depths (100-1100 m) of the SAZ, waters characterised as SAMW and AAIW carry slightly higher Pb concentrations (13-15 pmol/kg) than those in the mixed layer (Fig. 4.4; 4.5a). Lead isotope ratios are homogenous across SAMW and AAIW and the overlying mixed layer ($^{206}Pb/^{207}Pb$ = 1.150 $\pm$ 0.002, $^{208}Pb/^{207}Pb$ = 2.426 $\pm$ 0.002).

SAMW south of Tasmania is formed locally by deep convection of local mixed layer water during austral winters (Rintoul and Bullister, 1999; Hanawa and Talley, 2001). The pCFC-11 apparent age for SAMW in the studied region is approximately 3 years (Rintoul and Bullister, 1999). Therefore, the observed isotope homogeneity between the mixed layer and SAMW could reflect the stable isotope

signatures of the (polluted) Pb input from Australia over the recent few years before seawater sample collection in 2018.

In contrast, AAIW south of Tasmania constitutes of advected waters that originate from the Southwest Atlantic and/or Southeast Pacific Oceans (Sloyan and Rintoul, 2001; Herraiz-Borreguero and Rintoul, 2011). The low temperature ($\theta < 8$°C) and salinity (< 34.4) observed in the SAZ during the GS01 expedition indicates the presence of the cooler and fresher Atlantic-derived variety of AAIW (Fig. 4.3a). The pCFC-11 apparent age for AAIW in the area is 21-26 years (Rintoul and Bullister, 1999), in the order of the modelled residence time for Pb (< 30 years) at depths of 0-2000 m in the region (Henderson and Maier-Reimer, 2002). This suggests that the preformed Pb budget at the time of ventilation in the Southwest Atlantic Ocean (the 1990s) could impact the observed Pb signatures of AAIW in the studied region. The observed $^{206}Pb/^{207}Pb$ (1.147-1.152) and $^{208}Pb/^{207}Pb$ (2.423-2.427) signatures of the Tasmanian AAIW during GS01 are very similar to those of AAIW samples collected in the Southwest Atlantic Ocean in 2012, of $^{206}Pb/^{207}Pb \approx 1.153$ and $^{208}Pb/^{207}Pb \approx 2.426$, at station 18 of the GEOTRACES section GA10 (Fig. 4.8a) (data by Maxence Paul (ICL) and available in the GEOTRACES IDP 2021; GEOTRACES Intermediate Data Product Group, 2021). The Tasmanian AAIW data also overlap with the data of AAIW samples collected in the subtropical South Indian Ocean in 2009, of $^{206}Pb/^{207}Pb$ = 1.146-1.149 and $^{208}Pb/^{207}Pb$ = 2.421-2.427, at stations 11 and 12 along the GEOTRACES section GI04 (Fig. 4.8b) (Lee et al., 2015), which shares the same Southwest Atlantic origin and a similar ventilation age (< 25 years) as the Tasmanian AAIW (Fine et al., 2008). In summary, the Pb isotope signature of the Tasmanian AAIW agrees with upstream AAIW signatures in the Indian and Atlantic Oceans. Therefore, advection of AAIW that was ventilated about 25 years ago in the Southwest Atlantic Ocean seems a plausible explanation for the observed AAIW Pb signatures along the GS01 transect.

Sinking of particles from the mixed layer into the ocean interior and subsequent release of Pb into the dissolved pool ('vertical flux') was proposed by Griffiths (2019) to explain the enhanced anthropogenic contribution to the Pb budget of the intermediate depth waters of the GS01 transect. Such a vertical process could provide an alternative explanation for the observed enrichment in Pb concentrations, as well as the homogeneous isotope compositions of SAMW and AAIW relative to the overlying mixed layer (Fig. 4.5a). In addition, enrichment in dissolved Mn was observed in SAMW (100-300 m) and was attributed to the offshore transport of Tasmanian shelf waters that had been enriched with dissolved Mn from sediment redissolution (see Fig. A6 in the Appendix) (Latour et al., 2021). Release from sediment and riverine particles is widely recognised as a mechanism for injecting dissolved Pb near the seafloor and along continental margins and large estuaries (Annibaldi et al., 2009; Noble et al., 2015; Chien et al., 2017; Rusiecka et al., 2018), as dissolved Pb is reductively released from sediments and carried offshore by Fe-Mn oxyhydroxide colloids (Kalnejais et al., 2007; Noble et al., 2015). The observed co-enrichment in dissolved Pb and Mn in SAMW, therefore, supports lateral

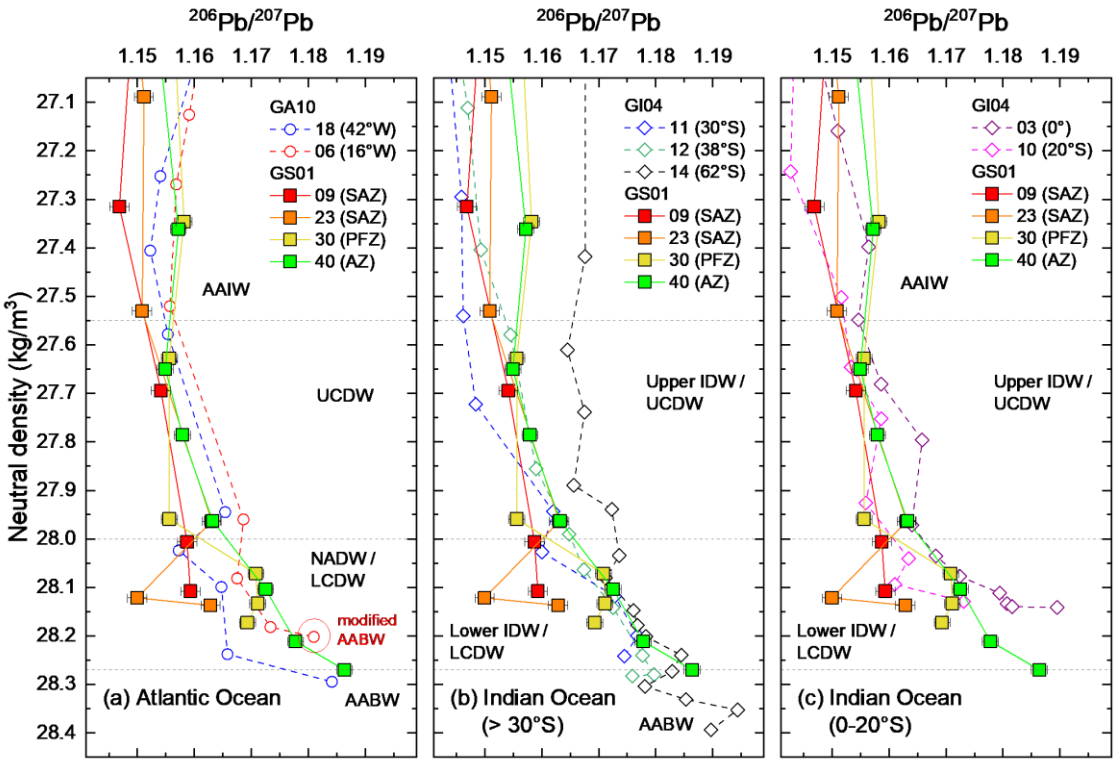


Figure 4.8. Profiles of $^{206}Pb/^{207}Pb$ versus neutral density (γ^n > 27.0) for four stations from the GS01 transect (colour-filled squares; stations 9, 23, 30 and 40) in comparison to published data from reference stations in the Atlantic and Indian Oceans. (a) Stations 6 and 18 from the GEOTRACES section GA10 in the South Atlantic Ocean (open circles; data by Maxence Paul (ICL); GEOTRACES Intermediate Data Product Group, 2021); (b-c) stations 11, 12 and 14 in the South Indian Ocean and stations 3 and 10 in the Central Indian Ocean, GEOTRACES section GI04 (open diamonds; Lee et al., 2015). Horizontal dashed lines mark the neutral density boundaries of major water masses.

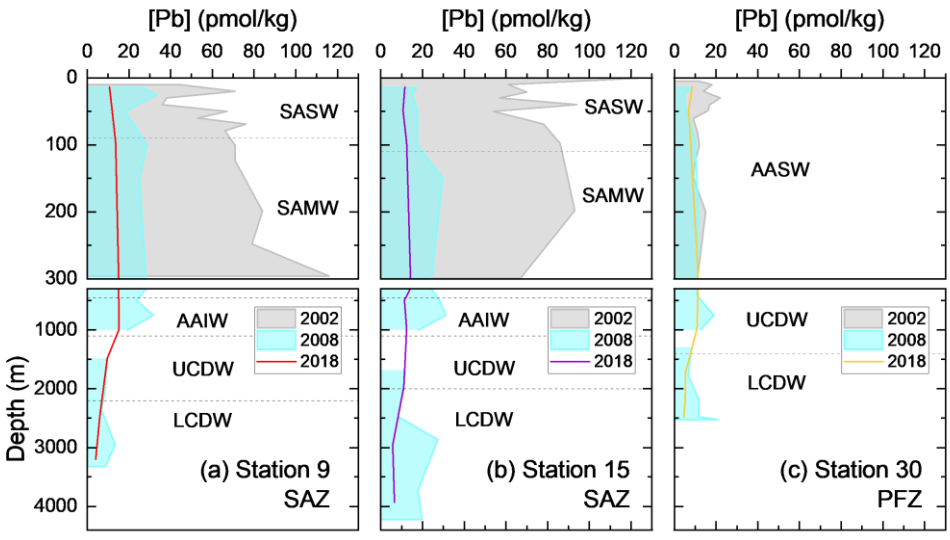


Figure 4.9. Time series profiles of Pb concentrations obtained near three GS01 stations (SAZ stations 9 and 15; PFZ station 30) during the period 2002-2018. Periods of sample collection: grey shaded regions – November 2002 (Lai et al., 2008); cyan shaded regions – March/April 2008 (data by Andrew Bowie et al. and available in the GEOTRACES IDP 2017; Schlitzer et al., 2018); solid lines – January/February 2018 (Griffiths, 2019 and this study).

input from Mn-rich sediments on the Tasmanian shelf and/or river particles from Tasmania as an additional source of dissolved Pb to the subsurface waters of the SAZ. The Pb isotope compositions of Tasmanian river sediments overlap with anthropogenic aerosols from Australia (Fig. 4.6a), making a local source a possibility.

4.5.4 Temporal Evolution of Dissolved Pb Concentrations in the SAZ

Near the SAZ stations 9 and 15 and the PFZ station 30, dissolved Pb concentrations were sampled and measured during two earlier expeditions in November 2002 (CLIVAR-SR3 expedition, Lai et al., 2008) and in March/April 2008 (GEOTRACES section GIPY06, data by Andrew Bowie et al. and available in the GEOTRACES IDP 2017; Schlitzer et al., 2018) (Fig. 4.9). Together with the GS01 data from the current study, this enables reconstruction of the temporal evolution of dissolved Pb concentrations in the region over the period 2002-18 across two oceanographic zones (SAZ and PF).

4.5.4.1 Upper and intermediate waters (2002-18)

The upper waters (< 300 m) of the SAZ (SASW and SAMW) showed significantly higher levels of dissolved Pb during 2002 (72 ± 22 pmol/kg), six times the levels in 2018 (12 ± 2 pmol/kg) (Fig. 4.9a, b). A strong, threefold decline in Pb concentration was observed during the initial interval from 2002 to 2008 (23 ± 6 pmol/kg), followed by an attenuated twofold decline to the 2018 levels. In contrast, the upper waters of the PFZ in 2002 (15 ± 4 pmol/kg) were only about two times the levels in 2018 (≈ 8 pmol/kg) (Fig. 4.9c). An enhanced latitudinal gradient in Pb concentration therefore existed across the Subantarctic Front in 2002, which weakened over time, as the upper waters of the SAZ experienced a dramatic decline in Pb concentrations.

The dramatic decline in upper water Pb concentrations over the period 2002-18 probably reflects the progress of phasing-out of leaded petrol in Australia, which involved the onset of nationwide regulation on the amount of allowable Pb in petrol in 1995-96, followed by a complete ban on leaded petrol consumption in 2002 (Kristensen, 2015; Kristensen et al., 2017). Lead concentrations in SASW and the subducting SAMW remained high in 2002 (72 ± 22 pmol/kg, Fig. 4.9a, b), due to continuous consumption of leaded petrol in Australia before the complete ban. High Pb input flux was likely delivered to the subantarctic upper waters through the westerly transport of heavily polluted aerosols from Australia, as well as the southward flow of subtropical waters that accumulated polluted riverine and atmospheric inputs near the Australian margin. The strong, threefold decline in Pb concentrations between 2002 and 2008 in the SAZ reflects the decrease in atmospheric input in response to the elimination of leaded petrol in Australia since 2002. Compared to the 2018 levels, dissolved Pb in these surface and subsurface waters were still about two times higher in 2008, six years since the elimination of leaded petrol in Australia. This could reflect the re-emission of previously deposited petrol-derived Pb from the land surface or changes in emission loads from other industrial activities between 2008 and 2018. In contrast, the upper waters of the more southerly PFZ showed much lower Pb concentrations in

2002 (15 ± 4 pmol/kg, Fig. 4.9c), which likely reflects lower atmospheric deposition, as well as efficient eastward advection of surface waters by the ACC along its major flow path.

4.5.4.2 Deep waters (2008-18)

Dissolved Pb concentrations for the ocean interior (> 300 m) along the SR3 line were also sampled and measured during the GEOTRACES GIPY06 expedition in March/April 2008 (data by Andrew Bowie et al. and available in the GEOTRACES IDP 2017; Schlitzer et al., 2018). Together with the GS01 data from the current study, the decadal evolution of deep water Pb concentrations in the studied area can be examined.

Across the SAZ and PFZ, significantly higher Pb concentrations were observed in 2008 in the deepest part of the water column (LCDW) compared to the data in 2018 (Fig. 4.9). At stations 9 and 30, Pb concentrations within the bottom 300-400 m (depths of 2954-3327 m, station 9; 2179-2522 m, station 30) in 2008 (9-13 pmol/kg) were about twice the levels in the same depth ranges in 2018 (4-5 pmol/kg). At station 30, the bottom sample (2522 m) from the 2008 dataset shows even higher Pb concentration of 21 pmol/kg. At station 15, the Pb concentrations in LCDW between depths of about 2900 and 4200 m in 2008 (18-27 pmol/kg) were up to four times the levels in 2018 (≈ 6 pmol/kg). In contrast, Pb concentrations at lesser depths in UCDW had remained relatively unchanged between 2008 (7-12 pmol/kg) and 2018 (5-11 pmol/kg).

The most reasonable explanation for the deep water enrichment in dissolved Pb in 2008 is provided by enhanced vertical flux driven by reversible scavenging of particles. The influx of Pb into the upper ocean was higher in 2008. These fluxes were even higher in the years before 2008. During 2008, the sinking particles derived from the upper ocean likely remained enriched in Pb, from their indigenous inventory and/or through additional scavenging from the seawater. These particles could release their enriched Pb budget into the deep seawater, during their sinking through the water column and/or following their deposition on the seafloor and subsequent resuspension in benthic nepheloid layers. The latter mechanism has been suggested to explain observations of near-bottom enrichment in dissolved Pb in the North Atlantic Ocean (Noble et al., 2015; Chapter 3 of this thesis). In contrast, the Pb released from the surface-derived particles in more recent time (2018) could have decreased following the decline in Pb input to the upper ocean, which resulted in lower amounts of Pb that were delivered to the deep ocean by sinking particles.

4.5.5 Sources and Cycling of Pb in the Deep Water of the SAZ (UCDW and LCDW)

In the Australian sector of the Southern Ocean, UCDW (γ^n = 27.55-28.00) originates predominantly from IDW, whilst LCDW (γ^n = 28.00-28.27) originates from NADW (Rintoul and Bullister, 1999; Talley, 2013). IDW (γ^n = 27.7-28.1) in turn originates from a dense mixture of NADW and AABW that flows northward into the Indian Ocean (defined as 'Lower IDW', γ^n = 28.0-28.1), where the water mass undergoes modification, upwells and flows southward into the Southern Ocean (defined as 'Upper

IDW', γ^n = 27.7-28.0), forming UCDW (Park et al., 1993; McDonagh et al., 2008; Talley, 2013) (Fig. 4.2a). Both types of Circumpolar Deep Water are advected eastward by the ACC.

In this study, sharp latitudinal gradients are observed in the Pb isotope compositions of LCDW across the Subantarctic Front (Fig. 4.4b; 4.5). In detail, LCDW in the SAZ is characterised by markedly lower $^{206}Pb/^{207}Pb$ (1.160 ± 0.002) and $^{208}Pb/^{207}Pb$ (2.438 ± 0.002) ratios than at the four PFZ and AZ stations across the main ACC belt ($^{206}Pb/^{207}Pb$ = 1.175 ± 0.005 and $^{208}Pb/^{207}Pb$ = 2.452 ± 0.007). Such a latitudinal gradient is absent for Pb concentration, as the LCDW samples of the SAZ stations and the more southern stations are uniformly low in Pb concentration (5.4 ± 1.0 pmol/kg and 5.9 ± 1.9 pmol/kg, respectively) (Fig. 4.4a; 4.5).

4.5.5.1 Advective inputs to UCDW (and LCDW) along the GS01 transect

The strong circumpolar flow of the ACC across the Southern Ocean advocates for advection as a key control on the Pb budget to the Circumpolar Deep Water of the studied region (Griffiths, 2019). This can be assessed by comparing the Pb isotope signatures of CDW along the GS01 transect with upstream deep water data from the South Indian Ocean (GEOTRACES section GI04; Lee et al., 2015) and the South Atlantic Ocean (GEOTRACES section GA10; data by Maxence Paul (ICL) and available in the GEOTRACES IDP 2021; GEOTRACES Intermediate Data Product Group, 2021) (Fig. 4.2a; 4.8).

Across both the SAZ and the ACC region (PFZ/AZ) along the GS01 section, the observed Pb isotope signatures for UCDW ($^{206}Pb/^{207}Pb$ = 1.154-1.163, $^{208}Pb/^{207}Pb$ = 2.430-2.439) overlap with the signatures of Upper IDW within the same neutral density range (γ^n = 27.6-28.0) at GI04 stations 11 and 12 in the subtropical South Indian Ocean (1.148-1.165, 2.431-2.441; 30°S and 38°S), and fall below the UCDW signatures at the upstream region of ACC at GI04 station 14 in the Indian sector of the Southern Ocean (1.165-1.172, 2.443-2.447; 62°S) (Fig. 4.8b). This observation is consistent with the known (Upper) IDW origin of the UCDW that is advected to the Australian sector of the Southern Ocean (Park et al., 1993; van Aken et al., 2004).

In contrast, the observed Pb isotope compositions of LCDW along the GS01 section cannot be explained by the upstream (i.e. advected) ACC signature alone. Within the neutral density range of LCDW (γ^n = 28.0-28.2), the LCDW signature observed for GS01 stations in the ACC region ($^{206}Pb/^{207}Pb$ = 1.169-1.178, $^{208}Pb/^{207}Pb$ = 2.445-2.458; PFZ station 30 and AZ station 40) broadly agrees with the signature of NADW – the principal source of LCDW in the Southern Ocean, at GA10 station 6 in the Southeast Atlantic Ocean (≈ 1.168, ≈ 2.441), as well as the Lower IDW and LCDW signatures at GI04 stations 11, 12 and 14 across the South Indian Ocean (1.167-1.178, 2.443-2.454) (Fig. 4.8a, b). However, the LCDW signature for GS01 stations in the SAZ (≈ 1.160, ≈ 2.438; stations 9 and 23) is distinctively lower than the upstream signatures. Whilst similarly low $^{206}Pb/^{207}Pb$ (≈ 1.165) and $^{208}Pb/^{207}Pb$ (≈ 2.439) ratios were observed in the NADW samples at GA10 station 18, near the major flow path of NADW from the Southwest Atlantic Ocean into the Southern Ocean (Stramma and England, 1999) (Fig. 4.2a; 4.8a), this source is unlikely to explain the observed Pb isotope signature of LCDW in the SAZ along

the GS01 section. In particular, higher $^{206}Pb/^{207}Pb$ and $^{208}Pb/^{207}Pb$ ratios were consistently observed in LCDW samples across the Southeast Atlantic and South Indian Oceans (Fig. 4.8a, b), which suggest that the NADW-derived Pb signature has been modified by high- $^{206}Pb/^{207}Pb$ and $^{208}Pb/^{207}Pb$ source(s) of Pb along the ACC path as it reaches the Australian sector of the Southern Ocean.

Based on physical oceanographic knowledge, another source region for the deep water Pb signature in the SAZ is feasible: the lower southern latitudes in the Southeast Indian Ocean (Fig. 4.10a). While the ACC is traditionally considered as the major conveyor of the deep water filling the South Australian Basin (e.g. Rintoul and Bullister, 1999), the Deep Eastern Boundary Current (DEBC) has been increasingly recognised as a deep advective pathway to the basin, which carries IDW from the Southeast Indian Ocean, and propagates it along the West and South Australian continental slopes to join the ACC south of Tasmania (Fig. 4.2) (Talley, 2013; Tamsitt et al., 2019). Lagrangian particle transport modelling across the SR3 line indicated maximum eastward transport within the latitudinal range of the SAZ (48°S and 51°S), at the depth ranges of CDW between 1800 and 3500 m (Tamsitt et al., 2019), while velocity measurements at ~32°S west of Australia revealed net southward transport (4-9 Sv) across both the Upper and Lower IDW layers (γ^n = 27.7-28.11) along the West Australian continental slope (McDonagh et al., 2008).

The upstream signatures of the DEBC can be inferred from the limited dissolved Pb isotope data from east of the Central-Southeast Indian Ridge in the Central Indian Ocean (Fig. 4.2a; 4.8c) (Lee et al., 2015). At GI04 station 3 (0°) in the Bay of Bengal, the Pb isotope ratios in IDW ($^{206}Pb/^{207}Pb$ = 1.159-1.179, $^{208}Pb/^{207}Pb$ = 2.440-2.461; γ^n = 27.7-28.11) are significantly higher than the compositions of CDW at the two SAZ stations south of Tasmania (1.154-1.163, 2.430-2.440) within the same neutral density range, and therefore cannot explain the Pb budget of the latter. In contrast, the IDW samples at GI04 station 10 (20°S) in the Central Indian Basin reveal relatively low $^{206}Pb/^{207}Pb$ (1.153-1.163) and $^{208}Pb/^{207}Pb$ (2.434-2.440) ratios, which agree well with the Pb isotope signatures of CDW at the Tasmanian SAZ stations. Whilst the upstream dynamics of the DEBC north of the Perth Basin (~32°S) remain poorly constrained (Tamsitt et al., 2019), the above comparison nevertheless suggests that a type of IDW, characterised by Pb isotope signatures that are congruent with CDW in the SAZ south of Tasmania, is circulating on the east side of Central-Southeast Indian Ridge and could feasibly contribute to the advected Pb budget in the studied region.

4.5.5.2 Role of particulate exchange processes along the GS01 transect

An alternative explanation for the incongruence between the observed LCDW signatures in the SAZ and the advected ACC signatures stems from the observation that the LCDW Pb isotope signature seems to change quite abruptly at or near the position of the Subantarctic Front (i.e. between the SAZ and the ACC region) (Fig. 4.4b; 4.10b). The Subantarctic Front marks a biogeochemical boundary, which could hence separate different vertical processes on either side (e.g. particle compositions and associated behaviour of Pb). The sinking particles in the SAZ to the north and the PFZ to the south

exhibit distinct compositions, due to the distinct phytoplankton communities in their respective euphotic zones (Nissen et al., 2021). In the SAZ, productivity is dominated by calcifying coccolithophores and the sinking particles are dominated by calcium carbonate ($CaCO_3$, dominantly in calcite form), whilst in the PFZ to the south, productivity is dominated by silicifying diatoms and the sinking particles are dominated by biogenic silica (opal) (Kopczynska et al., 2001; de Salas et al., 2011; Ebersbach et al., 2011; Rigual-Hernández et al., 2015).

Experimental studies demonstrated distinct partitioning behaviour of the radionuclide ^{210}Pb into coccolithophores and diatoms (Lin et al., 2017). In coccolithophores, ^{210}Pb is scavenged primarily into the carbonate shells (coccosphere) due to favourable substitution of Pb^{2+} for Ca^{2+} in $CaCO_3$, whilst in diatoms, ^{210}Pb is scavenged into organic macromolecules embedded in the diatom frustules or inside the cells (Chuang et al., 2015; Lin et al., 2017). Assuming similar partitioning behaviour for the stable isotopes of Pb, the release of Pb from the scavenging particles would be dependent on the reactivity of the carrier phases in the deep ocean. Calcite remains relatively stable in the deep ocean above the calcite saturation horizon, i.e. the depth below which the extent of calcite dissolution increases significantly (Milliman et al., 1999). The modelled calcite saturation depth for the subantarctic latitudes south of Tasmania is about 3150 m (Bostock et al., 2011), which coincides with the depth range of LCDW in the SAZ (2200 m depth to the seafloor). Increased dissolution of the carbonate-rich ballast at LCDW depth will hence likely release the scavenged Pb content, characterised by the low $^{206}Pb/^{207}Pb$ (≈ 1.150) and $^{208}Pb/^{207}Pb$ (≈ 2.426) signatures of the upper ocean, into the dissolved pool, and this will modify the advected Pb signature from the ACC (≈ 1.17; ≈ 2.45). In contrast, opal ballasts are known for their substantial loss of organic carbon as they sink through subsurface and mesopelagic depths (100-1000 m) (Francois et al., 2002; Klaas and Archer, 2002; Ebersbach et al., 2011; Rosengard et al., 2015). In the PFZ, substantial release of the organically bound Pb from the opal ballast is hence expected at intermediate depths where UCDW is present, whilst the opaline particles that reach LCDW depths (> 1100 m depth) would be depleted in scavenged Pb and thus release only minor Pb flux to LCDW.

Notably, Pb concentrations in LCDW are uniformly low across the SAZ and the ACC region (Fig. 4.4a). This contrasts with observations in the deep North Pacific Ocean, where modifications of deep water Pb isotope compositions by vertical fluxes are coupled with an increase in seawater Pb concentrations (Wu et al., 2010; Lanning et al., 2023). This apparent mismatch can be reconciled by different Pb concentration baselines across the Subantarctic Front. LCDW is more poorly ventilated in the SAZ than in the ACC region (Rintoul and Bullister, 1999), which could lead to a greater loss of its preformed Pb budget to particle scavenging (i.e. more time to scavenge Pb). If LCDW in the SAZ is more depleted of preformed Pb, the replenishment of dissolved Pb in the SAZ through vertical fluxes may not result in higher Pb concentrations compared to the LCDW in the ACC region. Constraints on deep water Pb scavenging rates in the region are required to further test this hypothesis.

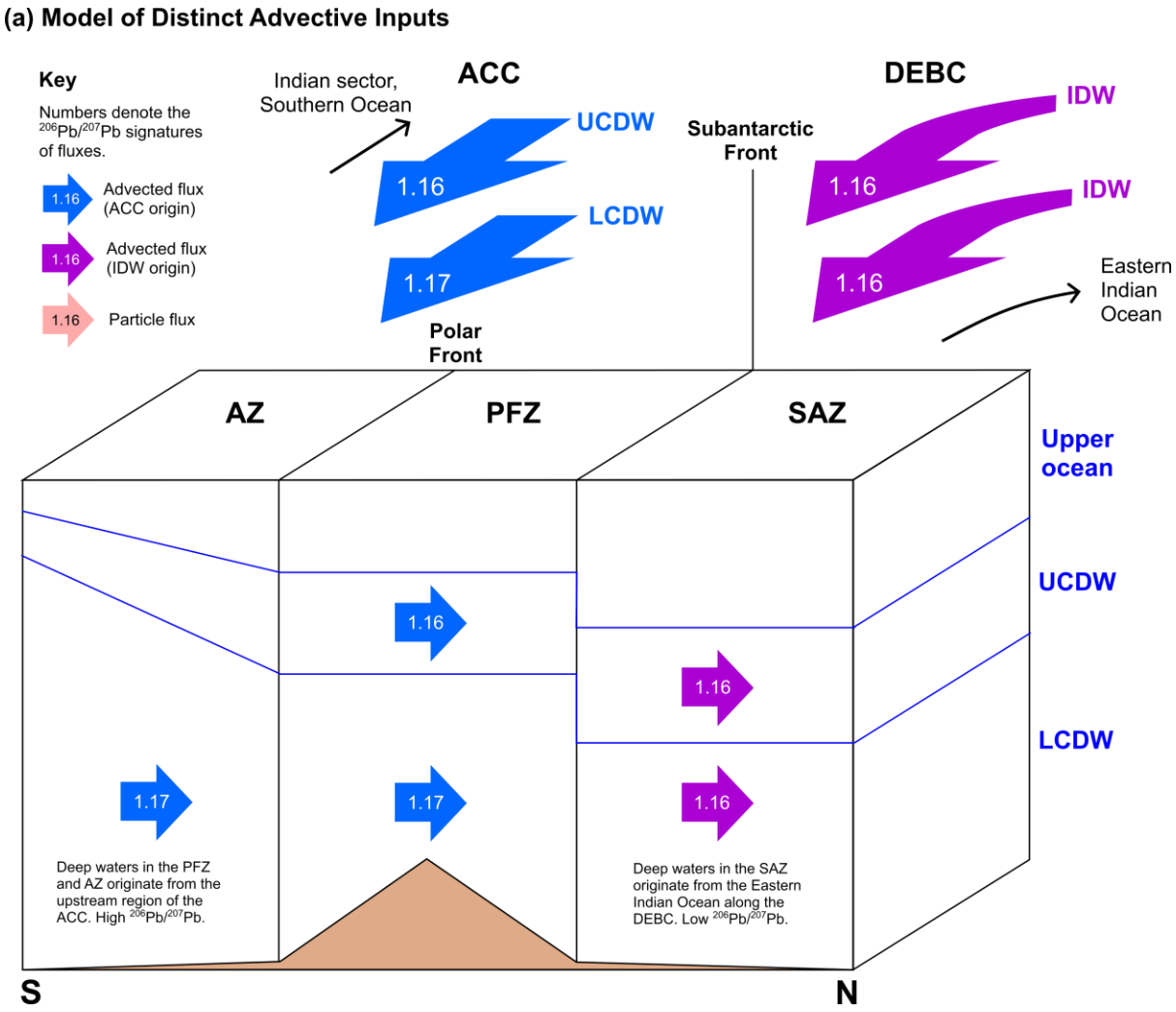

(a) Model of Distinct Advective Inputs
Key
Numbers denote the 206Pb/207Pb signatures of fluxes.
1.16 Advected flux (ACC origin)
1.16 Advected flux (IDW origin)
1.16 Particle flux
Indian sector, Southern Ocean
ACC
UCDW
LCDW
1.16
1.17
Polar Front
Subantarctic Front
DEBC
IDW
IDW
1.16
1.16
Eastern Indian Ocean
AZ
PFZ
SAZ
Upper ocean
UCDW
LCDW
1.16
1.16
1.17
1.17
1.16
Deep waters in the PFZ and AZ originate from the upstream region of the ACC. High 206Pb/207Pb.
Deep waters in the SAZ originate from the Eastern Indian Ocean along the DEBC. Low 206Pb/207Pb.
S
N

Figure 4.10.

(b) Model of Distinct Particulate Exchange Dynamics

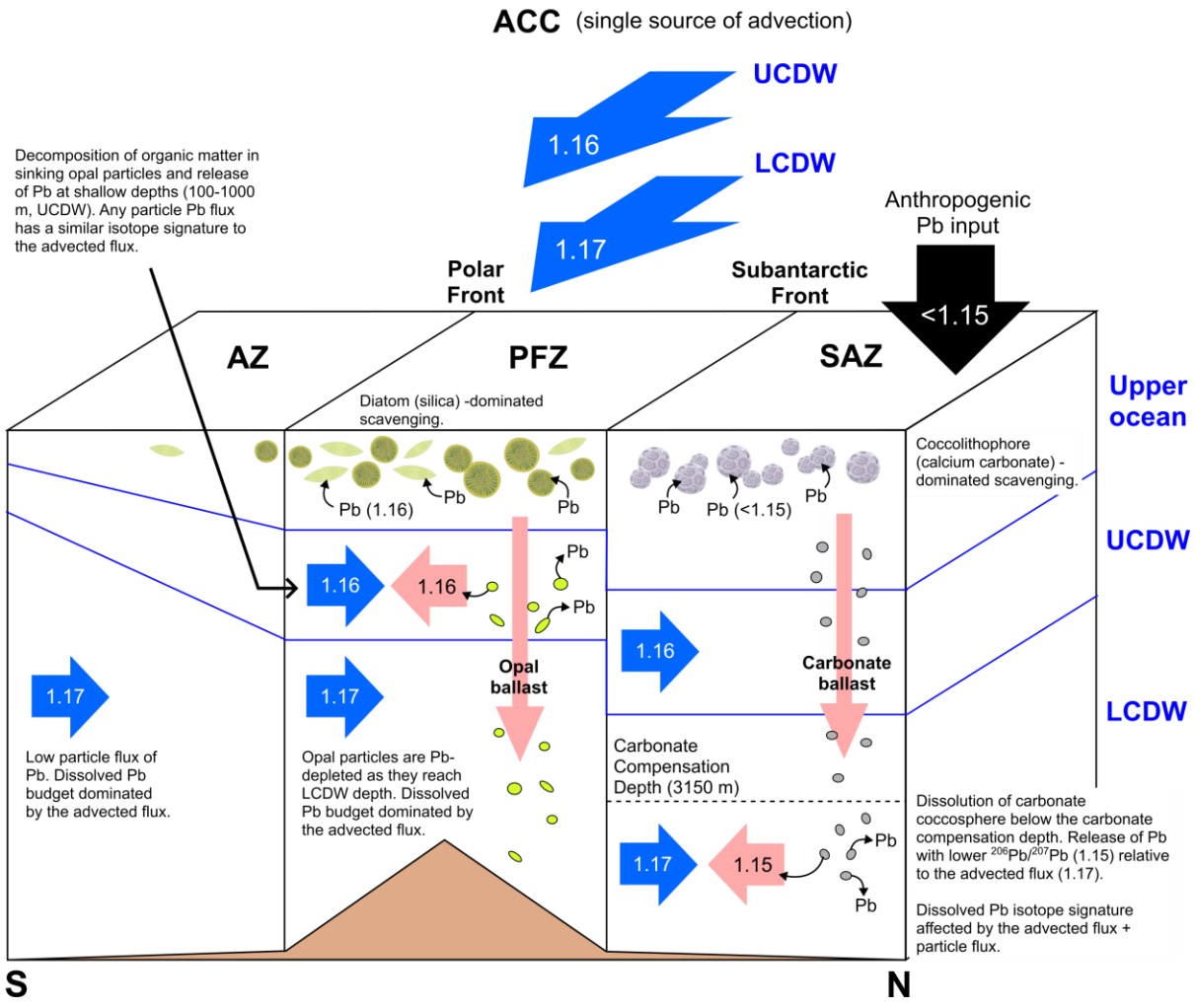


Figure 4.10 (cont'd). Conceptual illustration of the explanatory models for the observed deep water Pb isotope variations across the oceanographic zones (AZ, PFZ and SAZ) along the GS01 section. (a) Model of distinct advective inputs; (b) model of distinct particulate exchange dynamics. For simplicity, only $^{206}Pb/^{207}Pb$ ratios are shown in the illustration.

4.6 Conclusions

The first full set of results of dissolved Pb concentrations and isotopes in seawater samples from the GEOTRACES section GS01 across the Southern Ocean provides novel insights into water mass origin and vertical flux dynamics. The most pristine Pb signatures are found in Antarctic Bottom Waters close to the Antarctic continent, and the most polluted signatures are located in the upper and intermediate parts of the water column in the northern part of the section. $^{206}Pb/^{207}Pb$ and $^{208}Pb/^{207}Pb$ signatures of seawater from the SAZ (i.e. north of the main flow of the ACC) are consistent with mixing between anthropogenic sources from Australian emissions, as well as natural mineral dust from Australia. Deep water Pb signatures in the SAZ, in particular LCDW in the SAZ, is characterised by

distinctively lower $^{206}Pb/^{207}Pb$ and $^{208}Pb/^{207}Pb$ signatures compared to the same water mass to the south of the Subantarctic Front (i.e. within the ACC). This observation might point to the significance of a Deep Eastern Boundary Current in advecting Indian Ocean signatures to the Australian sector of the Southern Ocean. Alternatively, the observation could reflect differences in the remineralisation behaviour of Pb associated with the types of sinking particles between the SAZ and the ACC region. In such a model, carbonate-rich ballast in the Subantarctic Zone would undergo dissolution at depth and thereby generate significant modification of the deep water Pb isotope signatures. In contrast, opal-rich ballast in the more southern ACC region would undergo relatively shallow remineralisation, which therefore restricts the vertical transport of polluted Pb isotope signatures to shallower depths.

Better data coverage and process studies would enable deciphering of the relative significances of advection versus vertical flux of Pb in the area. In particular, dissolved Pb isotope data in the Southeast Indian Ocean and other Southern Ocean transects would be critical to test the ideas that are proposed in this study. In addition, process studies, dedicated to Pb behaviour during scavenging and redissolution / remineralisation by different particle types, would allow a more quantitative assessment of the migration of pollution signals within the ocean.

4.7 Researcher Contributions

The dissolved Pb concentration and isotope results of seawater samples from GS01 stations 9 and 23 that are presented in this study were obtained by the author. The dissolved Pb concentration and isotope data of seawater samples from GS01 stations 15, 30, 40, 45, 51 and 56 were obtained by Alex Griffiths and were presented in Alex Griffith's PhD thesis (Griffiths, 2019). Dissolved Pb concentrations of the same sample set were measured at the University of Tasmania by Andrew Bowie et al. (University of Tasmania, Australia) and are available in the GEOTRACES Intermediate Data Product 2021 (GEOTRACES Intermediate Data Product Group, 2021). The author led the interpretations of the results presented in this study, with insightful comments from Tina van de Flierdt, Mark Rehkämper and Alex Griffiths. Andrew Bowie, Melanie East and all the participants of the GEOTRACES GS01 expedition are thanked for collecting the seawater samples for this study.

Chapter 5

Summary

The primary aim of this thesis is to improve understanding of the marine source and sink fluxes of Pb and the internal cycling of the element in two marine settings that are poorly addressed, including the vicinity of hydrothermal activities and the Southern Ocean. Towards this end, geochemical analyses were performed for sediment and seawater samples from three different oceanic regions. In detail these are:

(1) The Pb (and Nd) isotope compositions of metalliferous sediments from two locations in the Eastern Equatorial Pacific Ocean.
(2) The dissolved Pb concentrations and isotope compositions of seawater depth profiles collected from above and in the vicinity of the TAG Hydrothermal Field in the North Atlantic Ocean (GEOTRACES section GA13, 'FRIDGE').
(3) The dissolved Pb concentrations and isotope compositions of seawater depth profiles collected from a transect across the Australian sector of the Southern Ocean (GEOTRACES section GS01).

In the following, the key findings of each chapter will first be presented. This is followed by a discussion on the wider implications of the new results and areas of further research (Fig. 5.1).

5.1 Key Findings

5.1.1 Chapter 2: Terrigenous and Hydrothermal Inputs of Pb and Nd in the Eastern Equatorial Pacific Ocean

In Chapter 2, the Pb and Nd isotope results are presented for bulk, detrital and leachate fractions of core-top sediment samples collected from MANOP Sites H (6°33'N, 92°48'W) and M (8°48'N, 104°00'W) in the Guatemala Basin, Eastern Equatorial Pacific Ocean. A key result entails the detection of a mantle-derived isotope signature for Pb but not Nd in the leachate fractions at MANOP Site M close to the East Pacific Rise (~25 km). This observation reflects the decoupling in the behaviours of the two elements in proximity to hydrothermal activity. In particular, the presence of hydrothermally derived Pb in the sediment fallout away from the ridge crest suggests its stabilisation in the dissolved pool for transport by the hydrothermal plume, whilst the absence of hydrothermally derived Nd is in accord with its efficient scavenging and removal close to source (e.g. German et al., 1990; Halliday et al., 1992). For the provenance of terrigenous sediments deposited in the Guatemala Basin, the combined Pb-Nd isotope data for the detrital sediment fractions in this study reinforce the findings of previous provenance studies for the wider Eastern Equatorial Pacific Ocean (Stancin et al., 2006; Höfig et al., 2016; Erhardt et al., 2021). In particular, the results suggest the predominance of proximal inputs from Mexico and the Northern Andean sector of South America to the Guatemala Basin. It highlights two types of climatic-tectonic settings that are conducive to high input fluxes of terrestrial detritus to marginal ocean basins: (i) semi-arid / arid terranes that are favourable for high dust emissions, and (ii) continental runoff from an active margin setting.

5.1.2 Chapter 3: Fluxes and Cycling of Pb Above and in the Vicinity of the TAG Hydrothermal Field

In Chapter 3, dissolved Pb concentration and isotope data are presented for five seawater depth profiles above and in the vicinity of the TAG Hydrothermal Field in the North Atlantic Ocean. The Pb concentration results reinforce the conclusion from previous studies (Godfrey et al., 1994; Noble et al., 2015) that despite the significant enrichment of Pb in TAG vent fluids, there is a net loss in dissolved Pb within the buoyant TAG plume. This is due to the intense scavenging of Pb by hydrothermal particles. The observed deep water variabilities in Pb isotope compositions, furthermore, reveal novel insights into the cycling of Pb in hydrothermal plumes. In particular, unusually low $^{206}Pb/^{207}Pb$ and $^{208}Pb/^{207}Pb$ signatures were observed across some of the deep water samples that were collected from within the buoyant and neutrally buoyant TAG plume and within a benthic nepheloid layer. These isotope anomalies predominantly reflect mixing between background NADW and anthropogenic Pb of European and/or North African origin, with only minor presence of mantle-derived Pb. The influence of recent anthropogenic Pb signatures on the deep water samples is thought to be caused by the exchange of anthropogenic Pb from sinking aerosol particles (or resuspended sediments in the nepheloid layer) with dissolved Pb in ambient seawater. These exchange reactions may be enhanced by the distinct physicochemical conditions within the TAG plume, such as the depletion of dissolved Pb in seawater due to scavenging by hydrothermal particles, elevated levels of dissolved organic ligands and reducing conditions in the buoyant plume. An additional observation of this study relates to significant small-scale vertical and lateral heterogeneities in dissolved Pb concentrations and isotopes in the upper ocean. These observations most likely reflect the release of anthropogenic Pb from aerosol particles in the upper water column.

5.1.3 Chapter 4: Variations in the Sources of Input and the Redistribution Mechanisms of Pb across the Southern Ocean between Antarctica and Tasmania

In Chapter 4, dissolved Pb concentration and isotope data are presented for two seawater depth profiles collected from the Subantarctic Zone (47-52°S) in the Australian sector of the Southern Ocean, near Tasmania. Together with results for higher southern latitudes (52-65°S) that were previously reported by Griffiths (2019), the complete dataset represents the first meridional section of dissolved Pb concentrations and isotopes across the Southern Ocean. The dataset reveals that the most pristine Pb signatures are found in Antarctic Bottom Waters close to the Antarctic continent. The most polluted signatures, on the other hand, are found in upper and intermediate depth waters in the Subantarctic Zone close to Tasmania. A key observation relates to the Pb isotope variations within the Lower Circumpolar Deep Water (LCDW): distinctively low $^{206}Pb/^{207}Pb$ and $^{208}Pb/^{207}Pb$ (i.e. more polluted) signatures are observed in the Subantarctic Zone but not in the same water mass to the south of the Subantarctic Front within the Antarctic Circumpolar Current (ACC). Whilst the LCDW signature of Pb within the ACC is

consistent with lateral advection from the Indian sector of the Southern Ocean, the more polluted signature in the Subantarctic Zone cannot be reconciled by advection along the ACC. Variable vertical fluxes driven by exchange with distinct compositions of sinking particles are proposed to explain the abrupt variation in deep water Pb isotope compositions across the Subantarctic Front. In particular, deep remineralisation of carbonate-rich ballast in the Subantarctic Zone could lead to significant vertical transfer of anthropogenic Pb from the upper into the deep ocean. In contrast, shallow remineralisation of opal-rich ballast within the ACC could limit the downward export of the polluted upper ocean Pb signature, allowing for a predominance of the advected signature. However, the significance of the Deep Eastern Boundary Current in supplying a distinct, advected source of Pb of Indian Ocean origin to the study area cannot be ruled out.

5.2 Implications and Future Work

5.2.1 Terrigenous Provenance Tracing in the Eastern Equatorial Pacific Ocean

For terrigenous provenance tracing in the Eastern Equatorial Pacific Ocean, the work in Chapter 2 of this thesis relies on a comparison of the Pb and Nd isotope fingerprints of detrital sediments with the bulk rock signatures of potential source areas. This work highlights the strength of a combined Pb-Nd isotope approach in achieving better terrigenous source identification but also discusses how artefacts from anthropogenic Pb contamination must be carefully excluded to avoid erroneous conclusions. In addition, this work also shows the challenges of the methodology in the setting of the Eastern Equatorial Pacific Ocean, as this is surrounded by a large number of potential source areas with highly variable and overlapping bulk rock Pb and Nd isotope signatures. Improved provenance tracing for the region may be achieved through better characterisation of the radiogenic isotope fingerprints of sources and sinks. For the former, analyses of direct erosional products, especially for the North American source areas, would provide a better characterisation of the terrestrial source signatures. For the latter, systematic mapping of the detrital isotope signatures could be carried out in the region. For example, the occurrence of isotope trends emerging from the continental margin would define transport vectors, which would help to locate the key contributing source areas.

5.2.2 Hydrothermal Activities and the Marine Pb Cycle: Net Flux and Sources of Pb in the Hydrothermal Plume

The dissolved Pb concentration and isotope data presented for the TAG hydrothermal plume, Mid-Atlantic Ridge (~26°N) in Chapter 3 of this thesis represent the second dataset for this plume (after Noble et al., 2015), whilst providing the first dissolved data for the neutrally buoyant TAG plume or any neutrally buoyant plume in the Atlantic Ocean. Together with results presented for an unnamed plume at ~15°S on the East Pacific Rise (Boyle et al., 2020), the seawater data for two major mid-ocean ridge hydrothermal systems (Mid-Atlantic Ridge and East Pacific Rise) provide critical observations

for evaluating earlier conclusions on Pb cycling in hydrothermal plumes and offer new insights into the complex distribution of Pb in the vicinity of hydrothermally active mid-ocean ridges (lower inset figure, Fig. 5.1). In addition, the sedimentary Pb isotope data presented for MANOP Site M in Chapter 2 of this thesis enable assessment of the fate of hydrothermally derived Pb in the vicinity of another hydrothermally active region (~8°N) at the East Pacific Rise.

Dissolved data at both the TAG plume (Chapter 3 of this thesis; Noble et al., 2015) and the plume at ~15°S on the East Pacific Rise (Boyle et al., 2020) suggest that hydrothermal fluids are negligible sources of Pb to the ocean, and that there is net removal of dissolved Pb in the hydrothermal plumes. Such consistent findings reinforce earlier conclusions that mid-ocean ridge hydrothermal systems probably act as an overall net sink of Pb in seawater. However, the new data presented in Chapter 3 show negligible scavenging of dissolved Pb in the neutrally buoyant TAG plume, which contrasts with the observed deficit in dissolved Pb for the neutrally buoyant plume at the East Pacific Rise. This reveals significant variability in the scavenging behaviour of Pb between different hydrothermal plumes, which calls for caution when making estimates in global Pb fluxes based on observations at individual vent sites or ridge systems. Furthermore, the Pb isotope signatures of metalliferous sediments and hydrothermal Fe-Mn crusts, located 25 to 1000 km away from the East Pacific Rise, including MANOP Site M in Chapter 2 and previous work (Barrett et al., 1987; van de Flierdt et al., 2004), indicate significant influences by mantle-derived Pb. These observations imply distal transport of hydrothermally derived Pb in ancient seawater away from the vent source – a conclusion which appears to contrast with the observed depletion of mantle-derived Pb in present-day seawater near hydrothermal vents. This apparent discrepancy may be reconciled by the transport of mantle-derived Pb in small, suspended Fe oxyhydroxide particles. Recent studies revealed the distal transport of dissolved Fe of hydrothermal origin away from the sources at the East Pacific Rise (Resing et al., 2015) and the Mid-Cayman Spreading Centre (Lough et al., 2019). Such transport has been attributed to the movement of suspended Fe oxyhydroxide particles along with the hydrothermal circulation, and whereby the particles are affected by coagulation and disaggregation reactions, such that they can remain suspended over long distances (Fitzsimmons et al., 2017; Lough et al., 2019). The close affinity of Pb to Fe oxyhydroxides (Koschinsky and Hein, 2003) may hence support the distal transport of hydrothermally derived Pb, through Pb incorporation into Fe oxyhydroxide phases that are carried along with the hydrothermal circulation.

A novel, surprising result of this thesis (Chapter 3) is the enhanced release of anthropogenic Pb from sinking particles into the dissolved Pb pool in the buoyant and neutrally buoyant TAG plumes. The vertical shuttling of Pb, as mediated by sinking aerosol particles and Pb exchange, is one of the key mechanisms (other than advection) for the downward export of Pb in the water column. The results of this thesis suggest a possible enhancement of such vertical Pb shuttling in hydrothermal plumes, which

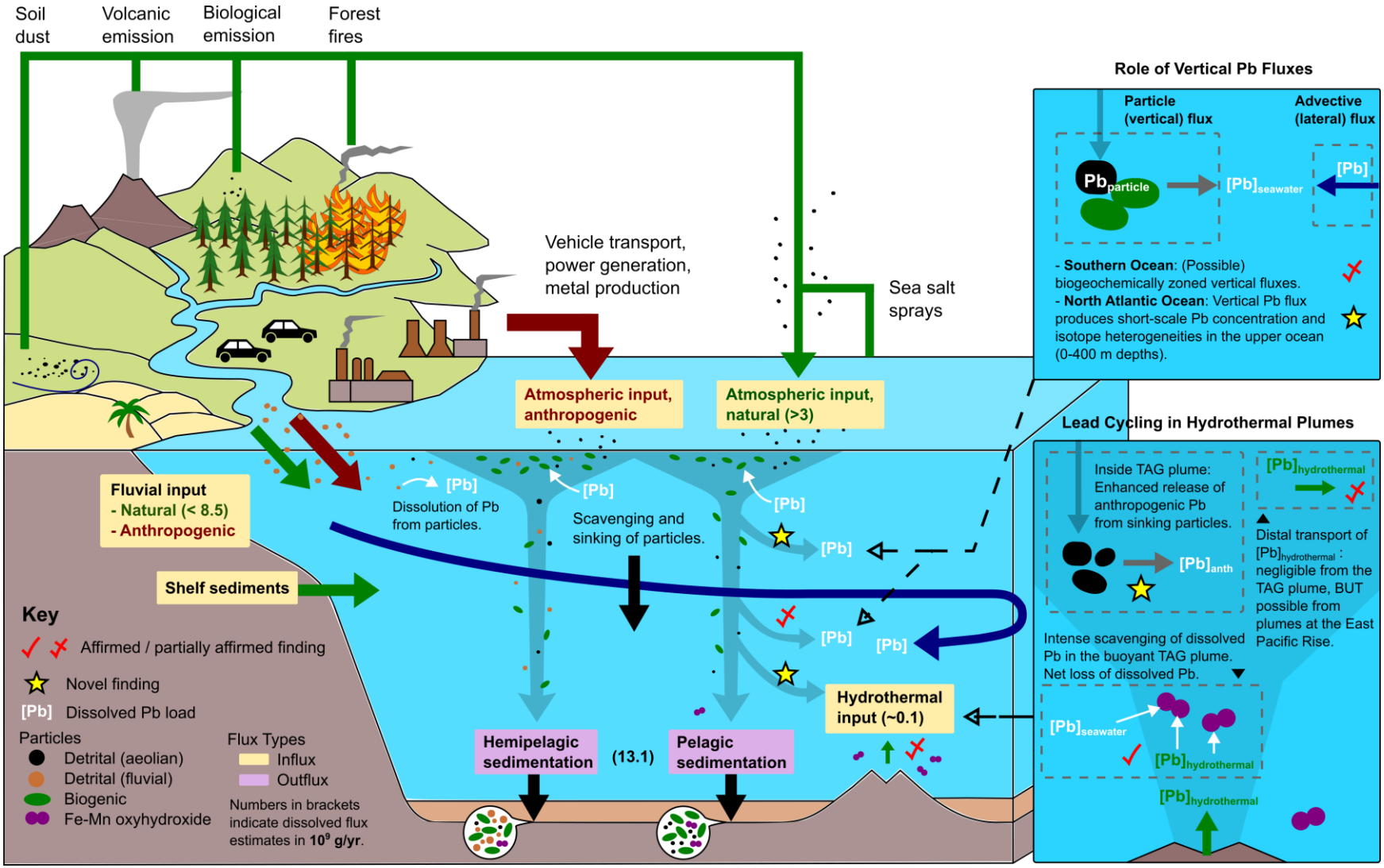


Figure 5.1. Summary illustration of the major findings in this thesis relevant to the Pb cycle in the modern global ocean.

may therefore have a yet uncharacterised but possibly more widespread impact on the marine cycling of Pb. An important next step would be to conduct combined Pb concentration and isotope studies of filtered seawater and particulate samples for hydrothermal systems. Such analyses would improve understanding of how Pb (and other trace metals) are exchanged between the dissolved and particulate phases, and how the physicochemical conditions of hydrothermal systems may impact exchange processes. Lead isotope analyses of additional hydrothermal vent sites and plumes would thereby capture any variabilities in scavenging intensity and other Pb exchange processes at mid-ocean ridge systems across the global ocean.

5.2.3 Lateral Versus Vertical Fluxes of Pb in the Ocean Traced by Isotope Signatures

Finally, the new seawater data presented in the thesis reveal the importance of vertical processes for the cycling of Pb in the Southern and Atlantic Oceans (upper inset figure, Fig. 5.1). In the Australian sector of the Southern Ocean (Chapter 4), a model of variable vertical Pb fluxes in different biogeochemical regimes is introduced to explain the observed Pb isotope variations within a single deep water mass. Whilst such dynamics may be unique to the Southern Ocean, which is characterised by a distinct zonation in phytoplankton compositions (e.g. Henley et al., 2020), they could potentially also play a role in other parts of the global ocean. However, as advective Pb fluxes from variable sources may also impact the observed Pb isotope variations, more work is needed to address the importance of lateral versus vertical Pb fluxes in the Southern Ocean, and this should focus on the acquisitions of dissolved Pb isotope data for the Southeast Indian and the Atlantic sector of the Southern Ocean. In the North Atlantic Ocean, the observed small-scale spatial heterogeneities in Pb signatures in the upper part of the water column (Chapter 3) may point to an oceanographic regime, in which vertical Pb fluxes dominate over advective fluxes. This interpretation challenges the traditional, advection-dominant model for the surface and subsurface Pb budgets of the North Atlantic Ocean (Boyle et al., 1986; Shen and Boyle, 1988; Noble et al., 2015; Bridgestock et al., 2018). Further results presented in the same chapter reveal local enhancements in vertical Pb fluxes to the deep ocean in the presence of the TAG hydrothermal plume.

Significant vertical Pb fluxes are typically associated with poorly ventilated deep ocean regions, such as the deep waters of the North Pacific and North Indian Oceans (Wu et al., 2010; Lee et al., 2015; Zurbrick et al., 2017; Lanning et al., 2023). However, the observations in this thesis suggest that such process may also be significant in the North Atlantic and (potentially) the Southern Ocean, which are characterised by strong physical circulation and therefore thought to be dominated by advective transport of Pb (Sherrell et al., 1992; Noble et al., 2015; Bridgestock et al., 2018). Process studies and laboratory experiments, dedicated to unravelling the mechanisms and rates of scavenging and remobilisation of Pb in the presence of different particle types and under different physicochemical conditions, will be crucial for testing the newly proposed particulate flux models for the vertical cycling of Pb in the Southern Ocean and in the TAG hydrothermal plume. Such mechanistic understanding

would also provide the key constraints for modelling the relative roles of advective and vertical fluxes of Pb.

Bibliography

Abouchami W. and Goldstein S. L. (1995) A lead isotopic study of circum-antarctic manganese nodules. *Geochim Cosmochim Acta* **59**, 1809–1820.

Alleman L. Y., Church T. M., Ganguli P., Véron A. J., Hamelin B. and Flegal A. R. (2001) Role of oceanic circulation on contaminant lead distribution in the South Atlantic. *Deep Sea Res 2 Top Stud Oceanogr* **48**, 2855–2876.

Alleman L. Y., Véron A. J., Church T. M., Flegal A. R. and Hamelin B. (1999) Invasion of the abyssal North Atlantic by modern anthropogenic lead. *Geophys Res Lett* **26**, 1477–1480.

Amador J. A., Alfaro E. J., Lizano O. G. and Magaña V. O. (2006) Atmospheric forcing of the eastern tropical Pacific: A review. *Prog Oceanogr* **69**, 101–142.

Amakawa H., Sasaki K. and Ebihara M. (2009) Nd isotopic composition in the central North Pacific. *Geochim Cosmochim Acta* **73**, 4705–4719.

Anderson R. F., Ali S., Bradtmiller L. I., Nielsen S. H. H., Fleisher M. Q., Anderson B. E. and Burckle L. H. (2009) Wind-Driven Upwelling in the Southern Ocean and the Deglacial Rise in Atmospheric CO_2. *Science (1979)* **323**, 1443–1448.

Annibaldi A., Truzzi C., Illuminati S. and Scarponi G. (2009) Recent sudden decrease of lead in Adriatic coastal seawater during the years 2000–2004 in parallel with the phasing out of leaded gasoline in Italy. *Mar Chem* **113**, 238–249.

Arhan M. (1990) The North Atlantic Current and Subarctic Intermediate Water. *J Mar Res* **48**, 109–144.

Artigue L., Lacan F., van Gennip S., Lohan M. C., Wyatt N. J., Woodward E. M. S., Mahaffey C., Hopkins J. and Drillet Y. (2020) Water mass analysis along 22 °N in the subtropical North Atlantic for the JC150 cruise (GEOTRACES, GApr08). *Deep Sea Res 1 Oceanogr Res Pap* **158**, 103230.

Bacon M. P., Spencer D. W. and Brewer P. G. (1976) $^{210}Pb/^{226}Ra$ and $^{210}Po/^{210}Pb$ disequilibria in seawater and suspended particulate matter. *Earth Planet Sci Lett* **32**, 277–296.

Baker E. T., Cormier M.-H., Langmuir C. H. and Zavala K. (2001) Hydrothermal plumes along segments of contrasting magmatic influence, 15°20′-18°30′N, East Pacific Rise: Influence of axial faulting. *Geochem, Geophys, Geosyst* **2**.

Baker E. T., Feely R. A., Mottl M. J., Sansone F. T., Wheat C. G., Resing J. A. and Lupton J. E. (1994) Hydrothermal plumes along the East Pacific Rise, 8°40′ to 11°50′N: Plume distribution and relationship to the apparent magmatic budget. *Earth Planet Sci Lett* **128**, 1–17.

Baker E. T., Haymon R. M., Resing J. A., White S. M., Walker S. L., Macdonald K. C. and Nakamura K. (2008) High-resolution surveys along the hot spot-affected Galápagos Spreading Center: 1. Distribution of hydrothermal activity. *Geochem, Geophys, Geosyst* **9**.

Balistrieri L., Brewer P. G. and Murray J. W. (1981) Scavenging residence times of trace metals and surface chemistry of sinking particles in the deep ocean. *Deep Sea Res A* **28**, 101–121.

Balkanski Y. J., Jacob D. J., Gardner G. M., Graustein W. C. and Turekian K. K. (1993) Transport and residence times of tropospheric aerosols inferred from a global three-dimensional simulation of ^{210}Pb. *J Geophys Res* **98**, 20573–20586.

Barbante C., Turetta C., Capodaglio G. and Scarponi G. (1997) Recent Decrease in the Lead Concentration of Antarctic Snow. *Int J Environ Anal Chem* **68**, 457–477.

Baringer M. O. N. and Price J. F. (1997) Mixing and Spreading of the Mediterranean Outflow. *J Phys Oceanogr* **27**, 1654–1677.

Barrett T. J., Taylor P. N. and Lugoqski J. (1987) Metalliferous sediments from DSDP Leg 92: The East Pacific Rise transect. *Geochim Cosmochim Acta* **51**, 2241–2253.

Basak C., Martin E. E. and Kamenov G. D. (2011) Seawater Pb isotopes extracted from Cenozoic marine sediments. *Chem Geol* **286**, 94–108.

Bau M. and Koschinsky A. (2009) Oxidative scavenging of cerium on hydrous Fe oxide: Evidence from the distribution of rare earth elements and yttrium between Fe oxides and Mn oxides in hydrogenetic ferromanganese crusts. *Geochem J* **43**, 37–47.

Bayon G., German C. R., Boella R. M., Milton J. A., Taylor R. N. and Nesbitt R. W. (2002) An improved method for extracting marine sediment fractions and its application to Sr and Nd isotopic analysis. *Chem Geol* **187**, 179–199.

Belkin I. M. and Gordon A. L. (1996) Southern Ocean fronts from the Greenwich meridian to Tasmania. *J Geophys Res Oceans* **101**, 3675–3696.

Benjamin M. M. and Leckie J. O. (1981) Multiple-site adsorption of Cd, Cu, Zn, and Pb on amorphous iron oxyhydroxide. *J Colloid Interface Sci* **79**, 209–221.

Bennett S. A., Achterberg E. P., Connelly D. P., Statham P. J., Fones G. R. and German C. R. (2008) The distribution and stabilisation of dissolved Fe in deep-sea hydrothermal plumes. *Earth Planet Sci Lett* **270**, 157–167.

Benninger L. K. and Krishnaswami S. (1981) Sedimentary processes in the inner New York Bight: Evidence from excess ^{210}Pb and ^{239,240}Pu. *Earth Planet Sci Lett* **53**, 158–174.

Bertram C. J. and Elderfield H. (1993) The geochemical balance of the rare earth elements and neodymium isotopes in the oceans. *Geochim Cosmochim Acta* **57**, 1957–1986.

Bi X.-Y., Li Z.-G., Wang S.-X., Zhang L., Xu R., Liu J.-L., Yang H.-M. and Guo M.-Z. (2017) Lead Isotopic Compositions of Selected Coals, Pb/Zn Ores and Fuels in China and the Application for Source Tracing. *Environ Sci Technol* **51**, 13502–13508.

Bi Z., Salaün P. and van den Berg C. M. G. (2013) The speciation of lead in seawater by pseudopolarography using a vibrating silver amalgam microwire electrode. *Mar Chem* **151**, 1–12.

Bohnenstiehl D. R. and Kleinrock M. C. (1999) Faulting and fault scaling on the median valley floor of the trans-Atlantic geotraverse (TAG) segment, ~26°N on the Mid-Atlantic Ridge. *J Geophys Res Solid Earth* **104**, 29351–29364.

Bollhöfer A. and Rosman K. J. R. (2001) Isotopic source signatures for atmospheric lead: The Northern Hemisphere. *Geochim Cosmochim Acta* **65**, 1727–1740.

Bollhöfer A. and Rosman K. J. R. (2000) Isotopic source signatures for atmospheric lead: the Southern Hemisphere. *Geochim Cosmochim Acta* **64**, 3251–3262.

Bostock H. C., Hayward B. W., Neil H. L., Currie K. I. and Dunbar G. B. (2011) Deep-water carbonate concentrations in the southwest Pacific. *Deep Sea Res 1 Oceanogr Res Pap* **58**, 72–85.

Bostock H. C., Opdyke B. N. and Williams M. J. M. (2010) Characterising the intermediate depth waters of the Pacific Ocean using δ13C and other geochemical tracers. *Deep Sea Res 1 Oceanogr Res Pap* **57**, 847–859.

Boström K., Peterson M. N. A., Joensuu O. and Fisher D. E. (1969) Aluminum-poor ferromanganoan sediments on active oceanic ridges. *J Geophys Res* **74**, 3261-3270.

Boutron C. F. and Patterson C. C. (1987) Relative levels of natural and anthropogenic lead in recent Antarctic snow. *Journal of Geophysical Research: Atmospheres* **92**, 8454–8464.

Boyle E. A., Chapnick S. D., Shen G. T. and Bacon M. P. (1986) Temporal variability of lead in the western North Atlantic. *J Geophys Res* **91**, 8573.

Boyle E. A., John S., Abouchami W., Adkins J. F., Echegoyen-Sanz Y., Ellwood M., Flegal A. R., Fornace K., Gallon C., Galer S., Gault-Ringold M., Lacan F., Radic A., Rehkamper M., Rouxel O., Sohrin Y., Stirling C., Thompson C., Vance D., Xue Z. and Zhao Y. (2012) GEOTRACES IC1 (BATS) contamination-prone trace element isotopes Cd, Fe, Pb, Zn, Cu, and Mo intercalibration. *Limnol Oceanogr Methods* **10**, 653–665.

Boyle E. A., Zurbrick C., Lee J.-M., Till R., Till C. P., Zhang J. and Flegal A. R. (2020) Lead and lead isotopes in the U.S. GEOTRACES East Pacific zonal transect (GEOTRACES GP16). *Mar Chem* **227**, 103892.

Boyle E., Lee J.-M., Echegoyen Y., Noble A., Moos S., Carrasco G., Zhao N., Kayser R., Zhang J., Gamo T., Obata H. and Norisuye K. (2014) Anthropogenic Lead Emissions in the Ocean: The Evolving Global Experiment. *Oceanography* **27**, 69–75.

Bridgestock L., van de Flierdt T., Rehkämper M., Paul M., Middag R., Milne A., Lohan M. C., Baker A. R., Chance R., Khondoker R., Strekopytov S., Humphreys-Williams E., Achterberg E. P., Rijkenberg M. J. A., Gerringa L. J. A. and de Baar H. J. W. (2016) Return of naturally sourced Pb to Atlantic surface waters. *Nat Commun* **7**.

Bridgestock L., Rehkämper M., van de Flierdt T., Paul M., Milne A., Lohan M. C. and Achterberg E. P. (2018) The distribution of lead concentrations and isotope compositions in the eastern Tropical Atlantic Ocean. *Geochim Cosmochim Acta* **225**, 36–51.

Broecker W. S. and Peng T. H. (1982) *Tracers in the Sea*., Eldigio Press, Palisades, N.Y.

Brown G. E. and Parks G. A. (2001) Sorption of Trace Elements on Mineral Surfaces: Modern Perspectives from Spectroscopic Studies, and Comments on Sorption in the Marine Environment. *Int Geol Rev* **43**, 963–1073.

Bruland K. W., Middag R. and Lohan M. C. (2014) Controls of Trace Metals in Seawater. In *Treatise on Geochemistry: Second Edition* (eds. H. Holland and K. Turekian). Elsevier. pp. 19–51.

Buckley M. W. and Marshall J. (2016) Observations, inferences, and mechanisms of the Atlantic Meridional Overturning Circulation: A review. *Rev Geophys* **54**, 5–63.

Callahan J. E. (1972) The structure and circulation of deep water in the Antarctic. *Deep-Sea Res Oceanogr Abstr* **19**, 563–575.

Campbell A. C., Palmer M. R., Klinkhammer G. P., Bowers T. S., Edmond J. M., Lawrence J. R., Casey J. F., Thompson G., Humphris S., Rona P. and Karson J. A. (1988) Chemistry of hot springs on the Mid-Atlantic Ridge. *Nature* **335**, 514–519.

Canales J. P., Sohn R. A. and DeMartin B. J. (2007) Crustal structure of the Trans-Atlantic Geotraverse (TAG) segment (Mid-Atlantic Ridge, 26°10′N): Implications for the nature of hydrothermal circulation and detachment faulting at slow spreading ridges. *Geochem, Geophys, Geosyst* **8**.

Candelone J., Hong S., Pellone C. and Boutron C. F. (1995) Post-Industrial Revolution changes in large-scale atmospheric pollution of the northern hemisphere by heavy metals as documented in central Greenland snow and ice. *J Geophys Res Atmos* **100**, 16605–16616.

Cantrell K. J. and Byrne R. H. (1987) Rare earth element complexation by carbonate and oxalate ions. *Geochim Cosmochim Acta* **51**, 597–605.

Capodaglio G., Coale K. H. and Bruland K. W. (1990) Lead speciation in surface waters of the eastern North Pacific. *Mar Chem* **29**, 221–233.

Capodaglio G., Turetta C., Toscano G., Gambaro A., Scarponi G. and Cescon P. (1998) Cadmium, Lead and Copper Complexation in Antarctic Coastal Seawater. Evolution during the Austral Summer. *Int J Environ Anal Chem* **71**, 195–226.

Chen J. H. (1987) U, Th, and Pb isotopes in hot springs on the Juan de Fuca Ridge. *J Geophys Res Solid Earth* **92**, 11411–11415.

Chen J. H., Wasserburg G. J., von Damm K. L. and Edmond J. M. (1986) The U-Th-Pb systematics in hot springs on the East Pacific Rise at 21°N and Guaymas Basin. *Geochim Cosmochim Acta* **50**, 2467–2479.

Chen M., Boyle E. A., Jiang S., Liu Q., Zhang J., Wang X. and Zhou K. (2023a) Dissolved Lead (Pb) Concentrations and Pb Isotope Ratios Along the East China Sea and Kuroshio Transect—Evidence for Isopycnal Transport and Particle Exchange. *J Geophys Res Oceans* **128**, e2022JC019423.

Chen M., Boyle E. A., Lee J.-M., Nurhati I., Zurbrick C., Switzer A. D. and Carrasco G. (2016a) Lead isotope exchange between dissolved and fluvial particulate matter: A laboratory study from the Johor River estuary. *Philos Trans A Math Phys Eng Sci* **374**, 20160054.

Chen M., Carrasco G., Zhao N., Wang X., Lee J. N., Tanzil J. T. I., Annammala K. V., Poh S. C., Lauro F. M., Ziegler A. D., Duangnamon D. and Boyle E. A. (2023b) Boundary exchange completes the marine Pb cycle jigsaw. *Proc Natl Acad Sci U S A* **120**, e2213163120.

Chen M., Goodkin N. F., Boyle E. A., Switzer A. D. and Bolton A. (2016b) Lead in the western South China Sea: Evidence of atmospheric deposition and upwelling. *Geophys Res Lett* **43**, 4490–4499.

Chen W., Guéguen C., Smith D. S., Galceran J., Puy J. and Companys E. (2018) Metal (Pb, Cd, and Zn) Binding to Diverse Organic Matter Samples and Implications for Speciation Modeling. *Environ Sci Technol* **52**, 4163–4172.

Chester R. and Hughes M. J. (1967) A chemical technique for the separation of ferro-manganese minerals, carbonate minerals and adsorbed trace elements from pelagic sediments. *Chem Geol* **2**, 249–262.

Chester R., Lin F. J. and Murphy K. J. T. (1989) A three stage sequential leaching scheme for the characterisation of the sources and environmental mobility of trace metals in the marine aerosol. *Environ Technol* **10**, 887–900.

Chien C.-T., Ho T. Y., Sanborn M. E., Yin Q. Z. and Paytan A. (2017) Lead concentrations and isotopic compositions in the Western Philippine Sea. *Mar Chem* **189**, 10–16.

Chow T. J. and Patterson C. C. (1962) The occurrence and significance of lead isotopes in pelagic sediments. *Geochim Cosmochim Acta* **26**, 263–308.

Chuang C., Santschi P. H., Xu C., Jiang Y., Ho Y., Quigg A., Guo L., Hatcher P. G., Ayranov M. and Schumann D. (2015) Molecular level characterization of diatom-associated biopolymers that bind ^{234}Th, ^{233}Pa, ^{210}Pb, and ^{7}Be in seawater: A case study with *Phaeodactylum tricornutum*. *J Geophys Res Biogeosci* **120**, 1858–1869.

Chuang C.-Y., Santschi P. H., Jiang Y., Ho Y.-F., Quigg A., Guo L., Ayranov M. and Schumann D. (2014) Important role of biomolecules from diatoms in the scavenging of particle-reactive radionuclides of thorium, protactinium, lead, polonium, and beryllium in the ocean: A case study with *Phaeodactylum tricornutum*. *Limnol Oceanogr* **59**, 1256–1266.

Clarke W. B., Beg M. A. and Craig H. (1969) Excess ^{3}He in the sea: Evidence for terrestrial primodal helium. *Earth Planet Sci Lett* **6**, 213–220.

Clementson L. A., Parslow J. S., Griffiths F. B., Lyne V. D., Mackey D. J., Harris G. P., McKenzie D. C., Bonham P. I., Rathbone C. A. and Rintoul S. (1998) Controls on phytoplankton production in the Australasian sector of the subtropical convergence. *Deep Sea Res 1 Oceanogr Res Pap* **45**, 1627–1661.

Cochran J. K. (1985) Particle mixing rates in sediments of the eastern equatorial Pacific: Evidence from ^{210}Pb, ^{239,240}Pu and ^{137}Cs distributions at MANOP sites. *Geochim Cosmochim Acta* **49**, 1195–1210.

Copin-Montegut G., Courau P. and Nicolas E. (1986) Distribution and transfer of trace elements in the Western Mediterranean. *Mar Chem* **18**, 189–195.

Cresswell G. (2000) Currents of the continental shelf and upper slope of Tasmania. *Pap Proc R Soc Tasm* **133**, 21–30.

Crocket K. C., Vance D., Foster G. L., Richards D. A. and Tranter M. (2012) Continental weathering fluxes during the last glacial/interglacial cycle: insights from the marine sedimentary Pb isotope record at Orphan Knoll, NW Atlantic. *Quat Sci Rev* **38**, 89–99.

Cullen J. T. and McAlister J. (2017) 2. Biogeochemistry of Lead. Its Release to the Environment and Chemical Speciation. In *Lead – Its Effects on Environment and Health* (eds. A. Sigel, H. Sigel and R. K. O. Sigel). De Gruyter. pp. 21–48.

Cziczo D. J., Stetzer O., Worringen A., Ebert M., Weinbruch S., Kamphus M., Gallavardin S. J., Curtius J., Borrmann S., Froyd K. D., Mertes S., Möhler O. and Lohmann U. (2009) Inadvertent climate modification due to anthropogenic lead. *Nat Geosci* **2**, 333–336.

Daniault N., Mercier H., Lherminier P., Sarafanov A., Falina A., Zunino P., Pérez F. F., Ríos A. F., Ferron B., Huck T., Thierry V. and Gladyshev S. (2016) The northern North Atlantic Ocean mean circulation in the early 21st century. *Prog Oceanogr* **146**, 142–158.

Davis R. E. (2005) Intermediate-Depth Circulation of the Indian and South Pacific Oceans Measured by Autonomous Floats. *J Phys Oceanogr* **35**, 683–707.

Deacon G. E. R. (1982) Physical and biological zonation in the Southern Ocean. *Deep Sea Res A* **29**, 1–15.

De Deckker P., Norman M., Goodwin I. D., Wain A. and Gingele F. X. (2010) Lead isotopic evidence for an Australian source of aeolian dust to Antarctica at times over the last 170,000 years. *Palaeogeogr Palaeoclimatol Palaeoecol* **285**, 205–223.

DeMartin B. J., Reves-Sohn R. A., Canales J. P. and Humphris S. E. (2007) Kinematics and geometry of active detachment faulting beneath the Trans-Atlantic geotraverse (TAG) hydrothermal field on the Mid-Atlantic Ridge. *Geology* **35**, 711–714.

DeMets C., Gordon R. G., Argus D. F. and Stein S. (1990) Current plate motions. *Geophys J Int* **101**, 425–478.

DePaolo D. J. and Wasserburg G. J. (1976) Nd isotopic variations and petrogenetic models. *Geophys Res Lett* **3**, 249–252.

de Salas M. F., Eriksen R., Davidson A. T. and Wright S. W. (2011) Protistan communities in the Australian sector of the Sub-Antarctic Zone during SAZ-Sense. *Deep Sea Res 2 Top Stud Oceanogr* **58**, 2135–2149.

Doe B. R. and Stacey J. S. (1974) The Application of Lead Isotopes to the Problems of Ore Genesis and Ore Prospect Evaluation: A Review. *Econ Geol* **69**, 757–776.

Dong D., Nelson Y. M., Lion L. W., Shuler M. L. and Ghiorse W. C. (2000) Adsorption of Pb and Cd onto metal oxides and organic material in natural surface coatings as determined by selective extractions: new evidence for the importance of Mn and Fe oxides. *Water Res* **34**, 427–436.

Donohue K. A., Tracey K. L., Watts D. R., Chidichimo M. P. and Chereskin T. K. (2016) Mean Antarctic Circumpolar Current transport measured in Drake Passage. *Geophys Res Lett* **43**, 760–767.

Dörr H., Münnich K. O., Mangini A. and Schmitz W. (1990) Gasoline lead in West German soils. *Naturwissenschaften* **77**, 428–430.

Douville E., Charlou J. L., Oelkers E. H., Bienvenu P., Jove Colon C. F., Donval J. P., Fouquet Y., Prieur D. and Appriou P. (2002) The rainbow vent fluids (36°14′N, MAR): The influence of ultramafic rocks and phase separation on trace metal content in Mid-Atlantic Ridge hydrothermal fluids. *Chem Geol* **184**, 37–48.

Draxler R. R. and Rolph G. D. (2003) HYSPLIT (HYbrid Single-Particle Lagrangian Integrated Trajectory) Model access via NOAA ARL READY Website. NOAA Air Resources Laboratory, Silver Spring, MD. https://www.ready.noaa.gov/HYSPLIT.php.

Duce R. A., Liss P. S., Merrill J. T., Atlas E. L., Buat-Menard P., Hicks B. B., Miller J. M., Prospero J. M., Arimoto R., Church T. M., Ellis W., Galloway J. N., Hansen L., Jickells T. D., Knap A. H., Reinhardt K. H., Schneider B., Soudine A., Tokos J. J., Tsunogai S., Wollast R. and Zhou M. (1991) The atmospheric input of trace species to the world ocean. *Global Biogeochem Cycles* **5**, 193–259.

Dymond J., Lyle M., Finney B., Piper D. Z., Murphy K., Conard R. and Pisias N. (1984) Ferromanganese nodules from MANOP Sites H, S, and R-Control of mineralogical and chemical composition by multiple accretionary processes. *Geochim Cosmochim Acta* **48**, 931–949.

Dymond J. and Roth S. (1988) Plume dispersed hydrothermal particles: A time-series record of settling flux from the Endeavour Ridge using moored sensors. *Geochim Cosmochim Acta* **52**, 2525–2536.

Ebersbach F., Trull T. W., Davies D. M. and Bray S. G. (2011) Controls on mesopelagic particle fluxes in the Sub-Antarctic and Polar Frontal Zones in the Southern Ocean south of Australia in

summer—Perspectives from free-drifting sediment traps. *Deep Sea Res 2 Top Stud Oceanogr* **58**, 2260–2276.

Echegoyen Y., Boyle E. A., Lee J. M., Gamo T., Obata H. and Norisuye K. (2014) Recent distribution of lead in the Indian Ocean reflects the impact of regional emissions. *Proc Natl Acad Sci U S A* **111**, 15328–15331.

Edmond J. M., Measures C., McDuff R. E., Chan L. H., Collier R., Grant B., Gordon L. I. and Corliss J. B. (1979) Ridge crest hydrothermal activity and the balances of the major and minor elements in the ocean: The Galapagos data. *Earth Planet Sci Lett* **46**, 1–18.

Elbaz-Poulichet F., Holliger P., Wen Huang W. and Martin J.-M. (1984) Lead cycling in estuaries, illustrated by the Gironde estuary, France. *Nature* **308**, 409–414.

Elderfield H., Mills R. A. and Rudnicki M. D. (1993) Geochemical and thermal fluxes, high-temperature venting and diffuse flow from mid-ocean ridge hydrothermal systems: the TAG hydrothermal field, Mid-Atlantic Ridge 26°N. *Geol Soc Spec Publ* **76**, 295–307.

Elderfield H. and Schultz A. (1996) Mid-ocean ridge hydrothermal fluxes and the chemical composition of the ocean. *Annu Rev Earth Planet Sci* **24**, 191–224.

EMEP/CEIP (2023) Officially reported emission data submitted by the Parties to the Air Convention (CLRTAP) to the EMEP programme. https://www.ceip.at/webdab-emission-database/reported-emissiondata.

Emerson S., Jahnke R., Bender M., Froelich P., Klinkhammer G., Bowser C. and Setlock G. (1980) Early diagenesis in sediments from the eastern equatorial Pacific, I. Pore water nutrient and carbonate results. *Earth Planet Sci Lett* **49**, 57–80.

Erel Y., Dubowski Y., Halicz L., Erez J. and Kaufman A. (2001) Lead concentrations and isotopic ratios in the sediments of the Sea of Galilee. *Environ Sci Technol* **35**, 292–299.

Erhardt A. M., Douglas G., Jacobson A. D., Wimpenny J., Yin Q. Z. and Paytan A. (2021) Assessing Sedimentary Detrital Pb Isotopes as a Dust Tracer in the Pacific Ocean. *Paleoceanogr Paleoclimatol* **36**.

Fagel N., Not C., Gueibe J., Mattielli N. and Bazhenova E. (2014) Late Quaternary evolution of sediment provenances in the Central Arctic Ocean: mineral assemblage, trace element composition and Nd and Pb isotope fingerprints of detrital fraction from the Northern Mendeleev Ridge. *Quat Sci Rev* **92**, 140–154.

Feely R. A., Lewison M., Massoth G. J., Robert-Baldo G., Lavelle J. W., Byrne R. H., Von Damm K. L. and Curl Jr. H. C. (1987) Composition and dissolution of black smoker particulates from active vents on the Juan de Fuca Ridge. *J Geophys Res* **92**, 11347–11363.

Ferrari R., Jansen M. F., Adkins J. F., Burke A., Stewart A. L. and Thompson A. F. (2014) Antarctic sea ice control on ocean circulation in present and glacial climates. *Proc Natl Acad Sci U S A* **111**, 8753–8758.

Fiedler P. C. and Talley L. D. (2006) Hydrography of the eastern tropical Pacific: A review. *Prog Oceanogr* **69**, 143–180.

Findlay A. J., Gartman A., Shaw T. J. and Luther G. W. (2015) Trace metal concentration and partitioning in the first 1.5m of hydrothermal vent plumes along the Mid-Atlantic Ridge: TAG, Snakepit, and Rainbow. *Chem Geol* **412**, 117–131.

Fine R. A., Smethie W. M., Bullister J. L., Rhein M., Min D.-H., Warner M. J., Poisson A. and Weiss R. F. (2008) Decadal ventilation and mixing of Indian Ocean waters. *Deep Sea Res 1 Oceanogr Res Pap* **55**, 20–37.

Finney B. P., Lyle M. W. and Heath G. R. (1988) Sedimentation at MANOP Site H (eastern equatorial Pacific) over the past 400,000 years: Climatically induced redox variations and their effects on transition metal cycling. *Paleoceanography* **3**, 169–189.

Fisher N., Burns K., Cherry R. and Heyraud M. (1983) Accumulation and cellular distribution of ^{241}Am, ^{210}Po, and ^{210}Pb in two marine algae. *Mar Ecol Prog Ser* **11**, 233–237.

Fishwick M. P., Ussher S. J., Sedwick P. N., Lohan M. C., Worsfold P. J., Buck K. N. and Church T. M. (2018) Impact of surface ocean conditions and aerosol provenance on the dissolution of aerosol manganese, cobalt, nickel and lead in seawater. *Mar Chem* **198**, 28–43.

Fitzsimmons J. N., John S. G., Marsay C. M., Hoffman C. L., Nicholas S. L., Toner B. M., German C. R. and Sherrell R. M. (2017) Iron persistence in a distal hydrothermal plume supported by dissolved-particulate exchange. *Nat Geosci* **10**, 195–201.

Flegal A. R., Maring H. and Niemeyer S. (1993) Anthropogenic lead in Antarctic sea water. *Nature* **365**, 242–244.

Flegal A. R. and Patterson C. C. (1983) Vertical concentration profiles of lead in the Central Pacific at 15°N and 20°S. *Earth Planet Sci Lett* **64**, 19–32.

Foustoukos D. I. and Seyfried W. E. (2005) Redox and pH constraints in the subseafloor root zone of the TAG hydrothermal system, 26° N Mid-Atlantic Ridge. *Earth Planet Sci Lett* **235**, 497–510.

Francois R., Honjo S., Krishfield R. and Manganini S. (2002) Factors controlling the flux of organic carbon to the bathypelagic zone of the ocean. *Global Biogeochem Cycles* **16**, 1–20.

Frank M. (2002) Radiogenic isotopes: Tracers of past ocean circulation and erosional input. *Reviews of Geophysics* **40**, 1–38.

Frank M., Marbler H., Koschinsky A., van de Flierdt T., Klemm V., Gutjahr M., Halliday A. N., Kubik P. W. and Halbach P. (2006) Submarine hydrothermal venting related to volcanism in the Lesser Antilles: Evidence from ferromanganese precipitates. *Geochem, Geophys, Geosyst* **7**.

Frank M., O'Nions R. K., Hein J. R. and Banakar V. K. (1999) 60 Myr records of major elements and Pb-Nd isotopes from hydrogenous ferromanganese crusts: Reconstruction of seawater paleochemistry. *Geochim Cosmochim Acta* **63**, 1689–1708.

Galer S. J. G. (1999) Optimal double and triple spiking for high precision lead isotopic measurement. *Chem Geol* **157**, 255–274.

Garreaud R., Vuille M. and Clement A. C. (2003) The climate of the Altiplano: observed current conditions and mechanisms of past changes. *Palaeogeogr Palaeoclimatol Palaeoecol* **194**, 5–22.

Gartman A., Findlay A. J. and Luther G. W. (2014) Nanoparticulate pyrite and other nanoparticles are a widespread component of hydrothermal vent black smoker emissions. *Chem Geol* **366**, 32–41.

GEOTRACES Intermediate Data Product Group (2021) The GEOTRACES Intermediate Data Product 2021 (IDP2021). *NERC EDS British Oceanographic Data Centre NOC*.

GEOTRACES Planning Group (2006) *GEOTRACES Science Plan*. Baltimore, Maryland: Scientific Committee on Oceanic Research.

German C. R. and Angel M. V. (1995) Hydrothermal fluxes of metals to the oceans: a comparison with anthropogenic discharge. *Geol Soc Spec Publ* **87**, 365–372.

German C. R., Campbell A. C. and Edmond J. M. (1991a) Hydrothermal scavenging at the Mid-Atlantic Ridge: Modification of trace element dissolved fluxes. *Earth Planet Sci Lett* **107**, 101–114.

German C. R., Casciotti K. A., Dutay J. C., Heimbürger L. E., Jenkins W. J., Measures C. I., Mills R. A., Obata H., Schlitzer R., Tagliabue A., Turner D. R. and Whitby H. (2016) Hydrothermal impacts on trace element and isotope ocean biogeochemistry. *Philos Trans A Math Phys Eng Sci* **374**, 20160035.

German C. R., Colley S., Palmer M. R., Khripounoff A. and Klinkhammer G. P. (2002) Hydrothermal plume-particle fluxes at 13°N on the East Pacific Rise. *Deep Sea Res 1 Oceanogr Res Pap* **49**, 1921–1940.

German C. R., Fleer A. P., Bacon M. P. and Edmond J. M. (1991b) Hydrothermal scavenging at the Mid-Atlantic Ridge: radionuclide distributions. *Earth Planet Sci Lett* **105**, 170–181.

German C. R., Klinkhammer G. P., Edmond J. M., Mura A. and Elderfield H. (1990) Hydrothermal scavenging of rare-earth elements in the ocean. *Nature* **345**, 516–518.

German C. R. and Seyfried W. E. (2014) Hydrothermal Processes. In *Treatise on Geochemistry: Second Edition* (eds. H. Holland and K. Turekian). Elsevier. pp. 191–233.

German C. R. and Sparks R. S. J. (1993) Particle recycling in the TAG hydrothermal plume. *Earth Planet Sci Lett* **116**, 129–134.

Gili S., Gaiero D. M., Goldstein S. L., Chemale F., Jweda J., Kaplan M. R., Becchio R. A. and Koester E. (2017) Glacial/interglacial changes of Southern Hemisphere wind circulation from the geochemistry of South American dust. *Earth Planet Sci Lett* **469**, 98–109.

Gili S., Gaiero D. M., Goldstein S. L., Chemale Jr F., Koester E., Jweda J., Vallelonga P. and Kaplan M. R. (2016) Provenance of dust to Antarctica: A lead isotopic perspective. *Geophys Res Lett* **43**, 2291–2298.

Ginoux P., Prospero J. M., Gill T. E., Hsu N. C. and Zhao M. (2012) Global-scale attribution of anthropogenic and natural dust sources and their emission rates based on MODIS Deep Blue aerosol products. *Rev Geophys* **50**.

Godfrey L. V., Mills R., Elderfield H. and Gurvich E. (1994) Lead behaviour at the TAG hydrothermal vent field, 26°N, Mid-Atlantic Ridge. *Mar Chem* **46**, 237–254.

Goldberg E. D. (1954) Marine Geochemistry 1. Chemical Scavengers of the Sea. *J Geol* **62**, 249–265.

Goldstein S. L. and Hemming S. R. (2003) Long-lived Isotopic Tracers in Oceanography, Paleoceanography, and Ice-sheet Dynamics. In *Treatise on Geochemistry* Elsevier. pp. 453–489.

Goldstein S. L., O'Nions R. K. and Hamilton P. J. (1984) A Sm-Nd isotopic study of atmospheric dusts and particulates from major river systems. *Earth Planet Sci Lett* **70**, 221–236.

Grasse P., Bosse L., Hathorne E. C., Böning P., Pahnke K. and Frank M. (2017) Short-term variability of dissolved rare earth elements and neodymium isotopes in the entire water column of the Panama Basin. *Earth Planet Sci Lett* **475**, 242–253.

Grasse P., Stichel T., Stumpf R., Stramma L. and Frank M. (2012) The distribution of neodymium isotopes and concentrations in the Eastern Equatorial Pacific: Water mass advection versus particle exchange. *Earth Planet Sci Lett* **353–354**, 198–207.

Graybeal A. L. and Ross Heath G. (1984) Remobilization of transition metals in surficial pelagic sediments from the eastern Pacific. *Geochim Cosmochim Acta* **48**, 965–975.

Griffith E. M. and Paytan A. (2012) Barite in the ocean – occurrence, geochemistry and palaeoceanographic applications. *Sedimentology* **59**, 1817–1835.

Griffiths A. (2019) Tracing water masses and pollution in the Southern Ocean using neodymium and lead isotopes. PhD Thesis, Imperial College London.

Griffiths A., Packman H., Leung Y.-L., Coles B. J., Kreissig K., Little S. H., van de Flierdt T. and Rehkämper M. (2020) Evaluation of Optimized Procedures for High-Precision Lead Isotope Analyses of Seawater by Multiple Collector Inductively Coupled Plasma Mass Spectrometry. *Anal Chem* **92**, 11232–11241.

Griscom H. P. and Ashton M. S. (2011) Restoration of dry tropical forests in Central America: A review of pattern and process. *For Ecol Manage* **261**, 1564–1579.

Gutjahr M., Frank M., Stirling C. H., Klemm V., van de Flierdt T. and Halliday A. N. (2007) Reliable extraction of a deepwater trace metal isotope signal from Fe–Mn oxyhydroxide coatings of marine sediments. *Chem Geol* **242**, 351–370.

Haley B. A., Frank M., Spielhagen R. F. and Fietzke J. (2008) Radiogenic isotope record of Arctic Ocean circulation and weathering inputs of the past 15 million years. *Paleoceanography* **23**.

Haley B. A., Wu Y., Muratli J. M., Basak C., Pena L. D. and Goldstein S. L. (2021) Rare earth element and neodymium isotopes of the eastern US GEOTRACES Equatorial Pacific Zonal Transect (GP16). *Earth Planet Sci Lett* **576**, 117233.

Halliday A. N., Davidson J. P., Holden P., Owen R. M. and Olivarez A. M. (1992) Metalliferous sediments and the scavenging residence time of Nd near hydrothermal vents. *Geophys Res Lett* **19**, 761–764.

Hamelin B., Ferrand J. L., Alleman L., Nicolas E. and Veron A. (1997) Isotopic evidence of pollutant lead transport from North America to the subtropical North Atlantic gyre. *Geochim Cosmochim Acta* **61**, 4423–4428.

Hanawa K. and Talley L. D. (2001) Chapter 5.4 Mode waters. In *International Geophysics* Academic Press. pp. 373–386.

Harlavan Y., Almogi-Labin A. and Herut B. (2010) Tracing Natural and Anthropogenic Pb in Sediments along the Mediterranean Coast of Israel Using Pb Isotopes. *Environ Sci Technol* **44**, 6576–6582.

Harvey J. and Arhan M. (1988) The Water Masses of the Central North Atlantic in 1983—84. *J Phys Oceanogr* **18**, 1855–1875.

Hassel D., Dursbeck F., Brosthaus J., Jost P. and Hofmann K. (1987) *Das Abgas-Emissionsverhalten von Personenkraftwagen in der Bundesrepublik Deutschland im Bezugsjahr 1985. UBA Berichte 7/87.*, Erich Schmidt Verlag, Berlin.

Hatta M., Measures C. I., Wu J., Roshan S., Fitzsimmons J. N., Sedwick P. and Morton P. (2015) An overview of dissolved Fe and Mn distributions during the 2010–2011 U.S. GEOTRACES north Atlantic cruises: GEOTRACES GA03. *Deep Sea Res 2 Top Stud Oceanogr* **116**, 117–129.

Hayes C. T., Anderson R. F., Fleisher M. Q., Huang K. F., Robinson L. F., Lu Y., Cheng H., Edwards R. L. and Moran S. B. (2015) ^{230}Th and ^{231}Pa on GEOTRACES GA03, the U.S. GEOTRACES North Atlantic transect, and implications for modern and paleoceanographic chemical fluxes. *Deep Sea Res 2 Top Stud Oceanogr* **116**, 29–41.

Hemming S. R. and McLennan S. M. (2001) Pb isotope compositions of modern deep sea turbidites. *Earth Planet Sci Lett* **184**, 489–503.

Henderson G. M. and Maier-Reimer E. (2002) Advection and removal of 210Pb and stable Pb isotopes in the oceans: A general circulation model study. *Geochim Cosmochim Acta* **66**, 257–272.

Henley S. F., Cavan E. L., Fawcett S. E., Kerr R., Monteiro T., Sherrell R. M., Bowie A. R., Boyd P. W., Barnes D. K. A., Schloss I. R., Marshall T., Flynn R. and Smith S. (2020) Changing Biogeochemistry of the Southern Ocean and Its Ecosystem Implications. *Front Mar Sci* **7**.

Herman J. R., Bhartia P. K., Torres O., Hsu C., Seftor C. and Celarier E. (1997) Global distribution of UV-absorbing aerosols from Nimbus 7/TOMS data. *J Geophys Res Atmos* **102**, 16911–16922.

Herraiz-Borreguero L. and Rintoul S. R. (2011) Regional circulation and its impact on upper ocean variability south of Tasmania. *Deep Sea Res 2 Top Stud Oceanogr* **58**, 2071–2081.

Herraiz-Borreguero L. and Rintoul S. R. (2010) Subantarctic Mode Water variability influenced by mesoscale eddies south of Tasmania. *J Geophys Res* **115**, C04004.

Hinkley T. K. and Tatsumoto M. (1987) Metals and isotopes in Juan de Fuca Ridge hydrothermal fluids and their associated solid materials. *J Geophys Res Solid Earth* **92**, 11400–11410.

Höfig T. W., Hoernle K., Hauff F. and Frank M. (2016) Hydrothermal versus active margin sediment supply to the eastern equatorial Pacific over the past 23 million years traced by radiogenic Pb isotopes: Paleoceanographic and paleoclimatic implications. *Geochim Cosmochim Acta* **190**, 213–238.

Holzer M., Smethie W. M. and Ting Y. H. (2018) Ventilation of the Subtropical North Atlantic: Locations and Times of Last Ventilation Estimated Using Tracer Constraints From GEOTRACES Section GA03. *J Geophys Res Oceans* **123**, 2332–2352.

Hülse D., Vervoort P., van de Velde S. J., Kanzaki Y., Boudreau B., Arndt S., Bottjer D. J., Hoogakker B., Kuderer M., Middelburg J. J., Volkenborn N., Kirtland Turner S. and Ridgwell A. (2022) Assessing the impact of bioturbation on sedimentary isotopic records through numerical models. *Earth Sci Rev* **234**, 104213.

Humphris S. E., Tivey M. K. and Tivey M. A. (2015) The Trans-Atlantic Geotraverse hydrothermal field: A hydrothermal system on an active detachment fault. *Deep Sea Res 2 Top Stud Oceanogr* **121**, 8–16.

Jacobsen S. B. and Wasserburg G. J. (1980) Sm-Nd isotopic evolution of chondrites. *Earth Planet Sci Lett* **50**, 139–155.

Jaffey A. H., Flynn K. F., Glendenin L. E., Bentley W. C. and Essling A. M. (1971) Precision measurement of half-lives and specific activities of ^{235}U and ^{238}U. *Phys Rev C* **4**, 1889.

James C., Tomczak M., Helmond I. and Pender L. (2002) Summer and winter surveys of the Subtropical Front of the southeastern Indian Ocean 1997–1998. *J Mar Syst* **37**, 129–149.

Jeandel C., Bishop J. K. and Zindler A. (1995) Exchange of neodymium and its isotopes between seawater and small and large particles in the Sargasso Sea. *Geochim Cosmochim Acta* **59**, 535–547.

Jeandel C., Delattre H., Grenier M., Pradoux C. and Lacan F. (2013) Rare earth element concentrations and Nd isotopes in the Southeast Pacific Ocean. *Geochem, Geophys, Geosyst* **14**, 328–341.

Jeandel C. and Oelkers E. H. (2015) The influence of terrigenous particulate material dissolution on ocean chemistry and global element cycles. *Chem Geol* **395**, 50–66.

Jenkins W. J., Edmond J. M. and Corliss J. B. (1978) Excess ^{3}He and ^{4}He in Galapagos submarine hydrothermal waters. *Nature* **272**, 156–158.

Jenkins W. J., Lott D. E., German C. R., Cahill K. L., Goudreau J. and Longworth B. (2018) The deep distributions of helium isotopes, radiocarbon, and noble gases along the U.S. GEOTRACES East Pacific Zonal Transect (GP16). *Mar Chem* **201**, 167–182.

Jenkins W. J., Lott D. E., Longworth B. E., Curtice J. M. and Cahill K. L. (2015a) The distributions of helium isotopes and tritium along the U.S. GEOTRACES North Atlantic sections (GEOTRACES GAO3). *Deep Sea Res 2 Top Stud Oceanogr* **116**, 21–28.

Jenkins W. J., Smethie W. M., Boyle E. A. and Cutter G. A. (2015b) Water mass analysis for the U.S. GEOTRACES (GA03) North Atlantic sections. *Deep Sea Res 2 Top Stud Oceanogr* **116**, 6–20.

Jewell A. M., Cooper M. J., Milton J. A., James R. H., Crocker A. J. and Wilson P. A. (2022) Chemical isolation and isotopic analysis of terrigenous sediments with emphasis on effective removal of contaminating marine phases including barite. *Chem Geol* **589**, 120673.

Jones C. E., Halliday A. N., Rea D. K. and Owen R. M. (2000) Eolian inputs of lead to the North Pacific. *Geochim Cosmochim Acta* **64**, 1405–1416.

Jones C. E., Halliday A. N., Rea D. K. and Owen R. M. (1994) Neodymium isotopic variations in North Pacific modern silicate sediment and the insignificance of detrital REE contributions to seawater. *Earth Planet Sci Lett* **127**, 55–66.

Kadko D. (1981) A detailed study of Uranium series nuclides for several sedimentary regimes of the Pacific. PhD Thesis, Columbia University.

Kadko D., Bacon M. P. and Hudson A. (1987a) Enhanced scavenging of ^{210}Pb and ^{210}Po by processes associated with the East Pacific Rise near 8°45′N. *Earth Planet Sci Lett* **81**, 349–357.

Kadko D., Cochran J. K. and Lyle M. (1987b) The effect of bioturbation and adsorption gradients on solid and dissolved radium profiles in sediments from the eastern equatorial Pacific. *Geochim Cosmochim Acta* **51**, 1613–1623.

Kadko D. and Heath G. R. (1984) Models of depth-dependent bioturbation at MANOP site H in the eastern equatorial Pacific. *J Geophys Res* **89**, 6567–6574.

Kalnay E., Kanamitsu M., Kistler R., Collins W., Deaven D., Gandin L., Iredell M., Saha S., White G., Woollen J., Zhu Y., Leetmaa A., Reynolds R., Chelliah M., Ebisuzaki W., Higgins W., Janowiak J., Mo K. C., Ropelewski C., Wang J., Jenne R. and Joseph D. (1996) The NCEP/NCAR 40-Year Reanalysis Project. *Bull Am Meteorol Soc* **77**, 437–471.

Kalnejais L. H., Martin W. R., Signell R. P. and Bothner M. H. (2007) Role of sediment resuspension in the remobilization of particulate-phase metals from coastal sediments. *Environ Sci Technol* **41**, 2282–2288.

Karson J. A. and Rona P. A. (1990) Block-tilting, transfer faults, and structural control of magmatic and hydrothermal processes in the TAG area, Mid-Atlantic Ridge 26°N. *Geol Soc Am Bull* **102**, 1635–1645.

Kato Y., Fujinaga K., Nakamura K., Takaya Y., Kitamura K., Ohta J., Toda R., Nakashima T. and Iwamori H. (2011) Deep-sea mud in the Pacific Ocean as a potential resource for rare-earth elements. *Nat Geosci* **4**, 535–539.

Kelly A. E., Reuer M. K., Goodkin N. F. and Boyle E. A. (2009) Lead concentrations and isotopes in corals and water near Bermuda, 1780-2000. *Earth Planet Sci Lett* **283**, 93–100.

Kessler W. S. (2006) The circulation of the eastern tropical Pacific: A review. *Prog Oceanogr* **69**, 181–217.

Klaas C. and Archer D. E. (2002) Association of sinking organic matter with various types of mineral ballast in the deep sea: Implications for the rain ratio. *Global Biogeochem Cycles* **16**, 1–14.

Kleinrock M. C. and Humphris S. E. (1996) Structural control on sea-floor hydrothermal activity at the TAG active mound. *Nature* **6587**, 149–153.

Klinkhammer G., Elderfield H., Greaves M., Rona P. and Nelsen T. (1986) Manganese geochemistry near high-temperature vents in the Mid-Atlantic Ridge rift valley. *Earth Planet Sci Lett* **80**, 230–240.

Klinkhammer G. P. (1980a) Early diagenesis in sediments from the eastern equatorial Pacific, II. Pore water metal results. *Earth Planet Sci Lett* **49**, 81–101.

Klinkhammer G. P. (1980b) Observations of the distribution of manganese over the East Pacific Rise. *Chem Geol* **29**, 211–226.

Klunder M. B., Laan P., Middag R., de Baar H. J. W. and Bakker K. (2012) Dissolved iron in the Arctic Ocean: Important role of hydrothermal sources, shelf input and scavenging removal. *J Geophys Res Oceans* **117**.

Klunder M. B., Laan P., Middag R., De Baar H. J. W. and van Ooijen J. C. (2011) Dissolved iron in the Southern Ocean (Atlantic sector). *Deep Sea Res 2 Top Stud Oceanogr* **58**, 2678–2694.

Koçak M., Kubilay N., Herut B. and Nimmo M. (2007) Trace Metal Solid State Speciation in Aerosols of the Northern Levantine Basin, East Mediterranean. *J Atmos Chem* **56**, 239–257.

Koch-Larrouy A., Morrow R., Penduff T. and Juza M. (2010) Origin and mechanism of Subantarctic Mode Water formation and transformation in the Southern Indian Ocean. *Ocean Dyn* **60**, 563–583.

Kopczynska E. E., Dehairs F., Elskens M. and Wright S. (2001) Phytoplankton and microzooplankton variability between the Subtropical and Polar Fronts south of Australia: Thriving under regenerative and new production in late summer. *J Geophys Res Oceans* **106**, 31597–31609.

Koschinsky A., Fritsche U. and Winkler A. (2001) Sequential leaching of Peru Basin surface sediment for the assessment of aged and fresh heavy metal associations and mobility. *Deep Sea Res 2 Top Stud Oceanogr* **48**, 3683–3699.

Koschinsky A. and Hein J. R. (2003) Uptake of elements from seawater by ferromanganese crusts: solid-phase associations and seawater speciation. *Mar Geol* **198**, 331–351.

Koschinsky A., Winkler A. and Fritsche U. (2003) Importance of different types of marine particles for the scavenging of heavy metals in the deep-sea bottom water. *Appl Geochem* **18**, 693–710.

Kozelka P. B. and Bruland K. W. (1998) Chemical speciation of dissolved Cu, Zn, Cd, Pb in Narragansett Bay, Rhode Island. *Mar Chem* **60**, 267–282.

Kozelka P. B., Sañudo-Wilhelmy S., Flegal A. R. and Bruland K. W. (1997) Physico-chemical Speciation of Lead in South San Francisco Bay. *Estuar Coast Shelf Sci* **44**, 649–658.

Kristensen L. J. (2015) Quantification of atmospheric lead emissions from 70 years of leaded petrol consumption in Australia. *Atmos Environ* **111**, 195–201.

Kristensen L. J., Taylor M. P. and Flegal A. R. (2017) An odyssey of environmental pollution: The rise, fall and remobilisation of industrial lead in Australia. *Appl Geochem* **83**, 3–13.

Lacan F. and Jeandel C. (2005) Neodymium isotopes as a new tool for quantifying exchange fluxes at the continent–ocean interface. *Earth Planet Sci Lett* **232**, 245–257.

Lai X., Norisuye K., Mikata M., Minami T., Bowie A. R. and Sohrin Y. (2008) Spatial and temporal distribution of Fe, Ni, Cu and Pb along 140°E in the Southern Ocean during austral summer 2001/02. *Mar Chem* **111**, 171–183.

Lalou C. (1993) New age data for Mid-Atlantic Ridge hydrothermal sites: TAG and Snakepit chronology revisited. *J Geophys Res* **98**, 9705–9713.

Lalou C., Reyss J. L. and Brichet E. (1998) Age of sub-bottom sulfide samples at the TAG active mound. In *Proceedings of the Ocean Drilling Program: 158 Scientific Results* (eds. P. M. Herzig, S. E. Humphris and E. A. Zierenberg). **158**, 111-117. Ocean Drilling Program.

Lalou C., Thompson G., Arnold M., Brichet E., Druffel E. and Rona P. A. (1990) Geochronology of TAG and Snakepit hydrothermal fields, Mid-Atlantic Ridge: witness to a long and complex hydrothermal history. *Earth Planet Sci Lett* **97**, 113–128.

Lam P. J., Ohnemus D. C. and Auro M. E. (2015) Size-fractionated major particle composition and concentrations from the US GEOTRACES North Atlantic Zonal Transect. *Deep Sea Res 2 Top Stud Oceanogr* **116**, 303–320.

Lambert C. E., Nicolas E., Veron A., Buatmenard P., Klinkhammer G., Lecorre P. and Morin P. (1991) Anthropogenic lead cycle in the northeastern Atlantic. *Oceanologica Acta* **14**, 59–66.

Langmuir C. H., Bender J. F. and Batiza R. (1986) Petrological and tectonic segmentation of the East Pacific Rise, 5°30′–14°30′ N. *Nature* **322**, 422–429.

Lanning N. T., Jiang S., Amaral V. J., Mateos K., Steffen J. M., Lam P. J., Boyle E. A. and Fitzsimmons J. N. (2023) Isotopes illustrate vertical transport of anthropogenic Pb by reversible scavenging within Pacific Ocean particle veils. *Proc Natl Acad Sci U S A* **120**, e2219688120.

Latour P., Wuttig K., van der Merwe P., Strzepek R. F., Gault-Ringold M., Townsend A. T., Holmes T. M., Corkill M. and Bowie A. R. (2021) Manganese biogeochemistry in the Southern Ocean, from Tasmania to Antarctica. *Limnol Oceanogr* **66**, 2547–2562.

Lattimore R. K., Rona P. A. and Dewald O. E. (1974) Magnetic anomaly sequence in the central North Atlantic. *J Geophys Res* **79**, 1207–1209.

Laumond F., Copin-Montegut G., Courau P. and Nicolas E. (1984) Cadmium, copper and lead in the western Mediterranean Sea. *Mar Chem* **15**, 251–261.

Lavín M. F., Fiedler P. C., Amador J. A., Ballance L. T., Färber-Lorda J. and Mestas-Nuñez A. M. (2006) A review of eastern tropical Pacific oceanography: Summary. *Prog Oceanogr* **69**, 391–398.

Lee J.-M., Boyle E. A., Echegoyen-Sanz Y., Fitzsimmons J. N., Zhang R. and Kayser R. A. (2011) Analysis of trace metals (Cu, Cd, Pb, and Fe) in seawater using single batch nitrilotriacetate resin extraction and isotope dilution inductively coupled plasma mass spectrometry. *Anal Chim Acta* **686**, 93–101.

Lee J.-M., Boyle E. A., Gamo T., Obata H., Norisuye K. and Echegoyen Y. (2015) Impact of anthropogenic Pb and ocean circulation on the recent distribution of Pb isotopes in the Indian Ocean. *Geochim Cosmochim Acta* **170**, 126–144.

Lee J.-M., Boyle E. A., Suci Nurhati I., Pfeiffer M., Meltzner A. J. and Suwargadi B. (2014) Coral-based history of lead and lead isotopes of the surface Indian Ocean since the mid-20th century. *Earth Planet Sci Lett* **398**, 37–47.

Lee S.-H., Povinec P. P., Wyse E., Pham M. K., Hong G.-H., Chung C.-S., Kim S.-H. and Lee H.-J. (2005) Distribution and inventories of ^{90}Sr, ^{137}Cs, ^{241}Am and Pu isotopes in sediments of the Northwest Pacific Ocean. *Mar Geol* **216**, 249–263.

Li F., Ginoux P. and Ramaswamy V. (2008) Distribution, transport, and deposition of mineral dust in the Southern Ocean and Antarctica: Contribution of major sources. *J Geophys Res* **113**, D10207.

Li M., Toner B. M., Baker B. J., Breier J. A., Sheik C. S. and Dick G. J. (2014) Microbial iron uptake as a mechanism for dispersing iron from deep-sea hydrothermal vents. *Nat Commun* **5**, 1–8.

Li Y.-H. and Schoonmaker J. E. (2014) Chemical Composition and Mineralogy of Marine Sediments. In *Treatise on Geochemistry: Second Edition* (eds. H. Holland and K. Turekian). Elsevier. pp. 1–32.

Liao J., Chen J., Sun X., Wu Z., Deng Y., Shi X., Wang Y., Chen Y. and Koschinsky A. (2022) Quantifying the controlling mineral phases of rare-earth elements in deep-sea pelagic sediments. *Chem Geol* **595**, 120792.

Liao J., Sun X., Wu Z., Sa R., Guan Y., Lu Y., Li D., Liu Y., Deng Y. and Pan Y. (2019) Fe-Mn (oxyhydr)oxides as an indicator of REY enrichment in deep-sea sediments from the central North Pacific. *Ore Geol Rev* **112**, 103044.

Lilley M. D., Feely R. A. and Trefry J. H. (1995) Chemical and biochemical transformations in hydrothermal plumes. *Geophys Monogr Ser* **91**, 369–391.

Lin P., Xu C., Zhang S., Sun L., Schwehr K. A., Bretherton L., Quigg A. and Santschi P. H. (2017) Importance of coccolithophore-associated organic biopolymers for fractionating particle-reactive radionuclides (^{234}Th, ^{233}Pa, ^{210}Pb, ^{210}Po, and ^{7}Be) in the ocean. *J Geophys Res Biogeosci* **122**, 2033–2045.

Ling H. F., Burton K. W., O'Nions R. K., Kamber B. S., von Blanckenburg F., Gibb A. J. and Hein J. R. (1997) Evolution of Nd and Pb isotopes in Central Pacific seawater from ferromanganese crusts. *Earth Planet Sci Lett* **146**, 1–12.

Ling H.-F., Jiang S.-Y., Frank M., Zhou H.-Y., Zhou F., Lu Z.-L., Chen X.-M., Jiang Y.-H. and Ge C.-D. (2005) Differing controls over the Cenozoic Pb and Nd isotope evolution of deepwater in the central North Pacific Ocean. *Earth Planet Sci Lett* **232**, 345–361.

Lion L. W., Altmann R. Scott. and Leckie J. O. (1982) Trace-metal adsorption characteristics of estuarine particulate matter: evaluation of contributions of iron/manganese oxide and organic surface coatings. *Environ Sci Technol* **16**, 660–666.

Little S. H., Archer C., McManus J., Najorka J., Wegorzewski A. V. and Vance D. (2020) Towards balancing the oceanic Ni budget. *Earth Planet Sci Lett* **547**, 116461.

Liu Y., Lo L., Shi Z., Wei K.-Y., Chou C.-J., Chen Y.-C., Chuang C.-K., Wu C.-C., Mii H.-S., Peng Z., Amakawa H., Burr G. S., Lee S.-Y., DeLong K. L., Elderfield H. and Shen C.-C. (2015) Obliquity pacing of the western Pacific Intertropical Convergence Zone over the past 282,000 years. *Nat Commun* **6**, 10018.

Livingston H. D. and Povinec P. P. (2002) A millennium perspective on the contribution of global fallout radionuclides to ocean science. *Health Phys* **82**, 656–668.

Livingston H. D. and Povinec P. P. (2000) Anthropogenic marine radioactivity. *Ocean Coast Manag* **43**, 689–712.

Loaëc M., Olier R. and Guezennec J. (1998) Chelating properties of bacterial exopolysaccharides from deep-sea hydrothermal vents. *Carbohydr Polym* **35**, 65–70.

Lonsdale P. (1976) Abyssal circulation of the southeastern Pacific and some geological implications. *J Geophys Res* **81**, 1163–1176.

Lonsdale P. and Klitgord K. D. (1978) Structure and tectonic history of the eastern Panama Basin. *Geol Soc Am Bull* **89**, 981.

Loranger S. and Zayed J. (1994) Manganese and lead concentrations in ambient air and emission rates from unleaded and leaded gasoline between 1981 and 1992 in Canada: A comparative study. *Atmos Environ* **28**, 1645–1651.

Lough A. J. M., Homoky W. B., Connelly D. P., Comer-Warner S. A., Nakamura K., Abyaneh M. K., Kaulich B. and Mills R. A. (2019) Soluble iron conservation and colloidal iron dynamics in a hydrothermal plume. *Chem Geol* **511**, 225–237.

Lough A. J. M., Klar J. K., Homoky W. B., Comer-Warner S. A., Milton J. A., Connelly D. P., James R. H. and Mills R. A. (2017) Opposing authigenic controls on the isotopic signature of dissolved iron in hydrothermal plumes. *Geochim Cosmochim Acta* **202**, 1–20.

Lough A. J. M., Tagliabue A., Demasy C., Resing J. A., Mellett T., Wyatt N. J. and Lohan M. C. (2023) Tracing differences in iron supply to the Mid-Atlantic Ridge valley between hydrothermal vent sites: implications for the addition of iron to the deep ocean. *Biogeosciences* **20**, 405–420.

Lupton J. E. (1995) Hydrothermal plumes: Near and far field. *Geophys Monogr Ser* **91**, 317–346.

Lupton J. E., Delaney J. R., Johnson H. P. and Tivey M. K. (1985) Entrainment and vertical transport of deep-ocean water by buoyant hydrothermal plumes. *Nature* **316**, 621–623.

Lyle M. (1992) Composition Maps of Surface Sediments of the Eastern Tropical Pacific Ocean. In *Proceedings of the Ocean Drilling Program, 138 Initial Reports* (eds. L. Mayer, N. Pisias, T. Janecek, et al.). **138**, 101-115. Ocean Drilling Program.

Lyle M., Heath G. R. and Robbins J. M. (1984) Transport and release of transition elements during early diagenesis: Sequential leaching of sediments from MANOP Sites M and H. Part I. pH 5 acetic acid leach. *Geochim Cosmochim Acta* **48**, 1705–1715.

Mantyla A. W. (1975) On the potential temperature in the abyssal Pacific Ocean. *J Mar Res* **33**.

Maring H. B. and Duce R. A. (1990) The impact of atmospheric aerosols on trace metal chemistry in open ocean surface seawater. 3. Lead. *J Geophys Res* **95**, 5341–5347.

Marsac R., Catrouillet C., Davranche M., Bouhnik-Le Coz M., Briant N., Janot N., Otero-Fariña A., Groenenberg J. E., Pédrot M. and Dia A. (2021) Modeling rare earth elements binding to humic acids with model VII. *Chem Geol* **567**, 120099.

Marshall J. and Speer K. (2012) Closure of the meridional overturning circulation through Southern Ocean upwelling. *Nat Geosci* **5**, 171–180.

Martin E. E., Macdougall J. D., Herbert T. D., Paytan A. and Kastner M. (1995) Strontium and neodymium isotopic analyses of marine barite separates. *Geochim Cosmochim Acta* **59**, 1353–1361.

Matsumoto K. (2007) Radiocarbon-based circulation age of the world oceans. *J Geophys Res* **112**, C09004.

McCaig A. M., Cliff R. A., Escartin J., Fallick A. E. and MacLeod C. J. (2007) Oceanic detachment faults focus very large volumes of black smoker fluids. *Geology* **35**, 935–938.

McCartney M. S. (1992) Recirculating components to the deep boundary current of the northern North Atlantic. *Prog Oceanogr* **29**, 283–383.

McCartney M. S. (1977) Subantarctic Mode Water. In *A Voyage of Discovery: George Deacon 70th Anniversary Volume* (ed. M. V. Angel). Deep-Sea Res. Suppl. pp. 103–119.

McCartney M. S. (1982) The subtropical recirculation of mode waters. *J Mar Res* **40**, 427–464.

McCartney M. S. and Donohue K. A. (2007) A deep cyclonic gyre in the Australian–Antarctic Basin. *Prog Oceanogr* **75**, 675–750.

McCartney M. S. and Talley L. D. (1982) The Subpolar Mode Water of the North Atlantic Ocean. *J Phys Oceanogr* **12**, 1169–1188.

McConnell J. R., Maselli O. J., Sigl M., Vallelonga P., Neumann T., Anschütz H., Bales R. C., Curran M. A. J., Das S. B., Edwards R., Kipfstuhl S., Layman L. and Thomas E. R. (2014) Antarctic-wide array of high-resolution ice core records reveals pervasive lead pollution began in 1889 and persists today. *Sci Rep* **4**, 5848.

McDonagh E. L., Bryden H. L., King B. A. and Sanders R. J. (2008) The circulation of the Indian Ocean at 32°S. *Prog Oceanogr* **79**, 20–36.

McGregor B. A., Harrison C. G. A., Lavelle J. W. and Rona P. A. (1977) Magnetic anomaly patterns on Mid-Atlantic Ridge crest at 26°N. *J Geophys Res* **82**, 231–238.

McLennan S. M., Taylor S. R., McCulloch M. T. and Maynard J. B. (1990) Geochemical and Nd-Sr isotopic composition of deep-sea turbidites: Crustal evolution and plate tectonic associations. *Geochim Cosmochim Acta* **54**, 2015–2050.

Meija J., Yang L., Sturgeon R. E. and Mester Z. (2010) Certification of natural isotopic abundance inorganic mercury reference material NIMS-1 for absolute isotopic composition and atomic weight. *J Anal At Spectrom* **25**, 384–389.

Metz S. and Trefry J. H. (2000) Chemical and mineralogical influences on concentrations of trace metals in hydrothermal fluids. *Geochim Cosmochim Acta* **64**, 2267–2279.

Michard A., Albarède F., Michard G., Minster J. F. and Charlou J. L. (1983) Rare-earth elements and uranium in high-temperature solutions from East Pacific Rise hydrothermal vent field (13 °N). *Nature* **303**, 795–797.

Middag R., de Baar H. J. W., Laan P. and Klunder M. B. (2011) Fluvial and hydrothermal input of manganese into the Arctic Ocean. *Geochim Cosmochim Acta* **75**, 2393–2408.

Middleton J. F. and Bye J. A. T. (2007) A review of the shelf-slope circulation along Australia's southern shelves: Cape Leeuwin to Portland. *Prog Oceanogr* **75**, 1–41.

Middleton J. F. and Cirano M. (2002) A northern boundary current along Australia's southern shelves: The Flinders Current. *J Geophys Res* **107**, 1–11.

Milliman J. D. and Syvitski J. P. M. (1992) Geomorphic/Tectonic Control of Sediment Discharge to the Ocean: The Importance of Small Mountainous Rivers. *J Geol* **100**, 525–544.

Milliman J. D., Troy P. J., Balch W. M., Adams A. K., Li Y.-H. and Mackenzie F. T. (1999) Biologically mediated dissolution of calcium carbonate above the chemical lysocline? *Deep Sea Res 1 Oceanogr Res Pap* **46**, 1653–1669.

Molina-Kescher M., Hathorne E. C., Osborne A. H., Behrens M. K., Kölling M., Pahnke K. and Frank M. (2018) The Influence of Basaltic Islands on the Oceanic REE Distribution: A Case Study From the Tropical South Pacific. *Front Mar Sci* **5**.

Mottl M. J. and McConachy T. F. (1990) Chemical processes in buoyant hydrothermal plumes on the East Pacific Rise near 21°N. *Geochim Cosmochim Acta* **54**, 1911–1927.

Murozumi M., Chow T. J. and Patterson C. (1969) Chemical concentrations of pollutant lead aerosols, terrestrial dusts and sea salts in Greenland and Antarctic snow strata. *Geochim Cosmochim Acta* **33**, 1247–1294.

Murphy D. M., Hudson P. K., Cziczo D. J., Gallavardin S., Froyd K. D., Johnston M. V., Middlebrook A. M., Reinard M. S., Thomson D. S., Thornberry T. and Wexler A. S. (2007) Distribution of lead in single atmospheric particles. *Atmos Chem Phys* **7**, 3195–3210.

Nakai S., Halliday A. N. and Rea D. K. (1993) Provenance of dust in the Pacific Ocean. *Earth Planet Sci Lett* **119**, 143–157.

National Atmospheric Emission Inventory (2023) UK emissions data: Heavy metals. https://naei.beis.gov.uk/data (accessed 05 December 2023).

Ndungu K., Zurbrick C. M., Stammerjohn S., Severmann S., Sherrell R. M. and Flegal A. R. (2016) Lead Sources to the Amundsen Sea, West Antarctica. *Environ Sci Technol* **50**, 6233–6239.

Nelsen T. A. and Forde E. B. (1991) The structure, mass and interactions of the hydrothermal plumes at 26°N on the Mid-Atlantic Ridge. *Earth Planet Sci Lett* **106**, 1–16.

Nicolas E., Ruiz-Pino D., Buat-Ménard P. and Bethoux J. P. (1994) Abrupt decrease of lead concentration in the Mediterranean sea: A response to antipollution policy. *Geophys Res Lett* **21**, 2119–2122.

Nishioka J., Obata H. and Tsumune D. (2013) Evidence of an extensive spread of hydrothermal dissolved iron in the Indian Ocean. *Earth Planet Sci Lett* **361**, 26–33.

Nissen C., Gruber N., Münnich M. and Vogt M. (2021) Southern Ocean Phytoplankton Community Structure as a Gatekeeper for Global Nutrient Biogeochemistry. *Global Biogeochem Cycles* **35**, e2021GB006991.

Noble A. E., Echegoyen-Sanz Y., Boyle E. A., Ohnemus D. C., Lam P. J., Kayser R., Reuer M., Wu J. and Smethie W. (2015) Dynamic variability of dissolved Pb and Pb isotope composition from the U.S. North Atlantic GEOTRACES transect. *Deep Sea Res 2 Top Stud Oceanogr* **116**, 208–225.

Nozaki Y., Thomson J. and Turekian K. K. (1976) The distribution of ^{210}Pb and ^{210}Po in the surface waters of the Pacific Ocean. *Earth Planet Sci Lett* **32**, 304–312.

Nriagu J. O. (1989) A global assessment of natural sources of atmospheric trace metals. *Nature* **338**, 47–49.

Nriagu J. O. (1979) Global inventory of natural and anthropogenic emissions of trace metals to the atmosphere. *Nature* **279**, 409–411.

Nriagu J. O. (1990) The rise and fall of leaded gasoline. *Sci Tot Environ* **92**, 13–28.

Nriagu J. O., Blankson M. L. and Ocran K. (1996) Childhood lead poisoning in Africa: a growing public health problem. *Sci Tot Environ* **181**, 93–100.

Nriagu J. O. and Pacyna J. M. (1988) Quantitative assessment of worldwide contamination of air, water and soils by trace metals. *Nature* **333**, 134–139.

O'Connor B. M., Fine R. A. and Olson D. B. (2005) A global comparison of subtropical underwater formation rates. *Deep Sea Res 1 Oceanogr Res Pap* **52**, 1569–1590.

Oelkers E. H., Jones M. T., Pearce C. R., Jeandel C., Eiriksdottir E. S. and Gislason S. R. (2012) Riverine particulate material dissolution in seawater and its implications for the global cycles of the elements. *C R Geosci* **344**, 646–651.

Olendrzyński K., Anderberg S., Stigliani W., Bartnicki J. and Pacyna J. (1996) Atmospheric emissions and depositions of cadmium, lead, and zinc in Europe during the period 1955–1987. *Environ Rev* **4**, 300–320.

Olivarez A. M., Owen R. M. and Rea D. K. (1991) Geochemistry of eolian dust in Pacific pelagic sediments: Implications for paleoclimatic interpretations. *Geochim Cosmochim Acta* **55**, 2147–2158.

Olivelli A., Murphy K., Bridgestock L., Wilson D. J., Rijkenberg M., Middag R., Weiss D. J., van de Flierdt T. and Rehkämper M. (2023) Decline of anthropogenic lead in South Atlantic Ocean surface waters from 1990 to 2011: New constraints from concentration and isotope data. *Mar Pollut Bull* **189**, 114798.

Orsi A. H., Johnson G. C. and Bullister J. L. (1999) Circulation, mixing, and production of Antarctic Bottom Water. *Prog Oceanogr* **43**, 55–109.

Orsi A. H., Smethie Jr. W. M. and Bullister J. L. (2002) On the total input of Antarctic waters to the deep ocean: A preliminary estimate from chlorofluorocarbon measurements. *J Geophys Res* **107**, 3122.

Orsi A. H., Whitworth T. and Nowlin W. D. (1995) On the meridional extent and fronts of the Antarctic Circumpolar Current. *Deep Sea Res 1 Oceanogr Res Pap* **42**, 641–673.

Pacyna E. G., Pacyna J. M., Fudala J., Strzelecka-Jastrzab E., Hlawiczka S., Panasiuk D., Nitter S., Pregger T., Pfeiffer H. and Friedrich R. (2007) Current and future emissions of selected heavy metals to the atmosphere from anthropogenic sources in Europe. *Atmos Environ* **41**, 8557–8566.

Pacyna J. M. (1984) Estimation of the atmospheric emissions of trace elements from anthropogenic sources in Europe. *Atmos Environ (1967)* **18**, 41–50.

Pacyna J. M. and Graedel T. E. (1995) Atmospheric Emissions Inventories: Status and Prospects. *Annu Rev Energy Environ* **20**, 265–300.

Pacyna J. M. and Munch J. (1988) *Atmospheric emissions of arsenic, cadium, mercury and zinc in Europe in 1982. Technical report NILU OR 17/88*., Norwegian Institute for Air Research (NILU), Lillestrøm.

Pacyna J. M. and Pacyna E. G. (2001) An assessment of global and regional emissions of trace metals to the atmosphere from anthropogenic sources worldwide. *Environ Rev* **9**, 269–298.

Pacyna J. M. and Pacyna E. G. (2000) *Atmospheric emissions of anthropogenic lead in Europe: improvements, updates, historical data and projections. Technical Report GKSS-2000/31.,* GKSS-Forschungszentrum Geesthacht GmbH, Geesthacht.

Park Y.-H., Gamberoni L. and Charriaud E. (1993) Frontal structure, water masses, and circulation in the Crozet Basin. *J Geophys Res* **98**, 12361.

Patterson C. C. and Settle D. M. (1987) Review of data on eolian fluxes of industrial and natural lead to the lands and seas in remote regions on a global scale. *Mar Chem* **22**, 137–162.

Paul M., Bridgestock L., Rehkämper M., van de Flierdt T. and Weiss D. (2015) High-precision measurements of seawater Pb isotope compositions by double spike thermal ionization mass spectrometry. *Anal Chim Acta* **863**, 59–69.

Pavia F., Anderson R., Vivancos S., Fleisher M., Lam P., Lu Y., Cheng H., Zhang P. and Lawrence Edwards R. (2018) Intense hydrothermal scavenging of ^{230}Th and ^{231}Pa in the deep Southeast Pacific. *Mar Chem* **201**, 212–228.

Pennington J. T., Mahoney K. L., Kuwahara V. S., Kolber D. D., Calienes R. and Chavez F. P. (2006) Primary production in the eastern tropical Pacific: A review. *Prog Oceanogr* **69**, 285–317.

Peters B. D., Jenkins W. J., Swift J. H., German C. R., Moffett J. W., Cutter G. A., Brzezinski M. A. and Casciotti K. L. (2018) Water mass analysis of the 2013 US GEOTRACES eastern Pacific zonal transect (GP16). *Mar Chem* **201**, 6–19.

Pettke T., Halliday A. N., Hall C. M. and Rea D. K. (2000) Dust production and deposition in Asia and the north Pacific Ocean over the past 12 Myr. *Earth Planet Sci Lett* **178**, 397–413.

Philander S. G. H., Gu D., Lambert G., Li T., Halpern D., Lau N.-C. and Pacanowski R. C. (1996) Why the ITCZ Is Mostly North of the Equator. *J Clim* **9**, 2958–2972.

Pichat S., Abouchami W. and Galer S. J. G. (2014) Lead isotopes in the Eastern Equatorial Pacific record Quaternary migration of the South Westerlies. *Earth Planet Sci Lett* **388**, 293–305.

Pickart R. S. (1992) Water mass components of the North Atlantic deep western boundary current. *Deep Sea Res A* **39**, 1553–1572.

Pickart R. S., Smethie W. M., Lazier J. R. N., Jones E. P. and Jenkins W. J. (1996) Eddies of newly formed upper Labrador Sea water. *J Geophys Res* **101**, 711–731.

Piepgras D. J. and Jacobsen S. B. (1988) The isotopic composition of neodymium in the North Pacific. *Geochim Cosmochim Acta* **52**, 1373–1381.

Pinheiro J. P., Mota A. M. and Benedetti M. F. (1999) Lead and Calcium Binding to Fulvic Acids: Salt Effect and Competition. *Environ Sci Technol* **33**, 3398–3404.

Pokrovsky O. S., Viers J. and Freydier R. (2005) Zinc stable isotope fractionation during its adsorption on oxides and hydroxides. *J Colloid Interface Sci* **291**, 192–200.

Pourret O., Davranche M., Gruau G. and Dia A. (2007) Rare earth elements complexation with humic acid. *Chem Geol* **243**, 128–141.

Poveda G. and Mesa O. J. (2000) On the existence of Lloró (the rainiest locality on Earth): Enhanced ocean-land-atmosphere interaction by a low-level jet. *Geophys Res Lett* **27**, 1675–1678.

Powell K. J., Brown P. L., Byrne R. H., Gajda T., Hefter G., Leuz A.-K., Sjöberg S. and Wanner H. (2009) Chemical speciation of environmentally significant metals with inorganic ligands. Part 3: The Pb^{2+} + OH^-, Cl^-, CO_3^{2-}, SO_4^{2-}, and PO_4^{3-} systems (IUPAC Technical Report). *Pure Appl Chem* **81**, 2425–2476.

Prospero J. M. and Bonatti E. (1969) Continental dust in the atmosphere of the Eastern Equatorial Pacific. *J Geophys Res* **74**, 3362–3371.

Prospero J. M., Ginoux P., Torres O., Nicholson S. E. and Gill T. E. (2002) Environmental characterization of global sources of atmospheric soil dust identified with the Nimbus 7 Total Ozone Mapping Spectrometer (TOMS) absorbing aerosol product. *Rev Geophys* **40**.

Rauch J. N. and Pacyna J. M. (2009) Earth's global Ag, Al, Cr, Cu, Fe, Ni, Pb, and Zn cycles. *Global Biogeochem Cycles* **23**, GB2001.

Rea D. K. (1994) The paleoclimatic record provided by eolian deposition in the deep sea: The geologic history of wind. *Rev Geophys* **32**, 159–195.

Rehkämper M., Frank M., Hein J. R., Porcelli D., Halliday A., Ingri J. and Liebetrau V. (2002) Thallium isotope variations in seawater and hydrogenetic, diagenetic, and hydrothermal ferromanganese deposits. *Earth Planet Sci Lett* **197**, 65–81.

Rehkämper M. and Halliday A. N. (1998) Accuracy and long-term reproducibility of lead isotopic measurements by multiple-collector inductively coupled plasma mass spectrometry using an external method for correction of mass discrimination. *Int J Mass Spectrom* **181**, 123–133.

Reimi M. A. and Marcantonio F. (2016) Constraints on the magnitude of the deglacial migration of the ITCZ in the Central Equatorial Pacific Ocean. *Earth Planet Sci Lett* **453**, 1–8.

Reimi M. A., Marcantonio F., Lynch-Stieglitz J., Jacobel A. W., McManus J. F. and Winckler G. (2019) The Penultimate Glacial Termination and Variability of the Pacific Intertropical Convergence Zone. *Geophys Res Lett* **46**, 4826–4835.

Ren Y., Wang X., Zhang C., Liu J., Shi X. and Li L. (2023) The distribution and speciation of dissolved Cd and Pb in the Bohai Sea and Yellow Sea, China. *Mar Pollut Bull* **186**, 114437.

Resing J. A., Sedwick P. N., German C. R., Jenkins W. J., Moffett J. W., Sohst B. M. and Tagliabue A. (2015) Basin-scale transport of hydrothermal dissolved metals across the South Pacific Ocean. *Nature* **523**, 200–203.

Reuer M. K. (2002) Centennial-scale elemental and isotopic variability in the tropical and subtropical North Atlantic Ocean. PhD thesis, Massachusetts Institute of Technology.

Reuer M. K., Boyle E. A. and Grant B. C. (2003) Lead isotope analysis of marine carbonates and seawater by multiple collector ICP-MS. *Chem Geol* **200**, 137–153.

Reuer M. K. and Weiss D. J. (2002) Anthropogenic lead dynamics in the terrestrial and marine environment. *Philos Trans A Math Phys Eng Sci* **360**, 2889–2904.

Rhein M., Kieke D. and Steinfeldt R. (2015) Advection of North Atlantic Deep Water from the Labrador sea to the southern hemisphere. *J Geophys Res Oceans* **120**, 2471–2487.

Richardson L. E., Middleton J. F., Kyser T. K., James N. P. and Opdyke B. N. (2019) Shallow water masses and their connectivity along the southern Australian continental margin. *Deep Sea Res 1 Oceanogr Res Pap* **152**, 103083.

Richardson P. L., McCartney M. S. and Maillard C. (1991) A search for meddies in historical data. *Dyn Atmos Oceans* **15**, 241–265.

Ridgway K. R. (2007) Seasonal circulation around Tasmania: An interface between eastern and western boundary dynamics. *J Geophys Res* **112**, C10016.

Ridgway K. R. and Condie S. A. (2004) The 5500-km-long boundary flow off western and southern Australia. *J Geophys Res* **109**, C04017.

Rigual-Hernández A. S., Trull T. W., Bray S. G., Cortina A. and Armand L. K. (2015) Latitudinal and temporal distributions of diatom populations in the pelagic waters of the Subantarctic and Polar

Frontal zones of the Southern Ocean and their role in the biological pump. *Biogeosciences* **12**, 5309–5337.

Rintoul S. R. (2018) The global influence of localized dynamics in the Southern Ocean. *Nature* **558**, 209–218.

Rintoul S. R. and Bullister J. L. (1999) A late winter hydrographic section from Tasmania to Antarctica. *Deep Sea Res 1 Oceanogr Res Pap* **46**, 1417–1454.

Rintoul S. R. and Sokolov S. (2001) Baroclinic transport variability of the Antarctic Circumpolar Current south of Australia (WOCE repeat section SR3). *J Geophys Res Oceans* **106**, 2815–2832.

Ritchie H. (2022) How the world eliminated lead from gasoline. https://ourworldindata.org/leaded-gasoline-phase-out (accessed 02 December 2023).

Rona P. A. (1980) TAG Hydrothermal Field: Mid-Atlantic Ridge crest at latitude 26°N. *J Geol Soc London* **137**, 385–402.

Rona P. A., Bogdanov Y. A., Gurvich E. G., Rimski-Korsakov N. A., Sagalevitch A. M., Hannington M. D. and Thompson G. (1993a) Relict hydrothermal zones in the TAG hydrothermal field, Mid-Atlantic Ridge 26°N, 45°W. *J Geophys Res Solid Earth* **98**, 9715–9730.

Rona P. A., Hannington M. D., Raman C. V., Thompson G., Tivey M. K., Humphris S. E., Lalou C. and Petersen S. (1993b) Active and relict sea-floor hydrothermal mineralization at the TAG hydrothermal field, Mid-Atlantic Ridge. *Econ Geol* **88**, 1989–2017.

Rona P. A., Klinkhammer G., Nelsen T. A., Trefry J. H. and Elderfield H. (1986) Black smokers, massive sulphides and vent biota at the Mid-Atlantic ridge. *Nature* **321**, 33–37.

Rona P. A., McGregor B. A., Betzer P. R., Bolger G. W. and Krause D. C. (1975) Anomalous water temperatures over Mid-Atlantic Ridge crest at 26° North latitude. *Deep-Sea Res Oceanogr Abstr* **22**, 611–618.

Rosengard S. Z., Lam P. J., Balch W. M., Auro M. E., Pike S., Drapeau D. and Bowler B. (2015) Carbon export and transfer to depth across the Southern Ocean Great Calcite Belt. *Biogeosciences* **12**, 3953–3971.

Roshan S., Wu J. and Jenkins W. J. (2016) Long-range transport of hydrothermal dissolved Zn in the tropical South Pacific. *Mar Chem* **183**, 25–32.

Rudge J. F., Reynolds B. C. and Bourdon B. (2009) The double spike toolbox. *Chem Geol* **265**, 420–431.

Rudnicki M. D. and Elderfield H. (1993) A chemical model of the buoyant and neutrally buoyant plume above the TAG vent field, 26 degrees N, Mid-Atlantic Ridge. *Geochim Cosmochim Acta* **57**, 2939–2957.

Rudnicki M. D., James R. H. and Elderfield H. (1994) Near-field variability of the TAG non-buoyant plume, 26°N, Mid-Atlantic Ridge. *Earth Planet Sci Lett* **127**, 1–10.

Rusiecka D., Gledhill M., Milne A., Achterberg E. P., Annett A. L., Atkinson S., Birchill A., Karstensen J., Lohan M., Mariez C., Middag R., Rolison J. M., Tanhua T., Ussher S. and Connelly D. (2018) Anthropogenic Signatures of Lead in the Northeast Atlantic. *Geophys Res Lett* **45**, 2734–2743.

Saito M. A., Noble A. E., Tagliabue A., Goepfert T. J., Lamborg C. H. and Jenkins W. J. (2013) Slow-spreading submarine ridges in the South Atlantic as a significant oceanic iron source. *Nat Geosci* **6**, 775–779.

Sander S. G. and Koschinsky A. (2011) Metal flux from hydrothermal vents increased by organic complexation. *Nat Geosci* **4**, 145–150.

Sangster D. F., Outridge P. M. and Davis W. J. (2000) Stable lead isotope characteristics of lead ore deposits of environmental significance. *Environ Rev* **8**, 115–147.

Sarmiento J. L., Gruber N., Brzezinski M. A. and Dunne J. P. (2004) High-latitude controls of thermocline nutrients and low latitude biological productivity. *Nature* **427**, 56–60.

Saukel C., Lamy F., Stuut J. B. W., Tiedemann R. and Vogt C. (2011) Distribution and provenance of wind-blown SE Pacific surface sediments. *Mar Geol* **280**, 130–142.

Sauvé S., Mart ı ´ nez C. E., McBride M. and Hendershot W. (2000) Adsorption of Free Lead (Pb^{2+}) by Pedogenic Oxides, Ferrihydrite, and Leaf Compost. *Soil Sci Soc Am J* **64**, 595–599.

Sauvé S., McBride M. B. and Hendershot W. H. (1997) Speciation of Lead in Contaminated Soils. *Environ Pollut* **98**, 149–155.

Sauvé S., McBride M. and Hendershot W. (1998) Soil Solution Speciation of Lead(II): Effects of Organic Matter and pH. *Soil Sci Soc Am J* **62**, 618–621.

Schaule B. K. and Patterson C. C. (1981) Lead concentrations in the northeast Pacific: evidence for global anthropogenic perturbations. *Earth Planet Sci Lett* **54**, 97–116.

Schijf J. and Byrne R. H. (2021) Speciation of yttrium and the rare earth elements in seawater: Review of a 20-year analytical journey. *Chem Geol* **584**, 120479.

Schlitzer R. (2020) Ocean Data View.

Schlitzer R., Anderson R. F., Dodas E. M., Lohan M., Geibert W., Tagliabue A… Zurbrick C. (2018) The GEOTRACES Intermediate Data Product 2017. *Chem Geol* **493**, 210–223.

Schmitz W. J. and McCartney M. S. (1993) On the North Atlantic Circulation. *Rev Geophys* **31**, 29–49.

Schneider T., Bischoff T. and Haug G. H. (2014) Migrations and dynamics of the intertropical convergence zone. *Nature* **513**, 45–53.

SCOR Working Group (2007) GEOTRACES – An international study of the global marine biogeochemical cycles of trace elements and their isotopes. *Geochemistry* **67**, 85–131.

Scott M. R., Scott R. B., Rona P. A., Butler L. W. and Nalwalk A. J. (1974) Rapidly accumulating manganese deposit from the median valley of the Mid-Atlantic Ridge. *Geophys Res Lett* **1**, 355–358.

Scott R. B., Rona P. A., McGregor B. A. and Scott M. R. (1974) The TAG hydrothermal field. *Nature* **251**, 301–302.

Settle D. M. and Patterson C. C. (1980) Lead in Albacore: Guide to lead pollution in Americans. *Science (1979)* **207**, 1167–1176.

Shen G. T. and Boyle E. A. (1988) Thermocline ventilation of anthropogenic lead in the western North Atlantic. *J Geophys Res Oceans* **93**, 15715–15732.

Sherman L. S., Blum J. D., Dvonch J. T., Gratz L. E. and Landis M. S. (2015) The use of Pb, Sr, and Hg isotopes in Great Lakes precipitation as a tool for pollution source attribution. *Sci Tot Environ* **502**, 362–374.

Sherrell R. M., Boyle E. A. and Hamelin B. (1992) Isotopic equilibration between dissolved and suspended particulate lead in the Atlantic Ocean: Evidence from ^{210}Pb and stable Pb isotopes. *J Geophys Res* **97**, 257–268.

Sholkovitz E. R., Landing W. M. and Lewis B. L. (1994) Ocean particle chemistry: The fractionation of rare earth elements between suspended particles and seawater. *Geochim Cosmochim Acta* **58**, 1567–1579.

Siddall M., Khatiwala S., van de Flierdt T., Jones K., Goldstein S. L., Hemming S. and Anderson R. F. (2008) Towards explaining the Nd paradox using reversible scavenging in an ocean general circulation model. *Earth Planet Sci Lett* **274**, 448–461.

Simonetti A., Gariépy C. and Carignan J. (2003) Tracing sources of atmospheric pollution in Western Canada using the Pb isotopic composition and heavy metal abundances of epiphytic lichens. *Atmos Environ* **37**, 2853–2865.

Sims K. W. W., Blichert-Toft J., Kyle P. R., Pichat S., Gauthier P.-J., Blusztajn J., Kelly P., Ball L. and Layne G. (2008) A Sr, Nd, Hf, and Pb isotope perspective on the genesis and long-term evolution of alkaline magmas from Erebus volcano, Antarctica. *J Volcanol Geotherm Res* **177**, 606–618.

Singh S. P., Singh S. K., Goswami V., Bhushan R. and Rai V. K. (2012) Spatial distribution of dissolved neodymium and ε_{Nd} in the Bay of Bengal: Role of particulate matter and mixing of water masses. *Geochim Cosmochim Acta* **94**, 38–56.

Sloyan B. M. and Rintoul S. R. (2001) Circulation, Renewal, and Modification of Antarctic Mode and Intermediate Water. *J Phys Oceanogr* **31**, 1005–1030.

Sohrin Y., Urushihara S., Nakatsuka S., Kono T., Higo E., Minami T., Norisuye K. and Umetani S. (2008) Multielemental determination of GEOTRACES key trace metals in seawater by ICPMS after preconcentration using an ethylenediaminetriacetic acid chelating resin. *Anal Chem* **80**, 6267–6273.

Sokolov S. and Rintoul S. (2000) Circulation and water masses of the southwest Pacific: WOCE Section P11, Papua New Guinea to Tasmania. *J Mar Res* **58**, 223–268.

Sokolov S. and Rintoul S. R. (2007) Multiple Jets of the Antarctic Circumpolar Current South of Australia. *J Phys Oceanogr* **37**, 1394–1412.

Sokolov S. and Rintoul S. R. (2002) Structure of Southern Ocean fronts at 140°E. *J Mar Syst* **37**, 151–184.

Soto-Jimenez M. F., Hibdon S. A., Rankin C. W., Aggarawl J., Ruiz-Fernandez A. C., Paez-Osuna F. and Flegal A. R. (2006) Chronicling a Century of Lead Pollution in Mexico: Stable Lead Isotopic Composition Analyses of Dated Sediment Cores. *Environ Sci Technol* **40**, 764–770.

Speer K. G. and Rona P. A. (1989) A model of an Atlantic and Pacific hydrothermal plume. *J Geophys Res Oceans* **94**, 6213–6220.

Speich S., Blanke B., de Vries P., Drijfhout S., Döös K., Ganachaud A. and Marsh R. (2002) Tasman leakage: A new route in the global ocean conveyor belt. *Geophys Res Lett* **29**, 55-1-55–4.

Stancin A. M., Gleason J. D., Rea D. K., Owen R. M., Moore T. C., Blum J. D. and Hovan S. A. (2006) Radiogenic isotopic mapping of late Cenozoic eolian and hemipelagic sediment distribution in the east-central Pacific. *Earth Planet Sci Lett* **248**, 840–850.

Stichel T., Pahnke K., Duggan B., Goldstein S. L., Hartman A. E., Paffrath R. and Scher H. D. (2018) TAG plume: Revisiting the hydrothermal neodymium contribution to seawater. *Front Mar Sci* **5**.

Stramma L. and England M. (1999) On the water masses and mean circulation of the South Atlantic Ocean. *J Geophys Res Oceans* **104**, 20863–20883.

Struve T., van de Flierdt T., Robinson L. F., Bradtmiller L. I., Hines S. K., Adkins J. F., Lambelet M., Crocket K. C., Kreissig K., Coles B. and Auro M. E. (2016) Neodymium isotope analyses after combined extraction of actinide and lanthanide elements from seawater and deep-sea coral aragonite. *Geochem, Geophys, Geosyst* **17**, 232–240.

Stumpf R., Frank M., Schönfeld J. and Haley B. A. (2010) Late Quaternary variability of Mediterranean Outflow Water from radiogenic Nd and Pb isotopes. *Quat Sci Rev* **29**, 2462–2472.

Sverdrup H. U., Johnson M. W. and Fleming R. H. (1942) *The Oceans: Their physics, chemistry, and general biology*., Prentice-Hall, New York.

Swift J. H. (1984) The circulation of the Denmark Strait and Iceland-Scotland overflow waters in the North Atlantic. *Deep Sea Res A* **31**, 1339–1355.

Tachikawa K., Arsouze T., Bayon G., Bory A., Colin C., Dutay J.-C., Frank N., Giraud X., Gourlan A. T., Jeandel C., Lacan F., Meynadier L., Montagna P., Piotrowski A. M., Plancherel Y., Pucéat E., Roy-Barman M. and Waelbroeck C. (2017) The large-scale evolution of neodymium isotopic composition in the global modern and Holocene ocean revealed from seawater and archive data. *Chem Geol* **457**, 131–148.

Tachikawa K., Athias V. and Jeandel C. (2003) Neodymium budget in the modern ocean and paleo-oceanographic implications. *J Geophys Res Oceans* **108**.

Tachikawa K., Jeandel C. and Roy-Barman M. (1999) A new approach to the Nd residence time in the ocean: the role of atmospheric inputs. *Earth Planet Sci Lett* **170**, 433–446.

Tagliabue A., Lough A. J. M., Vic C., Roussenov V., Gula J., Lohan M. C., Resing J. A. and Williams R. G. (2022b) Mechanisms Driving the Dispersal of Hydrothermal Iron From the Northern Mid Atlantic Ridge. *Geophys Res Lett* **49**, e2022GL100615.

Talley L. D. (2013) Closure of the Global Overturning Circulation Through the Indian, Pacific, and Southern Oceans: Schematics and Transports. *Oceanography* **26**, 80–97.

Talley L. D. and McCartney M. S. (1982) Distribution and Circulation of Labrador Sea Water. *J Phys Oceanogr* **12**, 1189–1205.

Talley L. D., Pickard G. L., Emery W. J. and Swift J. H. (2011) *Descriptive physical oceanography: An introduction: Sixth edition*., Academic Press.

Tamsitt V., Talley L. D. and Mazloff M. R. (2019) A Deep Eastern Boundary Current Carrying Indian Deep Water South of Australia. *J Geophys Res Oceans* **124**, 2218–2238.

Tanaka T., Togashi S., Kamioka H., Amakawa H., Kagami H., Hamamoto T., Yuhara M., Orihashi Y., Yoneda S., Shimizu H., Kunimaru T., Takahashi K., Yanagi T., Nakano T., Fujimaki H., Shinjo R., Asahara Y., Tanimizu M. and Dragusanu C. (2000) JNdi-1: a neodymium isotopic reference in consistency with LaJolla neodymium. *Chem Geol* **168**, 279–281.

Tang J. and Johannesson K. H. (2003) Speciation of rare earth elements in natural terrestrial waters: assessing the role of dissolved organic matter from the modeling approach. *Geochim Cosmochim Acta* **67**, 2321–2339.

Tanhua T., Olsson K. A. and Jeansson E. (2005) Formation of Denmark Strait overflow water and its hydro-chemical composition. *J Mar Syst* **57**, 264–288.

Thompson A. F., Stewart A. L., Spence P. and Heywood K. J. (2018) The Antarctic Slope Current in a Changing Climate. *Rev Geophys* **56**, 741–770.

Thompson G., Humphris S. E., Schroeder B., Sulanowska M. and Rona P. A. (1988) Active vents and massive sulfides at 26°N (TAG) and 23°N (Snakepit) on the Mid-Atlantic Ridge. *Can Mineral* **26**, 697–711.

Tian H. Z., Zhu C. Y., Gao J. J., Cheng K., Hao J. M., Wang K., Hua S. B., Wang Y. and Zhou J. R. (2015) Quantitative assessment of atmospheric emissions of toxic heavy metals from anthropogenic sources in China: historical trend, spatial distribution, uncertainties, and control policies. *Atmos Chem Phys* **15**, 10127–10147.

Tivey M. K., Mills R. A. and Teagle D. A. H. (1998) Temperature and salinity of fluid inclusions in anhydrite as indicators of seawater entrainment and heating in the TAG active mound. In: *Proceedings of the Ocean Drilling Program: 158 Scientific Results* (eds. P. M. Herzig, S. E. Humphris, D. J. Miller and R. A. Zierenberg). **158**, 179-190. Ocean Drilling Program.

Toner B. M., Fakra S. C., Manganini S. J., Santelli C. M., Marcus M. A., Moffett J. W., Rouxel O., German C. R. and Edwards K. J. (2009) Preservation of iron(II) by carbon-rich matrices in a hydrothermal plume. *Nat Geosci* **2**, 197–201.

Townsend A. T. and Seen A. J. (2012) Historical lead isotope record of a sediment core from the Derwent River (Tasmania, Australia): A multiple source environment. *Sci Tot Environ* **424**, 153–161.

Townsend A. T., Yu Z., Mcgoldrick P. and Hutton J. A. (1998) Precise lead isotope ratios in Australian galena samples by high resolution inductively coupled plasma mass spectrometry. *J Anal At Spectrom* **13**, 809–813.

Trocine R. P. and Trefry J. H. (1988) Distribution and chemistry of suspended particles from an active hydrothermal vent site on the Mid-Atlantic Ridge at 26°N. *Earth Planet Sci Lett* **88**, 1–15.

Tsuchiya M., Talley L. D. and McCartney M. S. (1992) An eastern Atlantic section from Iceland southward across the equator. *Deep Sea Res A* **39**, 1885–1917.

Turekian K. K. (1977) The fate of metals in the oceans. *Geochim Cosmochim Acta* **41**, 1139–1144.

UN Environment Programme (2021) Era of leaded petrol over, eliminating a major threat to human and planetary health [press release]. https://www.unep.org/news-and-stories/press-release/era-leaded-petrol-over-eliminating-major-threat-human-and-planetary (accessed 29 November 2023).

U.S. EPA (2000) *National Air Pollutant Emission Trends, 1900-1998. Technical Report EPA-454/R-00-002.*, Office of Air Quality Planning and Standards Research Triangle Park, NC.

Vallelonga P., Gabrielli P., Balliana E., Wegner A., Delmonte B., Turetta C., Burton G., Vanhaecke F., Rosman K. J. R., Hong S., Boutron C. F., Cescon P. and Barbante C. (2010) Lead isotopic compositions in the EPICA Dome C ice core and Southern Hemisphere Potential Source Areas. *Quat Sci Rev* **29**, 247–255.

Vallelonga P., Van de Velde K., Candelone J.-P., Morgan V. I., Boutron C. F. and Rosman K. J. R. (2002) The lead pollution history of Law Dome, Antarctica, from isotopic measurements on ice cores: 1500 AD to 1989 AD. *Earth Planet Sci Lett* **204**, 291–306.

van Aken H. M. (2000a) The hydrography of the mid-latitude northeast Atlantic Ocean I: The deep water masses. *Deep Sea Res 1 Oceanogr Res Pap* **47**, 757–788.

van Aken H. M. (2000b) The hydrography of the mid-latitude Northeast Atlantic Ocean II: The intermediate water masses. *Deep Sea Res 1 Oceanogr Res Pap* **47**, 789–824.

van Aken H. M., Ridderinkhof H. and de Ruijter W. P. M. (2004) North Atlantic deep water in the south-western Indian Ocean. *Deep Sea Res 1 Oceanogr Res Pap* **51**, 755–776.

van de Flierdt T., Frank M., Halliday A. N., Hein J. R., Hattendorf B., Günther D. and Kubik P. W. (2003) Lead isotopes in North Pacific deep water – implications for past changes in input sources and circulation patterns. *Earth Planet Sci Lett* **209**, 149–164.

van de Flierdt T., Frank M., Halliday A. N., Hein J. R., Hattendorf B., Günther D. and Kubik P. W. (2004) Tracing the history of submarine hydrothermal inputs and the significance of hydrothermal hafnium for the seawater budget - A combined Pb-Hf-Nd isotope approach. *Earth Planet Sci Lett* **222**, 259–273.

Van de Velde K., Vallelonga P., Candelone J.-P., Rosman K. J. R., Gaspari V., Cozzi G., Barbante C., Udisti R., Cescon P. and Boutron C. F. (2005) Pb isotope record over one century in snow from Victoria Land, Antarctica. *Earth Planet Sci Lett* **232**, 95–108.

Véron A., Church T. M., Patterson C. C., Erel Y. and Merrill J. T. (1992) Continental origin and industrial sources of trace metals in the Northwest Atlantic troposphere. *J Atmos Chem* **14**, 339–351.

Véron A., Flament P., Bertho M. L., Alleman L., Flegal R. and Hamelin B. (1999) Isotopic evidence of pollutant lead sources in northwestern France. *Atmos Environ* **33**, 3377–3388.

Véron A. J., Church T. M., Flegal A. R., Patterson C. C. and Erel Y. (1993) Response of lead cycling in the surface Sargasso Sea to changes in tropospheric input. *J Geophys Res Oceans* **98**, 18269–18276.

Véron A. J., church T. M., Patterson C. C. and Flegal A. R. (1994) Use of stable lead isotopes to characterize the sources of anthropogenic lead in North Atlantic surface waters. *Geochim Cosmochim Acta* **58**, 3199–3206.

Viers J., Dupré B. and Gaillardet J. (2009) Chemical composition of suspended sediments in World Rivers: New insights from a new database. *Sci Tot Environ* **407**, 853–868.

Vlastélic I., Abouchami W., Galer S. J. G. and Hofmann A. W. (2001) Geographic control on Pb isotope distribution and sources in Indian Ocean Fe-Mn deposits. *Geochim Cosmochim Acta* **65**, 4303–4319.

von Blanckenburg F., O'Nions R. K. and Hein J. R. (1996) Distribution and sources of pre-anthropogenic lead isotopes in deep ocean water from Fe-Mn crusts. *Geochim Cosmochim Acta* **60**, 4957–4963.

Von Damm K. L. (1990) Seafloor hydrothermal activity: black smoker chemistry and chimneys. *Annu Rev Earth Planet Sci* **18**, 173–204.

Von Damm K. L., Edmond J. M., Grant B., Measures C. I., Walden B. and Weiss R. F. (1985) Chemistry of submarine hydrothermal solutions at 21 °N, East Pacific Rise. *Geochim Cosmochim Acta* **49**, 2197–2220.

von Storch H., Costa-Cabral M., Hagner C., Feser F., Pacyna J., Pacyna E. and Kolb S. (2003) Four decades of gasoline lead emissions and control policies in Europe: a retrospective assessment. *Sci Tot Environ* **311**, 151–176.

Wang C. and Fiedler P. C. (2006) ENSO variability and the eastern tropical Pacific: A review. *Prog Oceanogr* **69**, 239–266.

Weber II E. T., Owen R. M., Dickens G. R., Halliday A. N., Jones C. E. and Rea D. K. (1996) Quantitative resolution of eolian continental crustal material and volcanic detritus in North Pacific surface sediment. *Paleoceanography* **11**, 115–127.

Wedepohl K. H. (1995) The composition of the continental crust. *Geochim Cosmochim Acta* **59**, 1217–1232.

Weis D., Kieffer B., Maerschalk C., Barling J., de Jong J., Williams G. A., Hanano D., Pretorius W., Mattielli N., Scoates J. S., Goolaerts A., Friedman R. M. and Mahoney J. B. (2006) High-precision isotopic characterization of USGS reference materials by TIMS and MC-ICP-MS. *Geochem, Geophys, Geosyst* **7**.

Weiss D., Boyle E. A., Wu J., Chavagnac V., Michel A. and Reuer M. K. (2003) Spatial and temporal evolution of lead isotope ratios in the North Atlantic Ocean between 1981 and 1989. *J Geophys Res* **108**, 3306.

Wells M. L., Kozelka P. B. and Bruland K. W. (1998) The complexation of `dissolved' Cu, Zn, Cd and Pb by soluble and colloidal organic matter in Narragansett Bay, RI. *Mar Chem* **62**, 203–217.

White S. N., Humphris S. E. and Kleinrock M. C. (1998) New observations on the distribution of past and present hydrothermal activity in the TAG Area of the Mid-Atlantic Ridge (26°08'N). *Mar Geophys Res (Dordr)* **20**, 41–56.

White W. M., Albarède F. and Télouk P. (2000) High-precision analysis of Pb isotope ratios by multi-collector ICP-MS. *Chem Geol* **167**, 257–270.

White W. M. and Klein E. M. (2014) Composition of the Oceanic Crust. In *Treatise on Geochemistry: Second Edition* (eds. H. Holland and K. Turekian). Elsevier. pp. 457–496.

Wilson D. J., Galy A., Piotrowski A. M. and Banakar V. K. (2015) Quaternary climate modulation of Pb isotopes in the deep Indian Ocean linked to the Himalayan chemical weathering. *Earth Planet Sci Lett* **424**, 256–268.

Wilson D. J., Piotrowski A. M., Galy A. and Clegg J. A. (2013) Reactivity of neodymium carriers in deep sea sediments: Implications for boundary exchange and paleoceanography. *Geochim Cosmochim Acta* **109**, 197–221.

Wilson D. J., van de Flierdt T. and Adkins J. F. (2017) Lead isotopes in deep-sea coral skeletons: Ground-truthing and a first deglacial Southern Ocean record. *Geochim Cosmochim Acta* **204**, 350–374.

Winter B. L., Johnson C. M. and Clark D. L. (1997) Strontium, neodymium, and lead isotope variations of authigenic and silicate sediment components from the Late Cenozoic Arctic Ocean:

Implications for sediment provenance and the source of trace metals in seawater. *Geochim Cosmochim Acta* **61**, 4181–4200.

Woosley R. J. and Millero F. J. (2013) Pitzer model for the speciation of lead chloride and carbonate complexes in natural waters. *Mar Chem* **149**, 1–7.

Wu J. and Boyle E. A. (1997) Lead in the western North Atlantic Ocean: Completed response to leaded gasoline phaseout. *Geochim Cosmochim Acta* **61**, 3279–3283.

Wu J., Rember R., Jin M., Boyle E. A. and Flegal A. R. (2010) Isotopic evidence for the source of lead in the North Pacific abyssal water. *Geochim Cosmochim Acta* **74**, 4629–4638.

Wu L., Taylor M. P., Handley H. K. and Wu M. (2016) Australian atmospheric lead deposition reconstructed using lead concentrations and isotopic compositions of archival lichen and fungi. *Environmental Pollution* **208**, 678–687.

Wuttig K., Townsend A. T., van der Merwe P., Gault-Ringold M., Holmes T., Schallenberg C., Latour P., Tonnard M., Rijkenberg M. J. A., Lannuzel D. and Bowie A. R. (2019) Critical evaluation of a seaFAST system for the analysis of trace metals in marine samples. *Talanta* **197**, 653–668.

Xie R. C. and Marcantonio F. (2012) Deglacial dust provenance changes in the Eastern Equatorial Pacific and implications for ITCZ movement. *Earth Planet Sci Lett* **317**, 386–395.

Yan X., Zhu M., Li W., Peacock C. L., Ma J., Wen H., Liu F., Zhou Z., Zhu C. and Yin H. (2021) Cadmium Isotope Fractionation during Adsorption and Substitution with Iron (Oxyhydr)oxides. *Environ Sci Technol* **55**, 11601–11611.

You C. F. and Bickle M. J. (1998) Evolution of an active sea-floor massive sulphide deposit. *Nature* **394**, 668–671.

Yücel M., Gartman A., Chan C. S. and Luther G. W. (2011) Hydrothermal vents as a kinetically stable source of iron-sulphide-bearing nanoparticles to the ocean. *Nat Geosci* **4**, 367–371.

Zhao M., Canales J. P. and Sohn R. A. (2012) Three-dimensional seismic structure of a Mid-Atlantic Ridge segment characterized by active detachment faulting (Trans-Atlantic Geotraverse, 25°55' N-26°20' N). *Geochem, Geophys, Geosyst* **13**, Q0AG13.

Zhu C., Tian H. and Hao J. (2020) Global anthropogenic atmospheric emission inventory of twelve typical hazardous trace elements, 1995–2012. *Atmos Environ* **220**, 117061.

Ziegler C. L., Murray R. W., Hovan S. A. and Rea D. K. (2007) Resolving eolian, volcanogenic, and authigenic components in pelagic sediment from the Pacific Ocean. *Earth Planet Sci Lett* **254**, 416–432.

Zonenshain L. P., Kuzmin M. I., Lisitsin A. P., Bogdanov Y. A. and Baranov B. V. (1989) Tectonics of the Mid-Atlantic rift valley between the TAG and MARK areas (26-24°N): Evidence for vertical tectonism. *Tectonophysics* **159**, 1–23.

Zurbrick C. M., Boyle E. A., Kayser R. J., Reuer M. K., Wu J., Planquette H., Shelley R., Boutorh J., Cheize M., Contreira L., Barraqueta J. L. M., Lacan F. and Sarthou G. (2018) Dissolved Pb and Pb isotopes in the North Atlantic from the GEOVIDE transect (GEOTRACES GA-01) and their decadal evolution. *Biogeosciences* **15**, 4995–5014.

Zurbrick C. M., Gallon C. and Flegal A. R. (2017) Historic and Industrial Lead within the Northwest Pacific Ocean Evidenced by Lead Isotopes in Seawater. *Environ Sci Technol* **51**, 1203–1212.

Zurbrick C. M., Morton P. L., Gallon C., Shiller A. M., Landing W. M. and Flegal A. R. (2012) Intercalibration of Cd and Pb concentration measurements in the northwest Pacific Ocean. *Limnol Oceanogr Methods* **10**, 270–277.

Appendices

Appendix 1. Literature Compilation of Source Signatures for the Eastern Equatorial Pacific Ocean (Chapter 2)

(1) Terrestrial Sources

The Pb and Nd isotope signatures of potential sources of terrestrial inputs to the Guatemala Basin were characterised based on the bulk rock compositions of major mountain segments along the American Cordillera and analyses of loess and silt deposits from regions of significant dust emissions (Fig. 2.5). For the terrestrial bulk rock compositions, extensive literature data were retrieved from the GEOROC database (https://georoc.eu/) on 27 October 2020, 16 February 2021 and 10 May 2021. These data were filtered largely based on the procedure of Pichat et al. (2014). Briefly, only whole rock data were used and results for xenoliths, ores, mineral separates and inclusions were excluded, to avoid a bias in the average bulk rock compositions available for weathering and erosion. Replicate analyses of the same sample were combined as single entries to ensure that all samples were weighed equally.

The Pacific margins of North and Central America are flanked by various mountain belts. Across the north-south extent of the Pacific margin of Mexico, major mountain belts include the Peninsular Ranges that traverses the Baja California Peninsula, the Sierra Madre Occidental (SMOc) that traverses the northwest part of mainland Mexico, and the Trans-Mexican Volcanic Belt (TMVB) and Sierra Madre del Sur (SMdS) in Southern Mexico (Fig. 2.5). The Pb isotope signatures of these Mexican terranes largely overlap with each other ($^{206}Pb/^{204}Pb$ = 18.5-18.9, $^{207}Pb/^{204}Pb$ = 15.52-15.67, $^{208}Pb/^{204}Pb$ = 38.2-38.8) (Fig. 2.6a, b). The Nd isotope compositions of TMVB, SMdS and the Peninsular Ranges are also similar, with ε_{Nd} values of between –1 and +8, while the composition of SMOc is less radiogenic, with ε_{Nd} of between –4 and +2 and a mean $\varepsilon_{Nd} \approx -1$ (Fig. 2.6c). The Central American Volcanic Arc (CAVA) traverses the Central American land bridge and can be subdivided into a northwest segment (CAVA-NW; Guatemala, El Salvador, Honduras and Nicaragua) with relatively low $^{206}Pb/^{204}Pb$ ratios (18.4-18.7), and a southeast segment (CAVA-SE; Costa Rica and Panama) with higher $^{206}Pb/^{204}Pb$ ratios (18.6-19.3). Both segments of the CAVA have high ε_{Nd} values of +3 to +9. Bulk rocks from the North American Basin and Range Province span large ranges of Pb and Nd isotope compositions, which can be geographically subdivided into a western sector (Great Basin and Mojave Deserts) with high $^{20x}Pb/^{204}Pb$ ratios ($^{206}Pb/^{204}Pb$ = 17.8-19.6, $^{207}Pb/^{204}Pb$ = 15.50-15.75, $^{208}Pb/^{204}Pb$ = 38.1-39.5), and an eastern sector (Mexican Highlands and Rio Grande Rift area) with $^{20x}Pb/^{204}Pb$ ratios that extend to very unradiogenic values ($^{206}Pb/^{204}Pb$ = 17.0-19.3, $^{207}Pb/^{204}Pb$ = 15.40-15.70, $^{208}Pb/^{204}Pb$ = 36.8-39.0) (Fig. 2.7). Lead isotope data by Erhardt et al. (2021) for silt from islands off the coast of Southern California ($^{206}Pb/^{204}Pb$ = 18.8-19.0, $^{207}Pb/^{204}Pb$ = 15.64-15.66, $^{208}Pb/^{204}Pb$ = 39.0-39.4) was taken to be representative for the average dust composition from the Western USA.

Western South America is dominated by the Andean Range, which can be divided into four latitudinal segments with distinct geological histories: the Northern Andes (12°N-5°S, Colombia and

Ecuador), the North-Central Andes (5-14°S, Peru), the Central Andes (14-33°S, Southern Peru, Northern Chile and Bolivia) and the Southern Andes (33-56°S, Chile and Argentina) (Fig. 2.5) (see review by Stern, 2004). The active volcanic arc dominates the Western Cordillera of the Andes and can be divided into the Northern Volcanic Zone (NVZ) in the Northern Andes, the Central Volcanic Zone (CVZ) in the Central Andes, and the Southern Volcanic Zone (SVZ) in the Southern Andes. Bulk rock compositions were compiled separately for these three volcanic zones. A Cenozoic volcanic gap occurs in the North-Central (Peruvian) segment of the Andes due to flat-slab subduction, and the rocks from this segment of the Western Cordillera are plutonic granitoids, known as the Peruvian Coastal Batholith (PCB). Data coverage for the Eastern Cordillera is scarce except for the Central Andean segment.

The NVZ and PCB are characterised by high $^{206}Pb/^{204}Pb$ (> 18.7), with some granitoids from the PCB having very high $^{206}Pb/^{204}Pb$ (~19.8) and $^{208}Pb/^{204}Pb$ (~39.8) ratios (Fig. 2.6a, b). These sources have relatively high ε_{Nd} values of –1 to +7 (Fig. 2.6c). In contrast, Central and Southern Andean rocks are relatively low in $^{206}Pb/^{204}Pb$. The CVZ spans a large range of Pb isotope compositions, and it can be divided into the northern Arequipa Domain, characterised by very low $^{206}Pb/^{204}Pb$ (17.7-18.4), and the southern Antofalla Domain, characterised by higher $^{206}Pb/^{204}Pb$ ratios (18.6-19.0). The Pb isotope compositions of lithologies from the Eastern Cordillera of the Central Andes are intermediate between the results obtained for rocks from the Arequipa and Antofalla Domains. The SVZ is characterised by low $^{20x}Pb/^{204}Pb$ ratios ($^{206}Pb/^{204}Pb$ = 18.3-18.7, $^{207}Pb/^{204}Pb$ = 15.56-15.65, $^{208}Pb/^{204}Pb$ = 38.1-38.7). Most Central Andean materials (CVZ and Eastern Cordillera) have negative ε_{Nd} values, while Southern Andean materials (SVZ) have positive ε_{Nd} signatures (0 to +5).

Several major dust-producing regions are present across the North-Central and Central Andes, including a continuous desert strip along the Peruvian and Northern Chilean coasts, and the plateaus of Puna and Altiplano between the Western and Eastern Cordilleras in the Central Andes (Ginoux et al., 2012). The Pb isotope compositions of surficial deposits from the Atacama Desert (Erhardt et al., 2021) fall on a trend between the SVZ and CVZ, suggesting derivation of erosional products from the terranes that border the desert region (Fig. 2.5; 2.6a, b). Similarly, the Pb and Nd isotope compositions of surficial deposits from Puna-Altiplano fall within the CVZ field (Gili et al., 2016, 2017), in accord with the derivation of erosional products from the Western and Eastern Cordilleras that bound this intermontane plateau. The Central Andean dust sources are characterised based on these surficial deposits, as they better represent the average composition of the aeolian materials that are exported to the atmosphere and ultimately the EEP.

The Pb and Nd isotope compositions of the silicate residue fractions of Chinese loess samples by Jones et al. (1994, 2000) were obtained to represent the East Asian dust source. This source has high $^{20x}Pb/^{204}Pb$ ($^{206}Pb/^{204}Pb$ > 18.9, $^{207}Pb/^{204}Pb$ > 15.67, $^{208}Pb/^{204}Pb$ > 39.2) and highly negative ε_{Nd} signatures of about –11.

(2) MORB

The literature data of Pb and Nd isotope compositions for MORB were retrieved from the PetDB database (https://search.earthchem.org/) on 10 March 2023 and the output was filtered based on the following criteria: (1) fresh basaltic glass samples only; (2) samples from near the axial valley of the EPR segment within 8-10°N. The selected MORB samples have very low $^{20x}Pb/^{204}Pb$ ($^{206}Pb/^{204}Pb$ = 18.2-18.4, $^{207}Pb/^{204}Pb$ = 15.45-15.50, $^{208}Pb/^{204}Pb$ = 37.8-38.1) and high ε_{Nd} values of about +10.

Appendix 2. Resin Coagulation during Nobias PA-1 Solid Phase Extraction (Chapter 3)

During processing of seawater samples which were collected from within the TAG hydrothermal plume, the Nobias PA-1 resin coagulated into larger clumps of about 1 mm size. These clumps adsorbed more strongly to the Teflon walls of the filter funnel in the extraction system and could not be rinsed off readily using the distilled water and 3 M HNO_3 that are used in the normal procedure (Fig. A2). Processed water samples from the plume were therefore subsequently treated with larger volumes of H_2O_2 to achieve a concentration of 0.1 mmol/L (instead of 0.01 mmol/L in the original procedure) before the extraction step. Resin clumping persisted but the clumps that formed were smaller.

This issue is likely related to distinct physicochemical properties of the seawater within the hydrothermal plume. Whilst such issue was previously not reported for the processing of seawater samples with Nobias PA-1 resin, it most likely reflect the presence of high levels of organic colloids, which led to a strong hydrophobic attraction between the Nobias PA-1 resin particles, thus resulting in particle coagulation.

The adsorbed resin was effectively removed from the walls of the filter funnel by rinsing with distilled ethanol. After processing of plume samples, the recovered resin was shaken at least twice in a large volume of 3 M HNO_3 (> 500 mL acid per 10 mL resin) until the clumps disaggregated and the resin texture was smooth. The calculated Pb yields for samples that were affected by Nobias PA-1 resin coagulation generally exceeded 90%, as for non-plume samples that were not impacted by resin coagulation. This demonstrates that resin coagulation was not associated with additional loss of sample Pb during processing or Pb carry-over between samples.

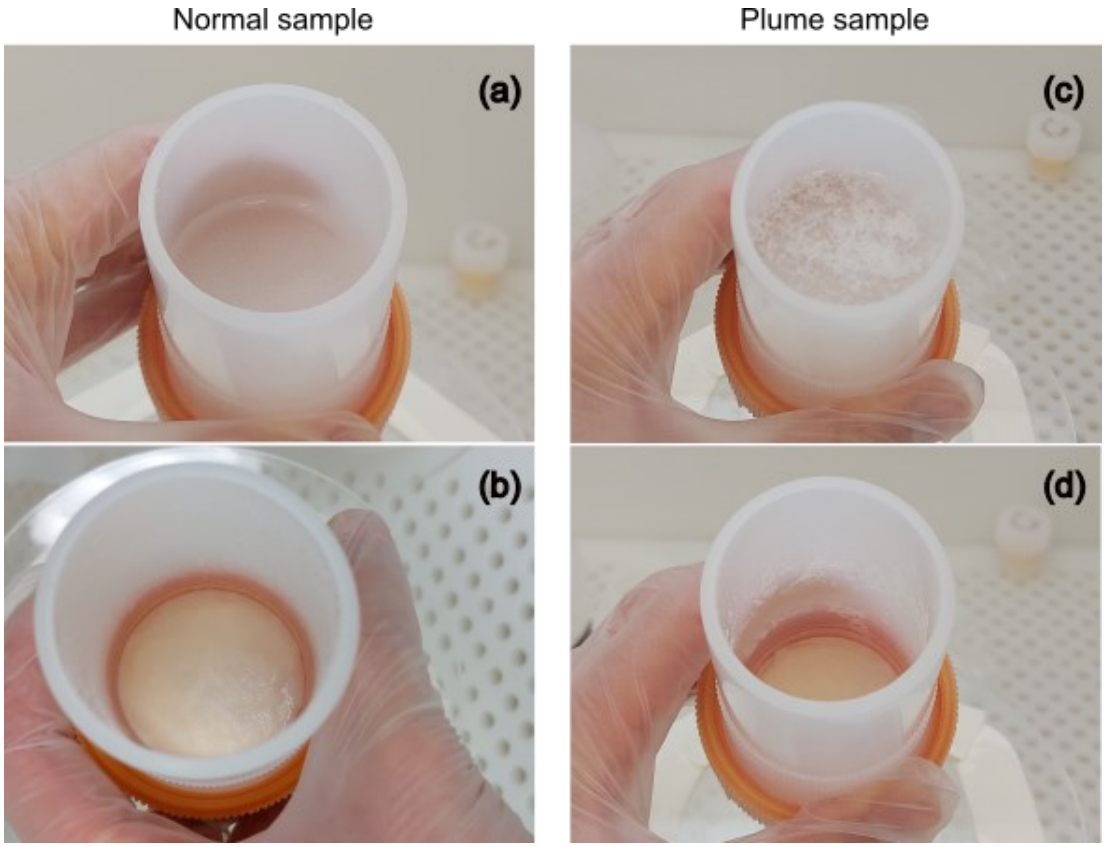


Figure A2. Images of the Nobias Chelate PA-1 resin in the Teflon filter funnel during processing of a normal (non-plume) seawater sample (90 m depth at valley wall station 37; a-b) and a sample from the buoyant TAG hydrothermal plume (3100 m depth at vent site station 35/39; c-d). The upper panels show the resin particles in a liquid suspension. The lower panels show the resin particles accumulated on the filter after the liquid was suctioned off. Note the larger resin clumps in suspension and adhering to the funnel wall in panels (c) and (d) respectively.

Appendix 3. Air Mass Back Trajectory Analyses for the TAG Hydrothermal Area (Chapter 3)

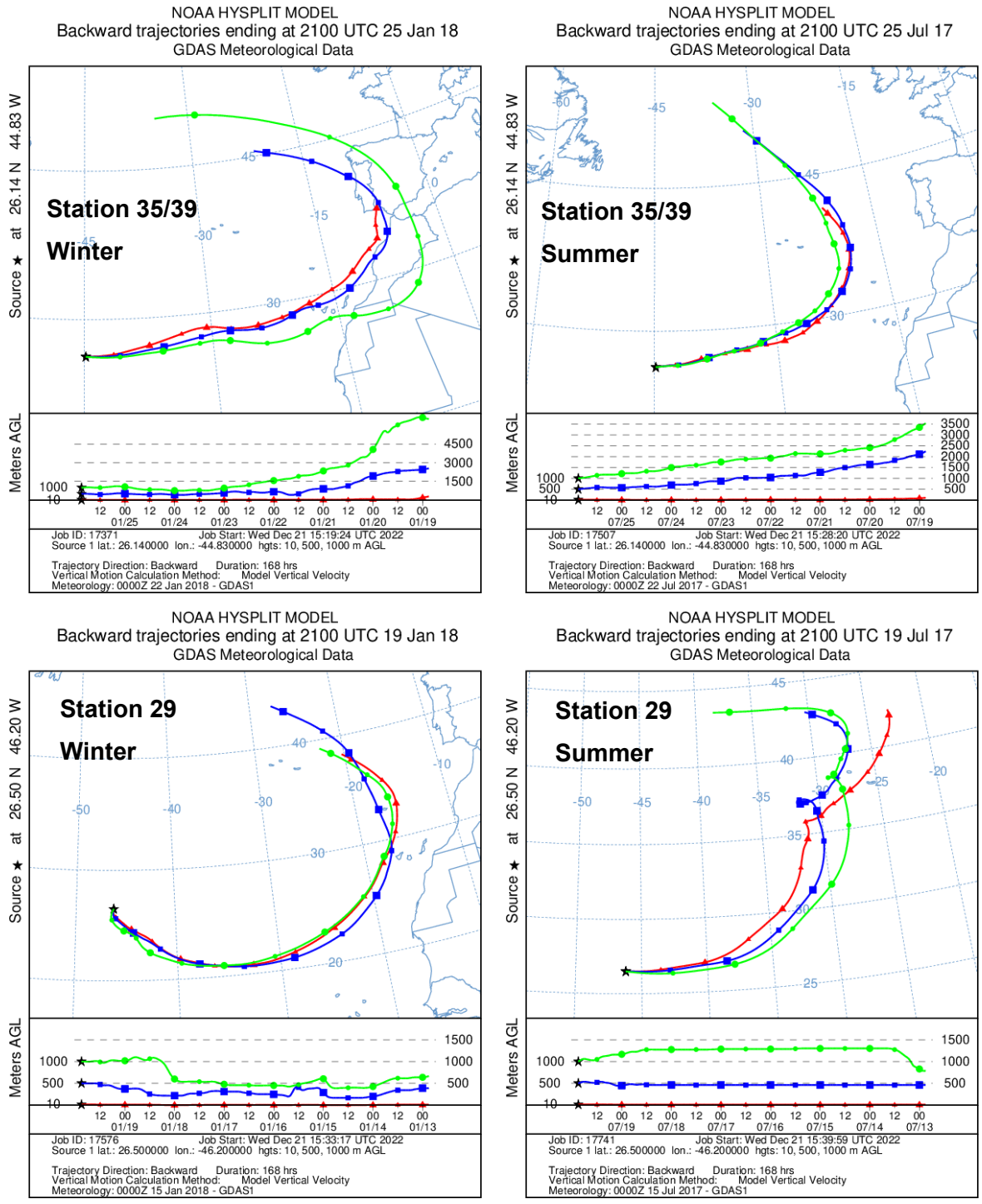


Figure A3. Results of air mass back trajectory analyses for distal W station 29 and vent site station 35/39. Models were run over two 7-day periods for the boreal winter (Jan 2018, 7 days before collection of the seawater samples) and summer (Jul 2017), to capture the annual variation of the atmospheric input. Arrival heights of 10, 500 and 1000 m were used with the model vertical velocity. The results were obtained with the NOAA HYSPLIT (National Oceanic and Atmospheric Administration's HYbrid Single Particle Lagrangian Integrated Trajectory) model using the GDAS Meteorological Data (Draxler and Rolph, 2003).

Appendix 4. Dissolved Pb Concentration Results and Isotope from the GEOTRACES Section GS01 by Griffiths (2019) (Chapter 4)

Table A4. Lead concentration and isotope data for seawater samples from the GEOTRACES section GS01 that were previously presented by Griffiths (2019).

Depth (m)	[Pb][a] (pmol/kg)	1sd[b]	$^{206}Pb/^{207}Pb$[c]	$^{208}Pb/^{207}Pb$[c]	$^{206}Pb/^{204}Pb$[c]	Neutral Density (kg/m^3)	Water Mass
Subantarctic Zone (SAZ)							
Station 15 (49.27°S, 144.09°E; bottom depth: 4292 m)							
14	11.5	0.8	1.149	2.425	17.93	26.51	SASW
49	10.6	0.8	1.151	2.427	17.96	26.52	SASW
97	12.4	0.8	1.153	2.430	18.00	26.62	SASW
295	14.2	0.8	1.147	2.423	17.89	26.96	SAMW
493	11.3	0.8	1.151	2.427	17.97	27.09	AAIW
987	12.4	0.8	1.152	2.427	17.96	27.51	AAIW
1972	11.0	0.8	ND[d]	ND	ND	27.95	UCDW
2953	5.7	0.8	ND	ND	ND	28.11	LCDW
3097	6.5	0.8	ND	ND	ND	28.16	LCDW
Polar Frontal Zone (PFZ)							
Station 30 (54.07°S, 141.60°E; 2563 m)							
13	8.6	0.8	1.153	2.428	17.98	26.88	AASW
48	6.8	0.8	1.156	2.433	18.06	26.94	AASW
98	7.8	0.8	1.158	2.433	18.06	27.35	AASW
296	11.4	0.8	1.156	2.430	18.02	27.63	UCDW
986	10.8	0.8	1.156	2.431	18.02	27.96	UCDW
1726	5.3	0.8	1.171	2.447	18.29	28.07	LCDW
2216	5.2	0.8	1.171	2.445	18.26	28.13	LCDW
2482	4.5	0.8	1.169	2.445	18.22	28.17	LCDW
Antarctic Zone (AZ)							
Station 40 (58.85°S, 139.84°E; 3929 m)							
14	8.6	0.8	1.151	2.426	17.94	26.98	AASW
49	8.1	0.8	1.154	2.429	17.99	26.99	AASW
97	9.8	0.8	1.157	2.432	18.06	27.36	AASW
295	14.5	0.8	1.155	2.430	18.01	27.65	UCDW
493	12.2	0.8	1.158	2.433	18.06	27.79	UCDW
985	10.1	0.8	1.163	2.439	18.16	27.96	UCDW
1971	5.6	0.8	1.173	2.449	18.31	28.10	LCDW
2948	6.7	0.8	1.178	2.458	18.41	28.21	LCDW
3730	6.0	0.8	1.186	2.470	18.54	28.27	AABW

Table A4 (cont'd).

Depth (m)	[Pb][(a)] (pmol/kg)	1sd[(b)]	$^{206}Pb/^{207}Pb$[(c)]	$^{208}Pb/^{207}Pb$[(c)]	$^{206}Pb/^{204}Pb$[(c)]	Neutral Density (kg/m^3)	Water Mass
Antarctic Zone (AZ) (cont'd)							
Station 45 (60.85°S, 139.85°E; 4405 m)							
14	8.5	0.8	1.149	2.425	17.90	27.03	AASW
48	10.2	0.8	1.159	2.435	18.06	27.15	AASW
97	9.2	0.8	1.161	2.437	18.10	27.49	AASW
295	11.6	0.8	1.159	2.435	18.08	27.81	UCDW
493	8.8	0.8	1.161	2.437	18.12	27.90	UCDW
986	9.4	0.8	1.167	2.443	18.21	28.02	LCDW
1970	4.4	0.8	1.174	2.452	18.34	28.13	LCDW
2461	{9.6}**	{0.8}**	1.177	2.457	18.40	28.19	LCDW
4216	7.7	0.8	1.195	2.481	18.70	28.32	AABW
Station 51 (63.86°S, 139.87°E; 3729 m)							
13	5.9	0.8	1.156	2.433	18.03	27.30	AASW
57	4.2	0.8	1.167	2.444	18.21	27.35	AASW
97	6.0	0.8	1.169	2.447	18.26	27.78	AASW
294	6.8	0.8	1.169	2.445	18.25	28.00	UCDW
493	9.7	0.8	1.172	2.449	18.30	28.04	LCDW
986	5.6	0.8	1.168	2.445	18.23	28.10	LCDW
1968	2.8	0.8	1.182	2.462	18.48	28.22	LCDW
3047	3.1	0.8	1.196	2.481	18.73	28.30	AABW
3612	3.6	0.8	1.191	2.472	18.66	28.34	AABW
Continental Zone (CZ)							
Station 56 (65.40°S, 139.85°E; 2386 m)							
13	5.4	0.8	1.167	2.445	18.23	27.38	AASW
48	4.4	0.8	1.175	2.452	18.36	27.40	AASW
97	6.6	0.8	1.185	2.467	ND[(d)]	27.78	AASW
296	6.8	0.8	1.184	2.463	18.51	28.04	LCDW
493	4.9	0.8	1.179	2.457	18.39	28.12	LCDW
986	6.1	0.8	1.179	2.457	18.43	28.22	LCDW
1478	4.6	0.8	1.189	2.466	18.57	28.27	AABW
1970	4.2	0.8	1.186	2.463	18.54	28.32	AABW
2313	5.6	0.8	1.191	2.471	18.64	28.33	AABW

(d) Reported Pb concentrations are the averages of triplicate measurements.
(e) 1× standard deviation of triplicate measurements of Pb concentration in pmol/kg.
(f) Precisions of Pb isotope measurements are given by the 2× standard deviations from replicate analyses of in-house reference materials, which correspond to ~1200 ppm, ~300 ppm and ~1200 ppm for $^{206}Pb/^{207}Pb$, $^{208}Pb/^{207}Pb$ and $^{206}Pb/^{204}Pb$ respectively.
(g) No data.
** Denote Pb concentration data from the ICL laboratory that was potentially affected by contamination, based on comparison with the result from the UTAS laboratory.

Appendix 5. Inter-Laboratory Comparison of Dissolved Pb Concentration Results from the GEOTRACES Section GS01 (Chapter 4)

Table A5. Lead concentration data for filtered seawater samples reported by the laboratories at Imperial College London (ICL) and the University of Tasmania (UTAS).

	ICL			UTAS		
Depth (m)	n-ID[a]	[Pb][b] (pmol/kg)	1sd	[Pb][b] (pmol/kg)	1sd	Deviation in [Pb][c]
Polar Frontal Zone (PFZ)						
Station 30 (54.07°S, 141.60°E; 2563 m)						
13	1	8.6	0.8	6.8	0.3	1.8
48	1	6.8	0.8	No data		
98	1	7.8	0.8	7.3	0.3	0.5
296	3	11.4	0.8	13.0	0.5	-1.6
986	3	10.8	0.8	12.8	0.5	-2.0
1726	1	5.3	0.8	7.5	0.3	-2.2
2216	1	5.2	0.8	6.0	0.2	-0.8
2482	3	4.5	0.8	4.9	0.2	-0.4
Antarctic Zone (AZ)						
Station 40 (58.85°S, 139.84°E; 3929 m)						
14	1	8.6	0.8	7.0	0.3	1.6
49	3	8.1	0.8	5.3	0.2	2.8
97	1	9.8	0.8	7.1	0.3	2.7
295	1	14.5	0.8	10.0	0.4	4.5
493	1	12.2	0.8	9.6	0.4	2.6
985	1	10.1	0.8	9.9	0.4	0.2
1971	1	5.6	0.8	5.1	0.2	0.5
2948	3	6.7	0.8	3.6	0.1	3.1
3730	3	6.0	0.8	3.8	0.2	2.2
Station 45 (60.85°S, 139.85°E; 4405 m)						
14	3	8.5	0.8	4.4	0.2	4.1
48	3	10.2	0.8	5.4	0.2	4.8
97	1	9.2	0.8	7.0	0.3	2.2
295	1	11.6	0.8	9.5	0.4	2.1
493	3	8.8	0.8	9.6	0.4	-0.8
986	1	9.4	0.8	7.7	0.3	1.7
1970	1	4.4	0.8	4.3	0.2	0.1
2461	1	{9.6}**	{0.8}	4.1	0.2	{5.5}
4216	1	7.7	0.8	5.6	0.2	2.1

Table A5 (cont'd).

Depth (m)	ICL n-ID[(a)]	ICL [Pb][(b)] (pmol/kg)	ICL 1sd	UTAS [Pb][(b)] (pmol/kg)	UTAS 1sd	Deviation in [Pb][(c)]
Polar Frontal Zone (PFZ)						
Station 30 (54.07°S, 141.60°E; 2563 m)						
13	1	8.6	0.8	6.8	0.3	1.8
48	1	6.8	0.8	{45.2}*	{1.8}	{-38.4}
98	1	7.8	0.8	7.3	0.3	0.5
296	3	11.4	0.8	13.0	0.5	-1.6
986	3	10.8	0.8	12.8	0.5	-2.0
1726	1	5.3	0.8	7.5	0.3	-2.2
2216	1	5.2	0.8	6.0	0.2	-0.8
2482	3	4.5	0.8	4.9	0.2	-0.4
Antarctic Zone (AZ)						
Station 40 (58.85°S, 139.84°E; 3929 m)						
14	1	8.6	0.8	7.0	0.3	1.6
49	3	8.1	0.8	5.3	0.2	2.8
97	1	9.8	0.8	7.1	0.3	2.7
295	1	14.5	0.8	10.0	0.4	4.5
493	1	12.2	0.8	9.6	0.4	2.6
985	1	10.1	0.8	9.9	0.4	0.2
1971	1	5.6	0.8	5.1	0.2	0.5
2948	3	6.7	0.8	3.6	0.1	3.1
3730	3	6.0	0.8	3.8	0.2	2.2
Station 45 (60.85°S, 139.85°E; 4405 m)						
14	3	8.5	0.8	4.4	0.2	4.1
48	3	10.2	0.8	5.4	0.2	4.8
97	1	9.2	0.8	7.0	0.3	2.2
295	1	11.6	0.8	9.5	0.4	2.1
493	3	8.8	0.8	9.6	0.4	-0.8
986	1	9.4	0.8	7.7	0.3	1.7
1970	1	4.4	0.8	4.3	0.2	0.1
2461	1	{9.6}**	{0.8}	4.1	0.2	{5.5}
4216	1	7.7	0.8	5.6	0.2	2.1

Table A5 (cont'd).

Depth (m)	ICL n-ID[(a)]	ICL [Pb][(b)] (pmol/kg)	ICL 1sd	UTAS [Pb][(b)] (pmol/kg)	UTAS 1sd	Deviation in [Pb][(c)]
Antarctic Zone (AZ) (cont'd)						
Station 51 (63.86°S, 139.87°E; 3729 m)						
13	1	5.9	0.8	7.9	0.3	-2.0
57	1	4.2	0.8	5.9	0.2	-1.7
97	1	6.0	0.8	7.8	0.3	-1.8
294	3	6.8	0.8	8.9	0.4	-2.1
493	1	9.7	0.8	7.2	0.3	2.5
986	1	5.6	0.8	5.9	0.2	-0.3
1968	1	2.8	0.8	3.9	0.2	-1.1
3047	1	3.1	0.8	4.2	0.2	-1.1
3612	1	3.6	0.8	5.1	0.2	-1.5
Continental Zone (CZ)						
Station 56 (65.40°S, 139.85°E; 2386 m)						
13	3	5.4	0.8	2.9	0.2	2.5
48	1	4.4	0.8	3.3	0.2	1.1
97	1	6.6	0.8	5.0	0.3	1.6
296	1	6.8	0.8	6.8	0.5	0.0
493	1	4.9	0.8	6.7	1.1	-1.8
986	1	6.1	0.8	3.8	0.3	2.3
1478	1	4.6	0.8	3.5	0.2	1.1
1970	1	4.2	0.8	3.1	0.2	1.1
2313	1	5.6	0.8	3.6	0.3	2.0

(a) Number of measurements conducted for Pb concentrations at the ICL laboratory.
(b) For samples with triplicate measurements, the averages of triplicate values are reported. Curly brackets highlight the Pb concentration values that were potentially affected by contamination, and their deviations to the values of the same sample from the other laboratory.
(c) Denote the deviation of the ICL value relative to the UTAS value. Positive is excess in the ICL value.
* Denote values that were flagged as bad by the UTAS laboratory (GEOTRACES Intermediate Data Product Group, 2021).
** Denote value from the ICL laboratory that is flagged as bad in this study based on inter-laboratory comparison.

Appendix 6. Behaviour of Pb in Hydrothermal Plumes along the GEOTRACES Section GS01 (Chapter 4)

During the GS01 transect, coupled enrichments in dissolved Mn and Fe above their background levels (~0.25 nmol/kg for Mn; ~0.6 nmol/kg for Fe) associated with hydrothermal activities on the Southeast Indian Ridge were detected above and in the vicinity of the ridge crest (Fig. A6) (Latour et al., 2021; Tagliabue et al., 2022a). These plumes of hydrothermal Mn and Fe enrichments primarily reside in the LCDW layer (γ^n = 28.00-28.17; > 2000 m depth) and extend latitudinally between ~47°S to the north (SAZ) and ~59°S to the south (northern part of the AZ), across an extent of about 1300 km. Relatively strong enrichments in dissolved Mn and Fe ("hotspots") were detected above and on the northern flank of the Southeast Indian Ridge. At PFZ station 30 above the ridge crest, the strongest enrichments in Mn (~10-fold) and Fe (~5-fold) were detected across depths of 1800 and 2400 m (γ^n = 28.09-28.17) near the seafloor, reaching maxima of 2.4 nmol/kg (Mn) and 3.4 nmol/kg (Fe) at 2216 m (Fig. A6d). On the northern ridge flank, hotspots up to 1-2 nmol/kg of Mn and ~1 nmol/kg of Fe were detected at the SAZ stations 15 and 23 (Fig. A6b, c), in a lighter density range (γ^n = 28.00-28.09; 2000-2700 m) at station 23 and across a larger vertical extent (1900-3300 m; γ^n = 27.95-28.17) at station 15.

The Pb concentration and isotope signatures in the hydrothermal plumes are assessed against the signatures at station 45 in the ACC region and station 9 in the SAZ respectively, which exhibit no hydrothermal enrichments in dissolved Mn and Fe and therefore define the ambient LCDW characteristics (Fig. A6a, e). Above the ridge crest (station 30), where the strongest plume signals were detected, the Pb concentrations (5.2 and 4.5 pmol/kg) within the plume depths (2216 and 2482 m) are analytically identical to the LCDW samples above the plume (5.3 pmol/kg, 1726 m) and at station 45 (4.4 pmol/kg, 1967 m), while the $^{206}Pb/^{207}Pb$ ratios within the plume depths (1.171, 1.169) are identical to that above the plume (1.171) and somewhat slightly lower than at station 45 (1.174) (Fig. A6d, e). At the SAZ station 15, the Pb concentration of the plume sample (5.7 pmol/kg, 2952 m) is also analytically identical to the ambient levels at station 9 in the same depth range (6.1 pmol/kg, 2457 m) (Fig. A6a, b).

Based on the limited data, it can be concluded that hydrothermal activities exert negligible impact on the dissolved Pb budget along the GS01 transect. This can be attributed to the distal locations of the plumes, > 300 km to the east of potential vent sources (Boulart et al., 2017; Latour et al., 2021), the quantitative removal of hydrothermal Pb close to the vent sources, as well as minimal hydrothermal scavenging of dissolved Pb by Fe-Mn oxyhydroxide particles. Alternatively, venting of low-temperature hydrothermal fluids (Latour et al., 2021), which are less enriched in Pb (< ~10 folds) compared to high-temperature fluids (between ~10^3 and ~10^4 folds) (Douville et al., 2002), could explain the lack of Pb concentration and isotope anomalies in the plumes.

At the SAZ station 23, anomalously higher Pb concentration (11.8 pmol/kg) and lower $^{206}Pb/^{207}Pb$ (1.150) and $^{208}Pb/^{207}Pb$ (2.426) ratios are found just below the plume depth (2953 m). This sample is found to also show an anomalous depletion in dissolved Mn and Fe (0.3 nmol/kg for both elements) (Fig. A6c). The low- $^{206}Pb/^{207}Pb$ and $^{208}Pb/^{207}Pb$ anthropogenic signature is most likely derived from surface-derived sinking particles or resuspended bottom sediments enriched in anthropogenic Pb. The enrichment in dissolved Pb concentration compared to the deficits in Mn and Fe for this sample is surprising. This observation can be attributed to unusual dissolved-particulate exchange processes near the base of the hydrothermal plume, in which most other trace metals were preferentially scavenged into the particulate phase, while anthropogenic Pb in the particulate phase, which is concentrated in relatively labile chemical species (Chester et al., 1989; Maring and Duce, 1990; Fishwick et al., 2018), is preferentially released.

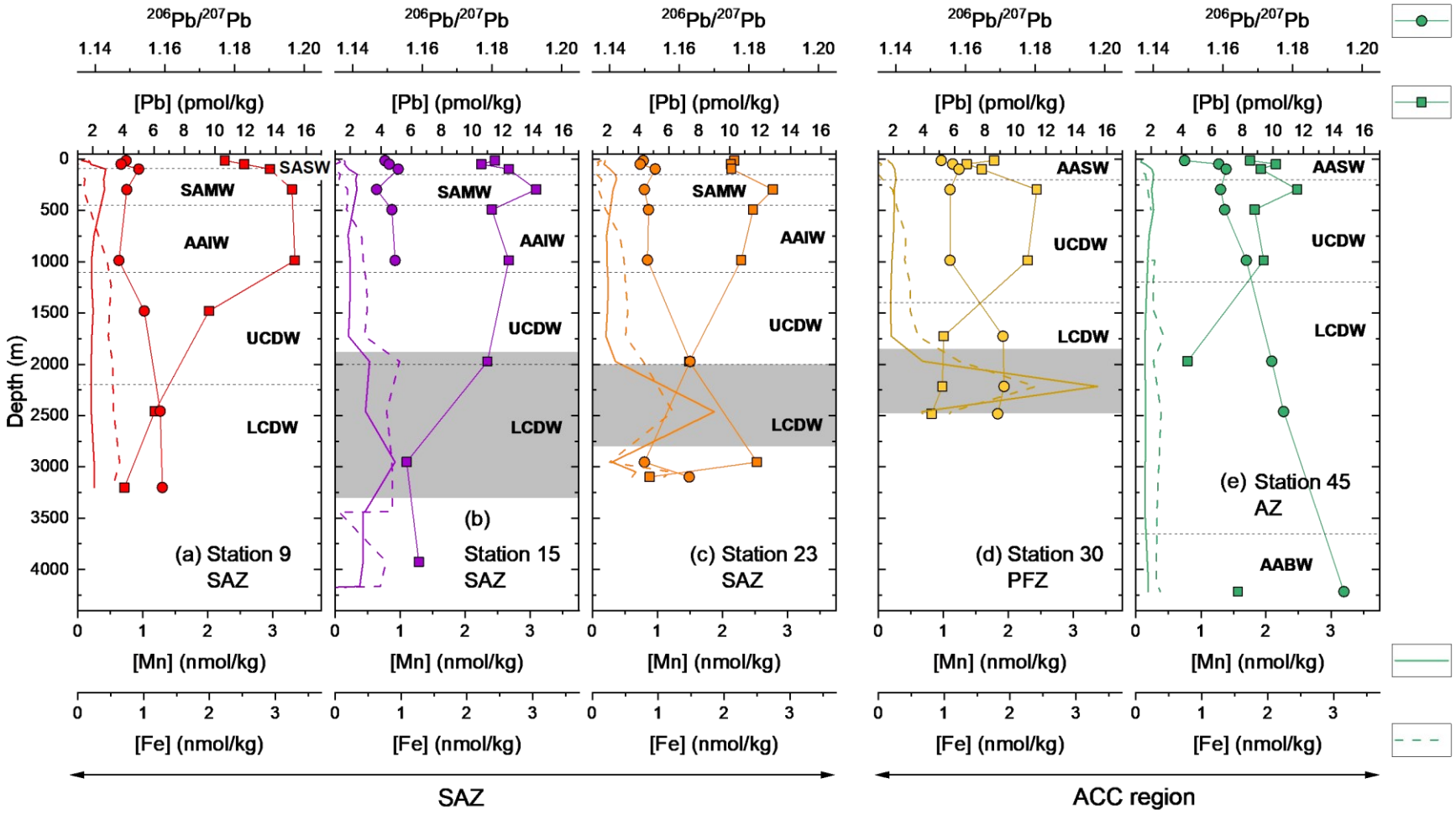


Figure A6. Detection of sediment dissolution and hydrothermal plume. Vertical profiles of dissolved Pb concentrations (squares), $^{206}Pb/^{207}Pb$ ratios (circles), Mn concentrations (solid lines) and Fe concentrations (dashed lines) for the three SAZ stations (9, 15 and 23, panels a-c), the PFZ station (30, panel d) and an AZ station (45, panel e). The dissolved Mn and Fe data were generated by Andrew Bowie et al. at UTAS and were retrieved from the GEOTRACES IDP 2021 (GEOTRACES Intermediate Data Product Group, 2021). Grey shades denote the depth ranges with plume-associated enrichments in dissolved Mn (> ~0.25 nmol/kg) and Fe (> ~0.6 nmol/kg) above the deep ocean background. Flagged value of Pb concentration is omitted for clarity. Thin, horizontal dashed lines mark the approximate depth horizons of major water masses.

Bibliography for the Appendices

Boulart C., Briais A., Chavagnac V., Révillon S., Ceuleneer G., Donval J.-P., Guyader V., Barrere F., Ferreira N., Hanan B., Hémond C., Macleod S., Maia M., Maillard A., Merkuryev S., Park S.-H., Ruellan E., Schohn A., Watson S. and Yang Y.-S. (2017) Contrasted hydrothermal activity along the South-East Indian Ridge (130°E-140°E): From crustal to ultramafic circulation. *Geochem, Geophys, Geosyst* **18**, 2446–2458.

Chester R., Lin F. J. and Murphy K. J. T. (1989) A three stage sequential leaching scheme for the characterisation of the sources and environmental mobility of trace metals in the marine aerosol. *Environ Technol* **10**, 887–900.

Douville E., Charlou J. L., Oelkers E. H., Bienvenu P., Jove Colon C. F., Donval J. P., Fouquet Y., Prieur D. and Appriou P. (2002) The rainbow vent fluids (36°14′N, MAR): The influence of ultramafic rocks and phase separation on trace metal content in Mid-Atlantic Ridge hydrothermal fluids. *Chem Geol* **184**, 37–48.

Draxler R. R. and Rolph G. D. (2003) HYSPLIT (HYbrid Single-Particle Lagrangian Integrated Trajectory) Model access via NOAA ARL READY Website. NOAA Air Resources Laboratory, Silver Spring, MD. https://www.ready.noaa.gov/HYSPLIT.php.

Erhardt A. M., Douglas G., Jacobson A. D., Wimpenny J., Yin Q. Z. and Paytan A. (2021) Assessing Sedimentary Detrital Pb Isotopes as a Dust Tracer in the Pacific Ocean. *Paleoceanogr Paleoclimatol* **36**.

Fishwick M. P., Ussher S. J., Sedwick P. N., Lohan M. C., Worsfold P. J., Buck K. N. and Church T. M. (2018) Impact of surface ocean conditions and aerosol provenance on the dissolution of aerosol manganese, cobalt, nickel and lead in seawater. *Mar Chem* **198**, 28–43.

GEOTRACES Intermediate Data Product Group (2021) The GEOTRACES Intermediate Data Product 2021 (IDP2021). *NERC EDS British Oceanographic Data Centre NOC*.

Gili S., Gaiero D. M., Goldstein S. L., Chemale F., Jweda J., Kaplan M. R., Becchio R. A. and Koester E. (2017) Glacial/interglacial changes of Southern Hemisphere wind circulation from the geochemistry of South American dust. *Earth Planet Sci Lett* **469**, 98–109.

Gili S., Gaiero D. M., Goldstein S. L., Chemale Jr F., Koester E., Jweda J., Vallelonga P. and Kaplan M. R. (2016) Provenance of dust to Antarctica: A lead isotopic perspective. *Geophys Res Lett* **43**, 2291–2298.

Ginoux P., Prospero J. M., Gill T. E., Hsu N. C. and Zhao M. (2012) Global-scale attribution of anthropogenic and natural dust sources and their emission rates based on MODIS Deep Blue aerosol products. *Rev of Geophys* **50**.

Griffiths A. (2019) Tracing water masses and pollution in the Southern Ocean using neodymium and lead isotopes. PhD Thesis, Imperial College London.

Jones C. E., Halliday A. N., Rea D. K. and Owen R. M. (2000) Eolian inputs of lead to the North Pacific. *Geochim Cosmochim Acta* **64**, 1405–1416.

Jones C. E., Halliday A. N., Rea D. K. and Owen R. M. (1994) Neodymium isotopic variations in North Pacific modern silicate sediment and the insignificance of detrital REE contributions to seawater. *Earth Planet Sci Lett* **127**, 55–66.

Latour P., Wuttig K., van der Merwe P., Strzepek R. F., Gault-Ringold M., Townsend A. T., Holmes T. M., Corkill M. and Bowie A. R. (2021) Manganese biogeochemistry in the Southern Ocean, from Tasmania to Antarctica. *Limnol Oceanogr* **66**, 2547–2562.

Maring H. B. and Duce R. A. (1990) The impact of atmospheric aerosols on trace metal chemistry in open ocean surface seawater. 3. Lead. *J Geophys Res* **95**, 5341–5347.

Stern C. R. (2004) Active Andean volcanism: its geologic and tectonic setting. *Rev Geol Chile* **31**.

Tagliabue A., Bowie A. R., Holmes T., Latour P., van der Merwe P., Gault-Ringold M., Wuttig K. and Resing J. A. (2022a) Constraining the Contribution of Hydrothermal Iron to Southern Ocean Export Production Using Deep Ocean Iron Observations. *Front Mar Sci* **9**.